Exploring photoswitching pathways in photomagnetic materials with ultrafast optical and X-ray spectroscopies

S. Zerdane

THÈSE / UNIVERSITÉ DE RENNES 1
sous le sceau de l'Université Bretagne Loire

pour le grade de

DOCTEUR DE L'UNIVERSITÉ DE RENNES 1

Mention : Physique

Ecole doctorale Matière, Molécules et Matériaux (3M)

Serhane Zerdane

Préparée à l'unité de recherche :
Institut de Physique de Rennes UMR CNRS 6251

Exploring photoswitching pathways in photomagnetic materials with ultrafast optical and X-ray spectroscopies

Thèse soutenue à l'Université de Rennes 1
Le 04 Octobre 2017

devant le jury composé de :

Corine MATHONIERE
Professeur, Université de Bordeaux / *rapporteur*

Philippe SAINCTAVIT
Directeur de recherche, CNRS, Université Pierre et Marie Curie / *rapporteur*

Anne BLEUZEN
Professeur, Université Paris-Sud / *examinateur*

Marco CAMMARATA
Chargé de recherche, CNRS, Université de Rennes1 / *co-directeur de Thèse*

Eric COLLET
Professeur, Université de Rennes1 / *directeur de Thèse*

À la mémoire de mon oncle

Lakhdar Zerdane

"*Nothing happens until something moves"*

Albert Einstein

Remerciements

J'aimerais tout d'abord adresser mes plus sincères remerciements à mes directeurs de thèse: ***Marco Cammarata*** *et* ***Eric Collet****. Je leurs suis très reconnaissant de leur soutien, aide, orientation et conseils permanant tout au long de ces trois ans de thèse. Je les remercie de m'avoir transmis une partie de leur savoir que j'ai essayé de retransmettre au mieux dans ce mémoire. Je suis ravi d'avoir travaillé avec eux.*

Je tiens à remercier tout particulièrement ***Corine Mathonière*** *et* ***Philippe Sainctavit****, qui ont accepté d'évaluer ce travail de thèse en tant que rapporteurs, pour leur lecture attentive et leurs remarques qui ont été très appréciable. Je tiens aussi à sincèrement remercier* ***Anne Bleuzen*** *d'avoir accepté de présider ce jury.*

Je remercie la Région Bretagne et l'Agence Nationale de la Recherche (ANR) pour le soutien financier au cours de ce travail de thèse.

Mes remerciements s'adressent également aux personnes extérieures qui ont largement contribué aux résultats présentés dans ce manuscrit, et avec qui nous avons développé une collaboration fructueuse:

- ***Marie-Laure Boillot****,* ***Talal Mallah****,* ***Olga Iasco****,* ***Sandra Mazerat*** *et* ***Laure Catala*** *de l'Institut de Chimie Moléculaire et des Matériaux d'Orsay (ICMMO).*
- ***Samir F. Matar*** *et* ***Guillaume Chastanet*** *de l'Institut de Chimie de la Matière Condensée de Bordeaux (ICMCB).*
- ***Ilaria Ciofini*** *et* ***Liam Wilbraham*** *de l'Ecole Nationale Supérieure de Chimie de Paris (ENSCP).*

Je tiens à remercier particulièrement ***Maciej Lorenc*** *auprès de qui j'ai beaucoup appris sur les spectroscopies femtosecondes, ainsi que* ***Roman Bertoni*** *pour m'avoir aidé et encouragé. Un grand merci à* ***Elzbieta Trzop*** *pour les mesures de diffraction de rayons X. Je remercie aussi* ***Jean-Claude Ameline****, pour son soutien technique dans les mesures à basse température optique et de diffraction de rayons X.*

J'aimerais aussi remercier toutes les personnes du département « Matériaux et Lumière »: ***Céline Mariette****,* ***Marina Servol****,* ***Bertrand Toudic****,* ***Claude Ecolivet****,* ***Hervé Cailleau****,* ***Laurent Guérin****,* ***Marylise Buron****, et* ***Philippe Rabiller****, pour leurs précieux conseils, les discussions scientifiques et non scientifiques.*

Un grand merci est réservé aux nouveaux Docteurs ***Andrea Marino*** *et* ***Liya Khadeeva****, et aux Doctorants:* ***Lodovico Balducci*** *et* ***Xu Dong****, pour leurs soutiens et les bons moments qu'on a passés ensemble.*

Je voudrais aussi remercier toutes les personnes que j'ai rencontrées auprès des grands instruments : ***Michael Wulff****,* ***Martin N. Pedersen*** *et* ***Matteo Levantino*** *sur la ligne de lumière ID09 à l'European Synchrotron Radiation Facility (ESRF, Grenoble) et* ***Pierre Fertey*** *sur la ligne de lumière Cristal au synchrotron Soleil et enfin* ***Sanghoon Soog*** *et* ***Roberto Alonso-Mori*** *sur la station expérimentale XPP au X-FEL LCLS de l'université de Stanford.*

J'aimerais remercier tout le personnel de l'IPR pour l'accueil et les moyens à disposition pour le bon déroulement de cette thèse et plus particulièrement l'équipe administrative: ***Nathalie Mabic****,* ***Nathalie Gicquiaux****,* ***Magali Marcault*** *et* ***Valérie Ferri****.*

Pour terminer, j'aimerai remercier mes parents, pour leur soutien et encouragement à distance. Merci à tous ceux qui m'ont soutenu de près ou de loin.

Trugarez, ⵜⴰⵏⵎⵎⵉⵔⵜ, Merci, Thank you, Grazie, Dziękuję!

Résumé

Le travail de thèse a pour objectif principal d'étudier la dynamique ultrarapide de photocommutation de matériaux magnétiques. Ces composés sont des systèmes moléculaires bistables possédant deux configurations électroniques et structurales distinctes. Deux types de composés ont été étudiés dans le cadre de ces travaux de recherche. Le premier type de composé concerne des systèmes à transition de spin dont le champ de ligand est non-octaédrique. Ce système présente deux états de multiplicité de spin différents, nommés Haut Spin (HS) et Bas Spin (BS), il peut transiter entre ces deux états sous l'effet d'une perturbation extérieure comme la température, la pression ou la lumière. Le mécanisme de commutation de l'état BS à l'état HS sous irradiation lumineuse est connu sous le nom de Light Induced Excited Spin State Trapping (LIESST). Le deuxième type de composé étudié est un Analogue du Bleu de Prusse. Ce système présente un transfert de charge, entre deux centres métalliques lié à une transformation entre deux états magnétiques. Cette transformation peut aussi être induite sous l'application d'un champ extérieur (lumière, pression ou température).

Le développement de nouvelles sources laser femtoseconde permet de photocommuter de façon ultrarapide (~ 100 fs) l'état de ces différents types de systèmes et d'étudier les processus de commutation photoinduits qui s'accompagnent d'une séquence de processus physiques hors équilibre thermodynamique durant lesquels différents degrés de liberté de ces systèmes vont évoluer vers un nouvel équilibre.

Afin d'étudier les processus élémentaires, nous avons utilisé différentes techniques ultrarapides pompe-sonde, basées toutes sur le principe de stroboscopie : un pulse initial excite le système dans un état voulu (pompe) et un autre pulse le sonde à différents temps de façon à reconstruire l'évolution de l'état du système suite à cette excitation initiale (Fig. 1).

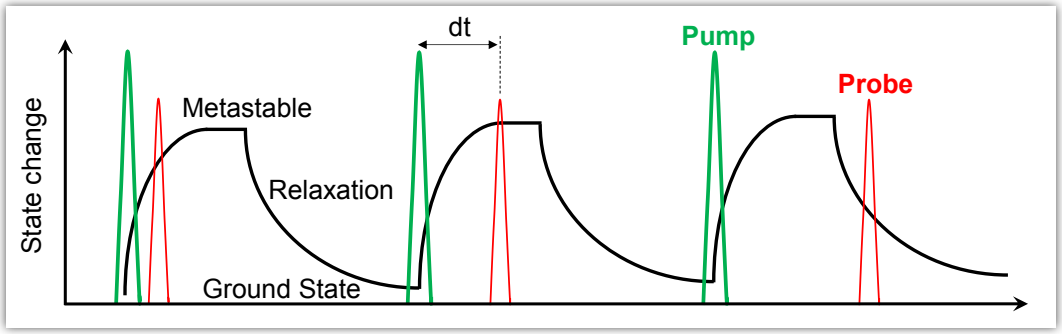

Figure 1: Schéma du principe de la méthode pompe-sonde.

Une partie des résultats présentés repose sur les mesures de spectroscopie optique ultrarapide réalisées sur la plateforme laser femtoseconde de l'Institut de Physique de Rennes. Ces mesures permettent de suivre la variation de l'absorption optique du composé avec une résolution temporelle de l'ordre de la centaine de femtosecondes. Cette technique est particulièrement sensible aux changements électroniques et elles permettent de déceler la formation d'états excités transitoires générés durant le processus de photocommutation et nous renseigne sur la présence d'une éventuelle dynamique cohérente.

Afin de mieux comprendre l'aspect structural et électronique impliqués dans ce processus de transformation ultrarapide, il nous a fallu compléter les mesures optiques femtoseconde par des mesures d'absorption de rayons X (XAS) résolues en temps. Pour cela, nous avons développé et réalisé des expériences de XAS sur la ligne de lumière ID09b à l'*European Synchrotron Radiation Facility* (ESRF, Grenoble). Celles-ci nous ont permis de suivre l'évolution du système après l'excitation avec une résolution temporelle de 100 ps. Nous avons également effectué des expériences de XAS femtoseconde au *X-ray Free Electron Laser* (X-FEL) LCLS de Stanford. Il s'agit du premier Laser à électron libre qui délivre des impulsions de rayons X extrêmement intenses avec une résolution temporelle de 30 fs. Ces expériences nous ont permis d'avoir une signature de la dynamique électronique et structurale sub-picoseconde du processus de transition de spin et de transfert de charge.

- **Systèmes à transition de spin non-octaédriques**

La première partie de ce travail de thèse porte sur l'étude la photocommutation ultrarapide dans des matériaux a transition de spin. Nous nous sommes particulièrement intéressés à la classe de systèmes moléculaires non-octaédriques à base de Fe(II) : $Fe^{II}(pap\text{-}5NO_2)_2$ et $Fe(L_{222}N_5)(CN)_2$. Ces systèmes offrent de nouvelles possibilités pour contrôler par la lumière et donc mieux comprendre l'effetLIESST grâce à leurs basses symétries moléculaires, donnant accès à différents types d'états électroniques -bandes MLCT (Metal Ligand Charge Tranfer) et d-d intenses-. Ces études se concentrent sur la nature de la dynamique structurale cohérente et le rôle des états intermédiaires dans la décohérence. L'objectif est de mieux comprendre comment la durée de vie et le nombre d'états intermédiaires peuvt affecter la cohérence structurale. Cependant, en raison de la symétrie presque octaédrique des systèmes FeN_6, la transition d-d est très faible ou interdite, Pour cette raison, le LIESST a été principalement étudié sur des échelles de temps femtoseconde avec des excitations MLCT.

Pour mieux comprendre la cohérence structurale liée à l'effet LIESST, nous avons directement comparé (sur la même molécule) les différents schémas d'excitation impliquant des intermédiaires possédant de temps de vie plus ou moins longs. En d'autres termes, la réduction du nombre d'intermédiaires ou de leur durée de vie devrait contribuer à accroître la cohérence.

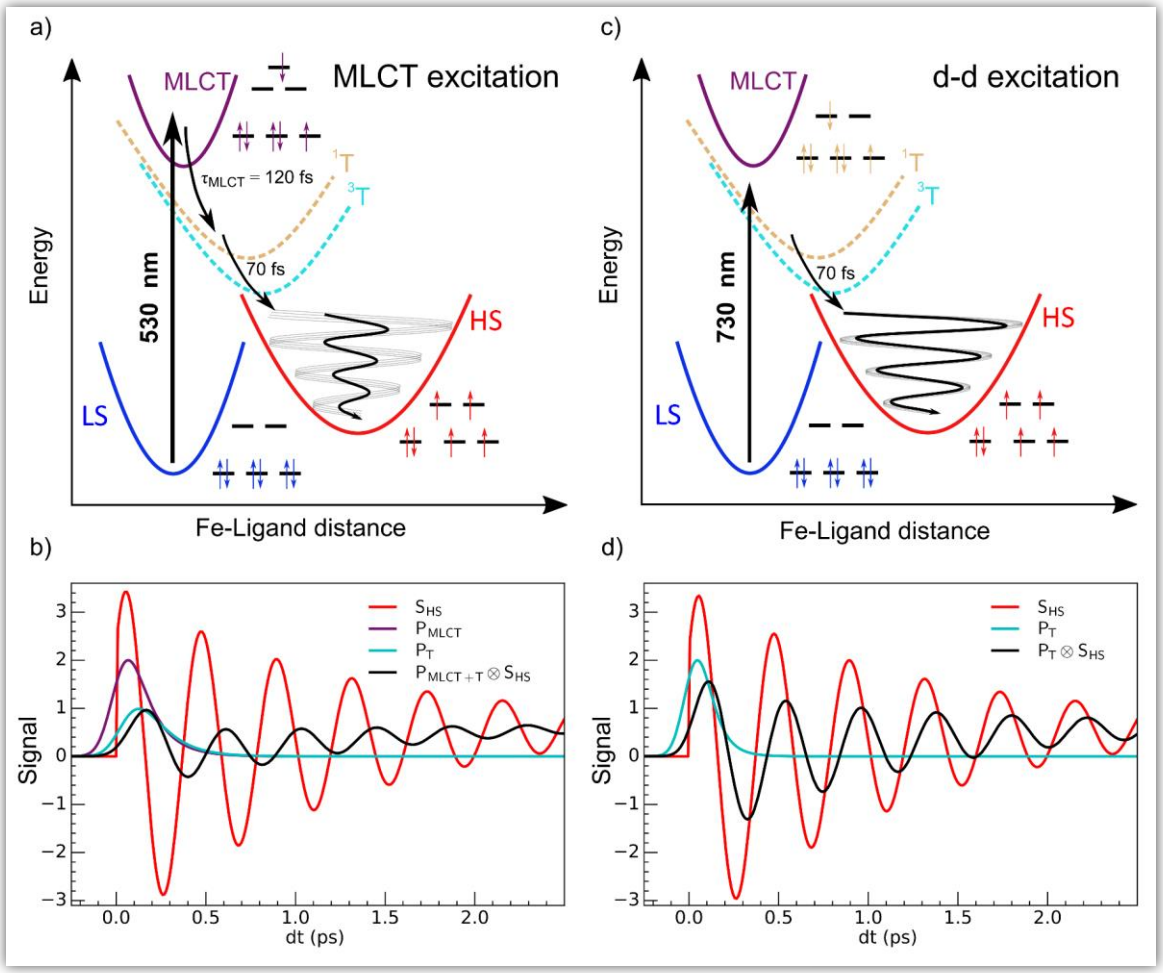

Figure 2 : Comparaison des processus LIESST avec l'excitation MLCT et d-d

La figure 2 compare deux chemins possibles de LIESST de l'état BS vers l'état HS sous la photo-excitation MLCT ou d-d. La dynamique femtoseconde observée dans les systèmes de basse symétrie est très similaire à celle de systèmes octaédriques FeN_6. L'effet LIESST est associé à l'activation et l'amortissement rapide du mode de respiration moléculaire : comme les orbitales anti-liant sont peuplées, cela augmente la distance d'équilibre Fe-Ligand et piège le système dans le potentiel HS comme démontré dans d'autres systèmes (Cammarata *et al.*, 2014; Bertoni *et al.*, 2015; Auböck & Chergui, 2015; Marino *et al.*, 2016; Consani *et al.*, 2009).

Nos résultats montrent qu'en réduisant la durée de vie des intermédiaires par rapport à l'excitation MLCT, l'excitation d-d permet transition LS→HS plus rapide et préserve la

cohérence de la respiration structurale lorsque la coordonnée de réaction moléculaire Fe-Ligand est activée et amortie pour piéger l'état HS.

- **Systèmes à transfert de charge (Analogue du Bleu de Prusse)**

Les Analogues du bleu de Prusse sont des systèmes prototypes constitués de réseaux cubiques formés de cations métalliques reliés entre eux par un pont de cyanure (CN). Nous nous sommes intéressé à l'étude de la dynamique structurale et électronique dans le compose $CsCoFe(CN)_6$. Ce système est formé essentiellement de paires diamagnétiques $Co^{III}_{(BS)}Fe^{II}_{(BS)}$, qui peuvent être convertie en paires paramagnétiques $Co^{II}_{(HS)}Fe^{III}_{(BS)}$ par irradiation lumineuse à très basse température de façon persistante et à haute température de façon transitoire. Ce changement d'état magnétique est piloté par le transfert d'un électron du Fe vers le Co et la transition de spin autour du Co (BS→HS), Malgré la grande variété d'études scientifiques dans ces dernières décennies, par exemple avec de l'optique (Arnett *et al.*, 1995), de la diffraction de rayons X (Moritomo *et al.*, 2009) et d'absorption de rayons X (Cafun *et al.*, 2012), le mécanisme de la commutation n'est pas encore compris. Le transfert de charge conduit-il la transition de spin de spin ou vice versa ? L'image physique est compliquée par le fait que beaucoup de bandes d'absorptions sont théoriquement prévues s'étendant d es excitations de transfert de charge aux excitations électroniques sur les métaux.

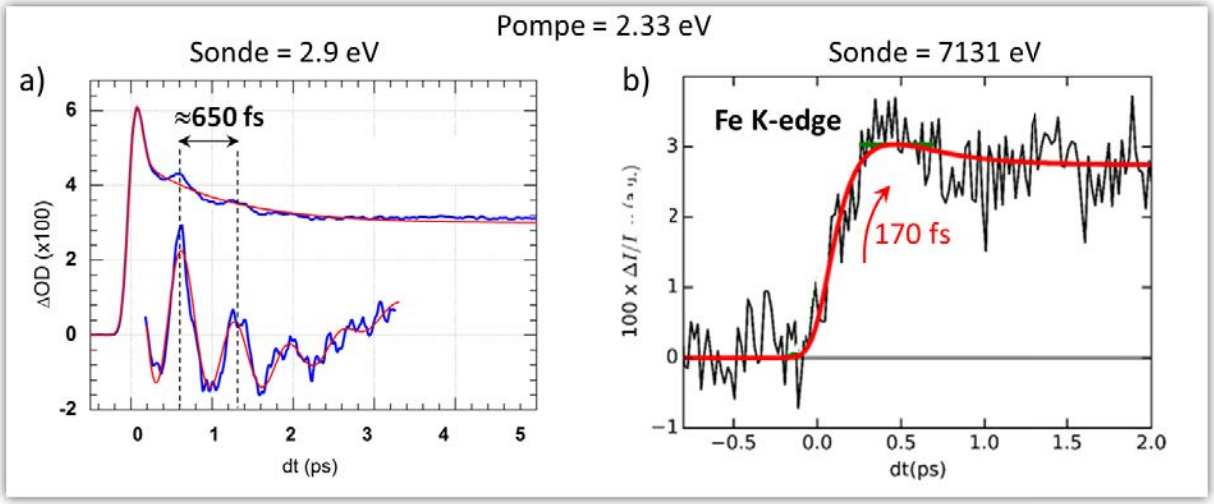

Figure 3: Réponse de $CsCoFe(CN)_6$ à une excitation femtoseconde 530nm pour différentes longueurs d'onde de sonde.

Nos résultats ont montré que le processus est lié à une photo-excitation initiale d-d centrée sur le Co et dont l'intensité n'est pas nulle dans la plage 530-560 nm, comme confirmé par calculs TD-DFT. Nos mesures optiques femtosecondes mettent en évidence un processus ultra-

rapide accompagné d'oscillation cohérentes. Les expériences XAS picoseconde, réalisées aux seuils de Fe et du Co, mettent en évidence le transfert de charge et la transition de spin ≈200 fs après excitation par impulsion laser à 530 nm.

Table of Contents

General Introduction

The current challenge in the science of bistable molecular materials is to control the physical properties (magnetism, conductivity …) which can change under an external perturbation such as pressure, temperature and light. For that, it is necessary to understand at the scale of the molecule and at atomic motion timescale, how these physical properties evolve under the effect of a stimulation. That is fundamental step for the development of new technologies, such as the storage of information on a single molecule which can lead to a very high density of information stored in a nanostructures.

The objective of this thesis is to study the ultrafast dynamics of photoswitching in photomagnetic materials, using complementary techniques in order to follow in real-time the electronic and structural changes after laser pulse excitation. Here we used x-ray powder diffraction, optical pump-probe and time resolved x-ray absorption. These techniques are particularly useful because they make it possible to detect the formation of transient excited states generated during the photo-switching process, informs us of the presence of a possible coherent dynamic and intermediate states, follow local structural changes at the femtosecond and picosecond scale.

During this thesis, we studied the photoswitching of two types of system:

Spin crossover materials: Two compounds are studied, the first is nanocrystals of $Fe^{II}(pap\text{-}5NO_2)_2$ complex which presents a first order transition at 297 K from the low spin (LS) to high spin stat (HS). The second is $Fe(L_{222}N_5)(CN)_2$ complex, this system possesses an stable photoinduced HS state below ~110 K.

Charge transfer materials: the other system studied is the nanocrystals of $CsCoFe(CN)_6$ Prussian Blue Analogues (PBA) which present a magnetic transition from diamagnetic to paramagnetic state at 10 K under light irradiation. This transformation involved two processes, charger transfer from Fe to Co sites and spin transition Co(LS) to Co(HS).

This manuscript is divided into four chapters:

The first chapter: is devoted to the very brief presentation of the thermal and photo induced phase transition and the ultrafast studies carried out by several research groups, of the dynamics in different spin crossover and charge transfer materials.

The second chapter: will be a description of experimental techniques used during my thesis (x-ray diffraction, femtosecond spectroscopy, time-resolved x-ray absorption). A detailed description of the x-ray absorption experiment which we developed at ID09b beamline at ESRF, will be presented in this section. We will detail the physical principles and the technical details of each experimental set-up and the methods of data analysis.

The third chapter: is devoted to the study of ultrafast photoswitching in spin-crossover (SCO) materials. Part of this work was recently published (Zerdane *et al.*, 2017). We introduce the main work carried out on ultrafast dynamics in SCO materials. Then we will discuss how the electronic and structural properties evolve with temperature. In a second step, we will present our optical pump-probe measurements, which will be interpreted using the DFT and TD-DFT calculations. We will then explain the elementary mechanisms of the ultrafast transition and the role of the intermediate state.

The fourth chapter: aims to investigate the ultrafast dynamics in charge transfer materials. For this purpose we have studied the nanocrystals of $CsCoFe(CN)_6$ Prussian Blue Analogue (PBA). We will present our pump-probe optical measurements and x-ray absorption. Part of this work was also recently published. We will propose an interpretation of the photoinduced switching processes based on theoretical and experimental results.

Chapter 1

Photomagnetic Materials

1.1 Thermal and photo induced phase transition

In the family of bistable materials, many molecular systems in solids can exhibit two stable states, possessing different physical properties. In such materials, it is possible to switch from one stable state to another by an external stimuli such as a variation of pressure, temperature and light (Sato et al., 2007). This bistabily driven by light is well experienced in spin and spin-crossover materials (Halcrow, 2013) from low to high spin states or by a charge transfer materials for example (Kahn, 1993; Nasu, 1997; Gütlich et al., 1994; Ohkoshi et al., 2001). Another kind of bistable materials present a transition from insulator to metal, such as the (EDO-TTF)PF6 (Figure 1.1 a), for which it has been proved experimentally that the metallic state can be induced not only by the temperature but also by light irradiation (Chollet et al., 2005; Gao et al., 2013). Another interesting organic system can present other type of transition, such as the transition from neutral paraelectric to the ionic ferroelectric phase, which the case for TTF-CA (Figure 1.1 b). This organic compound undergoes thermal transition at 81 K, which can also be photoinduced (Collet et al., 2003; Koshihara et al., 1999). One important point is that these thermal and photoinduced changes of electronic states are accompanied by structural changes such as symmetry breaking or distortion, which allow trapping of the thermal or photoinduced state. In addition, cooperative interactions between molecules is at the origin of a nonlinear behavior as a function of the external stimuli (Sato et al., 2007; Bousseksou et al., 2011, Bertoni et al., 2016).

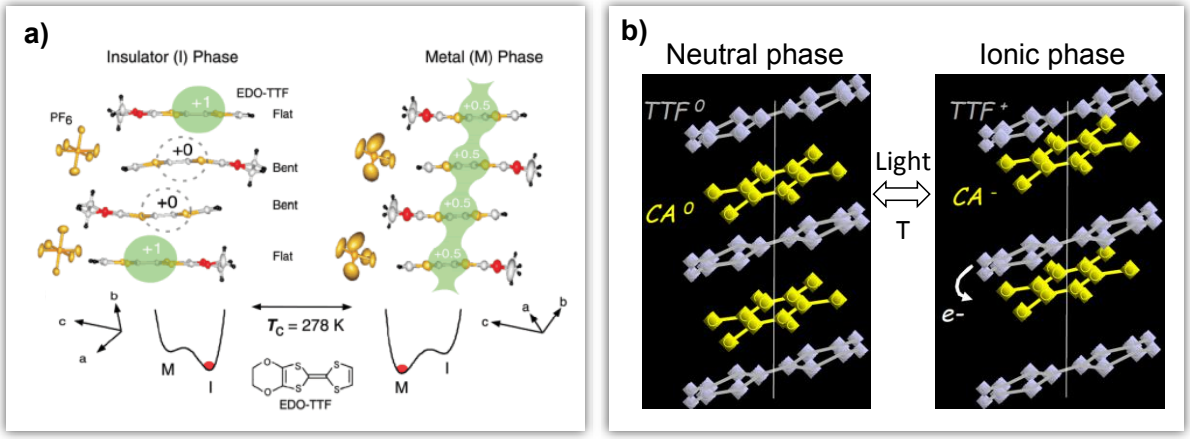

Figure 1.1: Schematic representation of the structure and the electronic changes accompanying the phase transition in: a) $(EDO\text{-}TTF)_2PF_6$ compound (Chollet *et al.*, 2005) and b) TTF-CA compound (Collet *et al.*, 2003).

1.2 Ultrafast phenomenon

In the field of ultrafast molecular physics, ultrashort time scales range from several tens of femtoseconds to several hundred picoseconds. To follow and solve the mechanisms at this time scale, it is necessary to use instruments based on ultrafast optics, because instruments based on the electronics are too slow. The invention of femtosecond lasers, based on the mode lock coupled with crystals Titanium doped Sapphire, allowed to go towards these characteristic times. The invention of the Chirped Pulse Amplification made it possible to combine short pulses with intense photo-excitation. These amplified femtosecond laser systems have thus rapidly established themselves as a mean of pumping excited states of matter and then probing their evolution in order to study the mechanisms related to photo-excitation. This technique is based on the stroboscopic principle, which helped to visualize the dynamics of macroscopic systems with an exposure time of few milliseconds (Muybridge, 1872; Marey, 1882) (Figure 1.2 left). One of the areas emerging with this technological advance is femtochemistry, for which Ahmed H. Zewail received the Nobel Prize in 1999 (Zewail, 1988; 2000). The aim of the femtochemistry research area is to study the dynamic of the transient states of chemical reactions. In particular, one of the pioneering experiments in femto-chemistry was the study of the dissociation of Sodium Iodide (NaI) after a photoexcitation (Mokhtari *et al.*, 1990) (Figure 1.2 right).

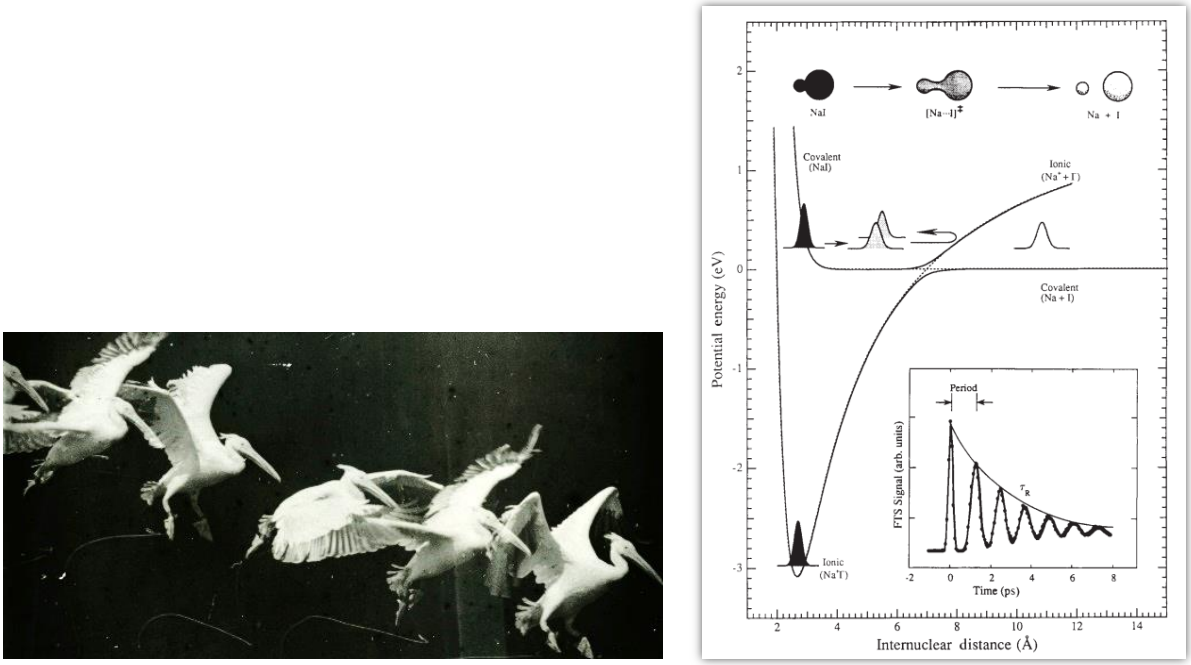

Figure 1.2: (Left) Sequence snapshots of Pelican in fly by E.J.Marey in 1882. (Right) Schema of the dynamic of the electronic wave packet created in the NaI dissociation (Mokhtari *et al*, 1990)

The characteristic time of the physical and chemical phenomena involved in each process depend strongly on the nature of the phase (gas, solid, liquid). We can distinguish two types of process: thermal and non-thermal. For the thermal processes, the time characteristic exceeds hundreds of picoseconds which are governed by the thermal motions of atoms and molecules, such as lattice vibration and the heat activation process of heat diffusion. The non-thermal processes are ultrafast, such as the electronic and atomic motions. These processes appear after an ultrashort pulse excitation which can bring the system from a stable state to the other out-of-equilibrium state where many different degrees of freedom can be involved (Cailleau *et al.*, 2010). In the case of condensed matter, the interactions are very strong and can extend to short distances therefore the associated times are small. For example, in the well-known case of Bismuth (Sokolowski-Tinten *et al.*, 2003; Fritz *et al.*, 2007; Johnson, 2013), the distance between the two atom which composes the elementary unit cell can be perturbed by light. During the interaction of light with electrons, the energy deposited in the electronic sub-system, which rapidly thermalize. This transient electronic temperature and electronic distribution around the Fermi level modifies the equilibrium structure and part of the energy is transferred into lattice by generation of optical phonon around the new equilibrium position.

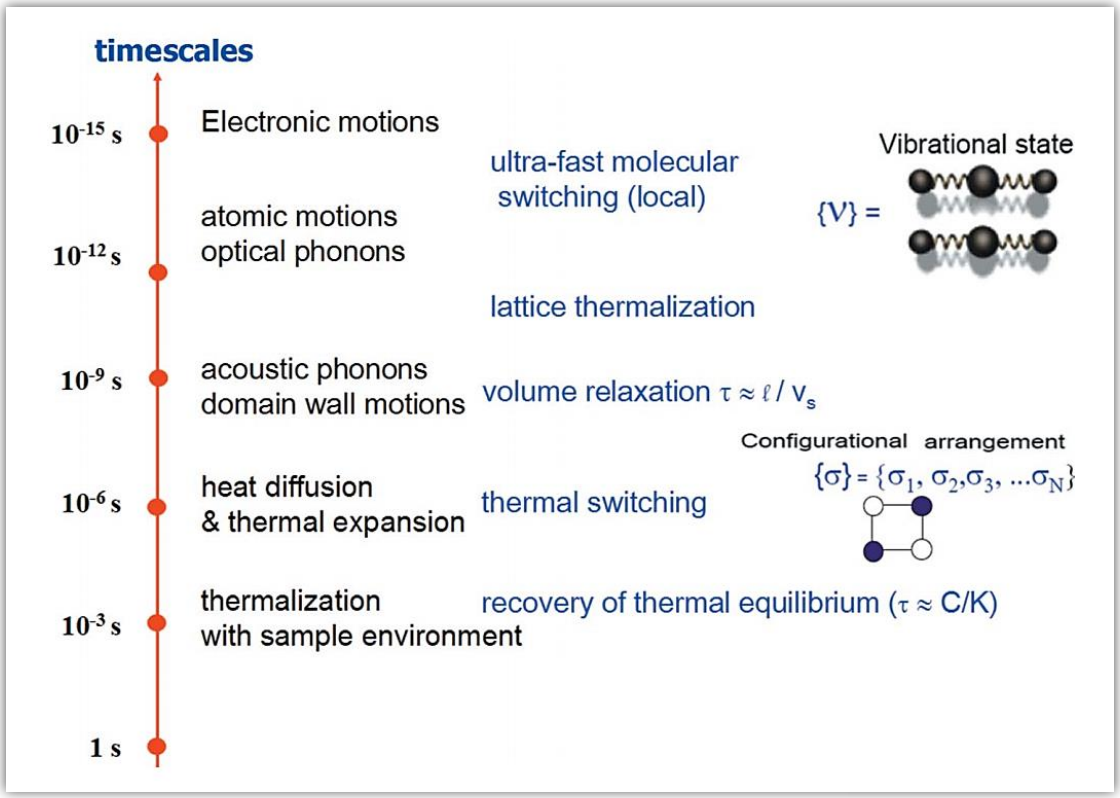

Figure 1.3: Characteristic timescale of different consecutive physical processes (Cailleau *et al.*, 2010).

1.3 Spin Transition and Charge Transfer materials

1.3.1 Spin Crossover phenomenon

The spin crossover (SCO) phenomenon was observed for the first time in 1930 in Fe(III) dithiocarbamate complex (Cambi & Gagnasso, 1931). A significant magnetization change in SCO complexes was observed as a function of temperature, which means that the electronic states in the Fe(III) ion changed. The SCO attracted the interest of scientists in the field since 1964, when Baker and Bobonich synthesized the first SCO complex (Baker & Bobonich, 1964). Then in 1967 Koenig and Madeja performed extensive magnetic and Mossbauer spectroscopy to study these complexes and explained the nature of thermal induced spin transition from the low spin (LS) to the high spin (HS) in the first Fe(II) SCO complexes (Koenig & Madeja, 1967). In 1982, it was found that a green light (530 nm) transforms the spin state from LS to HS at low temperature, this phenomenon is called the Light Induced Spin State Trapping (LIESST) (McGravey & Lawthers, 1982) observed in an Fe(II) complex in solution. They showed that by irradiating this complex using a nanosecond optical laser with a wavelength lies within the metal-to-ligand charge-transfer (MLCT) band, the system can be transferred into the HS state. Then the LIESST effect was observed in solid state in the compound $[Fe(ptz)_6](BF_4)_2$ for the first time in 1984 (Decurtins *et al.*, 1984). Now it is well known that the pressure and the magnetic field can also be used to switch the spin crossover systems (Gütlich *et al.*, 1994).

Ligand Field Theory

The ligand field theory is an extension of crystal field theory, which was proposed by the physicist H. A. Bethe in 1929 (Bethe, 1929), and modified by J. H. Van Vleck in 1935. This theory allows to explain the interaction between a central metal ion the ligands linked with this metal ion. It was developed to explore the properties of complexes (magnetic, spectral, coordination …). It is based on quantum mechanical description of the metal ion, which focused on the s, p and d orbitals. The ions around the central metal ion are considered as point charges. The figure 1.4 shows an example of representation of the five degenerate d orbitals, the lobes in this case represent the total electron probability. Where the lobes are lie in-between the x and y axes for d_{xy}, in-between the x and z axes for d_{xz} and in-between the y and z axes for d_{yz}. The $d_{x^2-y^2}$ orbital lie on the x and y axes and for d_{z^2} there are two lobes on the z axe and there is a donut shape ring lie on the xy plane around the two lobes.

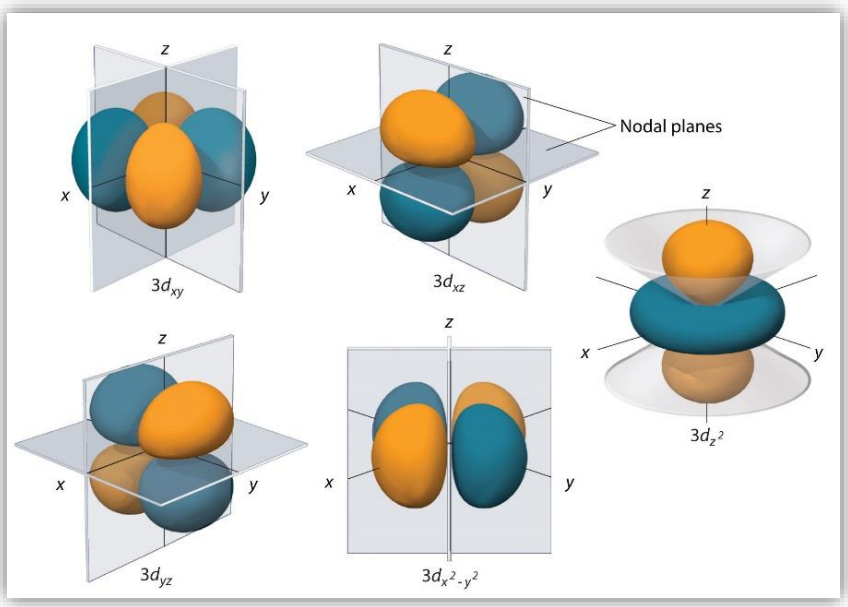

Figure 1.4: Representation of the 3d orbitals (Chemistry LibreTexts, Chap 2.5, 2017).

Case of octahedral complex

In an isolated atom, the energy levels of the five 3d orbitals are degenerate. Under the effect of a spherical electric field, the orbitals are destabilized by a quantity ΔE. Now, if the cation (central atom) is placed at the center of an octahedral environment, the six ligands will create an electrostatic field whose influence on the five 3d orbitals of the cation will depend on the orientation of these. In this case, the five orbitals are therefore no longer equivalent to the ligands. The d_{xy}, d_{xz} and d_{yz} pointing between the ligands are stabilized . An electron occupying one of these orbitals undergoes a lower repulsion by the ligands, so the energy of these orbitals is lowered. The $d_{x^2-y^2}$ and d_{z^2} orbitals are directed straight to the ligands and are destabilized. An electron occupying one of these orbitals undergoes a stronger repulsion of the ligands so the energy of these orbitals is increased. The three lower energy orbitals are collectively referred to as t_{2g} and the two higher energy orbitals as e_g (Figure 1.5).

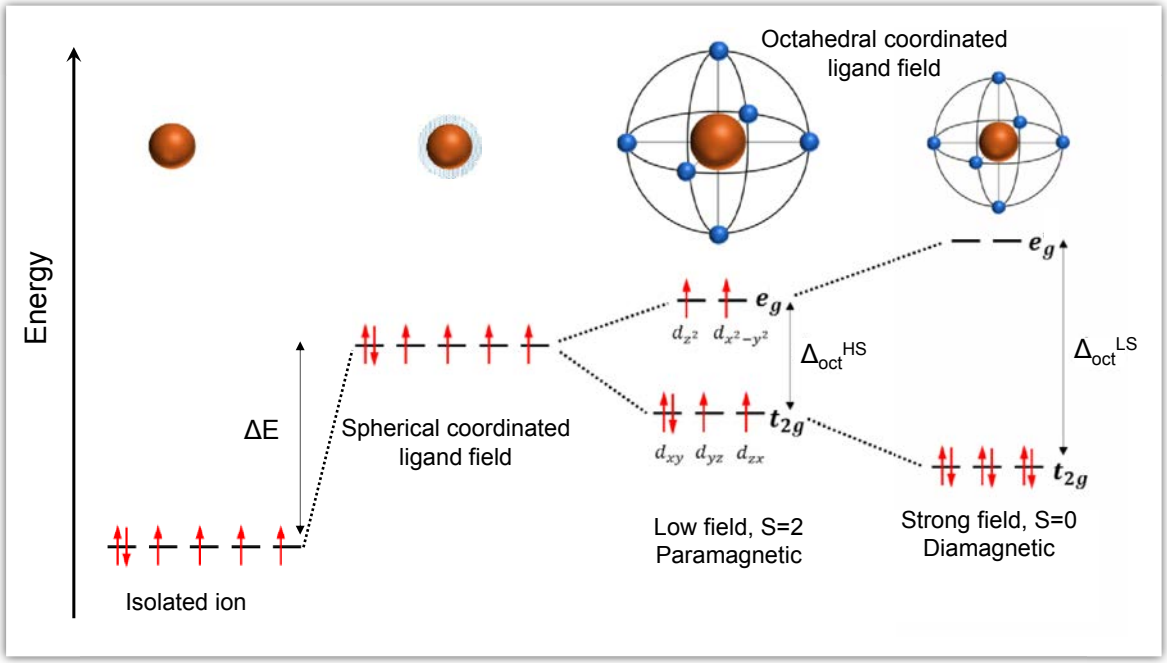

Figure 1.5: Electronic configuration of the Fe(II) ion according to its environment.

In the case of SCO octahedral systems, the crystal field splitting is denoted Δ_{oct} which plays an important role in the electron spin state of a coordination complex. It can be affected by several factors such as the nature of the metal ion, the charge and the ligand field strength which determines the electronic structure of $3d^4$ -$3d^7$ transition metal ion (Gütlich and Goodwin ; 2004). This configuration makes it possible to have access to two configurations according to the intensity of the interactions between the ligands and its orbitals: The $t_{2g}^4e_g^2$ configuration corresponds to a small splitting of t_{2g} (non-bonding orbital) and e_g (anti-bonding orbital) levels. In this case, the ligand field is weak. The SCO system is paramagnetic and the total spin is 2, which called high spin state (HS). The $t_{2g}^6e_g^0$ configuration corresponds a large splitting of the t_{2g} and e_g levels. In this case, the ligand field is strong. The SCO system is diamagnetic with a total spin equal to zero, which called low spin state (LS).

The strength of the ligand field depends both on the distance between the metal cation and the ligand, and on the nature of the ligand. For an uncharged ligand, this ligand field is expressed as: $\Delta oct \approx \mu / r^6$. With μ the dipole moment and r the distance metal-ligand, of the iron-ligand bond In the HS state, the e_g orbitals are occupied and lead to an extension of the Metal-Ligand distance with respect to the LS state. The spin state transition is therefore accompanied by an increase of the volume of the molecule (Gütlich *et al.*, 1994).

1.3.2 LIESST and reverse LIESST effect

In Fe spin crossover complex. It was demonstrated that the LS is converted in to HS state by light irradiation at low temperature (< 50 K) (Decurtins *et al.*, 1985). It has been shown that the system studied, initially in the LS (singlet, $^1A_{1g}$) state, could be changed by irradiation at 514 nm in the HS metastable state attributed to the HS (quintet, $^5T_{2g}$) state with a long lifetime at 10 K. The mechanism proposed by Hauser involves two successive intersystem crossing (Figure 6.1). The irradiation in the absorption band of the LS populates the excited level $^1T_1$. The system then relaxes non-radiatively to the intermediate triplet state $^3T_1$, and from this intermediate state to $^5T_2$ where it remains trapped because of a large variation of the metal-ligand distance, this mechanism is called Light Induced Excited Spin State Trapping (LIESST). This mechanism is based on the fact that the direct conversion from $^1A_1$ into $^5T_2$ is forbidden and that the passage through triplet intermediate state seems necessary. Hauser has demonstrated that the photo-conversion from $^5T_2$ into $^1A_1$ is possible (Hauser, 2004), by irradiating the molecules at HS with a different wavelength. The passage from the HS to the LS can be realized either by non-radiative direct relaxation from $^5T_2$ to $^1A_1$ or by irradiating the absorption band of the HS of the transition $^5T_2$ to ^5E. In this last case, the system relaxes towards to the LS via an intermediate triplet state $^3T_1$. This phenomena is known as reverse-LIESST.

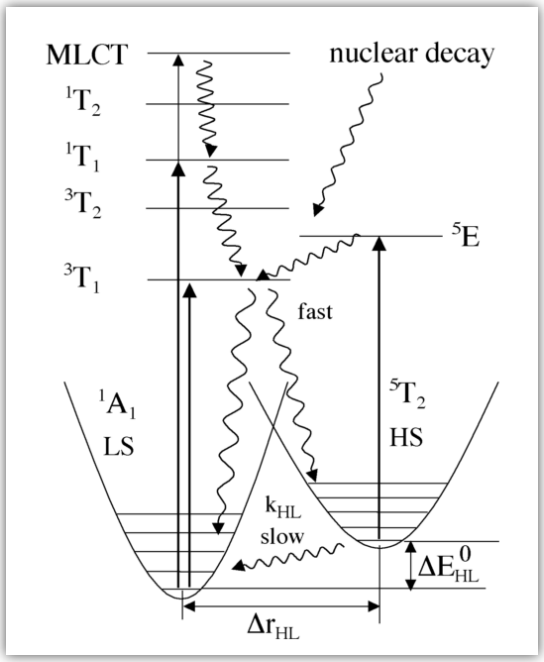

Figure 1.6: Mechanism of the LIESST and reverse-LIESST proposed by Hauser (Hauser, 2004).

Once irradiation is stopped, the system recovers the thermal equilibrium in the LS state. Depending on the temperature, the mechanisms involved during the relaxation process can differ and the lifetime of the metastable HS state varies from ms to several days. At very low temperatures, the thermal energy does not allow overcoming the potential barrier between the two states and the relaxation mainly occurs through quantum tunneling effect. At higher temperature, thermal energy allows passing the barrier through a classical vibrational process and molecules relax on s-ms time scale (Hauser, 2004).

By using photocrystallography at the Cristal beamline of the Soleil synchrotron, we have studied the complex relaxation from the photoinduced high-spin phase (PIHS) to the low spin phase of the bimetallic 2D coordination spin-crossover polymer $[Fe[(Hg(SCN)_3)_2](4,4'bipy)_2]_n$. During the thermal relaxation, commensurate and incommensurate spin-state concentration wave's (SSCW) form. However, contrary to the steps forming at thermal equilibrium, associated with long-range SSCW order, the SSCWs forming during the relaxation from the PIHS phase correspond to short-range order, revealed by diffuse X-ray scattering. This work published in Acta cryst. B is not in direct connexion with the topic of this thesis focussing on ultrafast processes and is therefore attached in the annex (Mariette *et al*, 2017)

1.3.3 Ultrafast LIESST in Spin Crossover materials

In 1992, the group of Hendrickson observed for the first time the ultrafast intersystem crossing (ISC) in Fe(II) complexes (McCusker *et al*., 1992), but the photoresponse observed was limited by the experimental time resolution (~50 ps). Since the development of femtosecond lasers and the electronic detection systems, several groups tried to explore the ISC at femtosecond timescale. The ultrafast ISC in Fe(II) complex in solution was studied by The group of M. Chergui, using the ultrafast femtosecond fluorescence upconversion spectroscopy, they proposed a whole mechanism of photoswitching LS/HS, according to the relaxation cascade $^1A_1 \rightarrow {}^3MLCT \rightarrow {}^5T_2 \rightarrow {}^1A_1$ (Figure 1.7 right), with three characteristic lifetimes, 120 fs, 960 fs, and 665 ps, obtained from the kinetic traces at the three characteristic wavelength (Figure 1.7 left). The first was interpreted as the decay of the ^{3}MLCT, the second as the population time of the $^5T_2$ (HS) state and the third as the decay time to the ground state (Gawelda, Cannizo *et al.*, 2007). Other experiments were performed by the same group, in order to follow the structural changes of Fe(II) complex. The use of picosecond x-ray absorption allowed to measure the elongation of the bond Fe-ligand by 0.2Å after passing from LS to HS (Gawelda, Pham *et al.*, 2007).

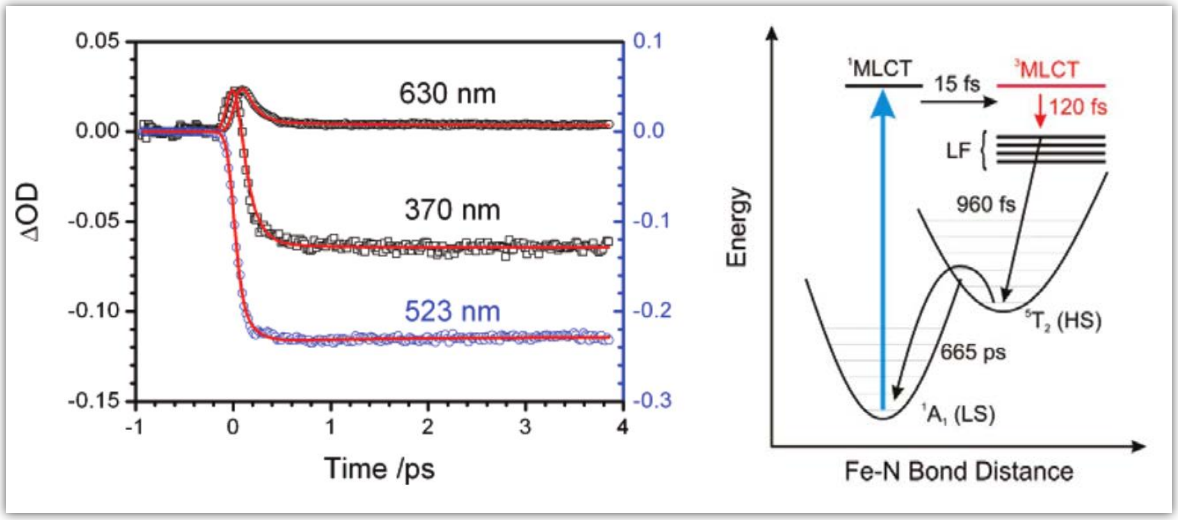

Figure 1.7: (Left) Time traces of ΔOD change at selected wavelengths. (Right) mechanism of photoswitching (Gawelda, Cannizo *et al.*, 2007).

The same experiment done with femtosecond x-ray pulses (Bressler *et al.*, 2009), reported a description of population mechanism of HS state, which was identified as a ^{1,3}MLCT to^{5}T cascade bypassing the triplet state of the ligand field. It was found that the decay time (150 fs) of the ^{3}MLCT to ^{5}T relaxation, is associated to the period of Fe-Ligand stretch band vibration. Another time resolved x-ray absoprtion study around the L-edge of iron, presented a similar description of the photoswitching mechanism Fe(II) SCO in solution (Huse *et al.*, 2012).

The study of Consani *el al.*, 2009, reported the first observation of the coherent vibrational coherence in Fe(II) complex in solution, which was interpreted as vibrational wave packets. In this study, only one coherent mode of low frequency (128 cm^{-1}) is identified and attributed to ligand vibrational mode. These oscillations are observed in the kinetic traces of the transmission change at several probe wavelengths (Figure 1.8), using the pump/UV continuum probe spectroscopy).

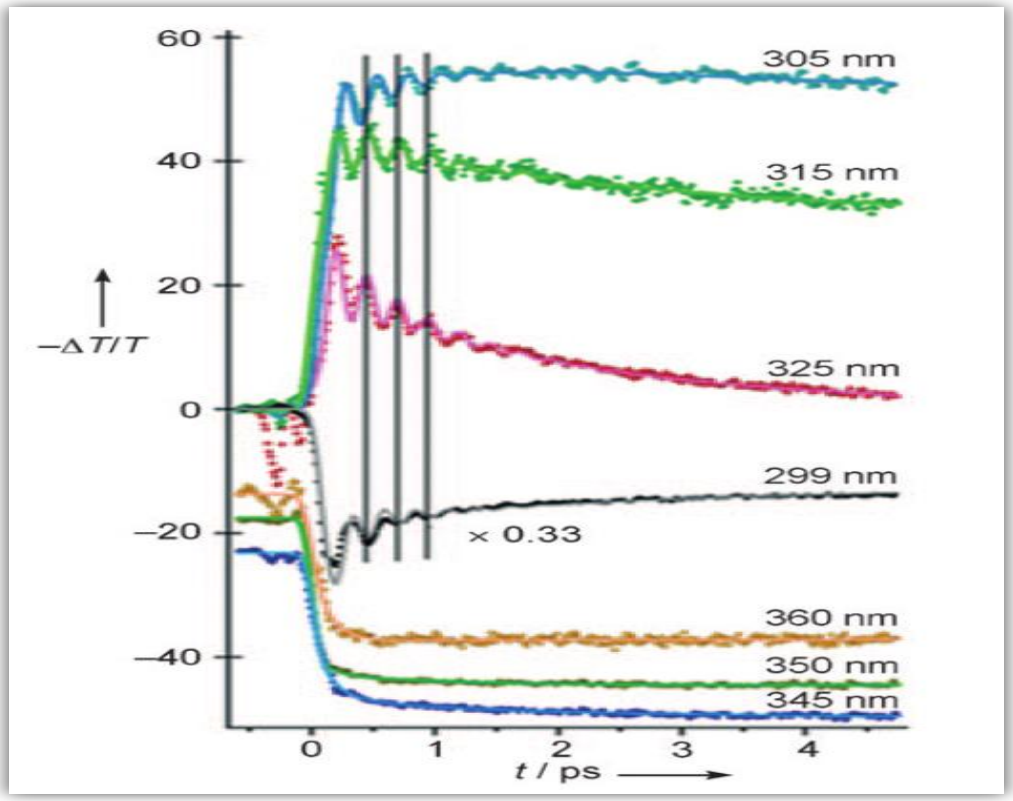

Figure 1.8: Time trace of transmission at selected wavelength in $[FeII(bpy)_3]^{2+}$ (Consani *et al.*, 2009).

Other studies of the LIESST effect were performed in solid state SCO materials (Lorenc *et al.*, 2012, Bertoni *et al.*, 2012, Collet *et al.*, 2012), in which the spin crossover complex is based on Fe(III) with a different electronic configuration of LS (S=1/2) and HS (S=5/2) states instead of Fe(II) complex LS(S=0) and HS(S=2). These studies evidenced a very similar photoswitching mechanism to the one reported in previous studies (Consani *el al.*, 2009; Gawelda, Cannizzo *et al.*, 2007; Gawelda, Pham *et al.*, 2007). It was found that the process of the photoexcitation includes two mains steps. The first corresponds to the relaxation from MLCT to HS with decay time of 200 fs (τ_1, Figure 1.9.left), which is in agreement with the early studies in Fe(II) in solution. The second step corresponds to the vibrational cooling with a longer time constant ($\tau 2$ = 500-800 fs), which is associated to the dissipation of excess energy to lattice (Bertoni *et al.*, 2012). At longer timescale (above 1ns), a thermal and elastic processes were observed by time resolved optical and x-ray diffraction (Lorenc *et al.*, 2012). It was reported that after the ultrafast transformation of a certain fraction of HS molecules, the volume of the system increases (step 2, Figure 1.9.right) allowing relaxation of pressure, which triggered a nonlinear amplification of HS fraction (step 3, Figure 1.9.right).

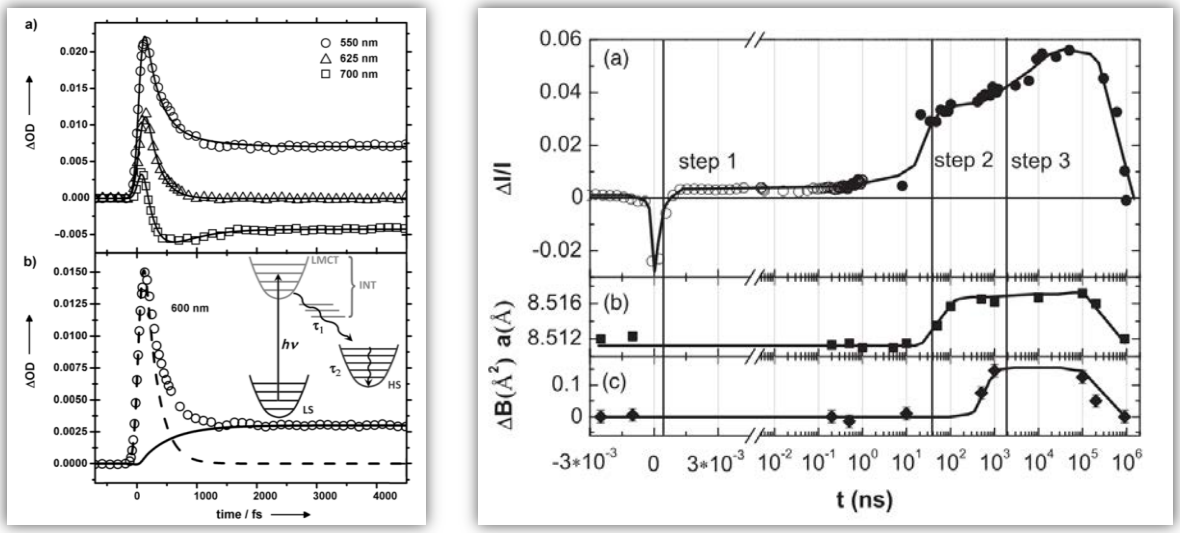

Figure 1.9: (Left) Kinetic traces at short timescale of OD change in Fe(III) complex nanocrystals at selected wavelengths (Bertoni *et al.*, 2012). (Right) Kinetic traces at long timescale of transmission and lattice parameter changes in Fe(III) (Lorenc *et al.*, 2012)

Another system based on Fe(II) spin crossover in solid state was investigated using the time resolved femtosecond optical and x-ray absorption (Cammarata *et al.*, 2014 Bertoni *et al.*, 2015). These studies revealed the activation of two coherent vibrational modes upon the MLCT excitation, the first activated mode (113 cm^{-1}) corresponds to the breathing mode which is characterized by a stretching in phase of the Fe-ligand bonds, and the fast damping of this mode allows an efficient trapping in the HS state. The second activated mode (85 cm^{-1}) corresponds to the bending phonons which is the distortion in the ligand-Fe-Ligand angle (Figure 1.10).

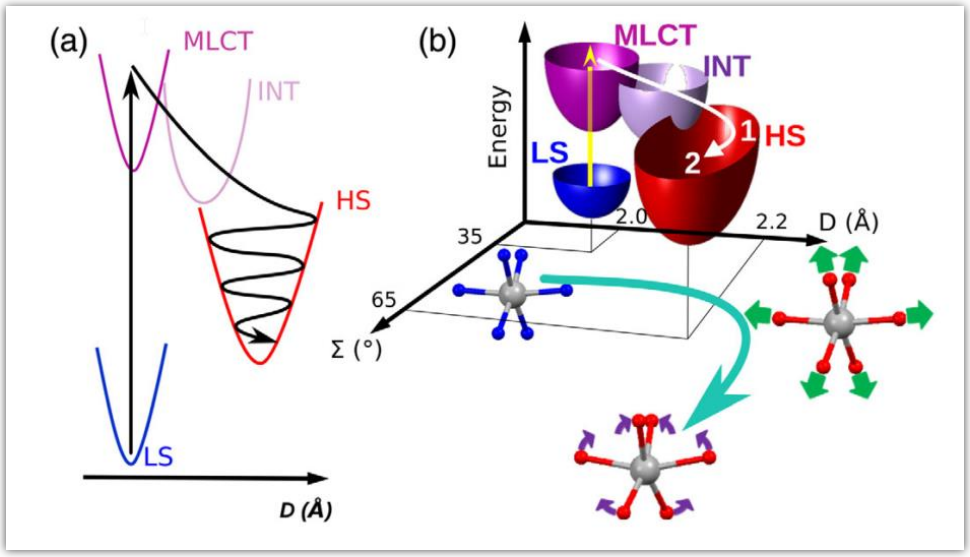

Figure 1.10: Schematic representation of the photoswitching pathway (Cammarata *et al.*, 2014).

A study (Zhang *et al.*, 2014) in Fe(II) complex with femtosecond x-ray emission spectroscopy, clearly identified a short passage via triplet intermediate state (^{3}T), and proposed the sequential relaxation model: ^{1,3}MLCT $\rightarrow$ ^{3}T $\rightarrow$ ^{5}T, with 150 fs time constant for MLCT decay and 70 fs time constant for triplet decay. A more recent study (Auböck and Chergui, 2015), using the pump/probe transient spectroscopy with a time resolution of 40 fs, was reported that the ^{5}T state is populated in less than 50 fs, and the photoswitching process proposed is very similar to the one previously described (^{1,3}MLCT $\rightarrow$ ^{5}T) (Bressler *et al.*, 2009, Consani *et al.*, 2009; Huse *et al.*, 2012; Gawelda *et al.*, 2007). According to this study (Auböck and Chergui, 2015), two oscillating modes at 127 and 157 cm^{-1} were observed at selected wavelength, and interpreted as activation of coherent wave packet due to the change of the angle N-Fe-N, which is induced by the high frequency of C=C elongation mode (1668 cm^{-1}), This study points out the fact that the time resolution of the previous study (150 fs FWHM, Zhang *et al.*, 2014), does not allow detection of the short lifetime of the ^{3}T intermediate state. A recent study (Lemke *et al.*, 2017), using femtosecond x-ray absorption spectroscopy, with time resolution <30 fs, clearly demonstrated that the coherent vibrational wave packet corresponds to the breathing mode and the lifetime of the MLCT is 120 fs, and underline the important role of the dephasing in the intermediate states in the structural decoherence.

1.4 Charge Transfer Materials

Some charge transfer materials which are made of metallic sites of different chemical nature, present an interesting physical properties. Light, Temperature and pressure can trigger a metal-to-metal charge-transfer process (MMCT) which can be accompanied by electronic configuration changes and also structural reorganization trapping of new electronic state on each metal center (Robin, 1962; Herrera *et al.*, 2008). Prussian Blue Analogues (PBA) are prototype systems made of cubic networks of metallic ions linked by cyanide bridge, the first PBA in solid state was discovered in Berlin at the beginning of the 18th century, which consists of two iron metals with the formula $Fe^{III}_4[Fe^{II}(CN)_6]_3$. It was found that this system crystallizes in a face-centered cubic (fcc) with space group Fm3m (Buser *et al.*, 1977). Others compounds of PBA, are obtained by replacing the metal ion by other metal atoms (cobalt, manganese, copper, nickel). The nature of metal affects strongly the physical properties and their evolution under external stimulations. For example, the $Mn^{II}Fe^{III}$ PBA presents a bistabilty between two states (ferromagnetic and antiferromagnetic) induced by a charge transfer under light irradiation

or variation of temperature (Figure 1.1.a, Tokoro *et al.*, 2008). The $Fe^{II}Cr^{III}$ compound, presents thermal and photo induced spin transition between two states without charge transfer: LT phase with $Fe^{II}(LS)Cr^{III}(LS)$ state and HT phase with $Fe^{II}(HS)Cr^{III}(LS)$ state (Ohkoshi *et al.*, 1999). Another example of PBA, is the CoFe compound which coupled the two processes, charge transfer and spin transition (Figure 1.1.b, Sato *et al,*. 1996), that kind of system is formed essentially of diamagnetic pairs $Co^{III}(LS)Fe^{II}(LS)$ at very low temperature which can be converted to paramagnetic pairs $Co^{II}(HS)Fe^{III}(LS)$ by light irradiation. This process is so-called Charge Transfer Induced Spin Transition (CTIST).

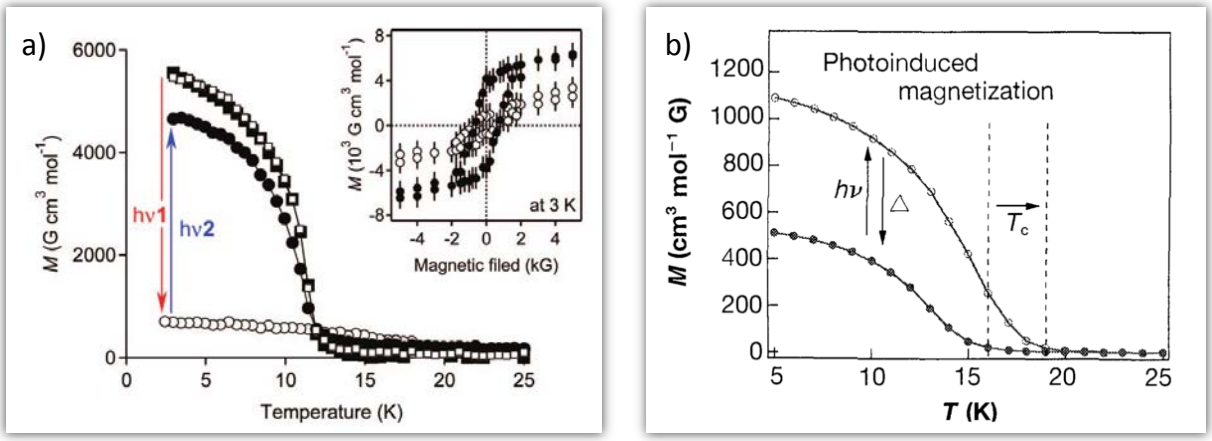

Figure 1.11: Variation of the magnetization as function of temperature and light irradiation in PBA: a) in $RbMnFe[(CN)_6]$ nanocrystals (Tokoro *et al.*, 2008) and b) in $KCoFe[(CN)_6]$ (Sato *et al.*, 1996).

In the literature, the studies of the charge transfer dynamic in PBA nanoparticles, are essentially based in the time resolved Raman and Infrared spectroscopies. The group of J. C. Owrutsky carried out IR visible pump – IR visible probe measurements in $Fe^{III}_4[Fe^{II}(CN)_6]_3$ nanoparticles. It was found that upon 800 nm excitation and probing at 800nm, the photoresponse of the system is characterized by a transient peak and a relaxation with two time constants (9 ps and 185 ps). Upon IR excitation and probing at 800 nm, they observed two steps, one was a bleach with time decay of 19 ps and other relaxation step was an absorption with time decay of 370 ps (Figure 1.12).

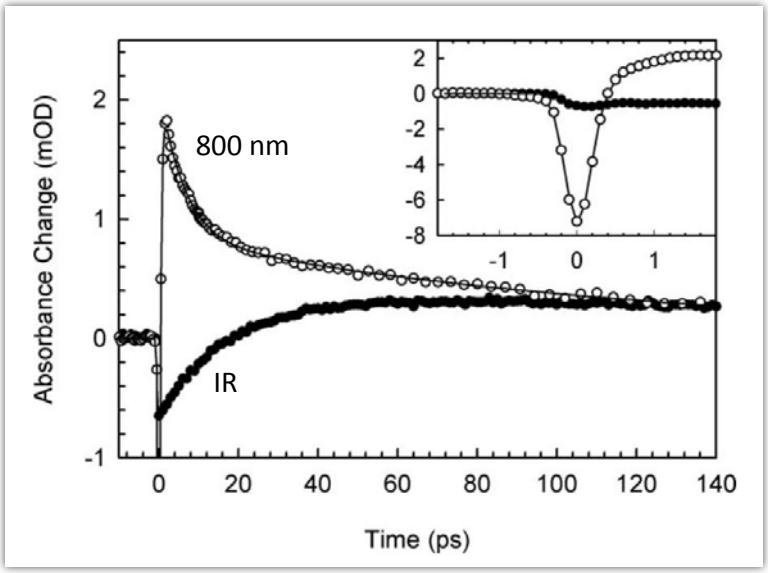

Figure 1.12: Time scan change of OD in $Fe^{III}_4[Fe^{II}(CN)_6]_3$ nanoparticles (Weidinger *et al.*, 2011)

An ultrafast study of the dynamic in $RbMn[Fe(CN)_6]$ microcrystals (Asahara et al., 2012) was performed by visible pump and IR probe spectroscopy. This study reported the transient behavior of the CN vibration after optical excitation between the low temperature (LT) phase: Fe^{II}-CN-Mn^{III} to the photoinduced phase high temperature (PIHT) phase: Fe^{III}-CN-Mn^{II} in rubidium manganese hexacyanoferrate at 4 K. by following the photoinduced change of the CN stretching vibration modes after an optical pulse excitation at 532 nm (Figure 1.13), which are sensitive to the valence states of the adjacent metal ions.

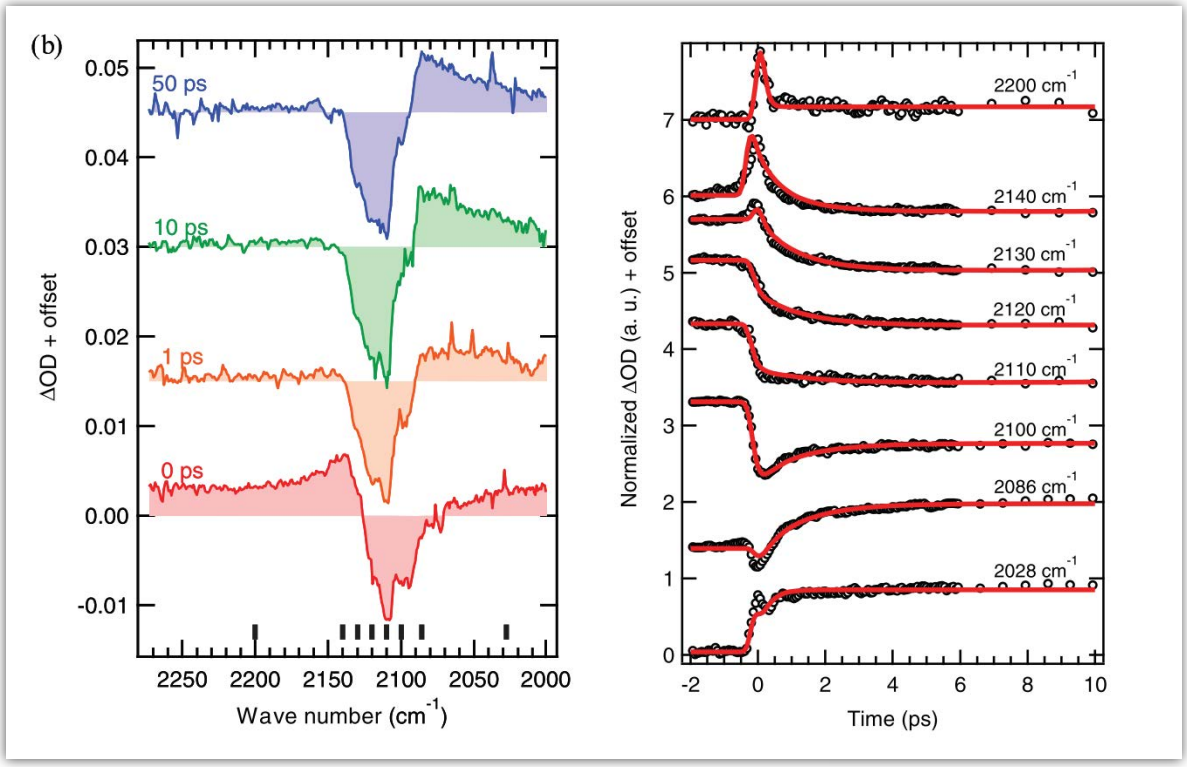

Figure 1.13: (Left) Absorption spectrum change in the Mid-IR region after pulse excitation at 532 nm and simultaneously under CW irradiation at 400 nm. (Right) Time traces ΔOD change at selected wavelength indicated by black segment line in the figure at left (Asahara *et al.*, 2012)

A recent study (Johansson *et al.*, 2016) of the ultrafast dynamic in V-Cr PBA at ambient temperature and at 50 K. they combined the time-resolved femtosecond magneto-optical Faraday technique and the TD-DFT calculation. The results obtained from this study, revealed a multi-step dynamic of charge and spin change upon the LMCT (ligand-metal charge transfer) excitation, it was found that the ^{5}E state of the Cr was populated from the change in the super-exchange interaction (Figure 1.14.right), in less than 250 fs with vibration cooling of 0.78 ps (at 50 K) and 1.1 ps (at 300 K).

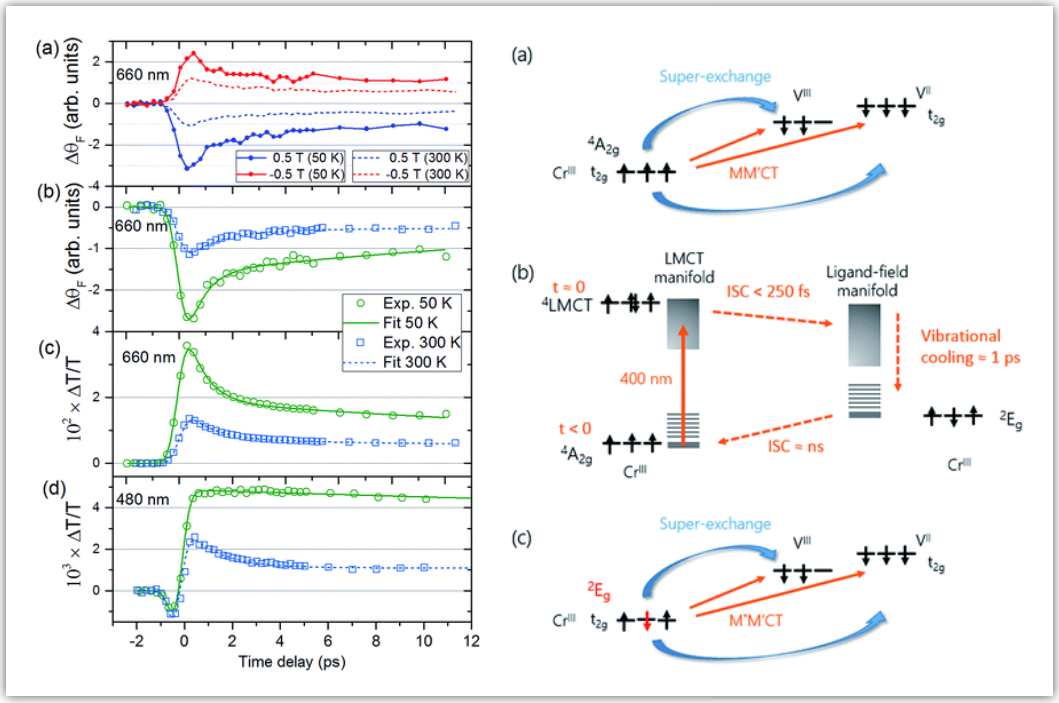

Figure 1.14: (Left) Time trances of the transmission change at selected wavelength of probe and as function of temperature and external magnetic field. (Right) Schematic representation of the charge and spin dynamic in V-Cr PBA (Johansson *et al.*, 2016).

1.5 Goal of this research project

The goal of the PhD work is to lay the foundations for physical properties light-control (magnetic, optical…) of molecular-based materials using the ultrafast and coherent response at ultrashort time-scale. This project at the physics-chemistry interface may have direct consequences for the development of new light-driven based technologies if we can understand how to control the proprieties of photoactive materials. This requires advanced experimental analysis and especially ultrafast structural science, as molecular reorganization play a key role in the stabilization of the photoinduced state.

The experimental developments will be presented in chapter 2 and will be used for understanding universal and specific aspects of these processes. These will be applied to investigate materials showing different origin or behaviour associated with photo-magnetism:

Spin-Crossover materials studied in chapter 3

Prussian Blue Analogues studied in chapter 4.

Chapter 2

Experimental techniques and data analysis methods

During my thesis, I used several experimental techniques to characterize the switching of the physical properties in photomagnetic materials and their evolution under light irradiation and temperature. In this chapter, I will detail the physical principle, the experimental conditions (acquisition data, detection) and the data analysis methods. I will begin by describing the x-ray diffraction and femtosecond optical pump-probe experiments, which were performed at IPR (Rennes, France). Then, I will describe the time resolved x-ray absorption spectroscopy, which we developed at ID09 beamline at ESRF synchrotron (Grenoble, France), by recalling the main concepts of this technique. Finally, I will briefly describe the first hard X-ray free electron laser Linac Coherent Light Source (LCLS, USA), in which, we have performed some x-ray absorption experiments, with high spatial and temporal resolution at the XPP beamline.

2.1. Probing of structure and electronic state in photomagnetic systems

The compounds that we have studied possess modular electronic and structural properties under the effect of light, temperature. To characterize their physical properties, we use several techniques. Such as the x-ray powder diffraction, which allows the extraction of structural information (the space group and lattice parameter). Also, the stationary optical absorption in UV-vis spectral region which gives a global assessment about the absorption bands and the evolution of their relative intensity and position as a function of temperature or light irradiation. For the ultrafast dynamic study, we use the femtosecond optical pump-probe spectroscopy to study the evolution of the electronic properties. I will first present two techniques, the x-ray powder diffraction and the optical pump-probe.

2.1.1. X-ray powder diffraction and data analysis

The x-ray diffraction (XRD) is a powerful method used to identify the nature and the structure of the crystallized matters. The principle of XRD is based on the scattering of an electromagnetic radiation with a wavelength of the order of few angstroms. The radiation is elastically scattered by a crystalline sample and exhibits constructive interferences (diffracted ray). The positions of the diffraction peaks are described by a simple formula, called Bragg's law, expressed as: $n \lambda = 2 d_{hkl} \sin(\theta)$

Where n is a positive integer (order of reflection), λ is the wavelength of the x-ray, d_{hkl} is the interplanar spacing which is the distance between two adjacent planes of atoms with the same Miller indices (hkl) and θ is the scattering angle (Figure 2.1).

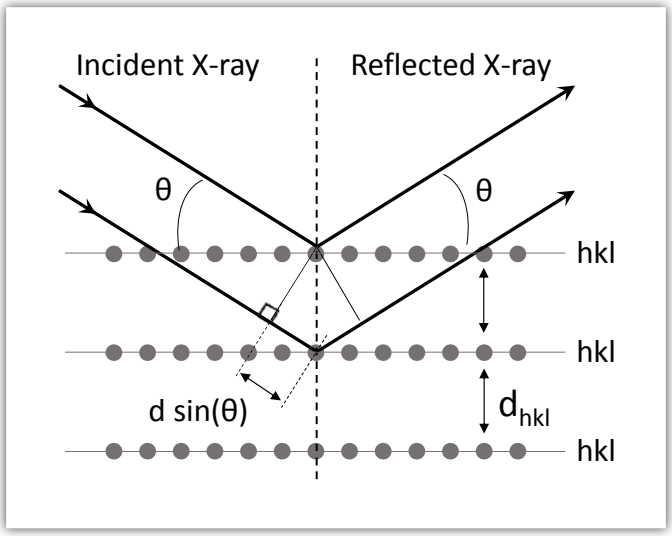

Figure 2.1: Schematic representation of the Bragg's law.

The intensity (I_{hkl}) of the diffracted peaks are determined by the arrangement of atoms in the crystal, which is proportional to $|F_{hkl}|^2$, where F_{hkl} is the structure factor, which sums the result of scattering from all atoms in the unit cell, to form a diffraction peak from the (hkl) planes of atoms, is expressed as:

$$F_{hkl} = \sum_{j=1}^{j=n} f_j e^{-2\pi i(h\,x_j + k\,y_j + l\,z_j)}$$

Where x_j, y_j and z_j are the atom positions within the unit cell, the atomic scattering factor f_j quantifies the efficiency of x-ray scattering at any angle by the electrons in each atom.

The powder XRD measurements were performed using the 4-circle diffractometer (XCalibur Oxford Diffraction) equipped with a two-dimensional CCD camera (Sapphire 3). The X-ray wavelength is the Kα of molybdenum (λ = 0.71073 Å) and the diffractometer is coupled to a nitrogen cryostat (Oxford diffraction) for temperature studies above 80 K or a helium-jet cryostat (Helijet Oxford diffraction) for very low temperature studies (~ 15 K). A continuous laser was used to study the LIESST effect at low temperature (Figure 2.2.b). Similar measurements were performed at Cristal beamline at Soleil synchrotron using the intense monochromatic x-ray beam at the wavelength λ = 0.5134 Å (Figure 2.2 a).

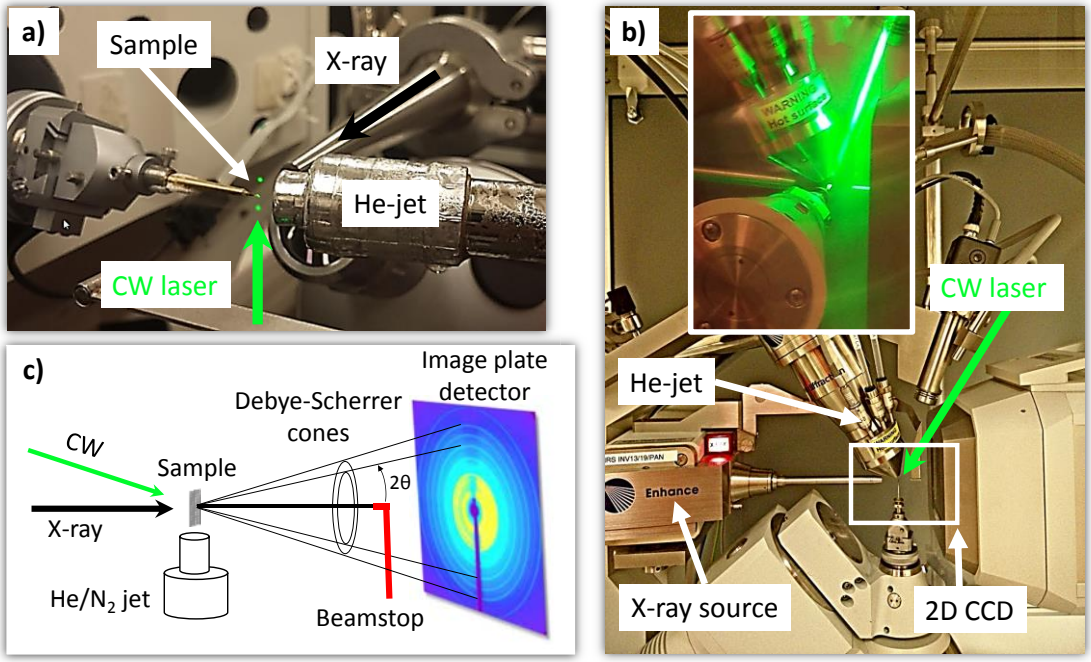

Figure 2.2: Photography of the x-ray diffraction setup, a) At Cristal beamline at Soleil synchrotron, b) At laboratory of IPR . c) Schematic diagram of the x-ray powder diffraction set-up.

In the transmission geometry as represented in the Figure 2.2.c, the random orientation of nanocrystals produces a large number of Bragg peaks, grouped in centred circle around the point $\theta = 0$, called Debey-Sherrer rings.

The 2D images were recorded using CrysAlis software (Oxford-diffraction Ltd) and were reduced in to 1D curves (azimuthal integration) using the python based open source library "PyFAI" (Kieffer & Karkoulis, 2013). These curves contain a Bragg reflections of nanocrystal and the background of the scattering of the polymer matrix (Figure 3.2). To remove it, I used a recent python library called "Dual-tree" developed by the Siwick research group (René de Cotret *et al.*, 2017; Galloway *et al.*, 2009; Kingsbury, 1998). In this way, I could follow the structural changes in nanocrystals, as presented in chapters 3 and 4.

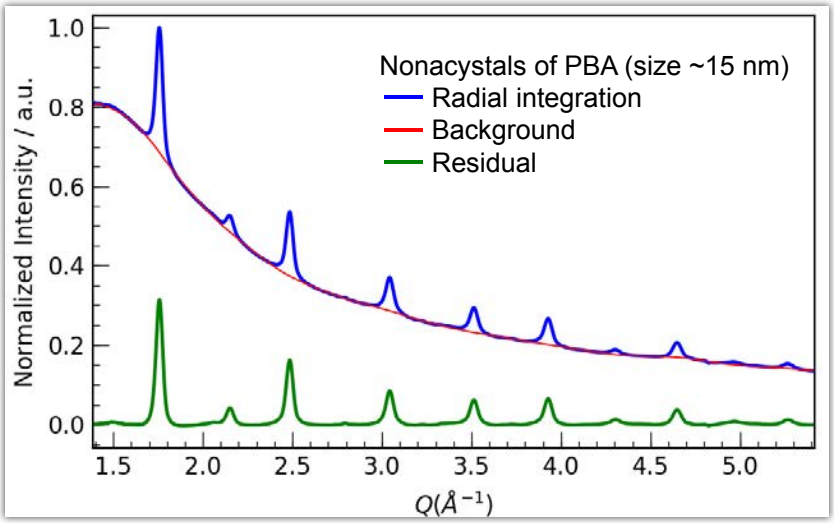

Figure 2.3: Representative X-ray diffraction pattern obtained with the nanocrystals of PBA at Cristal beamline (Soleil synchrotron).

2.1.2. Femtosecond optical pump probe spectroscopy

An important part of the work carried out during my thesis concerns the study of ultrafast phenomena in photomagnetic systems. In particular, one of the most widely used methods for this purpose is the so-called pump-probe spectroscopy technique, in which two optical pulses separated by a variable time delay are used to induce and to examine the time-dependent processes that occur after photoexcitation. The first pulse is the pump pulse which triggers the transition of the ground state into metastable state (Figure 3.2). The second pulse is the probe pulse, which probes the response of the system after a certain time interval after the start of the transition.

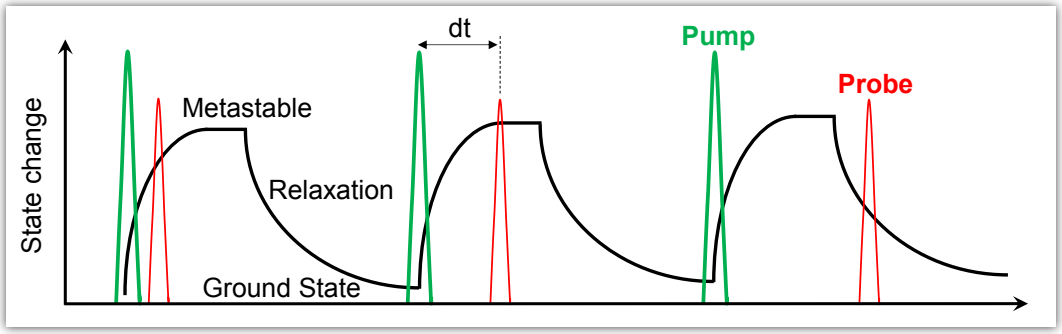

Figure 2.4: Schematic representative pump-probe principle.

With the increase of this interval and consequently the progression of the transition, the response of the system to the probe pulse varies. By sweeping the time delay dt between the pump and the probe pulses, it is possible to reconstitute the entire evolution of the transition.

As far as the time scales accessible by the pump-probe experiments are concerned, the temporal resolution is usually limited by the time duration of the probe pulse and the time delay between the two pulses; the latter contribution can easily be neglected for the optical data discussed here (as both pulses are generated by optical splitting of a single one). The extension of the scanning window, on the other hand, sees its ultimate limit imposed by the repetition period of the laser pump.

Femtosecond laser

The laser set-up used during my thesis consists of a femtosecond oscillator (Mira, Coherent), two regenerative amplifiers (Legend USP, Legend Elite), and four Optical parametric amplifiers (Topas, Coherent) delivering wavelengths from IR to UV region. The laser is placed in a temperature controlled hutch with a clean air, this avoid the instabilities due to the temperature fluctuation and avoid the deposition of dust on the optics.

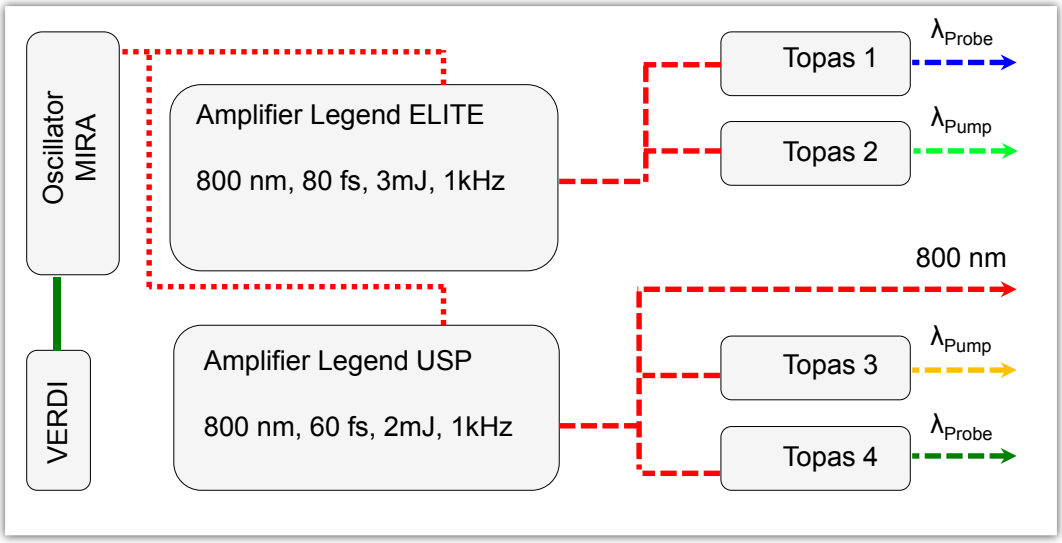

Figure 2.5: Schematic representation of femtosecond laser source at IPR.

The source of the femtosecond pulse begins with a continuous wave (CW) delivered by Verdi which pumps the Ti: Sapphire oscillator cavity with 4.5 W power at 532 nm. At the output there is a train of pulse with 76 MHz repetition rate with the following properties : all pulses are centered at 800 nm wavelength and have 40 nm bandwidth, which translates to pulse duration of 35 fs in Fourier transform limit. These pulses have low energy (~ 6 nJ) and by consequence are not suitable for pump probe experiments. The outgoing beam from the oscillator is split in two beams. One is sent to the amplifier Elite (~ 3mJ, ~ 80fs) and the second beam is sent to the

amplifier USP (~ 2mJ, ~ 60fs). The both outgoing beams from the amplifiers have a rate repetition of 1 kHz.

The principle of the amplifier is based on the technique called Chirped Pulse Amplification (CPA) developed by Mourou in 1985 (Strickland et Mourou, 1985). to amplify a very low energy pulse at the output of the oscillator, it is first necessary to stretch temporarily in order to obtain a longer pulse (order of a few hundred picoseconds), for this, a grating pars are used to introduce spatial dispersion, thus typically permitting stretching factors of as much as 10^4 inside the laser cavity. Then, the stretched pulse can be amplified with a high-energy pump lasers called optical pumping. Once amplified, the intense pulse is compressed temporally and it became again a femtosecond pulse. The simplified diagram in the Figure 2.6 summarizes these different steps of generation of intense pulse femtosecond.

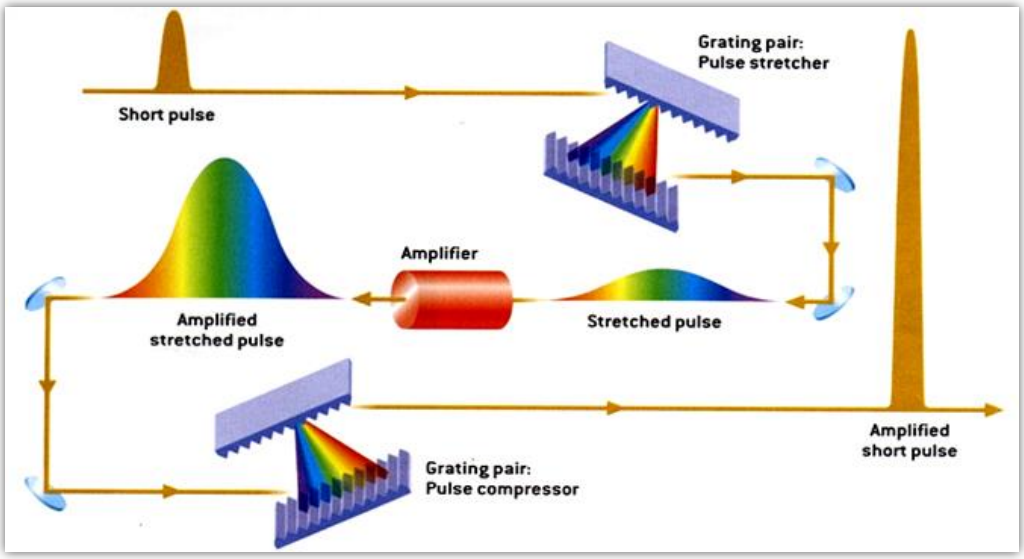

Figure 2.6: Schematic representation of CPA principle.

The amplified femtosecond laser was again splitted and sent in TOPAS to generatepulses at desired wavelength (from 280 to 2500 nm). The generation of these different wavelengths is based on several non-linear optical processes; by mixing the signal, idler and fundamental beams. To filter unwanted beams propagating through the OPA, we used a band pass filters (CVI). For reducing the power of the beam, we used a neutral density filters.

Optical pump-probe set-up

The time resolved set-up consists of two monochromatic wavelength and a Lockin-In detector. The probe laser at rate repetition of 1 kHz was splitted in two parts, one goes directly

on photodiode 2 which serves as reference intensity and the second part passes through the sample, then goes on photodiode 1(Figure 2.7). The photocurrents of reference and transmission are sent to the Lock-in amplifier (phase sensitive detection system, model SR 830 and triggered by the frequency of 500 Hz) which record the phase and the intensity of the differential signal. The pump beam at rate repetition of 500 Hz was overlapped spatially with the probe beam in the sample. The delay stage used to control mechanically (With a micrometric resolution) the time delay between the pump and probe pulses. When the sample is in the form of nanoparticles in solution, we used a magnetic stirrer, to circulate the solution at near laser spot. This system is more or less effective in certain conditions (low-viscosity solution, low rate repetition and the intensity of the pump laser).

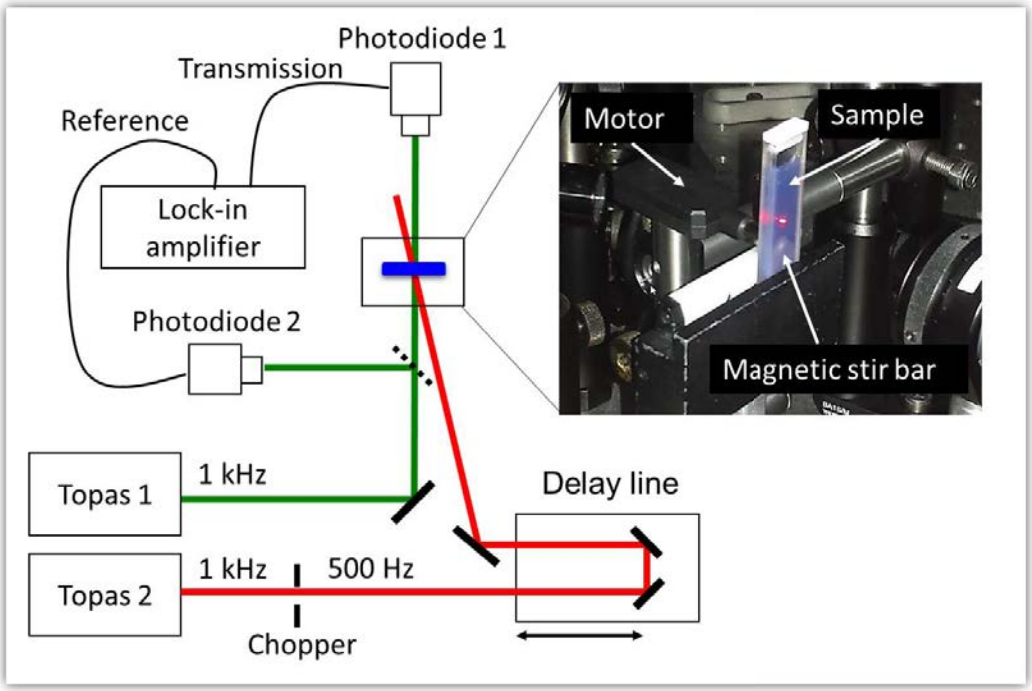

Figure 2.7: Schema of the monochromic pump (red) and probe (green) setup.

To record the time change of the visible spectrum after pulse excitation, we used the femtosecond white light spectroscopy with supercontinuum generation (Alfano, 2006). This set-up is similar to the one described previously. In this technique, the outgoing laser (800 nm, 1 kHz) from the USP amplifier is slowed down to 500 Hz by a mechanical chopper phase locked to the laser and attenuated to weak intensity using a neutral density filters. It sent to sapphire crystal which generate a supercontinuum and after re-collimation it was split into two parts: the one used for the reference is sent directly in the coupler (fiber collimator) and the one used for the transmission signal was focused on the sample and finally occur on the second coupler. The

ratio between them was checked before each experiment. The pump beam outgoing from the TOPAS at 1 kHz is slowed down to 500 Hz then to 250 Hz. Both beams were spatially and temporally overlapped on the sample (Figure 2.8). The detection system used to record the spectrum of the reference and signal, is consists a CCD camera (PIXIS 100) and a spectrometer (SpectraPro 2500i).

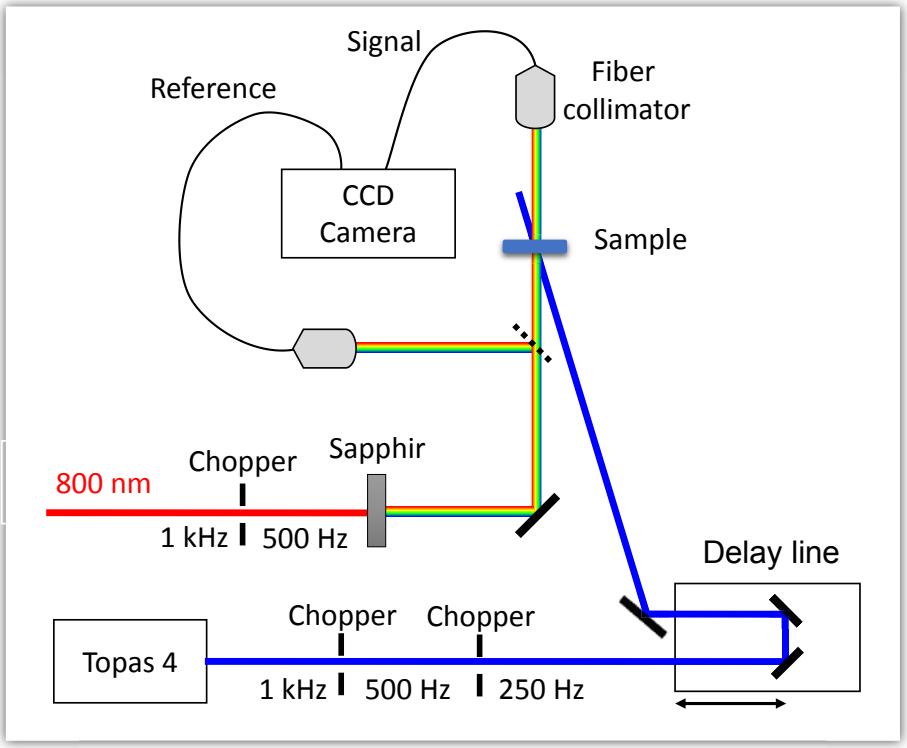

Figure 2.8: Schema of the pump-white light experiment.

2.2. Development of time-resolved X-ray absorption experiment at ID09B@ESRF

X-ray Absorption spectroscopy (XAS) is a powerful tool for probing the matter at the atomic scale, this technique allows the extracting of the both electronic and atomic structure information (spin state, oxidation state, …), at many different environment (solid, solution, gas), it turns out to be a selective local probe and allow to determine the environment close to a well-defined type of atom. One of the main advantages of this technique over structural diffraction techniques is that the long-range atomic periodicity in the sample is not required. This technique requires a very special light source: Indeed on hand it must be sufficiently intense and secondly energy must varies continuously, in order to scan an area of several hundred of electron volts around the absorption edge. However, in the field of X-rays, it turns out that only the synchrotron radiation sources meet these requirements. Since the emergence

of the field of the Photo-Induced Phase Transition (PIPT), several pump-probe time-resolved X-ray experiments are developed to explore a hidden state of matter under nonequilibrium conditions. In the same context, we have developed a new time-resolved time resolved x-ray absorption at ID09 beamline at ESRF which will be described in this section.

2.2.1. X-ray absorption principle

The X-ray absorption spectroscopy (XAS) is a method used for following the change of the absorption coefficient of a sample as a function of the energy of the incident beam. The physical phenomenon at the origin of the variations of this coefficient is the absorption of a photon x, followed by the ejection of an electron from the core-level in the absorbing atom. The Figure 2.9 represents a conventional absorption spectrum, in which three regions are distinguished: the pre-edge, edge and oscillation (Chergui & Collet, 2017). These different regions resulting from the same physical phenomenon, the boundaries are not basically defined. The pre-edge and the edge region, which extends up to about 50 eV after the absorption jump, are called XANES (X-ray Absorption Near Edge Structure). The oscillations part is called Extended X-Ray Absorption Fine Structure (EXAFS), this region that can extend up to 1000 or 2000 eV above the edge. These oscillations result when the atom studied is in a molecule or in a crystal, the wave scattered by the surrounding atoms. There is then interference between the outgoing wave from the central atom and this same wave, after scattering by the neighboring atoms. These interferences, sometimes constructive and sometimes destructive.

The energy scanning is carried out in the vicinity of an absorption edge ($E=h\nu$) of the atom whose environment it is desired to study. When the energy of the photons is less than that of the edge studied (E_0), the absorption is low and the absorption coefficient then shows a monotonic decrease. There may be electronic transitions to discrete states in this region. The variations in absorption in this zone are therefore related to the electron structure of the atom or molecule. When the ionization energy is reached, a sudden increase in the absorption coefficient is observed. An electron from the core-level is then ejected to the continuum, called a photoelectron. Its kinetic energy is $E_c = E-E_0$, where E is the energy of the photon.

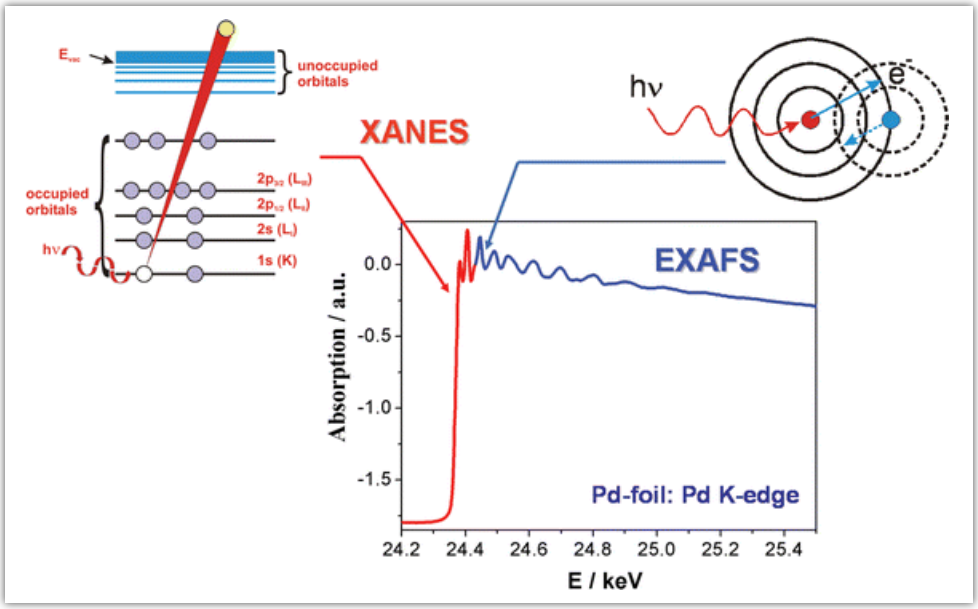

Figure 2.9: Example of XAS spectra around the the Pd K-edge and the principle of XANES and EXAFS (Grunwaldt & Baiker, 2005).

The Beer-Lambert law allows to express the intensity transmitted through the sample as a function of the incident intensity and the absorption coefficient, expressed as: $I = I_0\, e^{-\mu x}$. Where μ is the absorption coefficient, x is the thickness of the sample, I incident intensity and I_0 is the transmitted intensity. When the absorber element is in too small amount, the jump absorption is indistinguishable. One can avoid this problem by measuring the intensity of the fluorescence emitted by the irradiated sample. This radiation is due to the de-excitations of the ionized photo atom and can be expressed as follows: $I_f = \varepsilon_f\, I_0\, (1 - e^{-\mu x})$, where ε_f is the fluorescence yield. Measurement of fluorescence cannot be done after the sample, as for transmission, since the transmitted intensity would mask the fluorescence. The detector is therefore placed at an angle of 90° with respect to the incident beam (Figure 2.10) to lower any elastic contribution. The incident intensity and the intensity emitted by fluorescence gives us access to the absorption coefficient of the sample.

Figure 2.10: Schematic representation of a transmission and fluorescence configuration.

2.2.2. Synchrotron Radiation

Synchrotron radiation is an electromagnetic radiation emitted during acceleration of a high-energy charged particle (Veksler, 1944; McMlillan, 1945), which will be stored in storage rings with significantly improved performance. The introduction of insertion devices in the storage ring such as undulators and wigglers increases considerably the brightness of radiation, which can be used to study the material in different phases: solid, liquid or gas, under several conditions like pressure, temperature and light. In order to obtain wavelengths of the order of a few tenths of angstroms essential for certain researches in physics, biology, chemistry, etc., higher energies are necessary. The high energy (> 6 GeV) will automatically involve wider circles of storage rings, which will also allow to place several experimental stations. It is the case of the European Synchrotron Radiation Facility (ESRF) which produces one of the most intense synchrotron radiation.

The basic principle is due to Maxwell's theory of electromagnetic waves. This theory makes it possible to calculate all the quantities concerning the radiated electromagnetic field. The power radiated by a particle along a circular trajectory of radius ρ is given by the following formula:

$$P = \frac{2}{3}\frac{e^2\, c\, \beta^2 \gamma^4}{\rho^2}$$

Where c is the speed of light, e is the charge of the particle, $\beta = c/v$ (v: is the speed of particles) and $\gamma = {}^{E}/_{mc^2} = {}^{1}\Big/\sqrt{1-\beta^2}$ (E is the energy of the particle and mc^2 is the rest energy).

From these formulas, we can extract the following information: The radiation is more important for the light particles (at fixed energy and radius of curvature). The synchrotron radiation is a phenomenon related to the centripetal acceleration in the accelerators of electrons or of positrons. It will be very low in the proton or heavy ion accelerators. Only relativistic particles will radiate a consistent power ($\beta \approx 1$, $\gamma >> 1$). Figure 2.11 shows the shape of the emission in the two extreme cases of a very low particle velocity, or comparable to the velocity of light: while the radiation is approximately isotropic for a slow particle. The field radiated by a relativistic particle, by the effect of the Lorentz transformation is picked up for a portion of trajectory seen by the observer in a vertical opening cone Ψ.

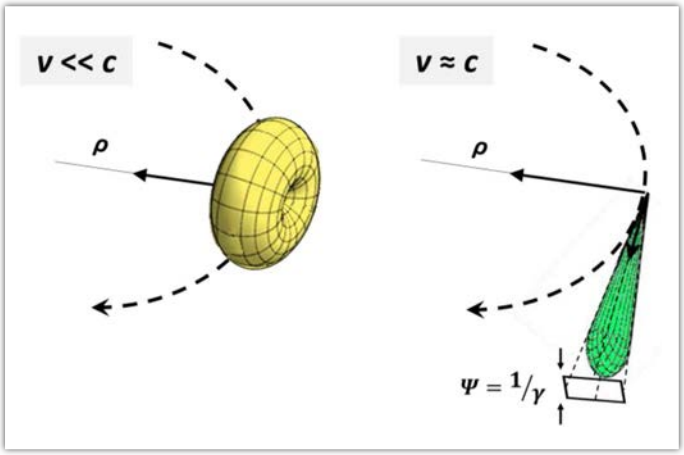

Figure 2.11: The emission by a charged particle subjected to a centripetal acceleration.

ESRF is a 3rd generation synchrotron source, produce a high quality of hard x-ray ranging from 5 to 100 keV with a very high collimation (~ mrad), a high quality, high spatial and temporal stability and small source size (~ 100 µm). The mains steps to generate the synchrotron radiation (Figure 2.12):

First step: the electrons are emitted at the start of the "linac", grouped in the form of packets and then accelerated progressively up to 200 MeV by electric fields to a speed very close to that of light. Second step: the electrons then pass into the "synchrotron booster", a 300-meter ring in which they make several thousand turns, gaining a little more energy each turn. As soon as they reach their final energy, 6 GeV - in just 50 milliseconds - they are sent to the storage ring. Third step: "The storage ring" with circumference of 844 meters, is the place where the electrons circulate at the speed of light, in a tube under the ultra-vacuum (~ 10^{-9} mbar). During their travel through the ring, electrons pass through different types of magnets: bending magnets, undulators and focusing magnets. They undergo acceleration and lose energy in the form of an electromagnetic radiation called "synchrotron light".

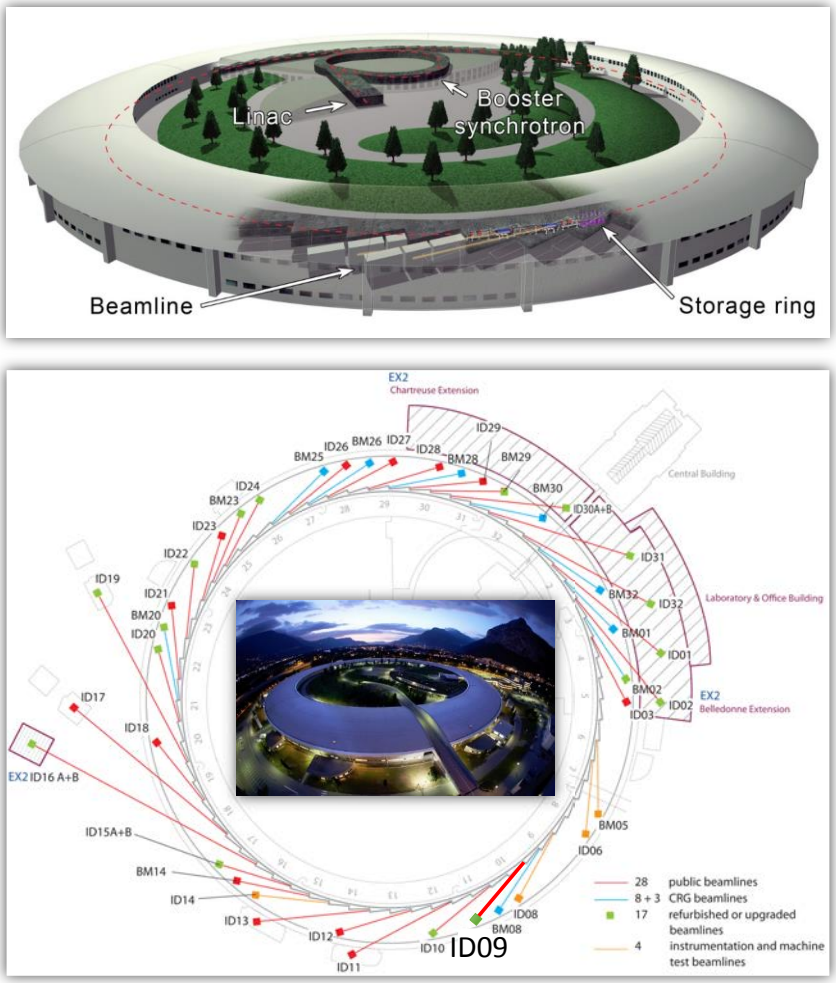

Figure 2.12: Schema of ESRF and beamline stations. (http://www.esrf.eu/about/press-room/intro-esrf-journalists)

The bending magnets force the electrons to change direction. These magnets also serve as synchrotron light sources which is emitted tangentially to the curvature of the electron beam, and is directed towards the "beamline". The undulators are magnetic structures formed of small magnets of alternating polarity (Figure 2.13). The beams of light they produced have a million times more intense than the beams from the bending magnets. They have brightness and coherence properties close to lasers. The Focus magnets, also called magnetic lenses, are used to concentrate the electron beam to make it as thin as possible.

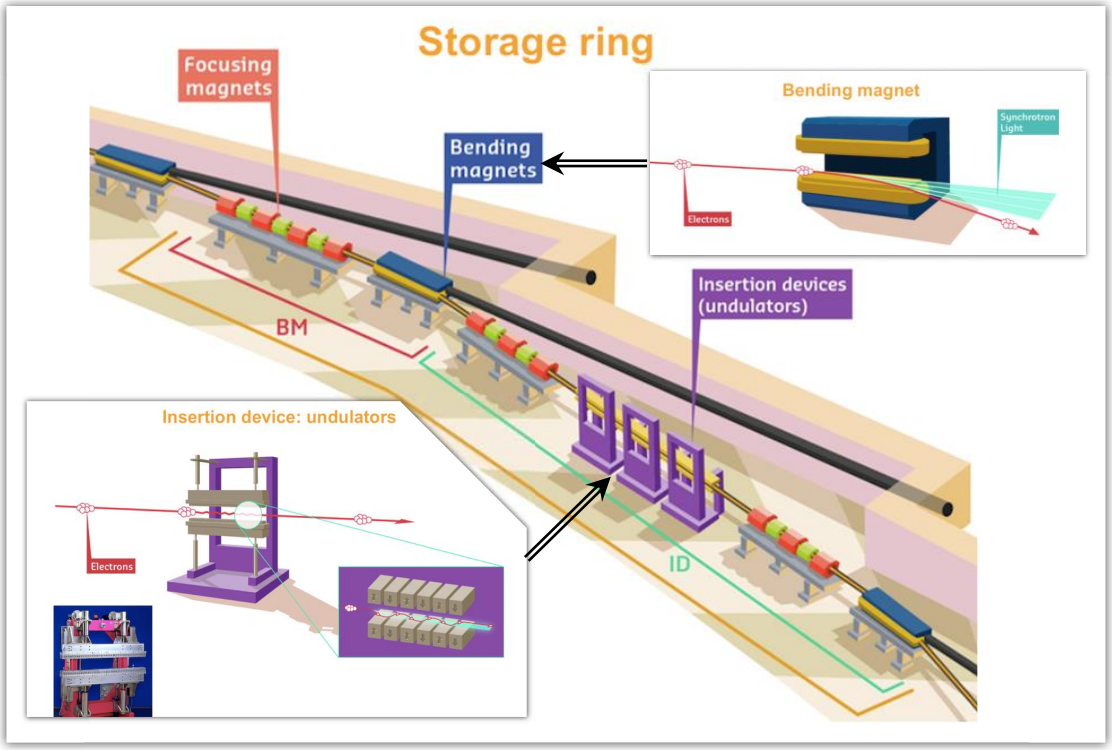

Figure 2.13: Schema of the insertion devices in a segment of the ESRF.
(http://www.esrf.eu/about/synchrotron-science/synchrotron)

2.2.3. ID09b beamline description

The beamline ID09b is a modular station experimental beamline, designed for time-resolved resolved measurements ultrafast structural changes in macromolecular crystallography and in liquids (Wulff *et al.*, 2003; Guérin *et al.*, 2004; Ihee *et al.*, 2005; Kong *et al.*, 2010). The unique feature of this beamline resides in the white light beam which can be used in time-resolved Laue diffraction on macromolecules.

X-ray source

The x-ray pulses delivered from ESRF have a time duration from 50 to 100 ps. The 16-bunch mode (16 bunches of electron in the storage ring, separated between them by 176 ns) is used for our experiment. This x-ray pulses leave the insertion devices at the beginning of the beamline, are formed spatially (slits, toroidal crystal focusing) and spectrally (primary slits, monochromator, mirror) before entering the experimental booth. The Figure 2.14 shows a schematic drawing of different main components an ID09B beamline at ESRF.

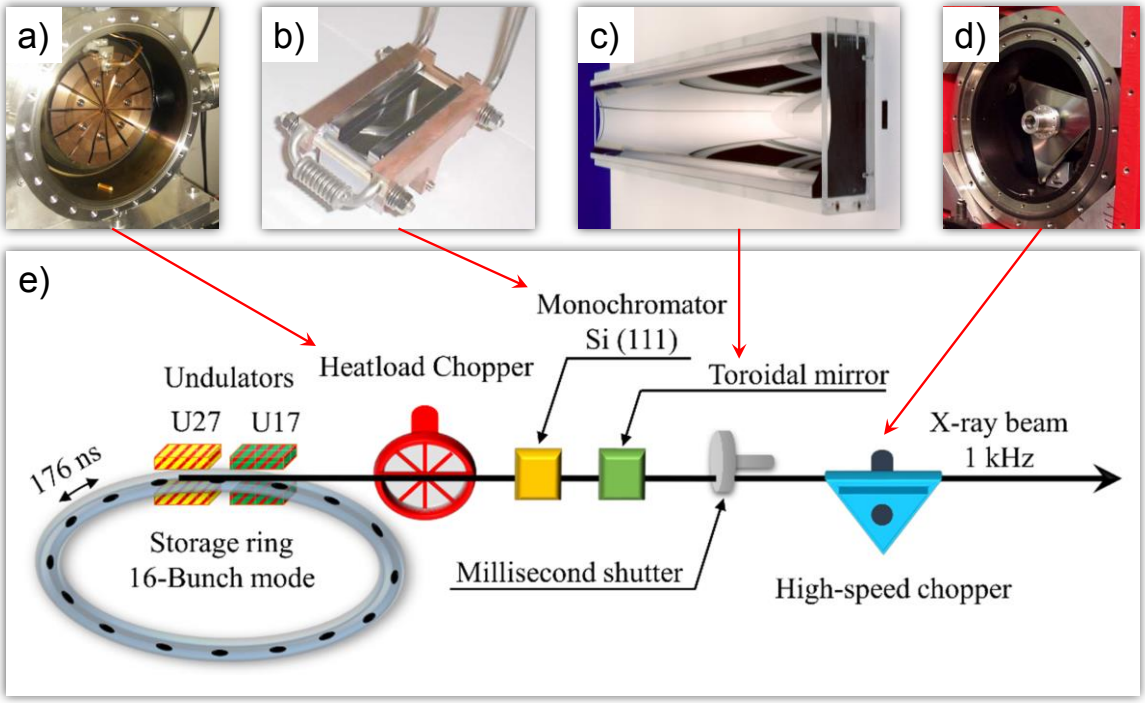

Figure 2.14: (a,b,c,d) Photography of main component at ID9b beamline, (c) Schematic drawing of the X-ray source.

Before entering in the optics hutch, the beam is reduced by a primary slits by removing the diffusion around the central cone. The two choppers are used to reduce the average power by a factor of 5600 for the 16-bunch mode accepting a train of non-attenuated pulses at 1 kHz. The fist chopper is the Heat-load chopper, is in the optics hutch. It chops the white beam into 50 µs pulses. The average power is reduced to 7.5 % of the incoming power. The second chopper, is the high-speed chopper, is placed in the focused beam. It is synchronized with the heat-load chopper. It chops the pulses a second time, down to the single pulse level. The pulses that escape the two choppers are very intense, only attenuated by the reflectivity of the mirror and the acceptance of the slits. When the storage ring is run in timing mode 16-bunch the bunch spacing is 176 ns. That is long enough for the high speed chopper to isolate single X-ray pulses. The exposure time is then dramatically lower than the chopper open window, 100 ps compared to 280 ns. A millisecond shutter upstream the high-speed chopper gates the CCD detector i.e. it controls the number of pulses in the exposure. The water-cooled monochromator is composed of two parallel crystal separated by a fixed orthogonal distance of 10 mm, designed to operate between 4.9 and 39.6 keV. The second optical element is a platinum coated toroidal mirror. It is placed 33.1 m from the source and it works at a fixed incidence angle of 2.772 mrad. The mirror focuses the radiation 22.4 m downstream.

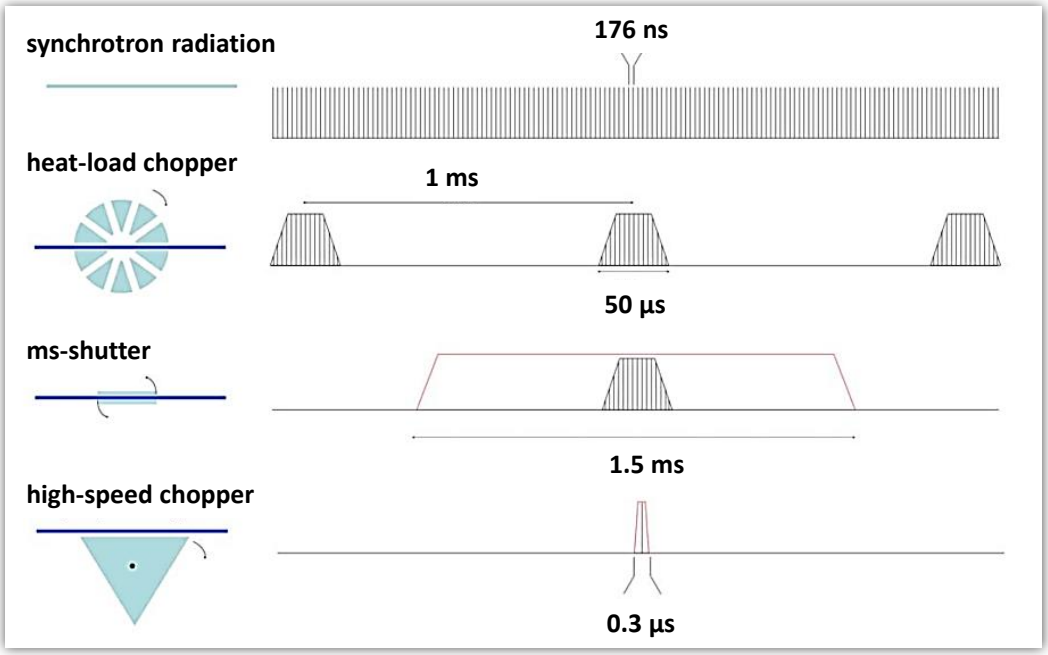

Figure 2.15:Schema to isolate single X-ray pulse (Cammarata *et al.*, 2009)

The magnetic sequence at ID09b beamline is formed by a combination of two undulators, U27 and U17 with a magnetic field periods of 27 and 17 mm, respectively. The emission spectrum depends on the undulator gap (by changing the vertical distance between the magnetics), the Figure 2.16 shows the energy emitted from the undulators which covers a wide spectral ranging from 6 to 30 keV. As part of our experience, we worked at different energies 6, 7 and 16 keV.

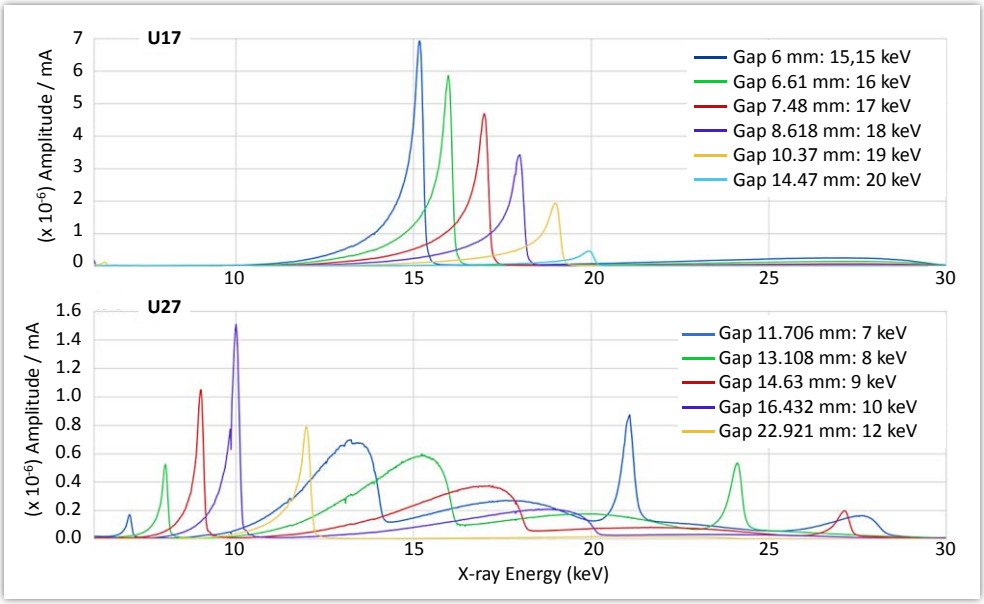

Figure 2.16: Undulator spectra as function of the gap on ID09b (Wulff, ID09b).

Femtosecond laser source

The main research areas of the beamline include laser induced processes in liquids and solids occurring in the picosecond temporal domain. In particular, the time-resolved scattering and diffraction have been successfully applied for studies on recombination of small molecules in solution as well as transient acoustics and phase transitions in crystals. Experiments of that kind require the laser pump pulses of very short duration (fs and ps). The ultrashort laser system (Figure 2.17) at ID09B is based on a standard Micra femtosecond oscillator, that is phase is locked to the synchrotron RF/4 and produce a very weak (~ 3nJ per pulse) ultrashort (70 fs) pulses with a repetition frequency of 88 MHz at wavelength of 800 nm, and a Ti: sapphire multipass chirped pulse amplifier (CTA). The incoming weak pulses from the oscillator are amplified in the CTA which is configured to emit pulses of 100 fs duration with an energy of a single pulse of 1.5 - 2.5 mJ. Before amplification, it is necessary to stretch in time the pulses using a pair of gratings, because the high peak power pulse (1 TW/cm-2) can cause damage and nonlinear absorption to several optical elements in the amplifier, including the pockels cell and the Ti: sapphire crystal. Then, the pulses are amplified in the Ti: sapphire crystal cavity, pumped with a green laser and exits after compression. The last stage, used a non-linear methods to generate a variety of wavelengths. On ID09B the wavelength of the femtosecond radiation can be tuned over a wide wavelength range, from UV to far IR, the optical parametric generator and amplifier called the TOPAS (Light Conversion). The typical tuning curves of the TOPAS covers the wavelength range from 240 nm to 2600 nm with conversion efficiency of up to 20%. Additionally the second (400 nm) and the third (267 nm) harmonics (SH and TH) of the 800 nm Ti:sapphire radiations are generated with efficiencies of 50% and 25% respectively.

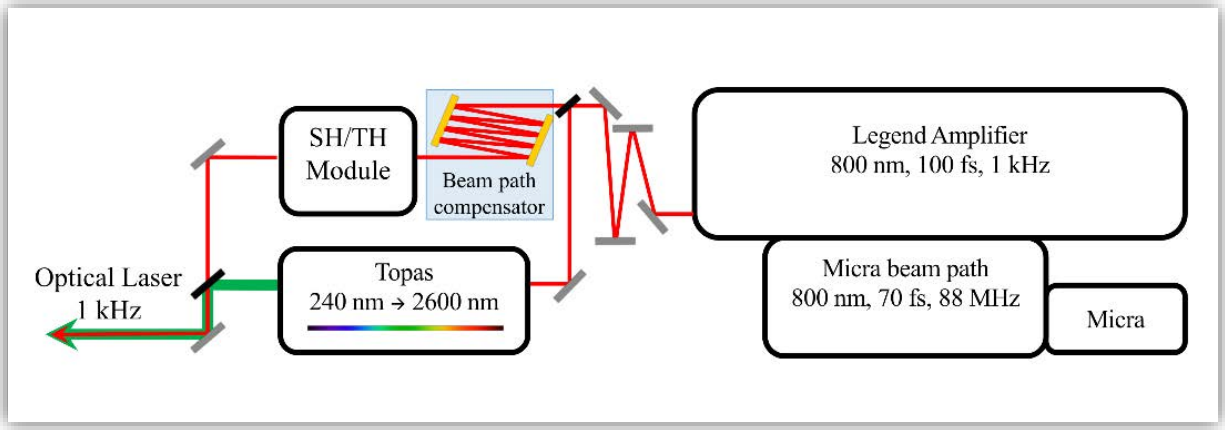

Figure 2.17: Schema of laser source on ID09b.

2.2.4. Experimental set-up

The aim of our work at ID09b beamline was to develop time resolved X-ray absorption spectroscopy (TR-XANES) using the x-ray beam and the femtosecond laser described in the previous sections. The idea is to follow the x-ray fluorescent signal after optical pulse excitation at wanted K-edge of the metal compound. The temporal overlap of the X-ray/optic pulses is measured with the GaAs detector which is sensitive to the both radiations with a precision of 25 ps and the time delay between the both pulses is controlled electronically. At the overlap position, the optical pump and the X-ray probe have respectively a pulse duration of 150 fs and 100 ps, with a focal area of 120 x 350 µm and 60 x 120 µm. The same was excited in quasi collinear geometry (angle between x-ray and laser beam of ~10°)(Figure 2.18).

The samples is circulated via a closed loop system through a 0.5 mm capillary tube and the speed flow is adjusted by the peristaltic pump (Gilson Minipuls-3) for having a fresh sample for every new X-ray and laser pulse. The detector is mounted close to the sample (~ 3 cm) perpendicular to the X-ray propagation direction to minimize the collection of elastic photon scattering. In this geometry the active window covers a solid angle of ~ 0.74 sr (5.89 % of 4π). We used a Pin diode to measure simultaneously the transmission (scattered X-ray) in order to correct the final fluorescence signal (Intensity fluctuation, the long decay of the current after each refill).

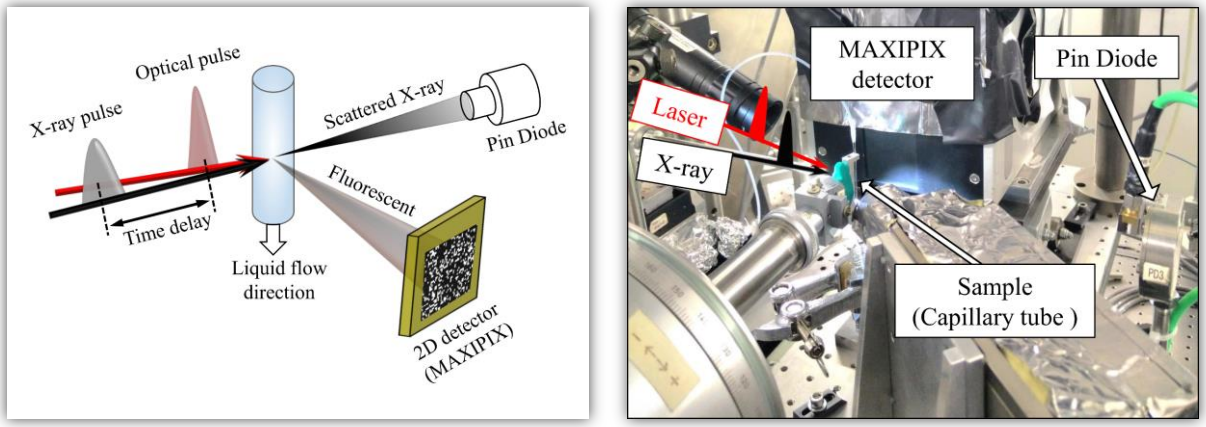

Figure 2.18: (left) Schema diagram of the time-resolved XANES. (Right) Photography of the set-up at ID09b beamline.

2.2.5. Detection and data acquisition

The 2D detector used during our development of the TR-XANES at ID09B beamline is a MAXIPIX (Multichip Area X-ray detector based on a photon-counting PIXel array) 2x2 detector (Ponchut *et al.*, 2011), developed by ESRF. It is based on the Medipix-2 photon-counting readout chips (Llopart *et al.*, 2001). This detector is best suited for the TR-XANES experiment because of their high spatial resolution with 516 x 516 pixels of 28.4 x 28.4 μm^2 size, high frame rate up to 1.4 kHz, noiseless detection, high dynamic and it can operate on a wide range of X-ray energies (from 5 keV to 25 keV) which is limited by the absorption efficient of the silicon sensor (100% at 8 keV, 68% at 15 keV, 37% at 20 keV). The data acquisition is controlled by the existing Linux workstation on ID09b. The images was collected by setting the time delay between the X-ray pulse and the laser pulse to a fixed values and a scanning of energy of the x-ray photon. Also, a scan times until some hundreds nanosecond were recorded at fixed energy.

2.2.6. XANES experiments at the ID09 beamline of the ESRF

During the development of the TR-XANES experiment, we checked different configurations of the set-up such as acquisition parameters (integration time, threshold) and we developed the macros that can drive the experiment and the data acquisition. Finally, we optimized the experimental set-up to find the optimal parameters such as detector-sample distance and angle, x-ray and laser alignment, thickness and concentration of the sample. As test sample we used the aqueous solution of $[Fe^{II}(bpy)_3]^{2+}$, which was studied extensively in the literature by TR-XANES (Lemke *et al.*, 2013; Van Kuiken *et al.*, 2016; Bressler & Chergui, 2004; Lemke *et al.*, 2017).

As we mentioned before, we used an aqueous solution of $[Fe^{II}(bpy)_3]^{2+}$ to improve the parameters of data collection and reduction. The results obtained from this analysis are in good agreement with the literature. The figure 2.19 shows the XANES spectrum recorded at room temperature at laser off and at 500 ps after laser excitation at 530 nm, the difference in x-ray absorption between the laser-excited sample and the unexcited sample shows an increase in absorption at 7123 eV. At this energy, we recorded a time scan of the signal as a function of laser pump/x-ray probe time delay which shows the kinetic relaxation and the fit with a single-exponential decay with a time constant of 618(29)ps, comparing with the values obtained in the

literature: (665ps, Van Kuiken *et al.*, 2016). I then used time-resolved XANES at ID09 ESRF for investigated charge-transfer process in CsCoFe PBA (Chapter 4)

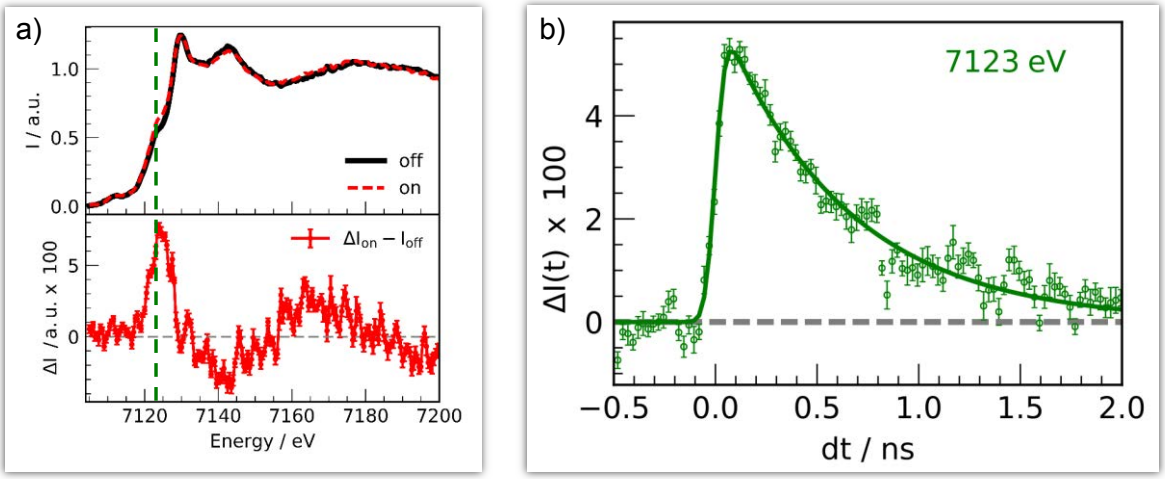

Figure 2.19: a) XANES profiles at LS and HS state of aqueous solution of $[Fe^{II}(bpy)_3]^{2+}$. b) Time scan recorded at 7123 eV (circles) upon 530 nm excitation.

2.3. X-ray Free-Electron Laser Radiation

The generation of the Free Electron Laser (FEL) radiation is based on the process called Self-Amplified Spontaneous Emission (SASE) (Kondratenko & Saldin, 1980; Bonifacio *et al.*,1984). This radiation covers a wide bandwidth (from VUV to x-ray) with ultrashort pulse duration of a few femtoseconds. Several FELs are already operational in the world in the domain of x-ray, such as the first soft X-ray FEL (FLASH) at Hamburg in 2005, which delivers a radiation from 5 to 44 nm (Ackermann *et al.*, 2007). Then, the Linac Coherent Light Source (LCLS) in 2009 at Stanford Linear Accelerator Center (SLAC), which operates in the bandwidth 1.2 - 22 Å (Emma *et al.*, 2010), and the SACLA in Japan in 2011 (Ishikawa *et al.*, 2012). New FEL in the X domain are under construction or operational, such as the European X-FEL in Germany, the PAL FEL in Korea (PAL FEL) and the SwissFEL in Switzerland.

The FEL radiation is the fourth generation, because of their brightness which is greater by a factor of 10^{10} than the synchrotron sources (Figure 2.20) with a short pulses (few tens of femtosecond). This radiation can be used in several field of science (physics, chemistry, biochemistry), to study the structure and time-resolved function of single molecules, to make movies of the chemistry reactions, perform 3D imaging and dynamical studies of the biological compounds and characterize the transient states of matter created by radiation.

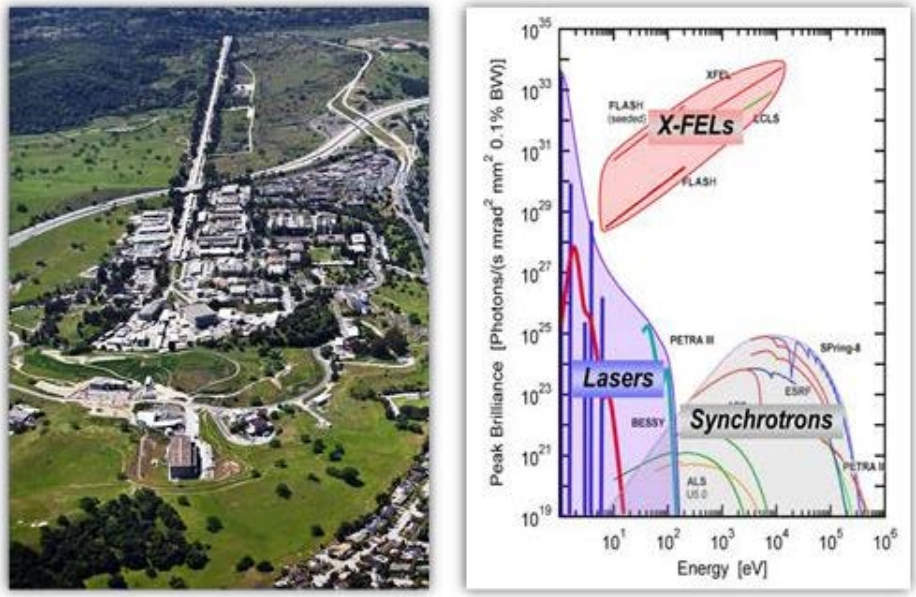

Figure 2.20: (Left) Aerial photography of LCLS at SLAC (https://portal.slac.stanford.edu/) , (Right) Peak of brightness as function of energy of conventional lasers, synchrotron and x-ray free electron lasers (Ullrich *et al.*, 2012)

Unlike the synchrotron radiation generated by the relativistic electrons in the storage ring in which the electron bunch is stored and used over and over, each bunch contains ~ 10^9 electrons which emitted spontaneously as incoherent photons (Figure 2.21), in the X-FEL, the storage ring is replaced by a linear accelerator, that allows compression of electron bunch used once. The coming electron bunch from the linear accelerator travels through a very long undulator line, (at LCLS, the undulator is made up of 33 undulators segments with a length of 3.4 m each). The X-FEL radiation is generated at the beginning of undulator by SASE. The electrons subjected to the magnetic fields of the undulator, oscillate and emit synchrotron radiation. Then, this radiation interacts gradually with electrons whenever they progress in the undulator an exchange of energy and an order inside the bunch occurs, some electrons lose energy and are slowed down, others gain energy and they find themselves in front of the bunch, which becomes density-modulated along the longitudinal direction at the wavelength of the x-ray light, and the emission is coherent. The light wave is then amplified as it progresses in the undulator.

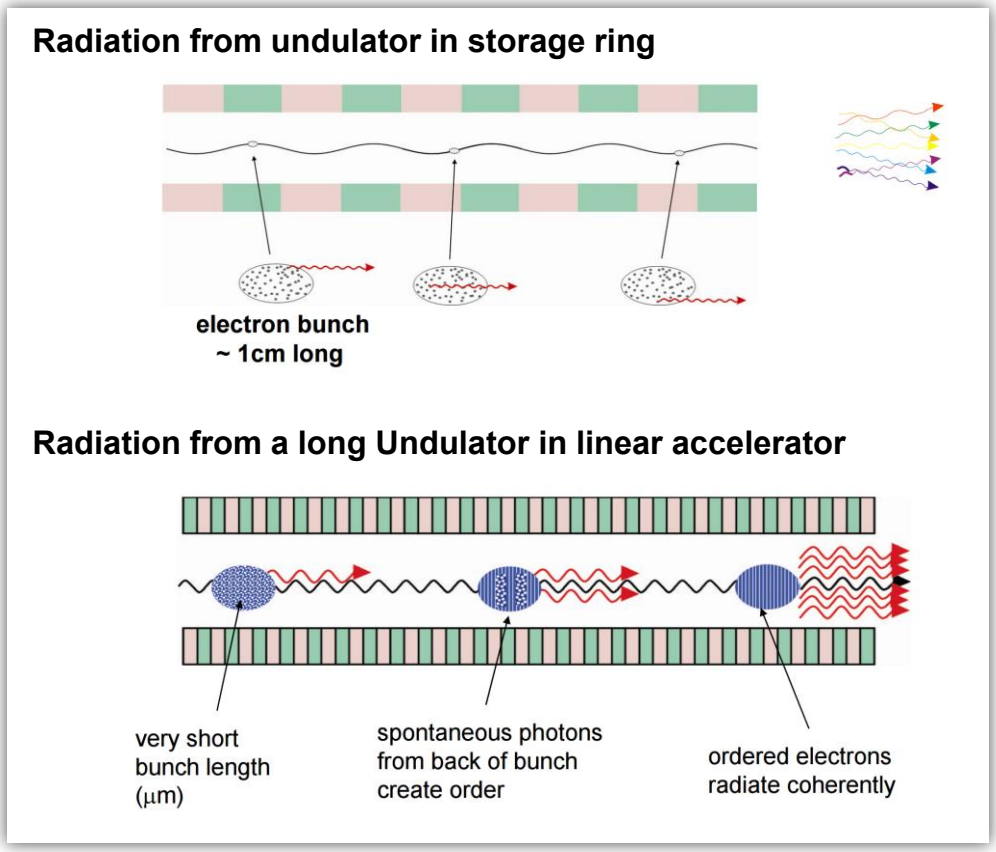

Figure 2.21: Schematic of comparison between a synchrotron radiation and FEL.

Ours TR-XANES measurements were performed in the X-ray Pump Probe (XPP) beam station of LCLS (X-FEL). We used the coherent x-ray laser emitted from the undulators with a pulse duration of few tens femtosecond. The set-up was very similar to the one developed at ESRF (ID9b, Grenoble). The idea was to combine two femtosecond lasers x-ray and optical to follow the electronic and the structure change after optical pulse excitation, by collecting the x-ray photons of fluorescence (Figure 2.22). The detection system is consisting of ePix camera, developed at SLAC (Dragone *et al.*, 2014), this detector provides a high dynamic range and a low noise (Blaj *et al.*, 2015). The ePix camera was placed at 90° respect to x-ray beam direction to collect the x-ray fluorescence photons. The PIPS diode was also placed at 90°, to recorded simultaneously the intensity of x-ray, that help in the reduction data, to improve the quality of the signal. The solution samples is circulated via a closed loop system through a 30 μm capillary tube and the speed flow is adjusted by HPLC pump. The sample chamber filled with helium gas, to avoid the unwanted scattering from the air. The detectors are placed close to the sample chamber.

We used femtosecond XANES to investigate LIESST in a spin-crossover molecule (chapter 3) and also to investigate charge-transfer process in the CsCoFe Prussian blue analogue (chapter 4).

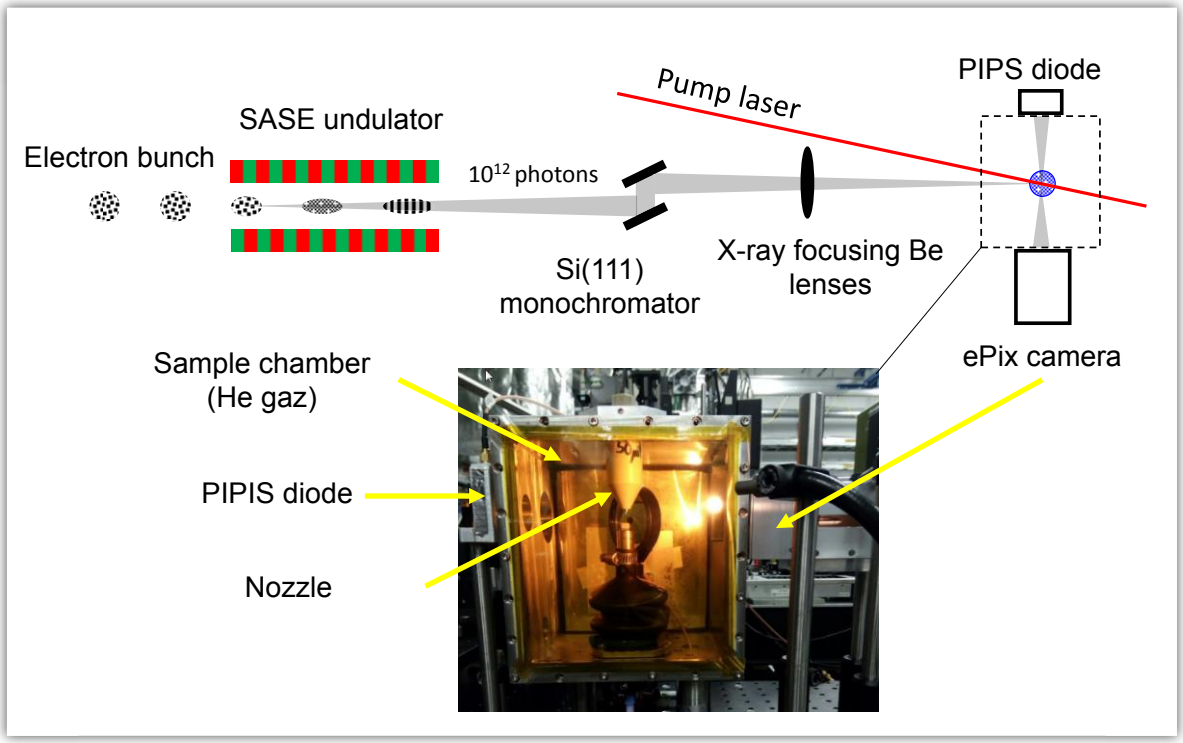

Figure 2.22: Schematic representation of the set-up at XPP (LCLS).

Chapter 3

Coherence and dynamics upon d-d vs MLCT light-induced spin state trapping

This chapter discusses the electronic and structural dynamics accompanying light-induced excited spin state trapping (LIESST) and in particular on the dependence of the structural coherence observed under different excitation mechanisms. We will begin by presenting the current state of the art of experimental and theoretical understanding of LIESST. The advent of femtosecond pulsed lasers has opened a new way to induce and explore the ultrafast photoswitching phenomena in spin crossover materials. This out-of-equilibrium process, involving coherent dynamics, strongly differs from thermal equilibrium transformations driven by temperature and pressure for example, during which the dynamical processes are hidden in a statistical average. We will start by introducing here the different mechanisms proposed for LIESST in different studies to explain the elementary process involved.

Then, we will focus on our new results on a particular system **(Fe^{II}(pap-5NO_2)$_2$** spin-crossover complex) which offers the possibility of a deeper understanding of LIESST thanks to its lower symmetry, providing access to different types of initially excited electronic states. These studies, partially published in Chemical Science (Zerdane, Wilbraham *et al.*, 2017) focus on the nature of the coherent structural dynamics and the role of the intermediate states for its decoherence. The goal is to better understand how the lifetime and the number of the intermediate states can affect the dynamical coherence. Experimental measurements of the magnetic, spectral and structural properties, performed by M.L. Boillot (ICMMO), will be presented in this section. We will then present the femtosecond optical pump-probe studies I performed. TD-DFT and DFT calculations on this compound, performed by I. Ciofini's group (ENSCP), are also introduced and help interpreting the experimental results in terms of structural and electronic dynamics related to modulation of optical properties of Fe^{II}(pap-5NO_2)$_2$. The last part of this chapter shows extension of this work to more complex **[Fe($L_{222}N_5$)(CN)$_2$]** SCO molecule of lower symmetry, for which the change of spin state is associated with a change of coordination. It was synthesized by G. Chastanet's group and TD-DFT calculation were performed by S. F. Matar. On the experimental side, I combined here fs optical spectroscopy, fs XANES at LCLS X-FEL to study LIESST in this system.

3.1. Ultrafast LIESST dynamics in iron spin-crossover

The LIESST effect is a process which is able to switch molecules between different spin states and it is the heart of the intensive development directed towards photomagnetism in spin-

crossover materials (Sato, 2003). Understanding the process and the role of the intermediate states is crucial for the development of photochemistry and photophysics of coordination compounds, especially systems based on iron, ruthenium, copper, cobalt, chromium or manganese (Juban & McCusker, 2005; Iwamura *et al.*, 2011). LIESST is intensively studied in $Fe^{II}N_6$ spin-crossover compounds, for which the Fe ion experiences an almost octahedral ligand-field. At low temperature the ground state is low spin (LS, S=0, $t_{2g}{}^6e_g{}^0L^0$), where L refers to unoccupied ligand orbitals. At high temperature the high spin state (HS, S=2, $t_{2g}{}^4e_g{}^2L^0$) of higher-entropy is favoured.

The photoinduced states are long-lived at low temperature, and Descurtins and Hauser discovered that the LIESST and reverse LIESST can be induced by weak continuous laser excitation (Decurtins *et al.*, 1984, 1985; Hauser, 2004). The photochromism in crystals associated with conversion between LS and HS states can be directly observed by optical spectroscopy. But since the LS and HS states have different electronic configurations and structures, a wealth of technique can be used to characterize the transformation, including magnetism, X-ray diffraction, Raman or IR spectroscopy (Halcrow SCO Book 2013). The photoinduced HS state has a "long" lifetime up to a characteristic temperature T(LIESST), above which the fast relaxation towards LS state makes the observation of LIESST difficult (Létard, 2006).

The LIESST and reverse LIESST processes can be transiently generated above T(LIESST) in spin-crossover solids (Bertoni *et al.*, 2012; Marino *et al.*, 2014; Cammarata *et al.*, 2014; Field *et al.*, 2016) (Figure 3.1a) or for LS molecules of Fe^{II} complexes in solution. Various ultrafast techniques were used to investigate the process, including optical and x-ray pump-probe techniques (Gawelda *et al.*, 2007; Lemke *et al.*, 2013; Auböck & Chergui, 2015) (Figure 3.1b). These studies investigated the lifetime of the MLCT state and the change of electronic state. More recently it was shown that the structural trapping process in the HS potential is associated with the activation and damping of the Fe-ligand breathing mode (Lemke *et al.*, 2017).

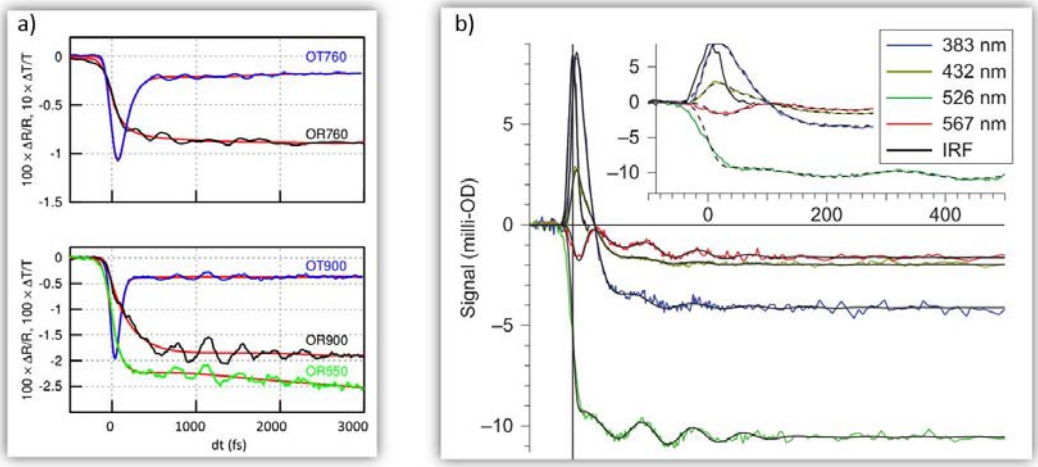

Figure 3.1: a) optical reflectivity (OR) and transmission/reflectivity (OT/OR) change of the SCO $[Fe(phen)_2(NCS)_2]$ crystal (Cammarata *et al.*, 2014). b) optical transient absorption of aqueous $[Fe(bpy)_3]^{2+}$ (Auböck & Chergui, 2015).

At short time scale (fs and ps), an important energy is deposited by the few eV photon (a photon at 500 nm has an energy of ~ 2.5 eV) absorbed by the molecule, and the vibrational cooling to the bottom of the HS potential takes several picoseconds via coupling with the surrounding environment (crystalline lattice or solvent). To better investigate this vibrational cooling process, infrared experiments are required in order to probe small energy levels (Wolf *et al.*, 2008).

A recent study carried out by the group of Kelly Gaffney (Pulse Institute, SLAC) has evidenced the LIESST involves a short passage via a $^3T_1$ state. This result has been achieved by time-resolved X-ray emission spectroscopy (TR-XES) in an iron (II) spin crossover. The sensibility of this technique to 3d spin state (which results from the exchange between the electrons of the orbitals 3p and 3d) allowed to clearly identify the spin state of the different intermediates between the LS and the HS state (Zhang *et al.*, 2014) (Figure 2.3). While the presence of MLCT was not surprising, the presence of a further state ($^3T_1$) was somewhat unexpected since it had been ruled out based on previous studies (Bressler *et al.*, 2009). The proposed sequence of states was thus:

$$\mathrm{MLCT} \xrightarrow{150\ \mathrm{fs}} {}^3\mathrm{T}_1 \xrightarrow{70\ \mathrm{fs}} \mathrm{HS}$$

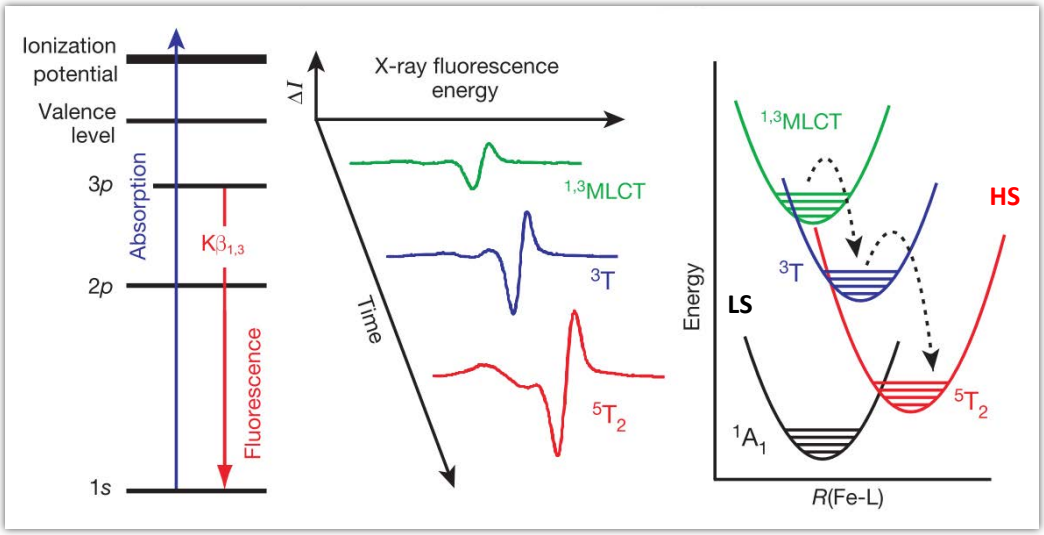

Figure 3.2: Schematic representation of ultrafast x-ray emission detection of spin crossover dynamics (Zhang *et al.*, 2014). From left to right: fluorescent emission de-excitation schema, Fingerprint of each state during the photo switching and a schematic process of dynamics during the ultrafast LIESST.

As mentioned previously, the HS photo excited state created after the MLCT excitation, is characterized by a change in the structure and the electronic state. To follow these changes during the photo switching LS/HS, the x-ray absorption near edge spectroscopy (XANES) is a powerful tool to probe directly the atomic core. A first study performed by Chergui et al, using the slicing technique at synchrotron, it was considered as the first proof that the HS state has been formed within few hundreds femtosecond. Moreover the authors claimed that their experimental results were incompatible with the passage through a triplet state. The relatively poor time resolution and low signal/noise ratio however make these claims somewhat uncertain. More recently, similar experiments (on the same molecule) have been performed at LCLS X-FEL (Lemke *et al.*, 2013, 2017). Figure 2.2 shows the important gain with X-FEL (right) compared to slicing (left) studies: the signature of the transient MLCT is observed and the structural changes clearly evidenced and accompanied by coherent oscillations.

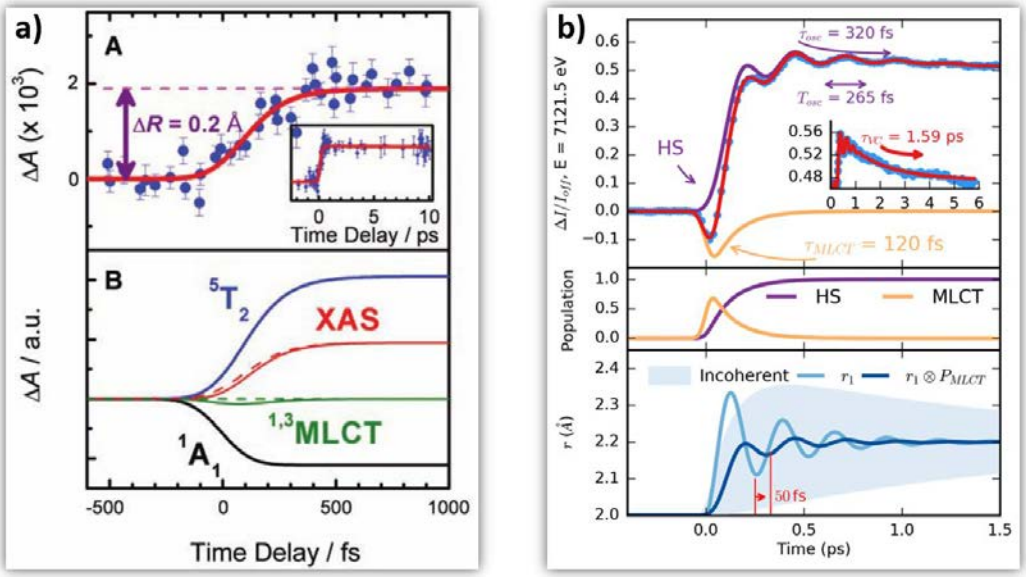

Figure 3.3 : Time resolved XANES around the Fe-K edge of the aqueous $[Fe(bpy)_3]^{2+}$. a) From (Bressler *et al.*, 2009) and b) from (Lemke *et al.*, 2017).

The recent study performed by Lemke et al, of the LIESST mechanism in Fe(II) systems upon MLCT excitation, was performed with 25 femtosecond time resolution. It revealed key features of the intersystem crossing, mainly in terms of change of electronic states and structures, as summarized in Figure 3.4.

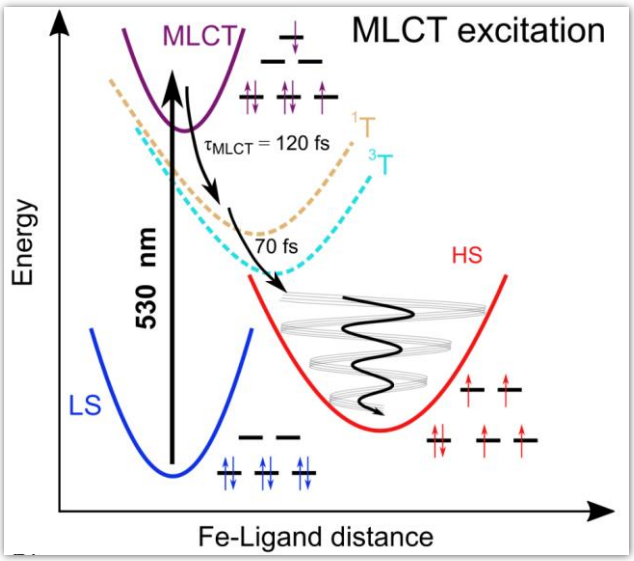

Figure 3.4: Schematic process of LIESST upon MLCT excitation.

The MLCT→HS conversion occurs through MLCT→^{3}T and ^{3}T→HS conversions of about 120 and 70 fs respectively. On the theoretical side, different approaches were used to describe the process. Theoretical electronic-structure calculations used time-dependent approaches to

provide intersystem-crossing rates in agreement with these experimental reports (Sousa *et al.*, 2013).

In addition to the description of the sequence of electronic state, the structural dynamics is another important aspect, as the HS state is structurally trapped in the HS potential through expansion of the FeN_6 core. The electronic population of anti- bonding e_g orbitals moves the equilibrium molecular structure towards longer Fe-L bonds within ≈ 170 fs. A more phenomenological theoretical study explained how this electron-phonon coupling activates the breathing of the Fe-L bonds (Van Veenendaal *et al.*, 2010), which was observed by different techniques sensitive to the change of the ligand field such as XANES (Lemke *et al.*, 2013, 2017), or optical spectroscopy (Bertoni *et al.*, 2015).

This breathing mode corresponds to the activation and damping – in the HS potential (Cammarata *et al.*, 2014; Bertoni *et al.*, 2012; Marino *et al.*, 2014)– of the average Fe-L distance, which is the main structural reaction coordinate, elongating from ≈ 2.0 (LS) to ≈ 2.2 Å (HS). Because of the relatively long MLCT and ^3T decays, the HS population occurs on a timescale approaching the half- period of the molecular breathing, inducing important structural dephasing. Consequently the amplitude of the signal oscillations is reduced, as explained by (Lemke *et al.,* 2017). The fast damping of the molecular breathing is due to dissipation of energy towards other modes such as ligand bending also observed by optical spectroscopy, whereas the vibrational cooling of these photoinduced states occurs typically within 2 ps. However, except the papers mentioned above, the resulting coherent structural dynamics accompanying LIESST, its decoherence and the role of intermediate states and their lifetime are still poorly described in the literature (Consani *et al*., 2009; Auböck & Chergui, 2015).

A further proof of such interpretation could come from a direct comparison (on the same molecule) of different excitation schemes that involve more or less long intermediates. In other words reducing the number of intermediates should help increasing coherence. However, because of the almost octahedral symmetry of FeN_6 systems, the d-d photoexcitation (from t_{2g} to e_g) is very weak or prevented by much more efficient CT excitations. For this reason, LIESST was mainly investigated at femtosecond timescales with MLCT excitations (t_{2g} ^5e_g $^0L^1$). However, Hauser has shown that both MLCT and d-d excitation can be used in some SCO materials to photoinduce the HS state or to measure HS → LS relaxation rates (Hauser, 1991). Juban and McCusker have also shown in Cr-$(acac)_3$ that $^4A_2 \rightarrow {}^2E$ conversion dynamics differs upon $^4T_2$ or ^{4}MLCT excitation (Juban & McCusker, 2005). In the following, we have

investigated LIESST in Fe(II) SCO materials, with intense MLCT and d-d bands for understanding better how structural coherence can be enhanced during LIESST.

3.2. Investigation of the $Fe^{II}(pap\text{-}5NO_2)_2$ spin-crossover

During my thesis, we studied the LIESST dynamics in the FeII spin crossover material $Fe^{II}(pap\text{-}5NO_2)_2$, characterized by a low symmetry (C_2) FeN_4O_2 core. This compound was synthesized and characterized (magnetic and spectral properties) by the team of Marie-Laure Boillot at ICMMO (Iasco *et al.*, 2015). The DFT and TD-DFT calculations were performed by the team of Ilaria Ciofini at ENSCP. I performed the experimental study of the ultrafast dynamics by using the femtosecond optical spectroscopy set-up available at the IPR.

3.2.1. Physical properties: Magnetic, Structural and Spectral

In the SCO $Fe(pap\text{-}5NO_2)_2$ complex, the central iron ion is linked to the four nitrogen and two oxygen atoms (Figure 3.5).

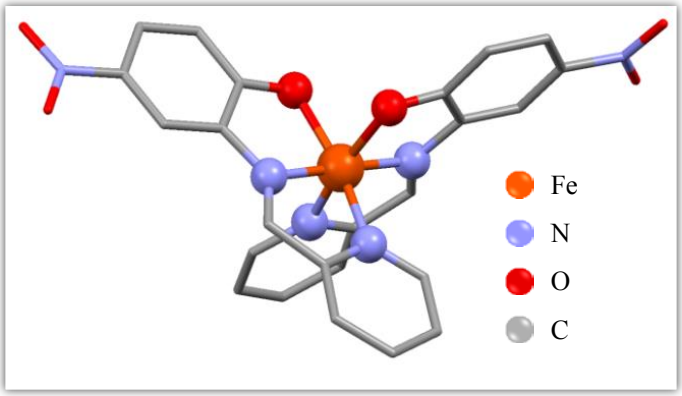

Figure 3.5: Chemical representation of the structure of $Fe(pap\text{-}5NO_2)_2$ molecule.

The SQUID measurements of the magnetic susceptibility show the conventional thermal conversion from LS to HS, which is characterized by a 1st order transition with a thermal hysteresis centered around 297 K (width ΔT= 26 K, Figure 2.1). The measurements were performed on nanoparticles dispersed in polymer film, which we have been used for optical fs spectroscopy. Compared to measurements performed on bulk samples, the films of nanoparticles show at low temperature a different $\chi_M T$ value, related to a fraction of paramagnetic residue and assigned to the presence of crystalline defects trapped in HS state ($x_{HS} \sim 0.15$). The photomagnetic behavior derived from LIESST is similar to the one reported

for the bulk with a 750 nm excitation. LIESST was also observed by illuminating the sample with 532 nm (20 mW cm-2) and 750 nm (15 mW cm^{-2}).

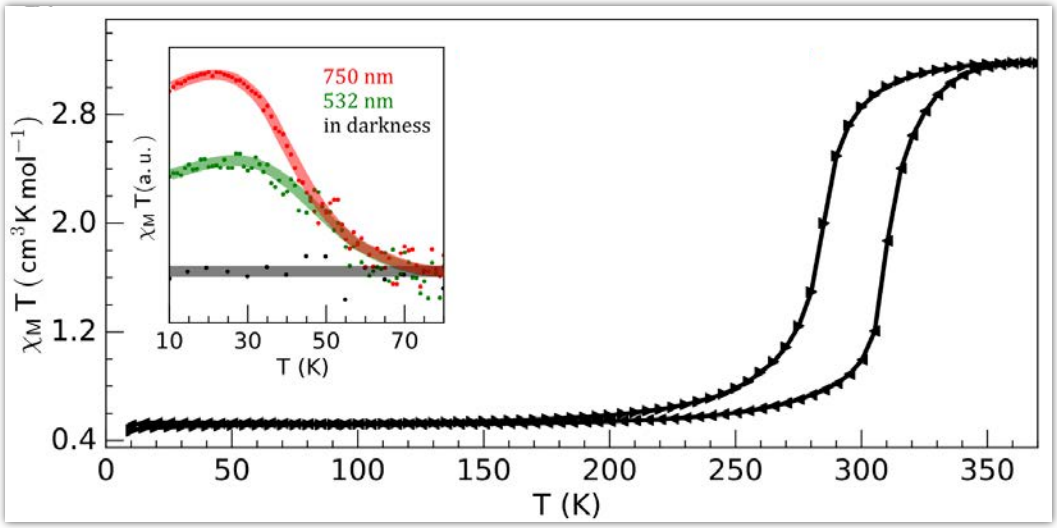

Figure 3.6: Temperature dependence of $\chi_M T$ determined with the sample of $Fe(pap\text{-}5NO_2)_2$.

We were interested in studying the SCO $Fe(pap\text{-}5NO_2)_2$ in the nanoparticles phase with a size of ≈ 1000 x 170 nm which have a good size dispersion as estimated via TEM (Figure 2.3). The particles size does not affect much the magnetic behavior of the transition from LS to HS expect a change in the width of hysteresis (Gudyma *et al.*, 2017) and the fraction of the photoconverted molecules in nanoparticles is more important than for single crystal due to the good penetration of laser through the nanoparticles (Bertoni *et al,*. 2012; Tissot *et al,*. 2011), improving so the quality of the photoresponse detected. At the picosecond time scale, the size does not contribute in the dynamic of photo switching as the process is located at the molecular level. Size effects appear at nanosecond time scale, where elastic cooperative effects come into play (Bertoni *et al.*, 2016).

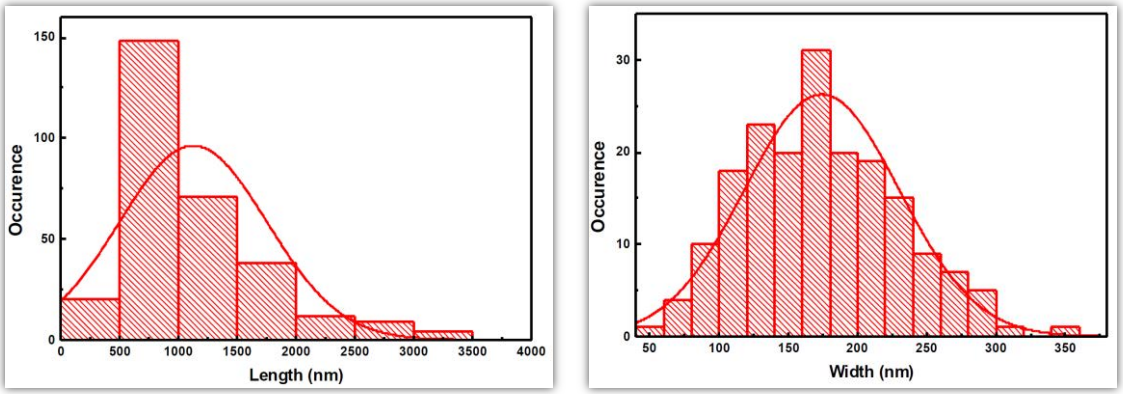

Figure 3.7: Histograms showing the particle size distributions of $Fe^{II}(pap\text{-}5NO_2)_2$ nanocrystals.

The brown green films of particles appear homogeneous at the sub-millimetric scale (Figure 3.8 left) they were characterized by variable temperature measurements CARY 5000 UV-vis double beam spectrophotometer equipped with the Eurolabo variable temperature cell 21525 KBr windows and Specac temperature controller 20120. The temperature dependence of the electronic and structural configuration is reflected in the optical density measurements, which show the different absorption band at 100 K (LS) and 440 K (HS). During the thermal LS to HS transition, the optical density around 800 nm decreases and increases around 500 nm (Figure 3.8 right). There is also an interesting feature provided by an isobestic point at 620 nm which indicates the same optical density of the LS and HS. Also, at the near infra-red region, there is another absorption band around 1000 nm and an isobestic point around 970 nm (Figure 3.8 right insert). The important optical density change, between LS and HS, is very useful for performing time resolved optical studies, as the polymer matrix of PVP (polyvinylpyrrolidone), which embedded the nanoparticles, does not absorb much in the visible and NIR region. In addition, since the nanoparticles in the polymer matrix are oriented randomly there is no light pump or probe beams polarization effect.

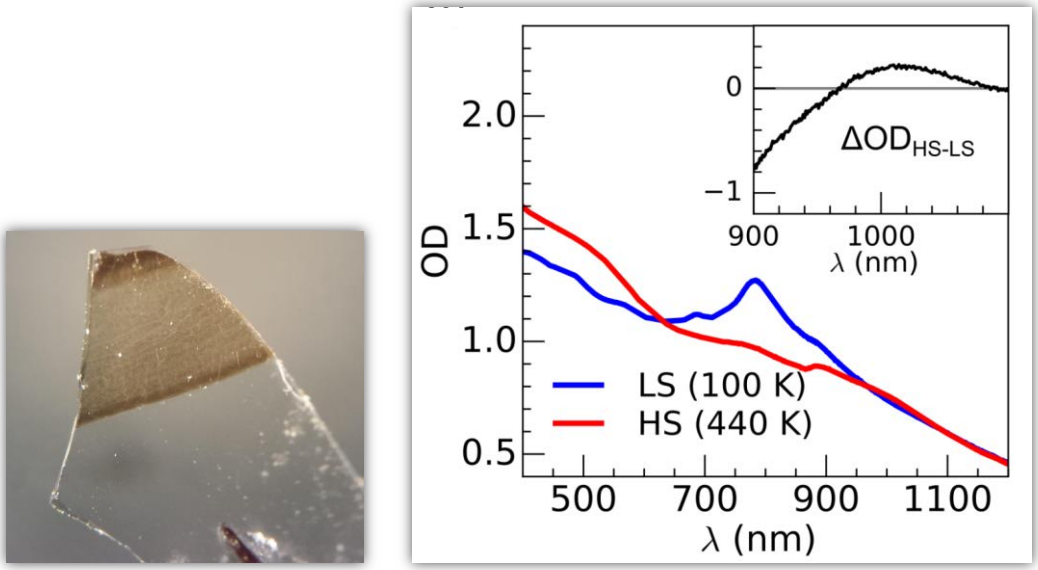

Figure 3.8: (Left) Microscope photographs of PVP polymer film containing homogeneously dispersed nanocrystals deposed on the glass substrate. (Right) Thermal variation of the optical density.

Structural study and crystallography of this compound in the form of single crystals was carried out by Iasco et al. (Iasco *et al.*, 2015). They were able to solve the LS (100 K) and HS (320 K) structures. Like all spin crossover systems studied previously, the LS to HS transition is accompanied by an increase in volume of the unit cell, which is mainly due to an elongation of the Fe-ligand bond (Bréfuel *et al.*, 2010; Lorenc *et al.*, 2009). For both spin states, the unit

cell is monoclinic and the space group C2/c is preserved during the thermal conversion. Important structural changes are the strong elongation along the *b* and *a* axis and the increase of the β angle.

The structural changes of $Fe^{II}(pap\text{-}5NO_2)_2$ nanocrystals, dispersed in the polymer PVP was characterized by x-ray powder diffraction. Different patterns were collected as function of temperature from 150 K to 420 K with step of 10 K, using the Xcalibur diffractometer (λ = 0.71073 Å) at IPR. At high temperature, the superposition of the experimental powder diffractogram and the one calculated from the single crystal, shows the same position of the Bragg reflections which characterized the monoclinic structure. At 150 K, the positions of the hkl reflections change because of the change in the lattice parameter (Figure 3.9). The diffuse background is due to the scattering of the PVP film. The position of (200) reflection as function of temperature indicates clearly a volume change associated with the phase transition centred around 300 K, which is close to the values found from the magnetic measurement. The difficulty for reproducible thermal cycling may be due to the PVP property; the heating at certain temperature, the adsorption of the nanoparticles can affect the processes of SCO.

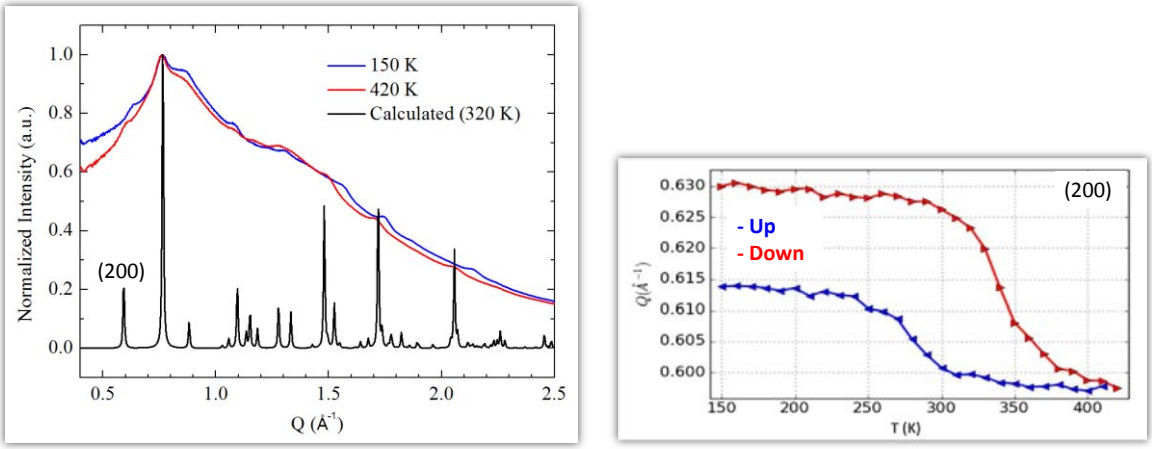

Figure 3.9: (Left) X-ray powder diffraction of the LS (150 K) and HS (420 K) and one calculated at 320 K. (Right) Trace of the 200 reflection position as function of temperature.

3.2.2. DFT and TD-DFT calculation

To better understand the electronic and structural properties in spin crossover systems, DFT calculations help determining with reasonable accuracy the energy levels and the optical absorption bands in different spin states: $^1A_1$, $^3T_1$ et $^5T_2$ (De Graaf & Sousa, 2010). For the $Fe^{II}(pap\text{-}5NO_2)_2$, an UV-vis and NIR absorption spectra were simulated by convoluting with Gaussian functions centred at the calculated wavelength for each transition. The full width at

half- maximum value for the Gaussian functions was set to 0.45 eV. Figure 3.10 shows the vertical absorption spectra calculated for the LS, HS and ^{3}T electronic states. Concerning the LS equilibrium geometry, for which singlet-to-singlet excitation energies were determined, two main absorption bands are computed at 500 nm and 749 nm.

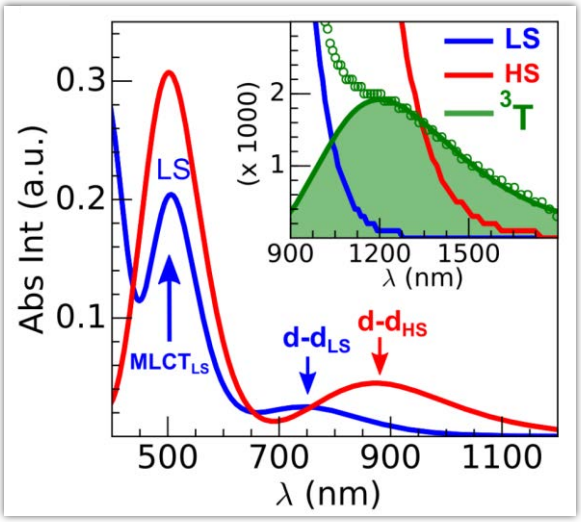

Figure 3.10: Calculated absorption spectra.

From inspection of the highest-contributing molecular orbitals involved in these transitions (Figure 3.11), it can be seen that, despite contributions from both metal and ligand centred orbitals, the transition centred at 500 nm has an MLCT character and is hereafter labelled $MLCT_{LS}$. Similarly, the transition centred at 749 nm has a d-d character and will be referred to as d-d_{LS}. Notably, this transition exhibits a small, but non-zero, oscillator strength (0.018 au), underlining that the reduced symmetry of the coordination environment from O_h, which is more usual for FeN_6 systems, to C_2 for this FeN_4O_2 system.

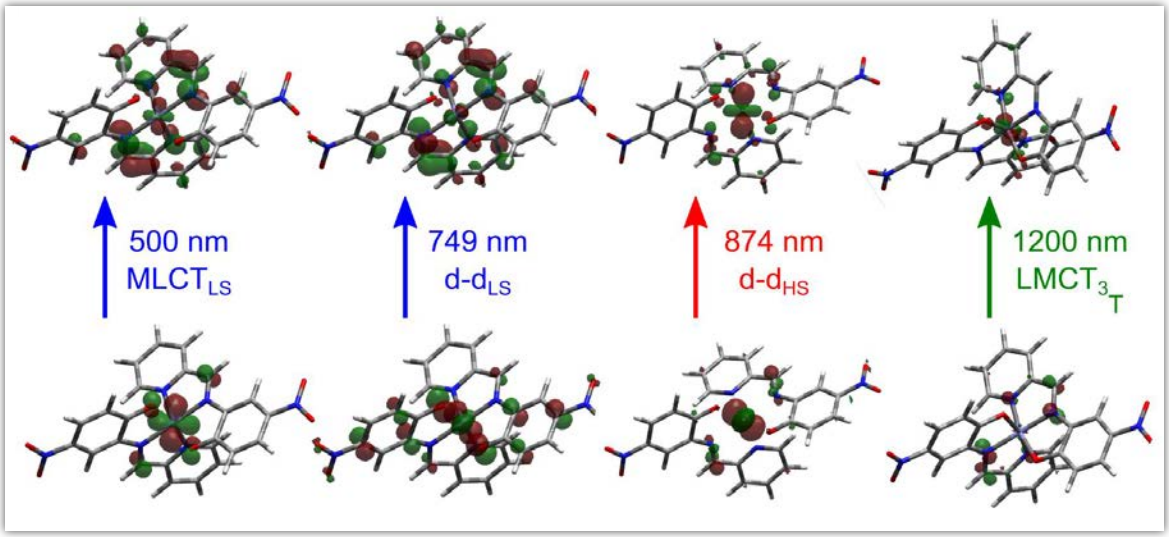

Figure 3.11: Characteristic orbitals of hole and particle for LS, HS and T states obtained by TD-DFT.

Consequently, the d-d transitions that are no longer completely forbidden. The character assigned to these transitions is further validated by inspecting plots of the difference in density between the ground and excited states (Figure 3.12). In contrast to Figure 3.11, these plots consider all determinants which form each excited state rather than just those with the largest coefficient.

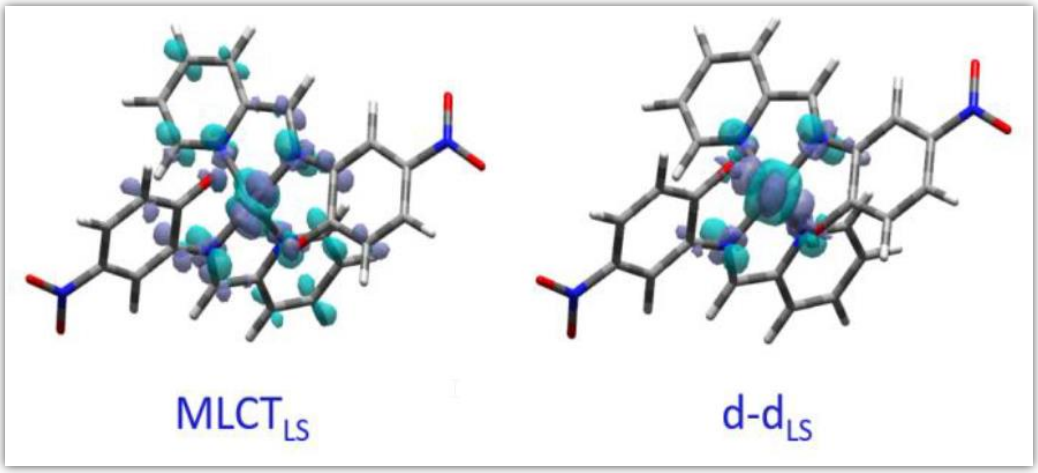

Figure 3.12: Density difference plots between ground and excited states for MLCT$_{LS}$ and d-d$_{LS}$ excitations. Dark (light) blue zones indicate areas which increase (decrease) in electronic density upon excitation.

3.2.3. Ultrafast LIESST in $Fe^{II}(pap\text{-}5NO_2)_2$ spin-crossover

For tracking LIESST dynamics in real time we used an optical pump-probe method with 60 fs time resolution (RMS) presented in chapter 2 on LS $Fe^{II}(pap\text{-}5NO_2)_2$ crystals embedded in a thin PVP film, spin coated on a glass substrate. This allows easy manipulation of samples with homogeneous dispersion at sub-millimetric scale.

3.2.4. Time-resolved optical studies

The optical pump probe measurements were performed at 100 K in the visible and NIR spectral regions. The repetition rates of the pump and the probe are 500 Hz and 1 kHz respectively. To avoid the degradation of the samples under the pump pulse irradiation, the excitation fluence is set to 4.0 +/- 1 $\mu J.mm^{-2}$. In the Figure 3.13, we show the time scan of the optical density after 730 nm wavelength excitation and probing at different wavelength around the isobestic point 970 nm.

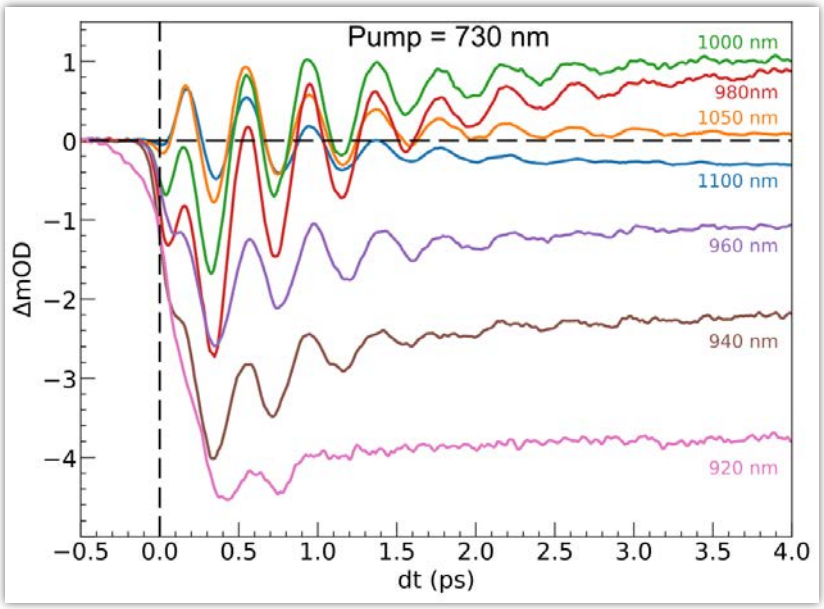

Figure 3.13: Time resolved of milli-OD change upon 730 nm excitation at in the 920-1100 nm range, at 100 K.

In all these measurements, the evolution of OD is accompanied by oscillations in phase, whose sign and amplitude depend on the probing wavelength. Given the previous results obtained in different SCO materials, it is natural to attribute these oscillations to the global shift and oscillation of the d-d_{HS} band with the Fe-L elongation. Time traces at 980 and 1000 nm

show signatures of the intermediate state, but are also affected by the proximity of the isobestic point, which shifts in time during the vibrational cooling, as observed in other SCO crystals. The signal of these time traces therefore changes sign between 100-500 fs (hot HS state) and after 5 ps (vibrationally cool HS state). Below 940 nm oscillations are more difficult to observe.

In order to assess the modulation of the ligand field through the d-d_{HS} gap with respect to this breathing mode, 30 structures were generated as a projection along the normal mode, assuming a harmonic mode. For each structure the energy of the d-d_{HS} band was vertically re-computed with TD-DFT (Figure 3.14). The deformation lies between changes in Fe-N (axial) from 2.074 to 2.172 Å and Fe-N (plane) from 2.144 to 2.307 Å and Fe-O (plane) from 1.967 to 2.074 Å. On the x-axis, 0 corresponds to the equilibrium while negative (positive) values indicate shorter (longer) Fe– L distances. The frequency of the breathing mode was calculated at 84 cm^{-1}.

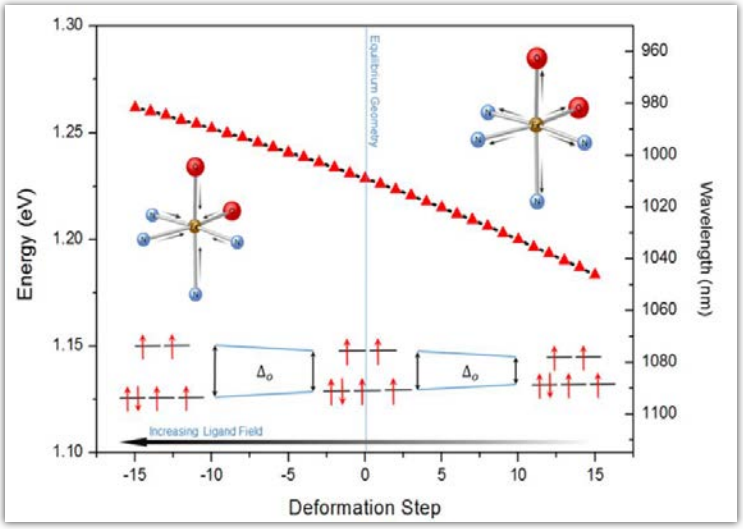

Figure 3.14: Modulation of Δ_0 (d-d_{HS} splitting) with respect to a harmonic structural deformation corresponding to the breathing mode of the in phase stretching of the Fe–N and Fe–O bonds and calculated at 84 cm^{-1}.

3.2.5. Role of intermediate states in the phenomenological model

To fit our experimental optical pump probe data, we used a phenomenological model already used to interpret time resolved X-ray absorption data on similar SCO system (Lemke *et al.*, 2017). In this model, we will consider two cases of mechanism of relaxation. The first case, describes the relaxation in HS stat from one intermediate state denoted as INT. The second describes the relaxation from MLCT to HS state, passing through the INT state (Figure 3.15).

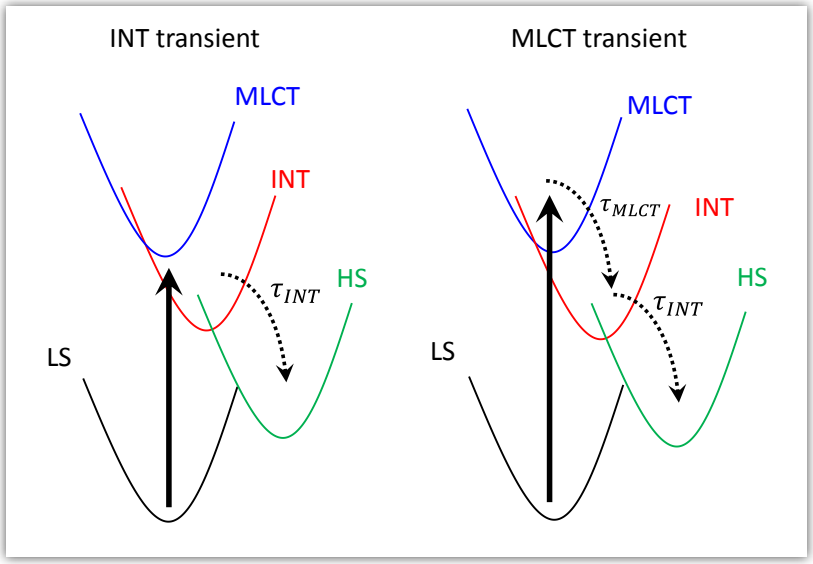

Figure 3.15: Schematic representation of phenomenological models of relaxation mechanism.

a) Case of the intermediate INT transient

In this case, the relaxation mechanism, can be expressed as follows:

$$INT \xrightarrow{\tau_{INT}} HS$$

The contribution of the INT state which decays with a time constant τ_{INT} is given by:

$$S_{INT}(t) = A_{INT} \times P_{INT}(t)$$

Where A_{INT} is the amplitude of the INT population used as source of HS molecules, is given by:

$$P_{INT}(t) = IRF(t) \otimes \left[\exp\left(-t/\tau_{INT}\right) \times H(t)\right]$$

Where $\otimes$ is the convolution operator, *IRF(t)* is the instrument response function assumed to be Gaussian, and *H(t)* is the Heaviside function are given by:

$$IRF(t) = \frac{1}{\sigma_{IRF}\sqrt{2\pi}} \exp\left(-t^2/2\sigma_{IRF}^2\right) \quad \& \quad H(t) = \begin{cases} 0 & if \ t < 0 \\ 1 & if \ t \geq 0 \end{cases}$$

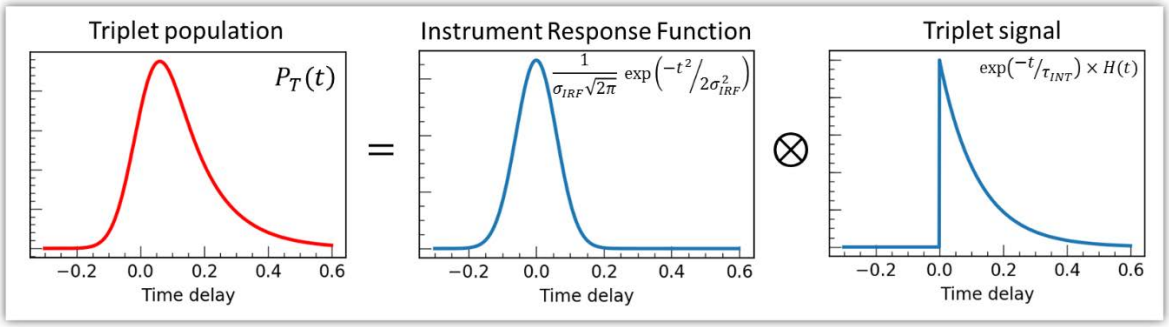

Figure 3.16: Plot of INT population which is obtained by convoluting a decreasing exponential with a Gaussian function representing the Instrument Response Function (IRF)

The signal due to the oscillation from HS state is described as:

$$s_{HS}(t) = [A_{HS} + A_{osc}\cos(2\pi\nu_{osc}t)\,exp(-t/\tau_{osc}) + A_{VC}\,exp(-t/\tau_{VC})] \times H(t)$$

Where A_{HS} is the signal due to the final HS state after cooling, A_{osc} is the amplitude of oscillation, τ_{osc} is the damping of the oscillation of frequency ν_{osc}. A_{VC} and τ_{VC} are the amplitude of the signal and the time scale of the vibrational cooling. In this case, the INT state is the source of molecules in the HS state, the s_{HS} is convoluted with the $P_{INT}(t)$ to give rise to the part of the signal due to the HS state $S_{HS}(t)$:

$$S_{HS}(t) = P_{INT}(t) \otimes s_{HS}(t)$$

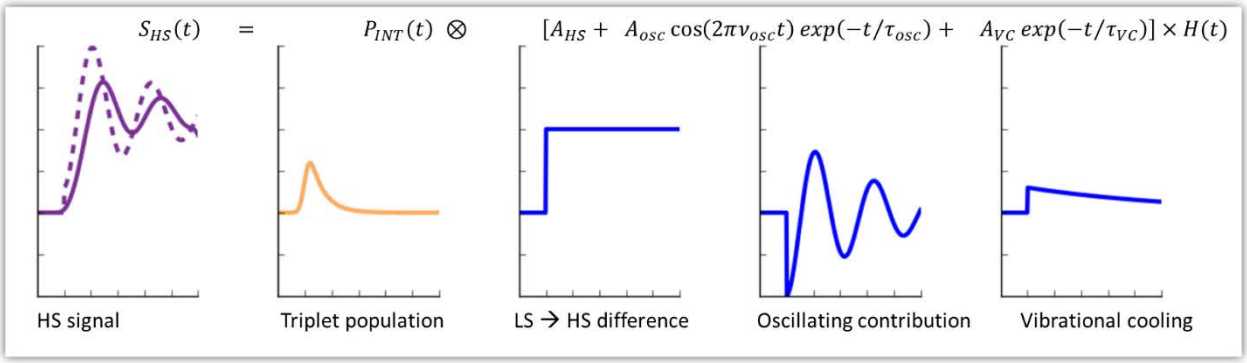

Figure 3.17 : Plot of $S_{HS}(t)$ and the different parts which contributed in the signal. The dashed line represents the HS before convolution with $P_{INT}(t)$.

The global signal $S_G(t)$ to fit experimental data including the signal of the INT state $S_T(t)$ is given by the following relation :

$$S_G(t) = S_{INT}(t) + P_{INT}(t) \otimes s_{HS}(t)$$

A longer INT state results in two main effects on the coherent oscillation: apparent dephasing towards higher time delay after photoexcitation and reduced amplitude due to dephasing of the molecules during the T to HS intersystem crossing (Figure 3.18).

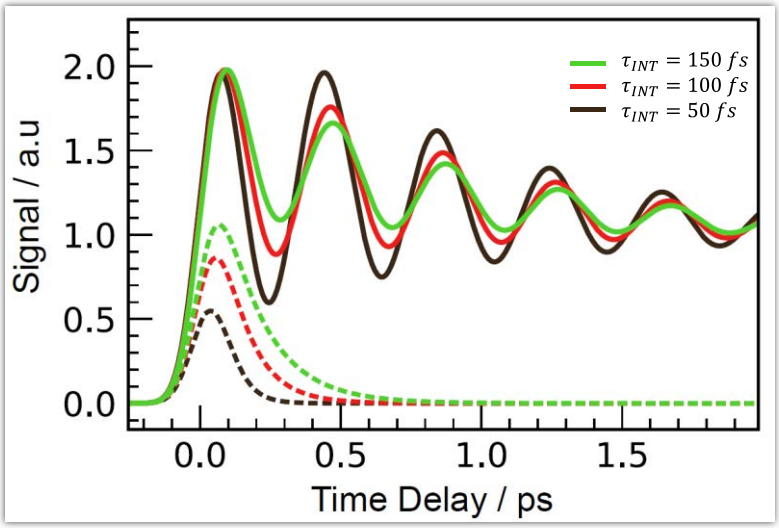

Figure 3.18: Plot of $S_G(t)$ signal at different lifetime of triplet state. The dashed lines represent the INT signal $S_{INT}(t)$.

b) Case of the MLCT transient

In this case, the relaxation mechanism, can be expressed as follows:

$$MLCT \xrightarrow{\tau_{MLCT}} INT \xrightarrow{\tau_{INT}} HS$$

The contribution of the MLCT state which decays with a time constant τ_{MLCT} is given by:

$$S_{MLCT}(t) = A_{MLCT} \times P_{MLCT}(t)$$

Where A_{MLCT} is the amplitude of the MLCT.

$$P_{MLCT}(t) = IRF(t) \otimes \left[\exp\left(-t/\tau_{MLCT}\right) \times H(t)\right]$$

The contribution of the triplet INT state which decays with a time constant τ_T is given by:

$$S_{INT} = A_{INT} \times P_{INT}(t)$$

Where A_{INT} and P_{INT} are the amplitude and population, respectively of the INT state, where P_{INT} is given by the following expression:

$$P_{INT}(t) = IRF(t) \otimes \left[\frac{\tau_{INT}}{(\tau_{MLCT} - \tau_{INT})} \left(exp\left(\frac{-t}{\tau_{MLCT}}\right) - exp\left(\frac{-t}{\tau_{INT}}\right) \right) \times H(t) \right]$$

In the case, the INT state is the source of molecules in the HS state, the s_{HS} is convoluted with the $P_{INT}(t)$ to give rise to the part of the signal due to the HS state $S_{HS}(t)$:

$$S_{HS}(t) = P_{INT}(t) \otimes s_{HS}(t)$$

The final global signal $S_G(t)$ to fit experimental data including the signal of the INT state $S_{INT}(t)$ and MLCT state $S_{MLCT}(t)$, is equal:

$$S_G(t) = S_{MLCT}(t) + S_{INT}(t) + P_{INT}(t) \otimes s_{HS}(t)$$

Here again longer intermediates, including now MLCT and INT states, results in apparent dephasing towards higher time delay after photoexcitation of the oscillation and reduced amplitude due to dephasing of the molecules during the intersystem crossings.

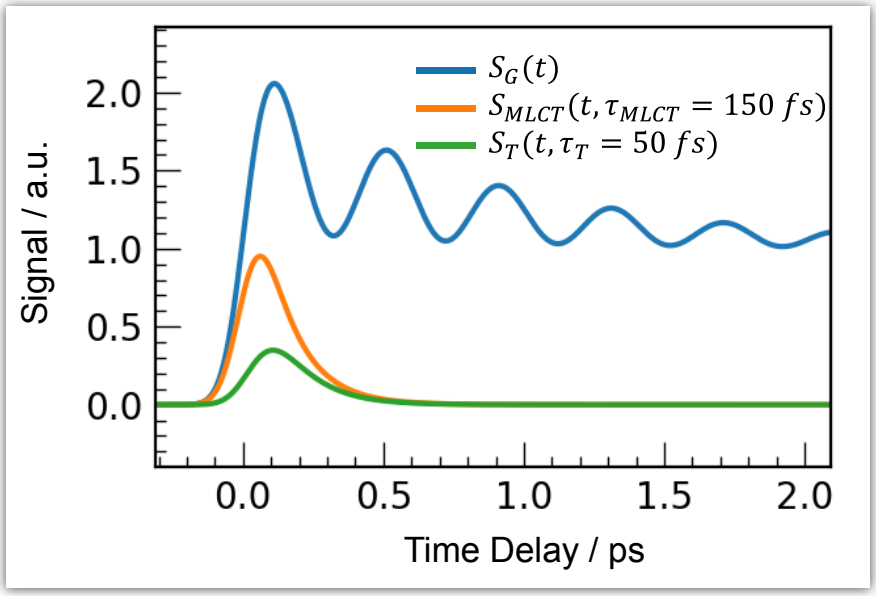

Figure 3.19 : Plot of $S_G(t)$, $S_{MLCT}(t)$ and $S_{INT}(t)$.

3.2.6. Ultrafast Photo-response at MLCT and d-d excitation

Following theoretical calculations and experimental OD measurements, we studied the photoresponse of $Fe(pap\text{-}5NO_2)_2$ to d-d and MLCT excitation. We performed two different types of measurements with the pump wavelength set to 530 nm for MLCT excitation and to 730 nm for d-d excitation. We used similar laser excitation fluences in both cases: 4.0(1) $\mu J.mm^{-2}$ at 530 nm and 4.2(1) $\mu J.mm^{-2}$ at 730 nm. Time-resolved OD change measurements were performed at selected wavelengths to track the photoswitching dynamics. The femtosecond optical pump-probe experiments were configured in NIR-transmission geometry with a quasi-collinear configuration of pump and probe beams. The sample temperature was controlled with a liquid nitrogen cryostream set for all experiments at 100 K, where the system is LS and the HS-to-LS back relaxation occurs within less than 1 millisecond.

Several studies in the field of femtosecond pump probe spectroscopy have shown that in some experimental conditions (laser pulse duration, pump power density, angle between the pump and probe beam, wavelength of pump and probe…), the photo response may contain others signal from the substrates or the solvent such as to Two-Photon Absorption (TPA), Stimulated Raman amplification (SRA) and Cross-Phase Modulation (CPM) (Lorenc *et al*., 2002; Auböck & Chergui, 2015). It is therefore important to check the existence of such artefacts and remove any unwanted signals generated during the transient absorption measurements with femtosecond resolution. For each experiment on the sample deposited on the glass substrate, we checked possible CPM signal, by performing measurements with the same conditions (overlap, position, lasers power) on the glass substrate. This made possible to find accurately the time zero (pump-probe overlap, Figure 3.20). The amplitude of the CPM is negligible compared to the real signal from the sample and sometime an increase the laser power by a factor of 2.5-12 to observe weak CPM, has been necessary.

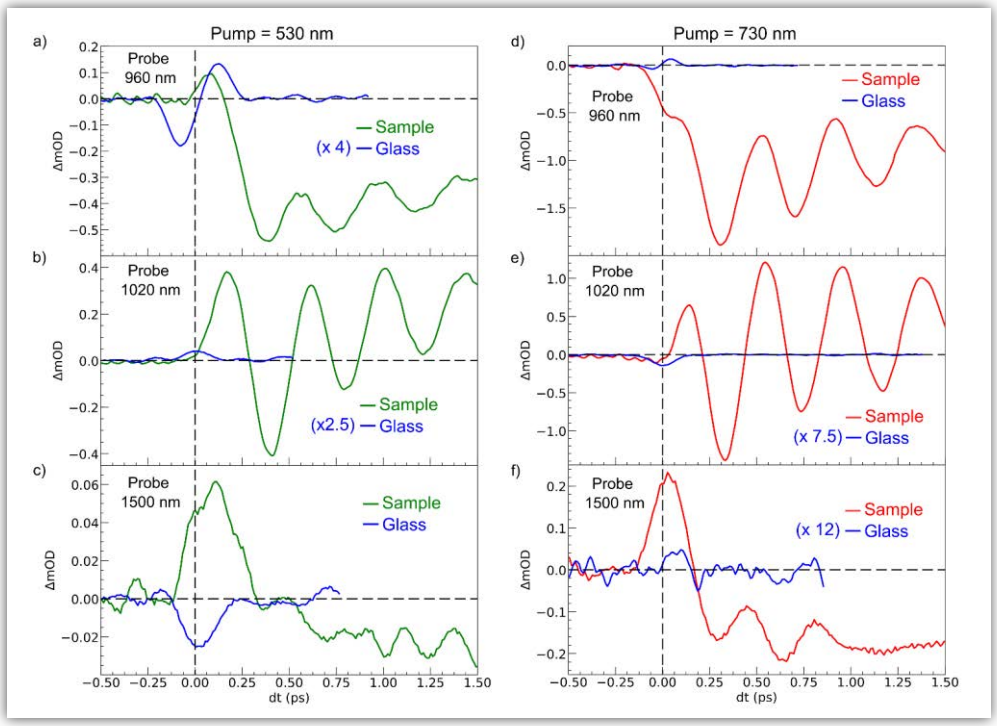

Figure 3.20: Time scans with and without the sample on the glass, showing weak cross-phase modulation.

MLCT excitation

The Figure 3.21 shows the OD time traces probed at 960, 1020, 1500 nm, after femtosecond pulse excitation of LS state of Fe(pap-5NO_2)$_2$ at 530 nm, i.e. in the $MLCT_{LS}$ band. The OD increase at 1020 nm and decrease at 960 reproduce the optical fingerprints characteristic of the LS → HS switching obtained with steady state spectra (Figure 3.10).

The time traces also indicate an intermediate signal, better seen at 1500 nm within the first 100s fs, and damped coherent oscillations at 960 and 1020 nm. These features are very similar to the ones reported for ultrafast optical studies of LIESST in $Fe^{II}N_6$ molecules in solution or in crystals (Cammarata *et al.*, 2014; Bertoni *et al.*, 2015; Auböck & Chergui, 2015; Marino *et al.*, 2016; Consani *et al.*, 2009). This is due to the local nature of the process in solids underlined some years ago (Bertoni *et al.*, 2012) confirmed by a direct comparison of the dynamics of $Fe(bpy)_3^{2+}$ in solution and in crystal (Field *et al.*, 2016).

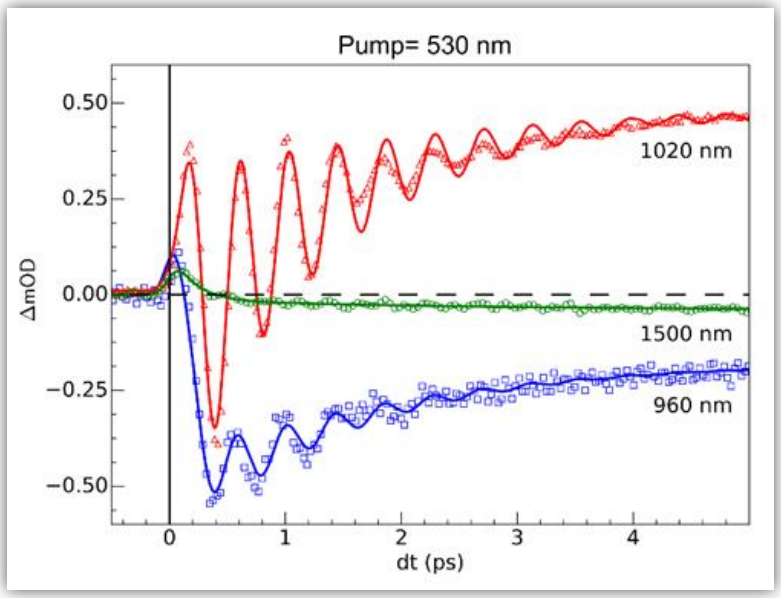

Figure 3.21: Time scans at 100 K of relative milli-OD change upon MLCT excitation at 530 nm.

Time- resolved analysis in spectral regions were HS and LS species absorb almost equally (such as 1500 nm) allows an isolated observation of the dynamics of the intermediate state(s) involved during the spin-state photo-switching. For photoexcitation at 530 nm, such intermediate states (INT) can include the initially photoexcited singlet ^{1,3}MLCT state ($t_{2g}^5e_g^0L^1$) and ^{1,3}T (d-d ligand-field states, $t_{2g}^5e_g^1L^0$) on the pathway towards the HS potential.

The TD-DFT calculation (Figure 3.10 and Figure 3.11) of the triplet spin state indicates a characteristic absorption band around 1200 nm. This band corresponds to an electron transfer from the ligand L to the metal M and therefore this 1200 nm band of the ^{3}T state has a LMCT character and is referred to as $LMCT_{3T}$. As we could not compute the absorption spectra for the ^{1}T and ^{1}MLCT states, we shall use $LMCT_{3T}$ as an approximate global signature of these intermediates using the following qualitative points: since the orbital energy levels are similar for the ^{1}T and ^{3}T states, the $LMCT_{1T}$ band of the ^{1}T state should also be centred at around 1200 nm. Additionally, the initial ^{1}MLCT state resulting from excitation of the LS state at 530 nm, should also have a similar low energy LMCT band due to the partial occupation of its t_{2g}-like orbitals. As we see from the $LMCT_{3T}$ state obtained from TD-DFT calculations, these low-energy optical transitions for ^{1,3}T and ^{1,3}MLCT states have no analogue in either the LS or HS species, even though the tail of the d-d_{HS} band extends up to 1500 nm. Experimentally, the optical absorption of LS and HS states is very low, but quite similar, around 1500 nm due to the broadening of the bands. Data around the isobestic point at 970 nm (Figure 3.13) are strongly affected by coherent oscillation and vibrational cooling. The transient absorption peak

measured at 1500 nm globally includes the OD signature of intermediates states (^{1,3}MLCT and ^{1,3}T).

An exponential fit of the data probed at 1500 nm, taking into account our 60 fs RMS instantaneous response function, indicates that the initial MLCT decays toward the HS state within τ_{MLCT} =188 (10) fs. A slower component τ_{VC} =2.8 (5) ps is also found and attributed to vibrational cooling, as already observed in other SCO materials. (Cammarata *et al.*, 2014; Bertoni *et al.*, 2015; Marino *et al.*, 2016). The time-resolved OD data at 960 and 1020 nm show similar features associated with an initial peak and a slower change accompanied by coherent vibrations.

We analyze these data with the phenomenological model in the case of MLCT transient, described previously (Section 3.2.5.b). It includes the exponential decay of the MLCT state excited at t=0 and other intermediate state INT such as ^{1,3}T, populating the final HS state within τ_{MLCT} and accompanied by a damped oscillation.

For the fit of the data probed at 960 and 1020 nm (Figure 3.21), the physical parameters ν_{OSC} = 80(3) cm^{-1}, τ_{MLCT} =120(12) fs τ_{INT} =70, and are the same for the different probing wavelengths. The vibrational cooling timescale τ_{VC} and the oscillation damping τ_{OSC} are however different for each wavelength. It is well known that these timescales depend on the spectral region. The damping constant is τ_{OSC} =1.001(0.05) ps at 1020 nm and 1.21(0.02) ps at 960 nm, and the vibrational cooling occurs within τ_{VC} =1.56(0.05) ps at 1020 nm and 1.68(0.05) ps at 960 nm. Again these timescales are similar to the values reported for other systems presenting LIESST in solids or in solution. (Boillot *et al.*, 2004; Bertoni *et al.*, 2015; Marino *et al.*, 2016; Zhang *et al.*, 2014; Auböck & Chergui, 2015).

The 80(3) cm^{-1} oscillations are observed once the HS state is reached in OD time traces at 960 and 1020 nm, i.e. close to the d-d$_{HS}$ band (Figure 3.11). These are associated with a strong modulation of the ligand field by molecular breathing (Figure 3.13). Similar findings were also reported in other SCO crystals and this oscillation probed around the d-d$_{HS}$ transition was attributed to the breathing of the ligand field (Cammarata *et al.*, 2014). For FeN_6 systems, this is the main reaction coordinate between the LS and HS structures, which corresponds to the in-phase elongation of the Fe-N bond lengths. The DFT study on $Fe^{II}(pap\text{-}5NO_2)_2$ reveals a breathing mode in the HS state at 84 cm^{-1}. This totally symmetric vibration involves mainly the

FeN_4O_2 core and also corresponds to in phase stretching of Fe-N and Fe-O bonds as shown in Figure 3.14.

These results indicate that the physical picture for MLCT- induced LIESST in $Fe(pap\text{-}5NO_2)_2$, driven by the MLCT decay towards lower states activating and damping molecular breathing, is similar to the one theoretically and experimentally reported for FeN_6 systems. The coherent oscillations observed during LIESST are sometimes attributed to an impulsive Raman process activating the LS breathing mode. This possibility can be excluded because the LS breathing frequency is significantly higher (146 cm^{-1}). In addition, an impulsive process will induce sine-like oscillations around zero OD change, whereas the band probed at 1020 nm, where oscillations are stronger, is sensitive to the formation of the HS state.

d-d excitation

Additional measurements were also performed at 100 K in the LS state upon d-d excitation at 730 nm generating ligand-field states ($^{1,3}T$, $t_{2g}^5e_g^1L^0$), with experimental conditions similar to ones used for MLCT excitation. Time-resolved OD changes for the different probing wavelengths are shown in Figure 3.22.

At 5 ps, the OD increase (respect. decrease) at 1020 nm (respect. 960 nm) and weak change at 1500 nm are characteristic of the formation of the HS state and similar to the changes observed upon MLCT excitation at 530 nm. However the OD change is larger for d-d excitation when similar laser fluence is used. For example, at 1020 nm the OD increases by 0.48 for 530 nm excitation and by 0.72 for 730 nm excitation (Figure 3.22). In SCO materials, the quantum efficiency is known to be close to unity and the OD changes linearly with the number of photons in such low fluence regimes (Bertoni *et al.*, 2016). The ratio of the number of photons contained in the pump laser pulses of 4.2 $\mu J.mm^{-2}$ at 730 nm and 4.0 $\mu J.mm^{-2}$ at 530 nm is $R_{ph} \approx 1.45$. This ratio is close to the ratio of OD change at 1020 nm between 730 nm and 530 nm excitations: $R_{OD}=1.5$. These results indicate that d-d and MLCT excitations generate the final HS state with very similar quantum yield. The comparison from data at 960 nm yields a value of the same order, but is more difficult to analyze because 960 nm is closer to the isobestic point, known to shift by lattice pressure and heating following femtosecond excitation (Bertoni *et al.*, 2012).

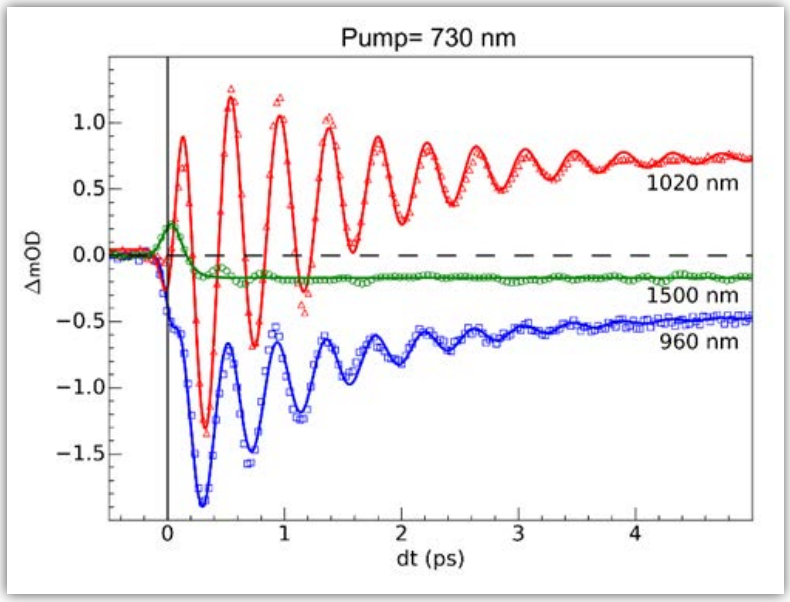

Figure 3.22: Time scans at 100 K of relative milli-OD change upon d-d excitation at 730 nm.

The Data at 1020 nm around the maximum of OD change (Figure 3.8 insert) are not sensitive to this effect and better suited to compare quantum yield. Around t=0 ps at 960 nm probing wavelength, the OD decreases for the 730 nm d-d excitation, contrary to the 530 nm MLCT excitation. In addition, the OD changes observed around t=0 ps at 1020 and 1500 nm probe for 730 and 530 nm. We identify the initial state as a ^{1,3}MLCT upon 530 nm excitation and as a ^{1,3}T state upon 730 nm excitation. Our calculations show that photoexcitation of the d-d$_{LS}$ band can induce a ^{1}T spin-allowed or ^{3}T spin-forbidden states, but the relative weight of these could not be calculated and two possible pathways may (co)exist, LS→^{1}T→^{3}T→HS and/or LS→^{3}T→HS. Since Sousa et al calculated ^{1}T→^{3}T inter-system crossing rates in the 400 - 2700 fs and ^{3}T→HS in the 60 fs range (Sousa *et al.*, 2013) it is possible that the d-d$_{LS}$ photoexcitation induces mainly the ^{3}T spin-forbidden states. Femtosecond X-ray fluorescence measurements, as performed by K. Gaffney on Fe(bpy)$_3^{2+}$(Zhang *et al.*, 2014), may be helpful in future to discriminate the nature of the initial photo-excited state.

In order to fit the time evolution of the optical fingerprints of the different states, we use the phenomenological model in the case of INT transient (Section 3.2.5.a), the INT state is associated the triplet state ^{3}T, now including as initial process the exponential decay of the photoinduced T state towards the final HS state:

$$T \xrightarrow{\tau_T} HS$$

The fit of the data indicates that the HS state is populated after d-d excitation within τ_T =70(10) fs. The process is also accompanied by a coherent oscillation, with frequency ν_{osc}= 80(3) cm^{-1} and damping constant τ_{osc}=1.21(0.02) ps at 1020 nm and 1.00(0.02) ps at 960 nm. The vibrational cooling occurs within τ_{VC}=1.33(0.04) ps at 1020 nm and 1.49(0.02) ps at 960 nm. The fact that the frequency of the oscillation corresponds to the one observed after MLCT (530 nm) excitation confirms that the final photoinduced state is the same under d-d (730 nm) excitation, as already indicated by the similar OD changes and photomagnetism. The main difference compared to the MLCT excitation is the faster population of the HS state, which makes sense since the number of intermediates is reduced in the case of d-d excitation compared to MLCT excitation.

MLCT vs d-d excitation

Figure 3.23 compares the OD changes for the different probing wavelengths on short timescales. The amplitudes of the changes were scaled for clarity. The OD peak probed at 1500 nm clearly appears longer around t=0 under MLCT than under d-d excitation. Regarding the oscillating components, we can notice two main differences between the two excitation processes. On the one hand there is a phase shift, of about 75 fs, between the oscillation observed after MLCT and d-d excitation. On the other hand, the relative amplitude of the oscillation, with respect to the OD change between LS and HS states, is larger under d-d excitation than under MLCT excitation.

These features are very well explained by our phenomenological model (Section 3.2.5a) which describes the signal as an initial photoexcited state (MLCT or T) which exponentially populates the HS potential, where molecules undergo damped oscillations. Both effects result from the shorter decay time $\tau_{T\rightarrow HS}$ = 75(10) fs under d-d excitation than $\tau_{MLCT\rightarrow HS}$ =188(10) fs under MLCT excitation. The T state, with schematic electronic structure $t_{2g}^5e_g^1L^0$, is a natural intermediate between MLCT ($t_{2g}^5e_g^0L^1$) and HS ($t_{2g}^4e_g^2L^0$) states, and it was observed by x-ray spectroscopy in $Fe(bpy)_3^{2+}$. We therefore performed another fit of the data in (Figure 3.23) to describe the consecutive decays under MLCT excitation:

$$^{1,3}MLCT \xrightarrow{\tau_{MLCT}} {}^3T \xrightarrow{\tau_T} HS$$

We independently found τ_T under d-d excitation as we identify 70(10) fs. Therefore, in the fit presented in Figure 3.23, we refine only the ^{1,3}MLCT→T decay time constant τ_{MLCT} =120(10) fs. We can underline that the faster HS population under d-d excitation maintains coherence

(amplitude of the oscillation) and launches HS state oscillation more rapidly, as illustrated by the oscillation phase shift in time. This is due to the fact that the HS population is much faster than the 210 fs half oscillation period, which is the upper limit timescale to maintain coherence of the oscillation in the HS state. Under MLCT excitation, the overall $\tau_{MLCT \rightarrow HS}$ = 188(10) fs HS population approaches the half oscillation period and is responsible for decoherence during the long MLCT-to-HS population, reducing the amplitude of the oscillation.

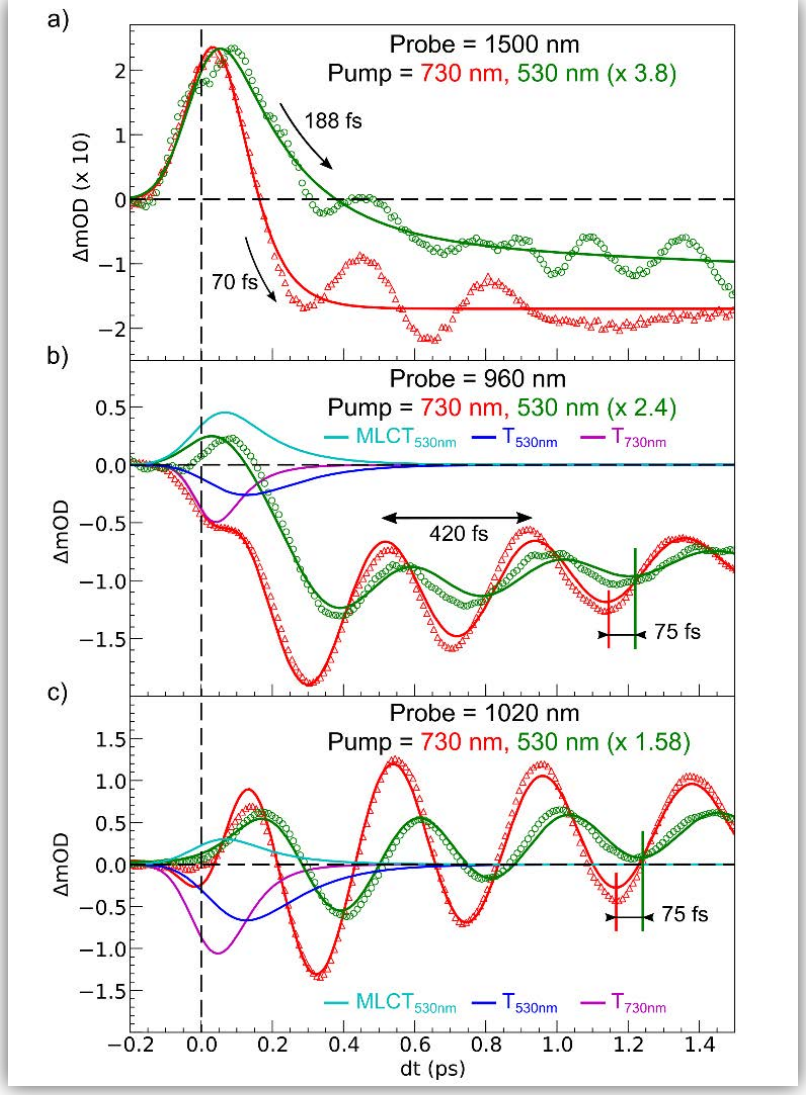

Figure 3.23: Comparison of short time scans of relative OD change at selected probing wavelength upon $MLCT_{LS}$ excitation at 530 nm and d-d_{LS} excitation at 730 nm. The fit for 530 nm excitation includes MLCT and T intermediates, whereas the fit for 730 nm includes T only.

3.2.7. Process of the LIESST: MLCT vs d-d excitation

For MLCT excitation, the electronic decays towards less bonding ^{3}T and HS states increases the equilibrium Fe-Ligand distance and launches coherent Fe-L breathing around the equilibrium position in the HS potential (Figure 3.24 a). The weak oscillation of an arbitrary schematic signal (black) due to Fe-L bond length change for MLCT excitation is due to decoherence during the relatively long MLCT-to-HS conversion compared to the oscillating signal of a single molecule in the HS potential (Figure 3.24 b).

For d-d excitation LIESST processes with faster ^{3}T-to-HS conversion (Figure 3.24 c), which maintains significant average structural coherence in the HS potential. The exponential growth of the HS population from the MLCT, or from the ^{3}T intermediate state, leads to average coherent oscillating trajectories with a more reduced amplitude and longer apparent phase shift as intermediates are longer, compared to the single trajectory in the HS state $S_{HS}(t)$.

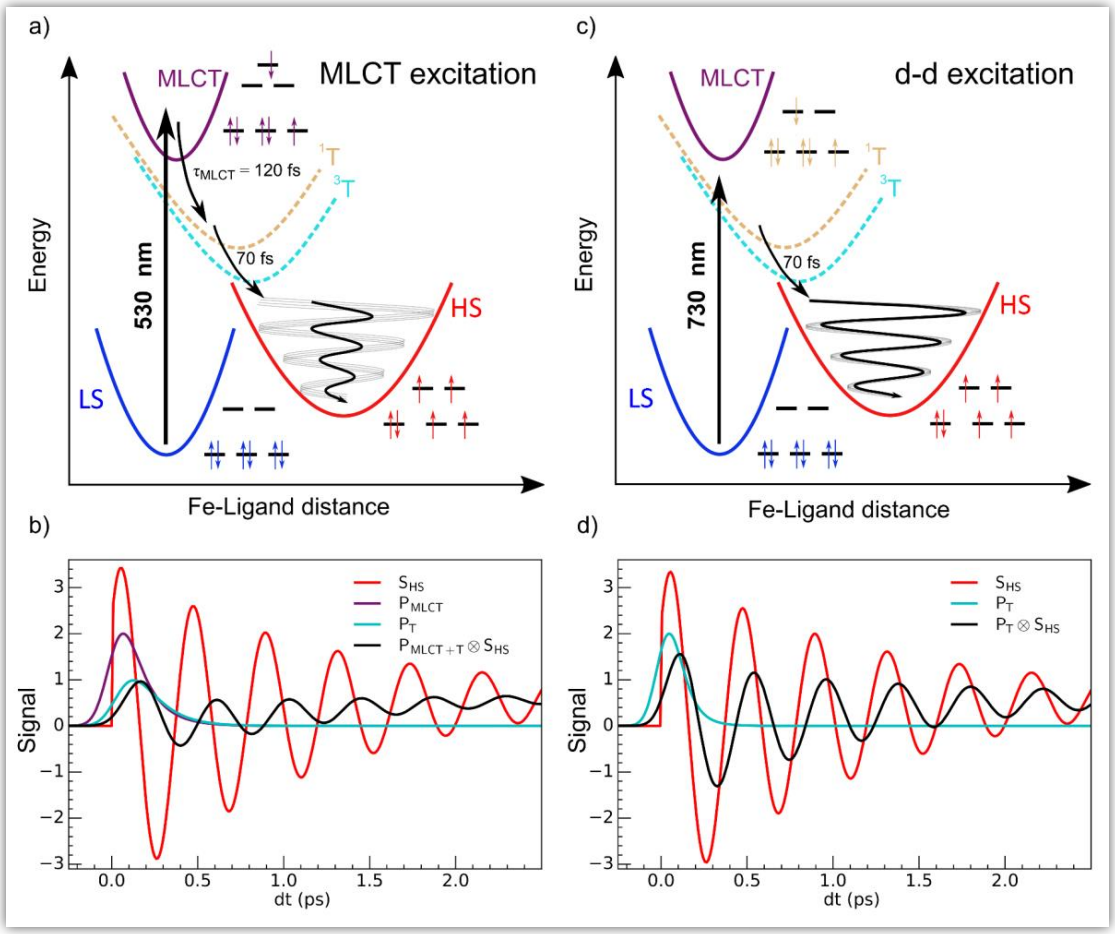

Figure 3.24: Schematic process of LIESST upon MLCT and d-d excitation.

3.2.8. Ultrafast Photo-response at different wavelength excitation

Since the dynamics and pathways followed during LIESST depends on the excitation wavelength, we decided to study the photoresponse dynamics as function of the pump wavelength to follow the evolution of efficiency or coherence. The Fast Fourier Transform (FFT) of the time resolved OD, normalized to 1 from 5 ps, allows detailed analysis of the data and provides frequencies, and the amplitude of modes that are activated during the process of photoswitching. In our experimental data, the different excitation wavelengths always shows the activation of two modes: the main mode around 80 cm^{-1} mentioned above corresponding to the breathing mode and another one around 50 cm^{-1} with lower spectral weight as shown in Figure 3.25 for 3 pump wavelengths (730, 580 and 530 nm).

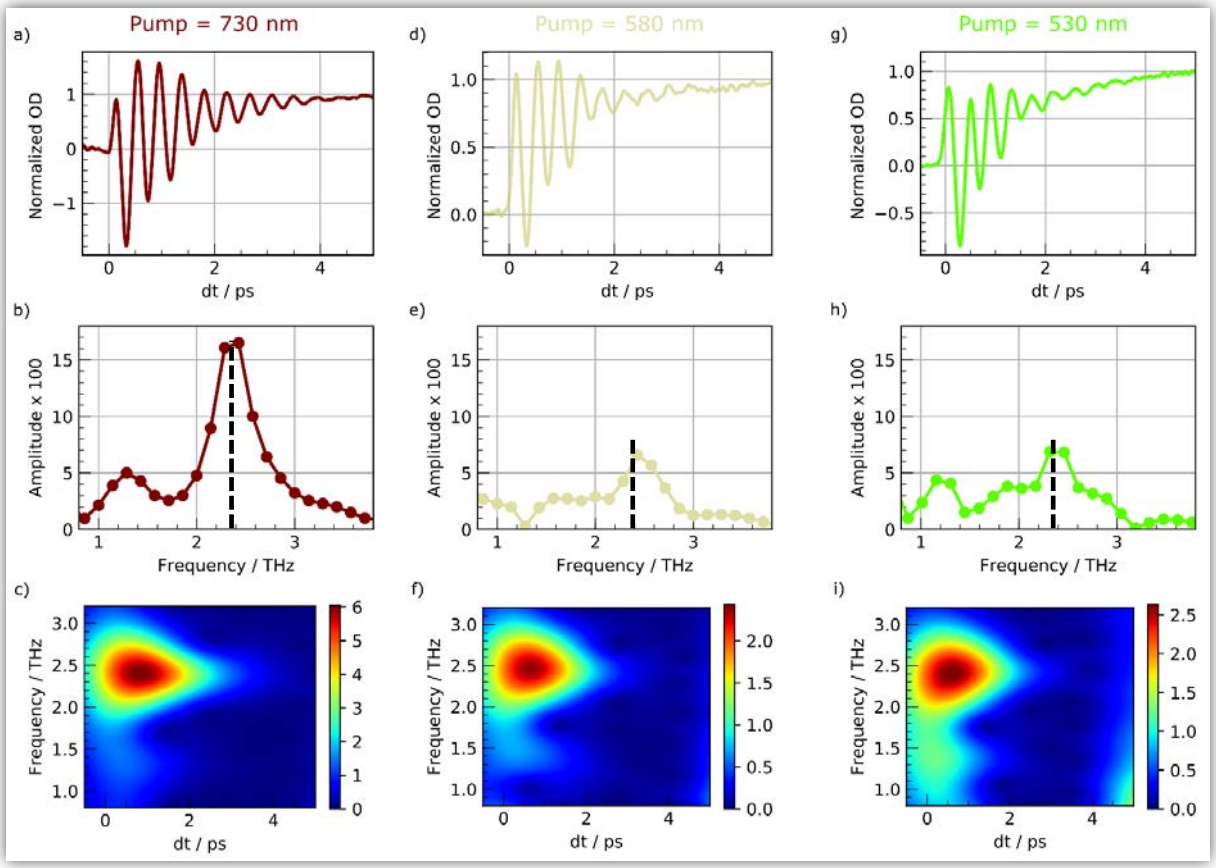

Figure 3.25: From above to below: time scan of normalized OD, the Fast Fourier Transform of the oscillatory component only and time dependent Fourier transform. (a, b and c at 730 nm), (d, e and f at 580 nm) and (g, h and i at 530 nm)

The results presented in the Figure 3.26, show the curves of the optical density as a function of time on a scale going to few picoseconds. The choice of the wavelength of the probe is based on the DFT calculations of the gap d-d splitting of HS state and the pump probe measurements

at different probe wavelength around 1020 nm (Figure 3.13). The change of the optical density at different pump wavelengths, presents a similar dynamics to the ones reported above: an exponential relaxation accompanied by a coherent oscillation. The sign of the signal around the time zero changes with the pump wavelength, which can reflects the signature of the different intermediate states (MLCT vs T).

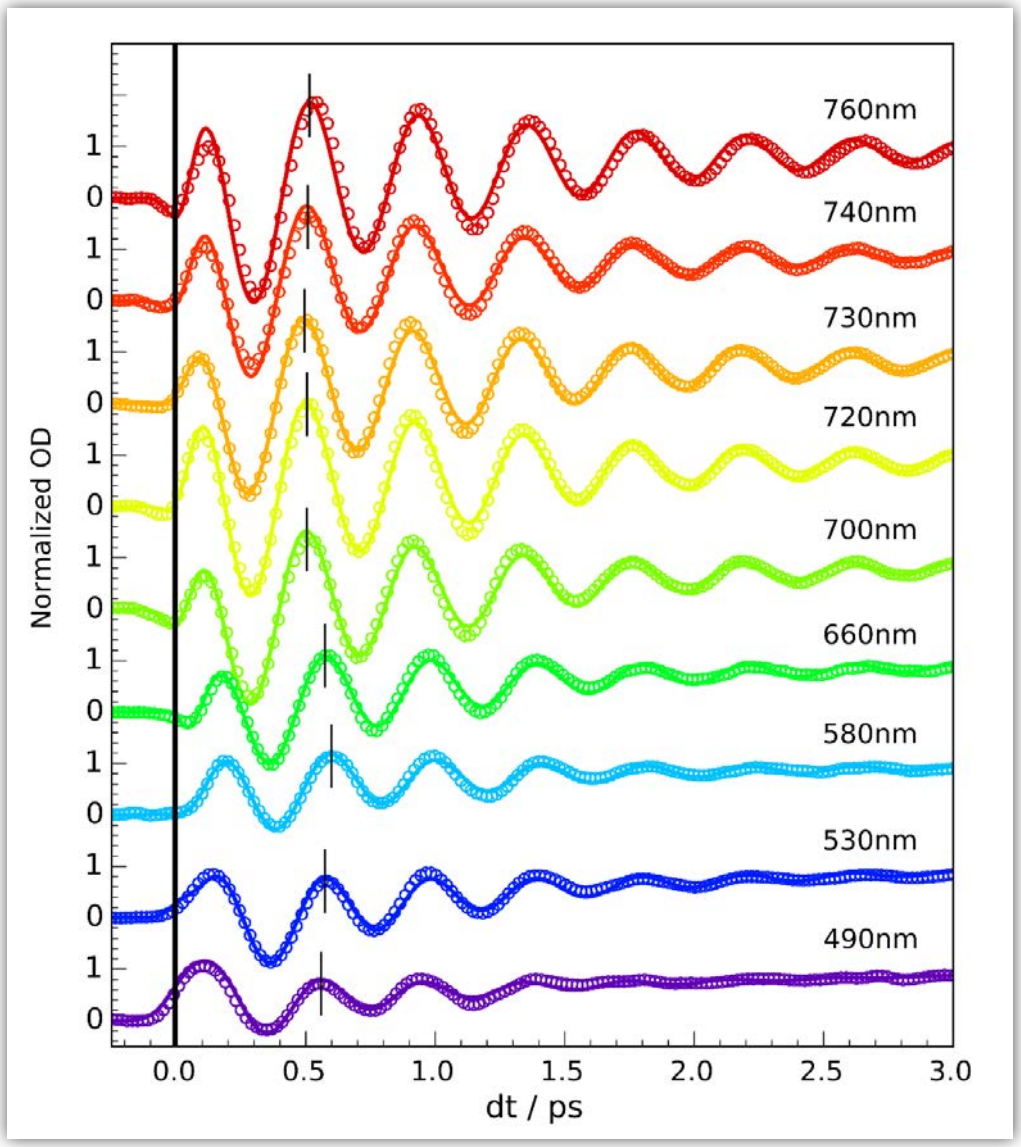

Figure 3.26: Normalized OD change as function of wavelength of pump. Probe = 1020 nm

The Figure 3.27.a shows the amplitude of the mode at 80 cm^{-1} obtained with the FFT for normalized OD change, presented in the Figure 3.26. The amplitude in the range from 760 nm to 700 nm remains high and similar, given the error bars. These data (above 700 nm) were fitted with the kinetic model in the case of INT transient (Section 3.2.5.a). Below 700 nm, we can see clearly that the amplitude begins to decay down to 0.3 at 490 nm. This is an illustration of the

loss of structural coherence between d-d and MLCT excitation. In a similar way, we plot in Figure.3.27.b the amplitude of the MLCT peak (A_{MLCT}) at t=0, obtained by fitting the data (below 700 nm) with the kinetic model in case of MLCT transient (Section 3.2.5.b). The apparent phase shift of the oscillation for the different pump wavelengths, which corresponds to the relative shift of the oscillation with respect to the oscillation at 760 nm excitation (black line segment, Figure 3.26). The amplitude of MLCT peak is strong below 650 nm, whereas the temporal shift phase is higher below 650 nm.

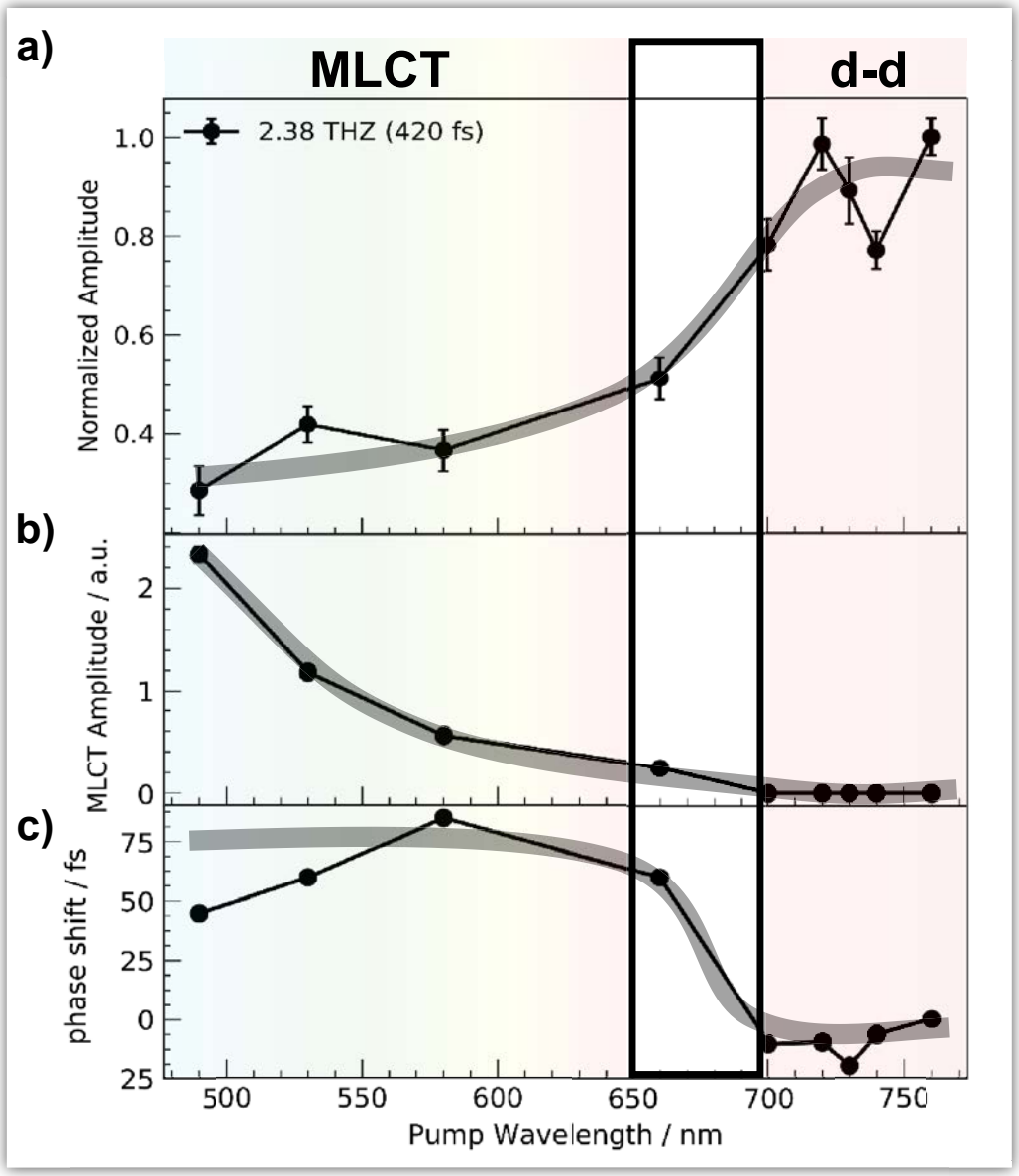

Figure 3.27: a) Normalized amplitude to wavelength range 700-750nm of the breathing mode as function of the wavelength of the pump excitation. b) Amplitude of MLCT c) Relative phase shift with respect to the oscillation at 760nm.

All these results indicate a crossover between d-d and MLCT pathways. At high energy (below 650 nm) the MLCT process is favored, as illustrated by a strong MLCT peak, with low structural coherence and high apparent dephasing of the oscillation, as it takes time to reach the HS potential where molecules oscillate. At low energy (above 650 nm) the d-d process is favored with no contribution from the MLCT. As the HS potential is reached more rapidly, the apparent time phase shift is reduced and the amplitude of the oscillation is higher as coherence is maintained (Figure 3.27.c). These findings are summarized in (Figure 3.24).

3.3. Investigation of the [Fe($L_{222}N_5$)$(CN)_2$] spin-crossover

Also, we studied another spin crossover system which presents a very interesting coupling between the structural and magnetic properties under the effect of temperature and light. The compound is **[Fe($L_{222}N_5$)$(CN)_2$]** which is a photomagnetic Fe^{II} based coordination compound. The LS is hexacoordinated and the HS state heptacoordinated. Here we study its ultrafast spin-state photoswitching dynamics. We performed femtosecond optical spectroscopy measurements at the Institut de Physique de Rennes (IPR) and femtosecond X-ray absorption measurements at the XPP station of the X-ray free-electron laser LCLS.

3.3.1. Description of the [Fe($L_{222}N_5$)$(CN)_2$] complex

This complex was originally synthesized by Nelson et al. and was found to be in the low-spin state at room temperature(Nelson *et al.*, 1986). [Fe($L_{222}N_5$)$(CN)_2$] also serves as linker for the design of trinuclear molecular complexes or one-dimensional compounds made of other types of coordinated metal bricks(Ababei *et al.*, 2013). Its photomagnetic properties allows for example to switch "on" and "off" the magnetic interaction between the photoinduced Fe(II) HS unit (S = 2) and the Mn^{III} ions in Mn-Fe-Mn trimers. The structure of this linker was revealed in the [Fe($L_{222}N_5$)$(CN)_2$].H_2O complex by Ababei et al, where the system is LS at 150 K. The Fe(II) ion is then hexacoordinated (Figure 3.28). With 2 cyanido ligands in axial positions (Fe-CN=1.94−1.96 Å)) and 4 N atoms from the macrocyclic ligand $L_{222}N_5$ equatorial plane (Fe-Neq =1.84−2.1 Å). The fifth N atom of the $L_{222}N_5$ ligand is uncoordinated since Fe-N = 3.5 Å. Costa et al, reported that this system remains LS up to 420 K and undergoes light-induced excited spin-state trapping from LS (S=0) to HS (S=2) states at low temperature, by photoexcitation at 532 nm. This photoinduced HS state remains stable up to a typical temperature T(LIESST) ≈110 K, as characterized magnetic susceptibility measurements after light irradiation (Costa *et al.*, 2007) (Figure 2.29).

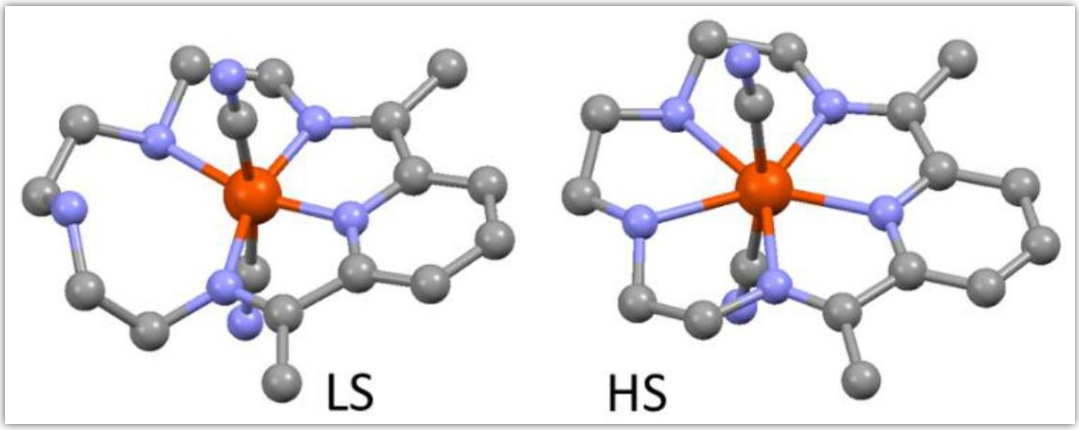

Figure 3.28: Structures obtained by Ababei (Ababei *et al.*, 2013) in LS $[Fe(L_{222}N_5)(CN)_2]\cdot H_2O$ crystals (left) and in the complex $[(Mn(saltmen))_2Fe(L_{222}N_5)(CN)_2](ClO_4)_2\cdot 0.5CH_3OH$, where HS $[Fe(L_{222}N_5)(CN)_2]$ (right) connects two [Mn(saltmen)] units.

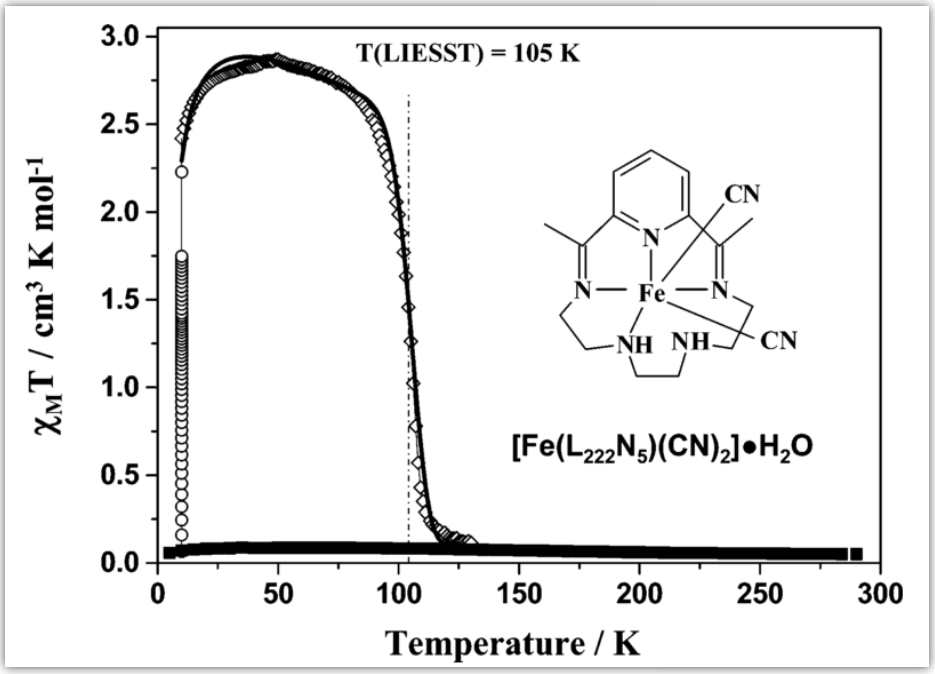

Figure 3.29: Temperature dependence of $\chi_M T$ of [Fe(L222N5)(CN)2].H_2O polycrystalline (Balde *et al.*, 2007)

Temperature-dependent diffuse absorption spectra of the hydrated $[Fe(L_{222}N_5)(CN)_2]$.H2O complex, measured in the 450-850 nm range was also used to characterize the change of electronic state. The switching from LS to HS is associated with an increase of optical absorption above ≈ 650 nm and a decrease below (Figure 3.30). In the following, we exploit these spectroscopic fingerprints, to study the ultrafast photoswitching dynamics.

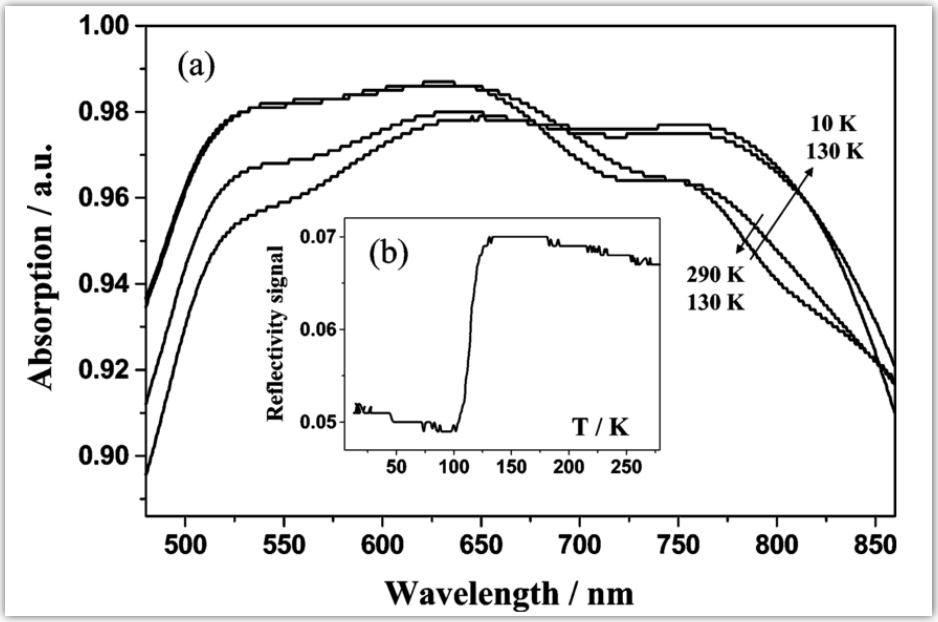

Figure 3.30: Diffuse absorption spectra as a function of the temperature. The inset graph shows the temperature dependence of the reflectivity signal recorded at 830 nm (Balde *et al.*, 2007)

3.3.2. Ultrafast LIESST studies

In order to explore in real time the photoswitching dynamics of $[Fe(L_{222}N_5)(CN)_2]$ in solution at femtosecond and picosecond time scale, Femtosecond optical spectroscopy and femtosecond X-ray absorption have been used.

3.3.3. Time-resolved white-light probe studies

In a first step we exploit the optical spectroscopic fingerprints to study with fs optical spectroscopy the ultrafast spin-state switching dynamics of $[Fe(L_{222}N_5)(CN)_2]$ dissolved in water at room temperature. We used different spectral zone for pump and probe wavelengths. We measured the global spectral optical density change (ΔOD) in the 500-770 nm range with white-light spectroscopy, after photoexcitation at 490 nm (≈10μJ.mm2). The Figure 3.31 shows the OD change measured 2 ps after photo-excitation. The OD decrease below ≈ 640 nm (visible) and OD increase above (IR) is characteristic of the LS to HS photoswitching, characterized by a more conventional optical LIESST experiment at low temperature.

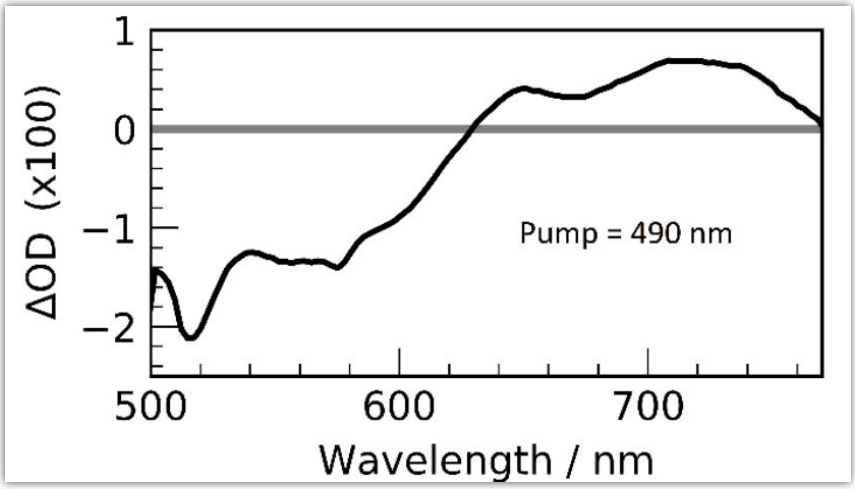

Figure 3.31: Variation of the optical density (ΔOD) recorded with white-light spectrometer 2 ps after photo-excitation at 490 nm.

3.3.4. Time-resolved x-ray absorption

We performed a transient X-ray absorption measurements (XAS) at the XPP end station of the LCLS X-FEL. We measured XAS changes $\Delta I(t)/I_{off}$ at 7125 eV induced by photoexcitation at 530 nm. XAS at 7125 eV is very sensitive to spin-state switching in Fe^{II} materials, because of electronic and structural reorganisations. Figure 3.32 shows the XAS increase, characteristic of the LS to HS transformation (Cammarata *et al.,* 2014; Bressler *et al,.*2009) and a short change of opposite sign within the first 100 fs, which highlights the presence of one (or several) short-lived intermediate(s). In addition, a damped oscillation with a 710 fs period (47 cm^{-1}) accompanies the process. These data show similar XANES signature of LIESST in this system to the ones observed in $Fe(bpy)_3^{2+}$ (Lemke *et al.*, 2017).

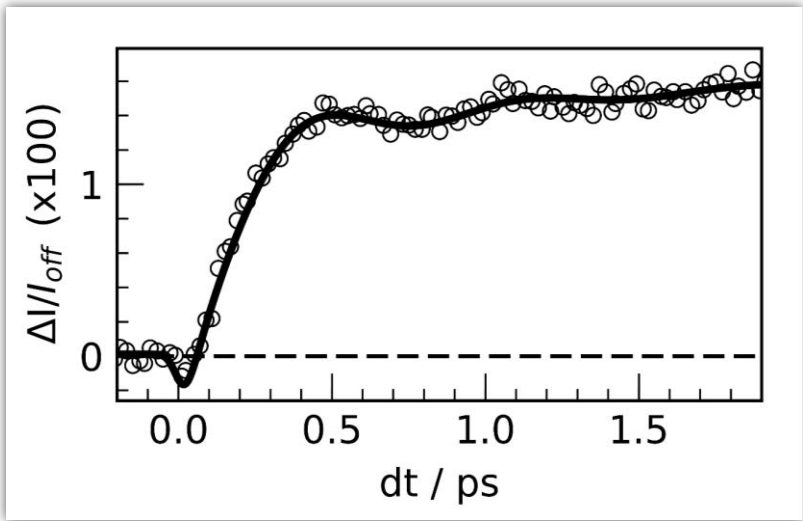

Figure 3.32: Time resolved change of X-ray absorption at 7125 eV at 530 nm excitation.

3.3.5. Time-resolved monochromatic pump and probe

Single-wavelength probe (680 nm) measurements gave more details about the switching dynamics induced by 490 nm pump (Figure 3.33.left.a). We observe two main steps: a transient peak immediately after laser excitation followed by a fast OD increase and a slower change towards a plateau on the ps timescale. These features are similar to the ones observed during LIESST in $Fe^{II}N_6$ systems with an almost octahedral coordination. The transient peak is the signature of the short lived MLCT (≈100 fs) which rapidly decays towards the HS state, whereas the ps signal corresponds to vibrational cooling in the HS potential(Cammarata *et al.*, 2014; Marino *et al.*, 2016; Bertoni *et al.*, 2016). The global optical density increase in IR and decrease in visible range, observed during conversion from LS to HS state on the ps timescale (Figure 3.33), is also observed for photoexcitation at 530, 580 and 680 nm (Figure 3.33.left.b-d). However, the photo-switching dynamics are different at the 490 nm probing wavelength (490 nm) for the different excitation wavelengths.

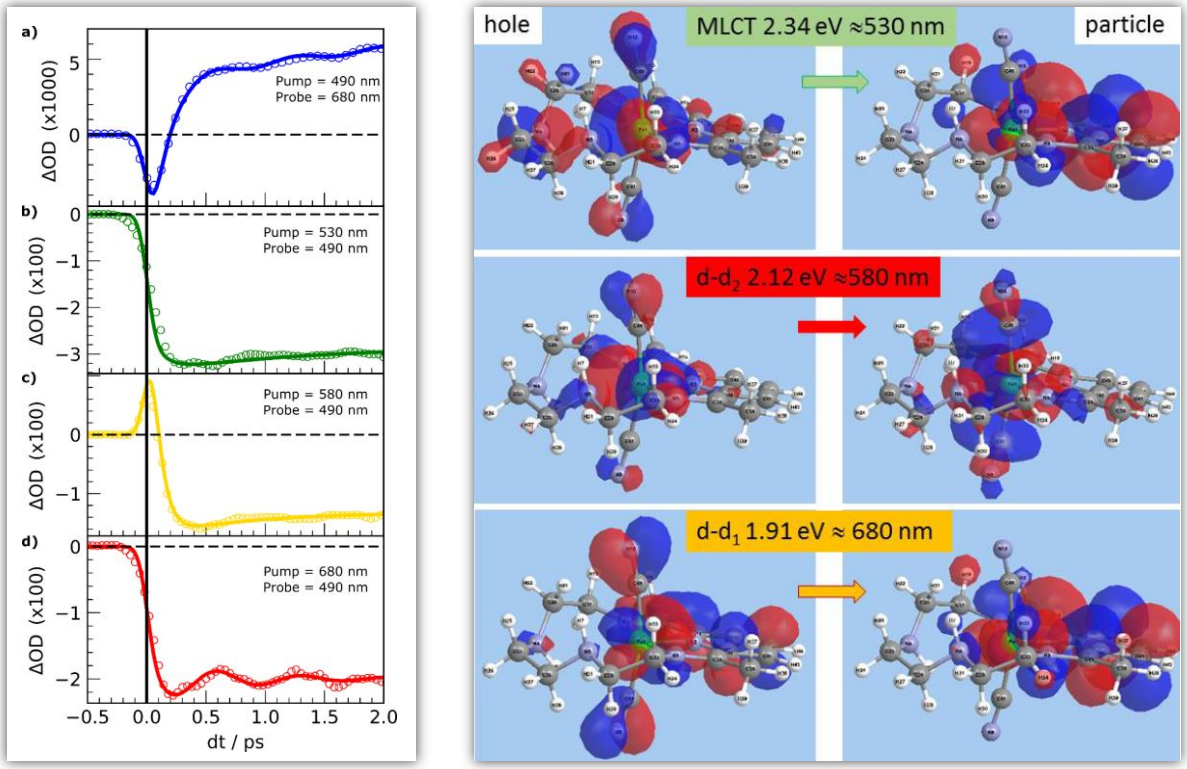

Figure 3.33: (Left) Kinetic traces of ΔOD at selected wavelengths obtained by two-color pump-probe experiment at room temperature. (Right) NTO of hole and particle for different excitation wavelengths, showing MLCT-like transition at high energy and d-d-like transitions at low energy.

These results obtained are the signatures of the LS to HS spin-state photo-switching. For understanding better the process, an accurate description of the initial excited states has been obtained by DFT and time dependent DFT (TD-DFT) calculations performed by S. F. Matar (Martin, 2003). TD-DFT lead to the natural transition orbitals (NTO), through an account for hole–particle pairs involved in the excited states induced by the pump light. TD-DFT as implemented in the Gaussian 09 package was applied for obtaining the NTO of LS $[Fe(L_{222}N_5)(CN)_2]$, starting from geometry optimized molecule with UB3LYP/6-31g(d,p) functional-basis set, found to be similar to the hexacoordinated structure found by X-ray diffraction(Ababei *et al.*, 2013). Because of the low symmetry of the molecule, the d orbitals of the Fe and the ligand orbitals are mixed. We can distinguish in Figure 3.33 (right), different types of photo-excitations. In the low energy excitation region, the 680 nm pump excitation corresponds well to the transition calculated at 1.91 eV. The hole has some d non-bonding character and the particle some d anti-bonding character. Both hole and particle NTOs involve ligand, but given the low symmetry of the system, this excitation is analogous to a d-d transition. We identify another type of d-d excitation at 2.12 eV (close to 580 nm). The hole has some d non-bonding character and the particle some d anti-bonding character, but the particle weight

is strong on the CN groups of the ligand. Excitation around 530 nm corresponds to a transition calculated at 2.34 eV, which has a stronger metal-to-ligand charge-transfer character, with high particle weight on the macrocyclic ligand equatorial plane. In the following discussion, 680 nm excitation is referred to as d-d_1, 580 nm as d-d_2 and 530 nm as MLCT for the sake of simplicity.

For understanding the nature of the oscillation observed in the photoinduced HS state, we carried DFT molecular vibration calculations in the heptacoordinated HS state. In the low frequency region, we found vibration modes at 30 cm^{-1}, 46 cm^{-1} and 52 cm^{-1}. The modes at 30 and 52 cm^{-1} correspond to ligand torsion modes. Figure 3.34 shows main atomic motions for the mode calculated at 46 cm^{-1} of specific interest for interpretation of the observed XANES oscillations. It corresponds to the bending of the NC-Fe-CN axis schematically indicated by the arrows showing opposite motions of Fe and CN groups. This induces small oscillation of some Fe-N bond lengths as the macrocycle remains almost rigid in this mode. In addition, we found a stretching mode at 183 cm^{-1}, where three Fe-N bonds oscillate in phase and two remains almost constant. We found another type of stretching mode at 263 cm^{-1}, with in-phase stretching of the Fe- CN bonds perpendicular to the macrocyclic ligand.

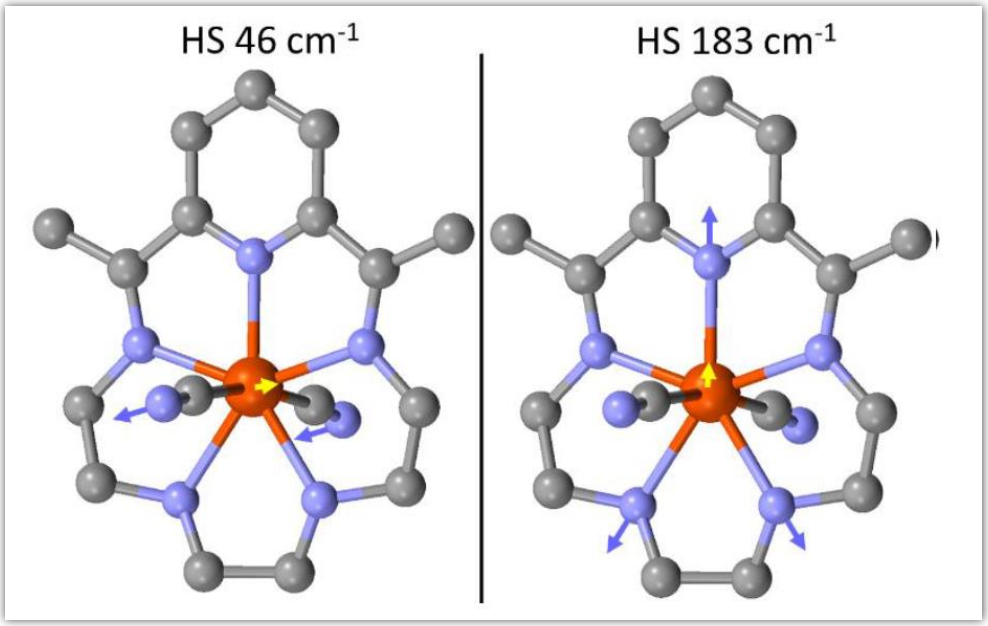

Figure 3.34: Representation of the vibration modes calculated at 46 cm^{-1} and 183 cm^{-1} for the heptacoordinated HS state.

We try now to build a scenario to explain the experimental results. As both optical and X-ray data evidence an intermediate state, with a transient peak and a fast change on the fs timescale, we use the phenomenological model described previously including an initially photoinduced

state (MLCT), which stochastically populates the final HS state where the system undergoes a damped oscillatory motion. This simple model, which was used for $Fe(bpy)_3^{2+}$ (Lemke *et al.*, 2017), is applied to our XAS data and is able to reproduce all main features of the experimental data. Photoexcitation at 530 nm (MLCT) creates a formal Fe^{3+} state. It was shown in $Fe(bpy)_3^{2+}$ that for the XAS data this change of oxidation state results in a transient negative peak at 7125 eV just after laser excitation, because of the global spectral shift by ≈1 eV of the XANES spectra of the MLCT state. The change towards the HS state (Fe^{II}), accompanied by an increase of the distance between the Fe and the neighbouring atoms is associated with an increase of XAS at 7125 eV, as reported in different systems.

The fit to the XAS time trace in Figure 3.32 indicates that the HS state is populated within 160(20) fs and that a 47 cm^{-1} molecular vibration (710 fs period) is activated and damped with a 800 fs time constant. Since DFT calculations did not revealed molecular vibrations in the LS state below 55 cm^{-1}, we identify the mode observed as the HS 46 cm^{-1} found by DFT (Figure 3.34). This is an indication that the HS state, with heptecoordinated structure, forms rapidly after photo-excitation, even though an EXAFS study would be required to affirm firmly that the complex changes from hexa to heptacoordinated structures, but we could not measure additional XANES spectral changes, because of the limited X-FEL beam time. We can also notice that optical pump-probe studies performed up to 80 ps after 490 nm excitation did not revealed slower transformation process (Figure 3.35), except the 3 ps vibrational cooling component. We analyse in a similar way the optical pump- probe data through the OD dynamical time traces shown in Figure 3.33.left, taking also into account a slower vibrational cooling component. The physical parameters used for the fits shown in Figure 3.33.left. A time constant ≈130(10) fs is found for excitation at 490 nm and 530 to describe the decay of the MLCT to the HS state, whereas a 75(10) fs time constant is found for lower energy excitation at 580 and 680 nm to describe the decay of the d-d excitations to the HS state. We also observe different optical fingerprints of the intermediates under 530, 580 and 680 nm excitation for the same probing wavelength. Vibrational cooling varies with the probe wavelength, as it is often the case. We also clearly observe the mode at 47 cm^{-1} in Figure. 33a & 33d, but not 33b and 33c, probably because of the signal/noise limitation.

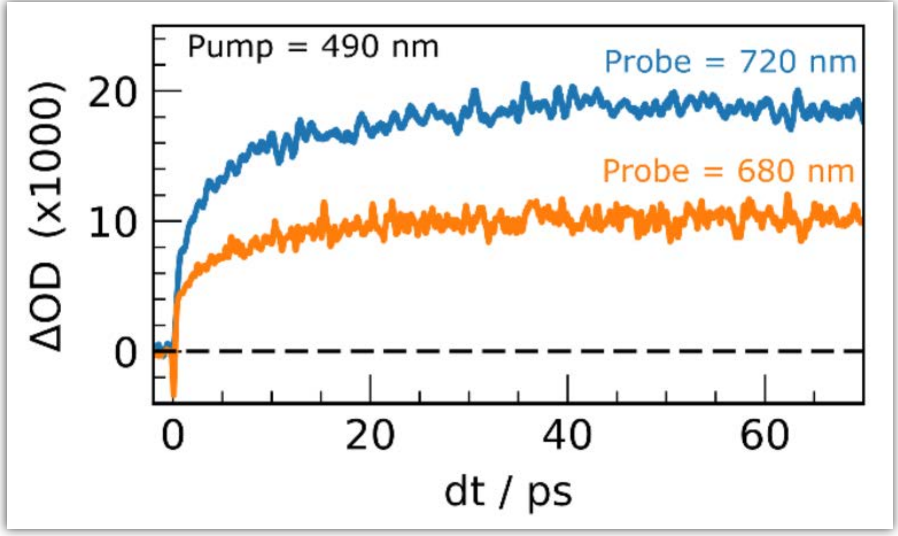

Figure 3.35: ΔOD time traces at 680 and 720 nm after photoexcitation at 490 nm.

The present femtosecond results of LIESST in $[Fe(L_{222}N_5)(CN)_2]$ are in good agreement with recent results obtained in different systems indicating that the MLCT state decays within 120 fs towards the HS and that the FeN_5 breathing mode in the 120 cm^{-1} range and other modes are coherently activated during this decay. For $[Fe(L_{222}N_5)(CN)_2]$, we find a similar 130 fs MLCT to HS decay for excitations at 530 and 490 nm. However, we could not observe the Fe-ligand stretching modes involving Fe-N (183 cm^{-1}) or Fe- CN (263 cm^{-1}) breathing-like bonds. It should be underlined that the periods of these modes correspond to 182 and 127 fs.

3.4. Conclusion

The results discussed in this chapter compare two possible LIESST pathways from LS to HS states under d-d or MLCT photo-excitations. The sequence MLCT→^{3}T within 120 fs and ^{3}T→HS within 70 fs are very similar for FeN_6 and the lower symmetry FeN_4O_2 system investigated here. LIESST is associated with the fast activation of the molecular breathing mode as anti-bonding orbitals are populated, increasing so the equilibrium Fe-L distance and trapping the system in the HS potential as demonstrated in other systems (Cammarata *et al.*, 2014; Bertoni *et al.*, 2015; Auböck & Chergui, 2015; Marino *et al.*, 2016; Consani *et al.*, 2009).

The short lifetime of intermediate states are therefore not thermally equilibrated states, since their population is shorter than the oscillation period in the potential. They correspond to an evolution of hot states within the manifold of electronic states involved in the process, where the coherent structural dynamics moves the system between different electronic potentials, on a timescale where wave functions of atomic nuclei and electrons are difficult to separate. The

resulting physical picture is consistent with the theoretical model introduced by van Veenendaal (Van Veenendaal *et al.*, 2010). The speed of the structural trapping through Fe-L elongation is limited by the decay of the MLCT towards the T state, where antibonding orbitals are populated, since the initial ^{1}MLCT state is equally bonding as the initial LS state. The molecular expansion only starts once the T state is reached, which takes about 120(10) fs, before decaying towards the final HS state within 70(10) fs. The d-d excitation process instantaneously populates antibonding orbitals and, in doing so, launches the Fe-L expansion and moves the system towards the HS potential. The HS state is then reached within 70(10) fs. Here we can study accurately the coherent structural dynamics during LIESST through the intense d-d_{HS} band in the FeN_4O_2 system, strongly modulated by the Fe-L distance. By reducing the lifetime of intermediates compared to MLCT excitation, d-d excitation allows a faster LIESST and preserves structural breathing coherence as this molecular reaction coordinate is activated and damped for trapping the HS state.

We also observed a similar spin stat switching mechanism in $[Fe(L_{222}N_5)(CN)_2]$ using the femtosecond optical and X-ray absorption spectroscopies, in which the low symmetry of the molecules allows MLCT and d-d like photoexcitations in the LS hexacoordinated state. We found optical fingerprints of these intermediates and a faster decay of from d-d to HS than from MLCT to HS. We found that this process induces a coherent structural dynamics, related to the bending of the N-C-Fe-C-N group. The structural relaxation in the HS state is complex with a change of coordination and a large ligand reorganization. It necessary to perform a femtosecond EXAFS measurements in order to follow in more detail the global structural change from hexacoordinated in the LS state to heptacoordinated in the HS state.

Chapter 4 Ultrafast photoswitching in Fe-Co Prussian Blue Analogues

4.1. Introduction

This chapter is devoted to study the ultrafast dynamics of charge transfer and spin transition in CsCoFe(CN)6. This compound was synthesized and characterized by the group of T.Mallah at ICMMO. The DFT and TD-DFT computations were carried out by S. F. Matar at ICMCB. I performed the x-ray powder diffraction and the optical pump-probe experiments at the IPR. The time resolved x-ray absorptions measurements were carried out at ESRF and at LCLS.

4.1. Description of $CsCoFe(CN)_6$ compound

$CsCoFe(CN)_6$ belongs to the Prussian Blue Analogues (PBA) class of materials, where two different kinds of metal ions are linked by cyanide (C-N) bridges. PBA can be written as AM'M"$(CN)_6$, with M' and M" are metal ions, and A is an alkali metal cation (Cs+, K+, Na+), which can be inserted in the structure. In the case of the PBA compound studied here, M'= Co, M"=Fe and A= Cs+. The crystalline structure forms a 3D network, with a face-centred cubic (FCC) packing and a Fm3m space group. The cell parameter is around ~10 Å which can be varied, by substituting the metal ions or/and alkali cations (Sato *et al.*, 1996; Bleuzen *et al.*, 2000; Escax *et al.*, 2001). The Figure 4.1 represents the tridimensional structure of the CsCoFe(CN)6. The Fe and Co are linked by cyanide bridges, which are bonded to C and N atoms respectively.

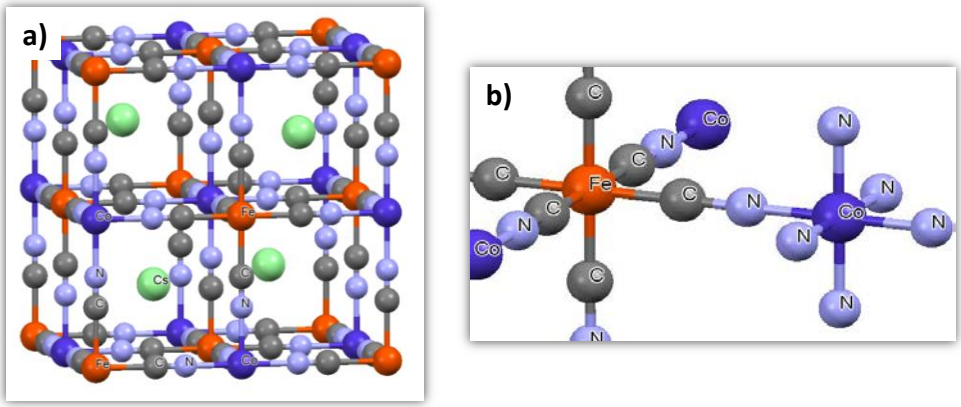

Figure 4.1: Representation of the crystallography structure of $CsCoFe(CN)_6$.

4.1.1. Charge Transfer and spin transition in CsCoFe PBA

Many studies on $A_xCo_y[Fe(CN)_6].nH_2O$ (A being an alkali) 3D materials like $CsCo[Fe(CN)_6]$, it has been shown that external control parameters like temperature or pressure can change the charge and spin state of this compound (Verdaguer *et al.*, 1999; Cafun *et al.*, 2012; Cartier dit Moulin *et al.*, 2000). In particular increasing the temperature usually destabilizes the low spin phase ($Fe^{II}_{S=0} - CN - Co^{III}_{S=0}$ where the subscript indicates the spin state and the superscript the oxidation state) and favors the charge transfer / high spin phase $Fe^{III}_{S=\frac{1}{2}} - CN - Co^{II}_{S=\frac{3}{2}}$. More recently researchers have managed to use light to reversibly control the state of the system (Sato *et al.*, 1996; Koumousi *et al.*, 2011) through ultrafast metal-to-metal charge-transfer processes (MMCT). At thermal equilibrium the change of spin state on the Co site is associated with a structural reorganization: as electron populate antibonding e_g orbitals in the HS state, the Co-N bonds expand (Figure 4.2).

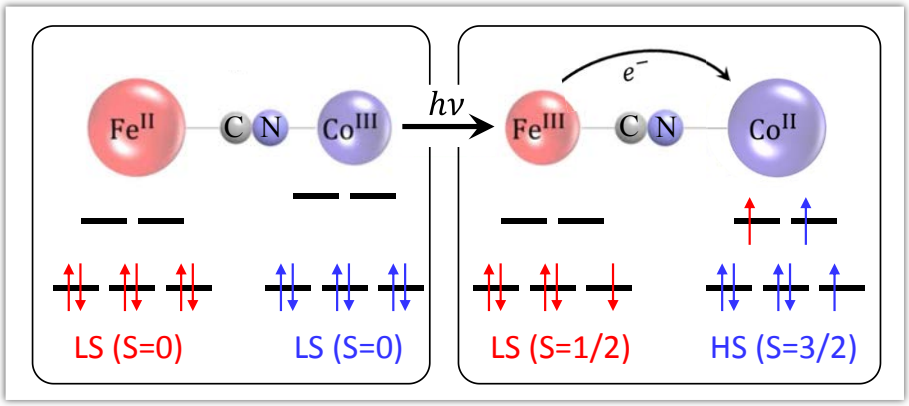

Figure 4.2: Schematic representation of the process CTIST in Fe-CN-Co.

Despite the large variety of scientific studies in the last decades, for example by optical (Arnett *et al.*, 1995), X-ray diffraction (Moritomo *et al.*, 2009) and Near Edge X-ray Absorption experiments (Cafun *et al.*, 2012). The mechanism of the switching is not yet understood. Is the charge-transfer driving the spin change or vice versa? Are the changes happening simultaneously? The physical picture is complicated by the fact that many absorption bands are theoretically predicted ranging from charge transfer to metal centered. X-ray absorption with its sensitivity to charge transfer (resulting in a "rigid shift" of the absorption spectrum) and structural rearrangement (change of the XANES spectrum) is an ideal probe to disentangle electronic and structural changes, especially at Fe and Co K-edges conveniently located within the limits of the X-ray energies reachable at LCLS.

4.1.2. Fingerprints of photoswitching in $CsCoFe(CN)_6$

The $CsCoFe(CN)_6$ nanocrystals was characterized by several techniques such as SQUID, XRD and visible absorption. The different signatures (magnetic, structural and spectral) of the low-temperature photoinduced state, are presented in the Figure 4.3. The magnetic measurements performed by the group T. Mallah in nanocrystals with size ~ 15 nm, shows an increase in the magnetization after CW irradiation with 642 nm at very low temperature (5 K) (Figure 4.3 a), that is due to photoconversion of the CoFe pairs from the $CsCo^{III}(LS)Fe^{II}(LS)$ diamagnetic state to paramagnetic state $CsCo^{II}(HS)Fe^{III}(LS)$.

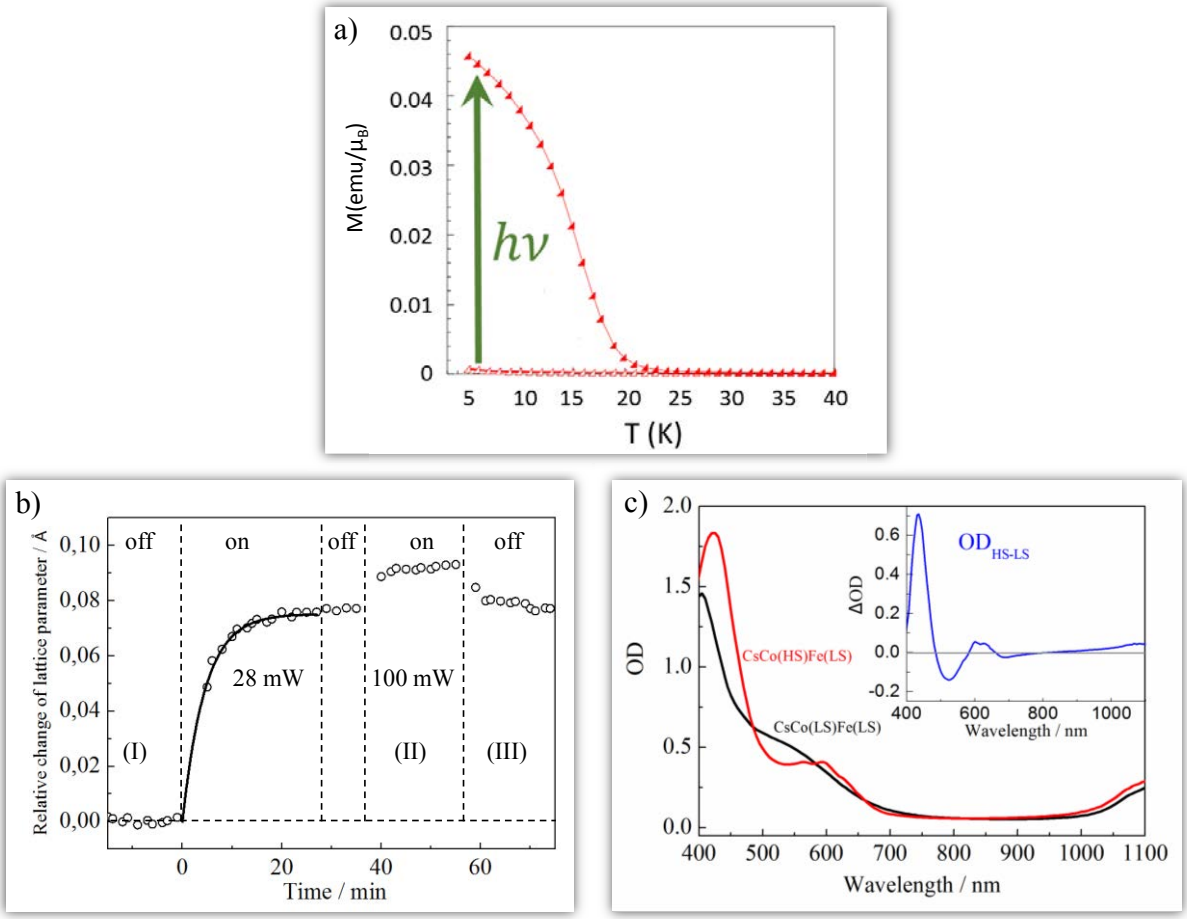

Figure 4.3: a) Temperature dependence of magnetic measurements in $CsCoFe(CN)_6$ before and after CW irradiation at 5 K (Dia, 2013). b) Relative change of the lattice parameter $CsCoFe(CN)_6$ at 15 K, under 650 nm CW excitation. c) Visible absorption spectra at 15 K, before (black) and after (red) irradiation at 650 nm, in inset (blue) the difference between them (red-black).

To characterize the structural properties of the $CsCoFe(CN)_6$ nanocrystals dispersed in the PVP polymer matrix under the effect of light, low temperature XRD patterns were collected using 4-circle diffractometer at IPR with monochromatic radiation ($\lambda = 0.71073$ Å). We used a continuous laser at 530 nm in order to switch the system at low temperature from the $CsCo^{III}(LS)Fe^{II}(LS)$ to the $CsCo^{II}(HS)Fe^{III}(LS)$ state. The diffraction patterns of nanocrystals collected before, during and after irradiations were used to determine the parameter lattice change. All diffractograms are characterize of face-centered cubic (fcc) structure but the position, the Full Width at Half Maximum (FWHM) and intensity of the reflections vary with irradiation, the diffuse background which characterizes the PVP matrix scattering is removed using the method described in the previous chapter (Section 2.1.1). The positions of hkl reflections have been determined for all pattern from the fitting using the pseudo-Voigt function. At 15 K, without laser irradiation the system is low spin with an initial lattice parameter of a ~ 10.07 Å. The diffraction pattern collected simultaneously with 28 mW irradiation show a shift of all reflection in the same direction, which corresponds to the increase of the lattice parameter of ~ 0.07 % Å this variation induced by the transformation of the system from the LS to metastable state directly reflects the electronic state of the cobalt atoms in the structure: $Co^{II}(HS)$ with long coordination a ~ 10.143 Å. the increase of the power of the irradiation (100 mW) causes a variation of ~ 0.1 % of the cell parameter which is the thermal expansion of the photo induced structure. After irradiation, the parameter lattice decreases by the same thermal variation to the parameter values of the high spin structure and it remains constant (Figure 4.3 b).

We have investigated the optical density change of $CsCoFe(CN)_6$ nanocrystals dispersed in PVP polymer film with a thickness of few hundreds micrometers. The absorption spectrum was measured before and after CW irradiation at 650 nm at 15 K, in the 400-1100 nm range (Figure 4.3.c). The differential spectra clearly shows changes which reflects a change in the electronic structure under light irradiation. The large absorption band around 530 nm of $CsCo^{III}(LS)Fe^{II}(LS)$ state is associated the metal-metal charge transfer band (Sato *et al.*, 1999; Yoshizawa *et al.*, 1998). This absorption band decreases after irradiation, which is associated with the depopulation of $CsCo^{III}(LS)Fe^{II}(LS)$ state.

4.2. Probing the charge transfer: Time-resolved XANES

The first observation of the charge transfer at room temperature in CoFe was carried out by the group of Bleuzen (Cafun *et al.*, 2012), it was found by probing around the Fe K-edges and Co K-edge (Figure 4.4), that under pressure and light irradiation, an electron is transferred from the Fe to Co which stabilize the photoinduced state $Co^{II}Fe^{III}$. The shift observed in absorption spectrum is due to the oxidation degree in $Fe^{II} \rightarrow Fe^{III}$ and $Co^{III} \rightarrow Co^{II}$. This measurements demonstrated a change in the spin state of Co from Co^{III}(LS) to Co^{II}(HS), which is due to a structural change around the Co site.

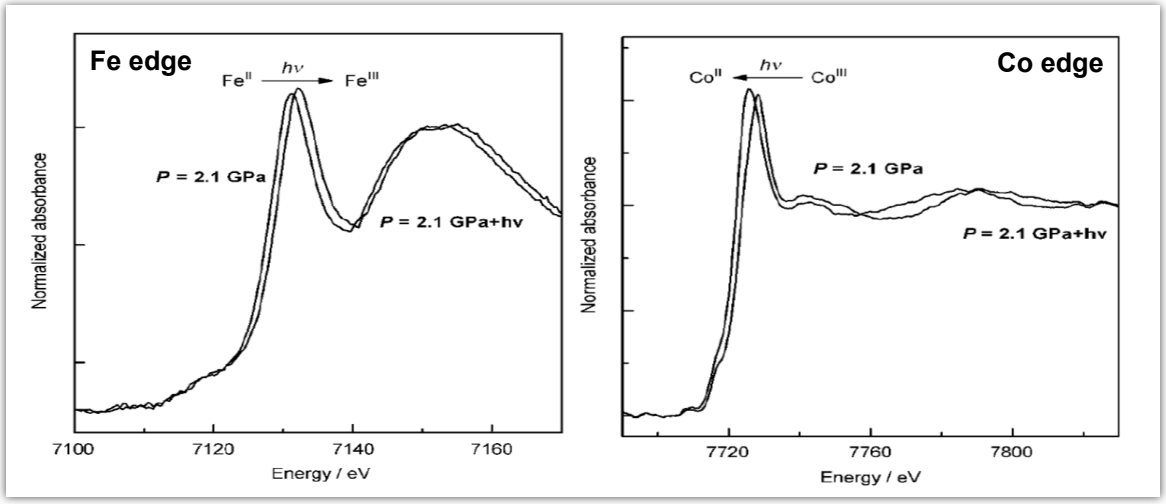

Figure 4.4: XANES profiles of LS and trapped photoinduced HS state for a (CoFe) PBA (Cafun *et al.*, 2012).

The $CsCoFe(CN)_6$ nanocrystals dispersed in water studied here are in the diamagnetic $Fe^{II}(S=0)$-$Co^{III}(S=0)$ state at room temperature, which allows performing the photo transformation experiments at room temperature. We acquired the XANES data from the 15 nm size nanocrystals dispersed in water and excited by 650 nm laser pulses (Figure 4.5). The XANES changes were monitored by the ~70 ps X-ray pulses at the ID09 beamline (Section 2.2). Before laser irradiation, the maxima of X-ray absorption intensity I(a.u.) are around 7728 eV at the Co K-edge and around 7130 eV at the Fe K-edge. These results are in good agreement with the results obtained from the study mentioned above (Cafun *et al.*, 2012). The spectral changes measured 500 ps after laser excitation (red dashed curve) are very weak. This is often the case in time-resolved studies, because the excitation density used is typically of the order of 1 photon per 100 active sites. Therefore, the spectral changes due to photoexcited species are

better observed on the spectral intensity change, $\Delta I = (I_{500ps}-I_{off})$, also shown in Figure 4.5. The difference spectra at the Co edge shows a spectral shift towards lower energy, characterized by an absorption increase below the Co edge and a decrease just above. Difference spectra at Fe edge shows the opposite spectral shift towards higher energy, with an absorption decrease below the Fe edge and an increase just above.

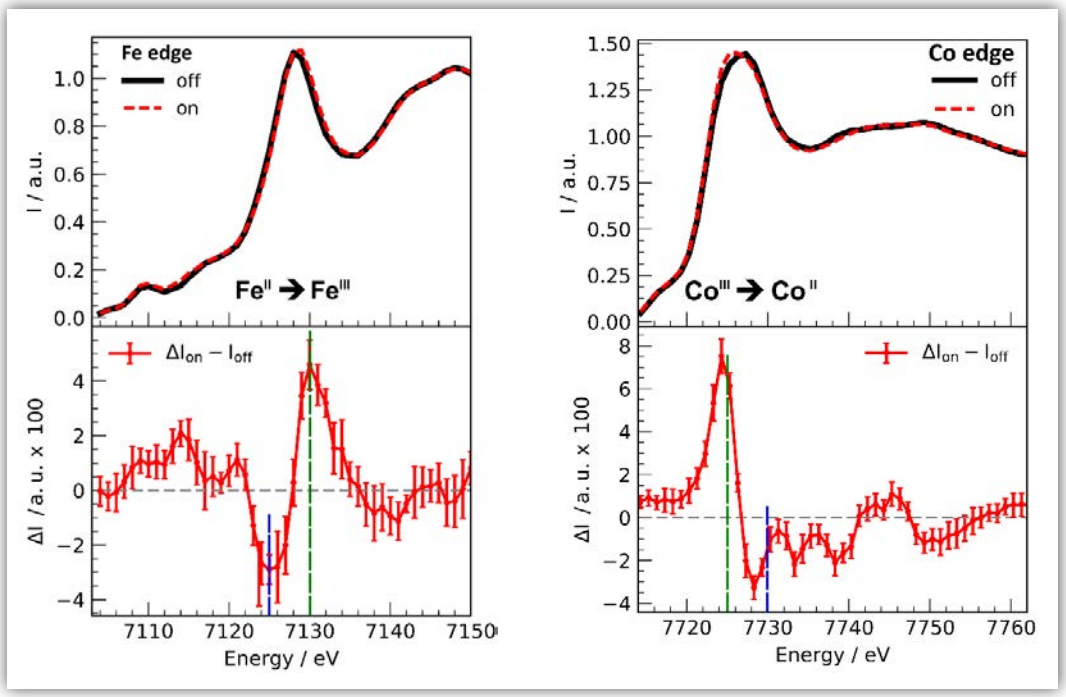

Figure 4.5: XANES spectra, for the CsCoFe nanocrystals, at the Fe and Co edges before (black) and 500 ps after laser excitation (red) and corresponding spectra change ΔI(t)

Such changes in the absorption spectra are characteristic of the change of the formal oxidation state of the metal ions and therefore of the $Co^{III}(LS)Fe^{II} \rightarrow Co^{II}(HS)Fe^{III}$ electron transfer (Cartier dit Moulin *et al.*, 2000; Yokoyama *et al.*, 1998; Cafun *et al.*, 2012). Additional oscillating changes above the Co edge are characteristic of the local structural change around Co due to the spin-crossover as already observed for Fe in the SCO systems. The transient XANES changes ΔI(t) after photoexcitation were measured at photon energies just above and below the Co and Fe absorption edges (Figure 4.6). These traces indicate that the electron transfer occurs within the 100 ps time resolution of the experiment and that the photoinduced $Co^{II}(HS)Fe^{III}(LS)$ state has a lifetime larger than 1 ns at room temperature. Cartier dit Moulin et al reported that the irradiation induces a shift for the pre-edge from 7711 to 7710 eV (Cartier dit Moulin *et al.*, 2000), hardly seen in Figure 4.5 due to experimental limitations, which will be interesting to track in real time with new XANES experiment with high flux.

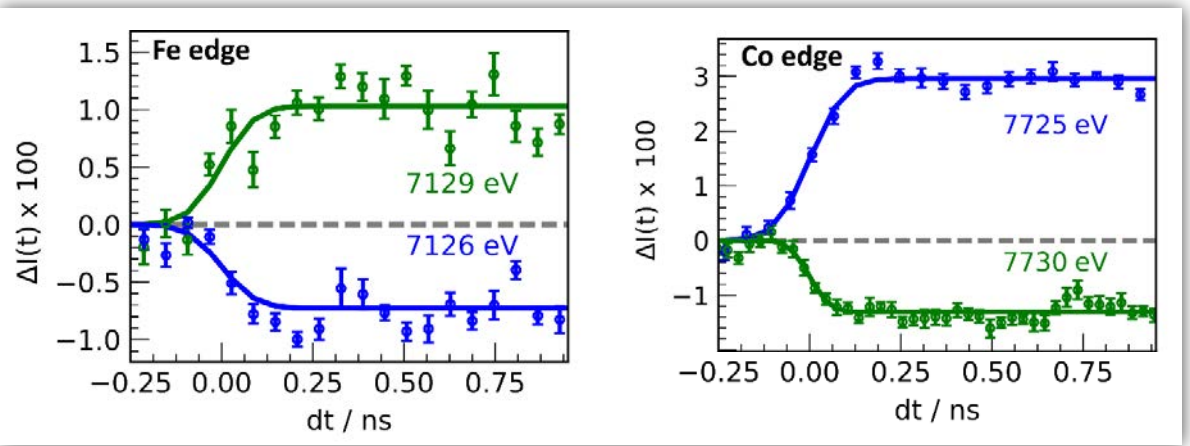

Figure 4.6: Time scans of relative absorption changes at selected X-ray energies below and above the Co and Fe edges, for the CsCoFe nanocrystals.

4.3. Time-dependent DFT calculations

The TD-DFT calculation were carried out in order to better understand the electronic and structural properties in CoFe PBAs. The periodic structure of this system renders very difficult to calculate the absorption spectra, whereas the calculation is possible for a single pair $Co(NC)_6$-$Fe(CN)_6$. UV-vis absorption spectra were simulated by convoluting with Gaussian functions (FWHM = 0.33 eV) centred at the calculated wavelength for each transition. The Figure 4.7 shows the absorption spectra calculated for Co^{III}(LS)Fe^{II}(LS) and Co^{II}(LS)Fe^{III}(LS) pair. Concerning the geometry of $Co^{III}Fe^{II}$, two main absorption bands are computed at 470 nm and 580 nm. For $Co^{II}Fe^{III}$, two absorption band centred at 440 nm and 540 nm.

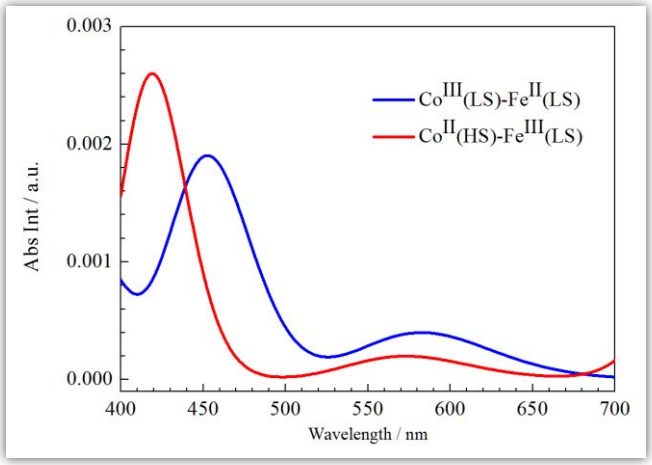

Figure 4.7: Absorption spectra calculated for Co-NC-Fe pair.

From the molecular orbitals simulations, the transition centred at 580 nm of the $Co^{III}Fe^{II}$ pair has a Co d-d character and will be associated to the d-d_{LS}, this transition is weak but non-zero. Another possible transition in the near IR region (centred at 1200 nm), which has a metal-metal charge transfer (MMCT) from the Fe t_{2g} to Co e_g orbital (Figure 4.8).

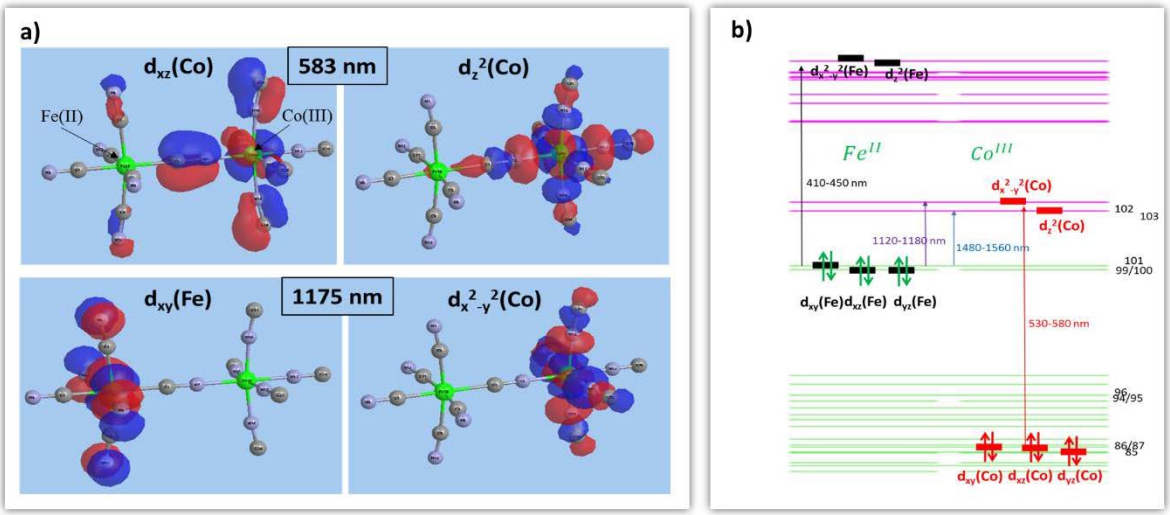

Figure 4.8: a) Characteristic orbitals of hole and particle for Co^{III}(LS)Fe^{II}(LS) state obtained by TD-DFT. b) Energy diagram of Co^{III}(LS)Fe^{II}(LS) calculated by TDF.

4.4. Femtosecond optical and XANES studies

For tracking the lifetime of the photoinduced $CsCo^{II}$(HS)Fe^{III}(LS) state, we performed complementary optical measurements on the experimental set-up available at the Institut de Physique de Rennes. We used time-resolved optical spectroscopy to study the relaxation process of CsCoFe nanocrystals in solution that were photo-excited at room temperature by 650 nm optical pulses. The probe wavelength was set to 520 nm, which corresponds to the maximum of the Co^{III}(LS)Fe^{II}→Co^{II}(HS)Fe^{III} absorption band. The time-resolved OD decrease after photoexcitation shown in Figure 4.9, is due to the depopulation of the Co^{III}(LS)Fe^{II} after photoexcitation and indicates that the Co^{II}(HS)Fe^{III}(LS) → Co^{III}(LS)Fe^{II}(LS) relaxation occurs within few µs at room temperature.

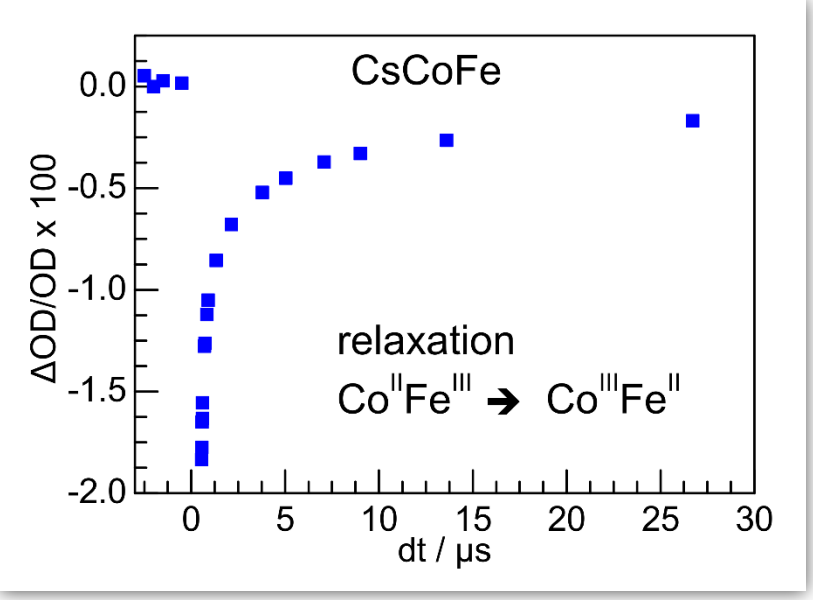

Figure 4.9: Time trace of OD change at 520 nm, after fs laser excitation at 650 nm, for the $CsCoFe(CN)_6$ nanocrystals.

For better understand the ultrafast dynamics of the charge transfer and spin transition, we performed a femtosecond optical pump-probe measurements in $CsCoFe(CN)_6$ nanocrystals embedded in PVP polymer and dispersed in water at room temperature, using the set-up descripted in the Section 2.1.2. The repetition rates of the pump and the probe are 500 Hz and 1 kHz respectively. The excitation fluence is set to 30 $\mu J.mm^{-2}$. In the Figure 4.10 (b,c), we show the time scan of OD after 650 nm wavelength excitation and probing at 427 and 1000 nm. The increase of OD at both wavelengths of probe, is characteristic of the formation of the $Co^{II}(HS)Fe^{III}(LS)$ state, as observed in the difference spectrum at low temperature between, before and after CW irradiation (Figure 4.10.a). The transient peak observed at 427 nm at t = 0, reflects the presence of an intermediate electronic state with a lifetime of ~150 fs, and a coherent oscillation accompanies the relaxation, with a period of 650 fs (~ 51 cm^{-1}) and damping of 670 fs. Given the previous results obtained in different SCO materials, we tentatively attribute these oscillations to Co-N oscillation accompanying the spin transition on the Co site, with a global increase of the Co-N bonds.

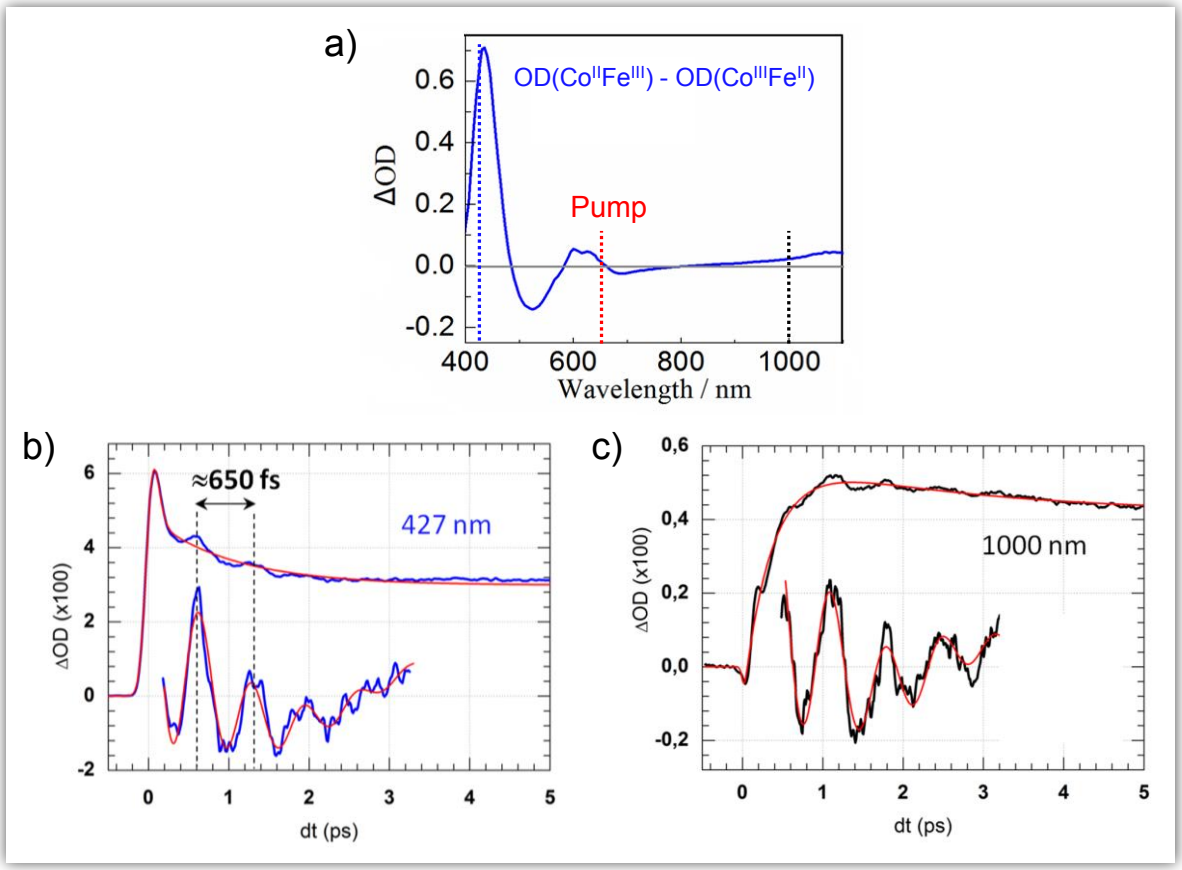

Figure 4.10: a) Difference spectrum of OD. Time trace of OD change after 650 nm pump: a) at 427 nm probe and b) at 1000 nm probe, in $CsCoFe(CN)_6$ nanocrystals.

In addition to the optical and TR-XANES at ESRF measurements, we performed a preliminary femtosecond XANES experiment in CsCoFe(CN)6 nanocrystals at LCLS, using the set-up described in the Section 2.3. The x-ray probe was at the Fe K-edge. The pump wavelength was 530 nm. the XANES spectrum recorded after 5 ps pulse excitation (Figure 4.11.a), indicated the change in oxidation state of Fe from Fe(II)→Fe(III), which is associated to the transfer of an electron from Fe to Co, as observed at 500 ps by XANES at ESRF (Figure 4.5.a). The time scans at selected energies 7131 and 7126 eV (Figure 4.11.b.c), shown that the electron arrives on the Fe within 170 fs time resolution of the experiment.

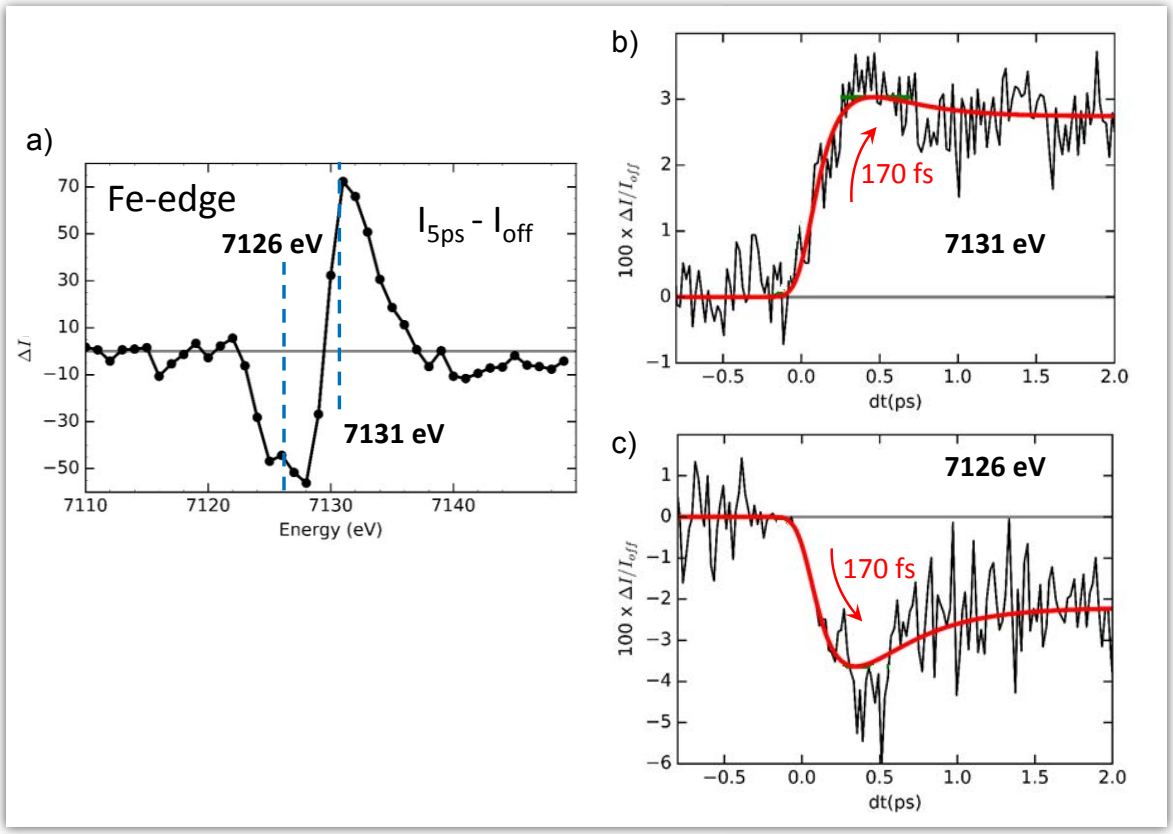

Figure 4.11: Femtosecond time-resolved XANES at Fe K-edge after 530 nm excitation. a) XANES spectra at 5ps. b) Time scans of relative absorption changes at selected X-ray energies below and above the Fe K-edge.

4.5. Photoswitching mechanism

To summarize, the TD-DFT calculations show that the d-d transition of Co is not zero and is in the 530-560 nm range. The picosecond XANES, evidences the charge transfer at 500 ps upon 650 nm pulse excitation. The femtosecond optical measurements shows a multistep dynamics and the breathing mode which concerns the Co-N_6 bonds. Finally, femtosecond XANES indicates that the charge transfer occurs within 170 fs.

We propose a tentative scenario of this multi-step process is shown in the Figure 4.12, which includes 4 steps as follow:

Step 0: Initially the system is in the ground diamagnetic state $Co^{III}(S=0)Fe^{II}(S=0)$.

Step I: The photo-excitation at 650 nm corresponds to a Co d-d electron transfer, as shown by DFT calculation, promoting one electron from the Co t_{2g} to the Co e_g orbitals. This transient electronic state is identified by a short OD peak observed with 427 nm probes.

Step II: The population of antibonding Co e_g orbital drives the elongation of the Co-N bonds (arrows), thereby closing the t_{2g}-e_g gap on the Co site.

Step III: the t_{2g}-e_g gap closing on the Co site, promotes another electron from the Co t_{2g} orbital to the Co e_g orbital, and induces a spin transition on the Co, forming a high spin Co^{II} S=2 state.

Step IV: the structural reorganisation redistributes energy levels and one electron is transferred from the Fe to the Co, forming so the final Fe^{III}(S=1/2)-Co^{III}(S=3/2) state. As there is no significant structural change on the Fe site between Fe^{II} to Fe^{III} states (electrons populate non-bonding states in both cases) the coherent oscillations are very likely due to the spin transition on the Co site, which should be accompanied by the activation and damping of the breathing mode. This process is therefore similar to the one reported in SCO materials in chapter 3.

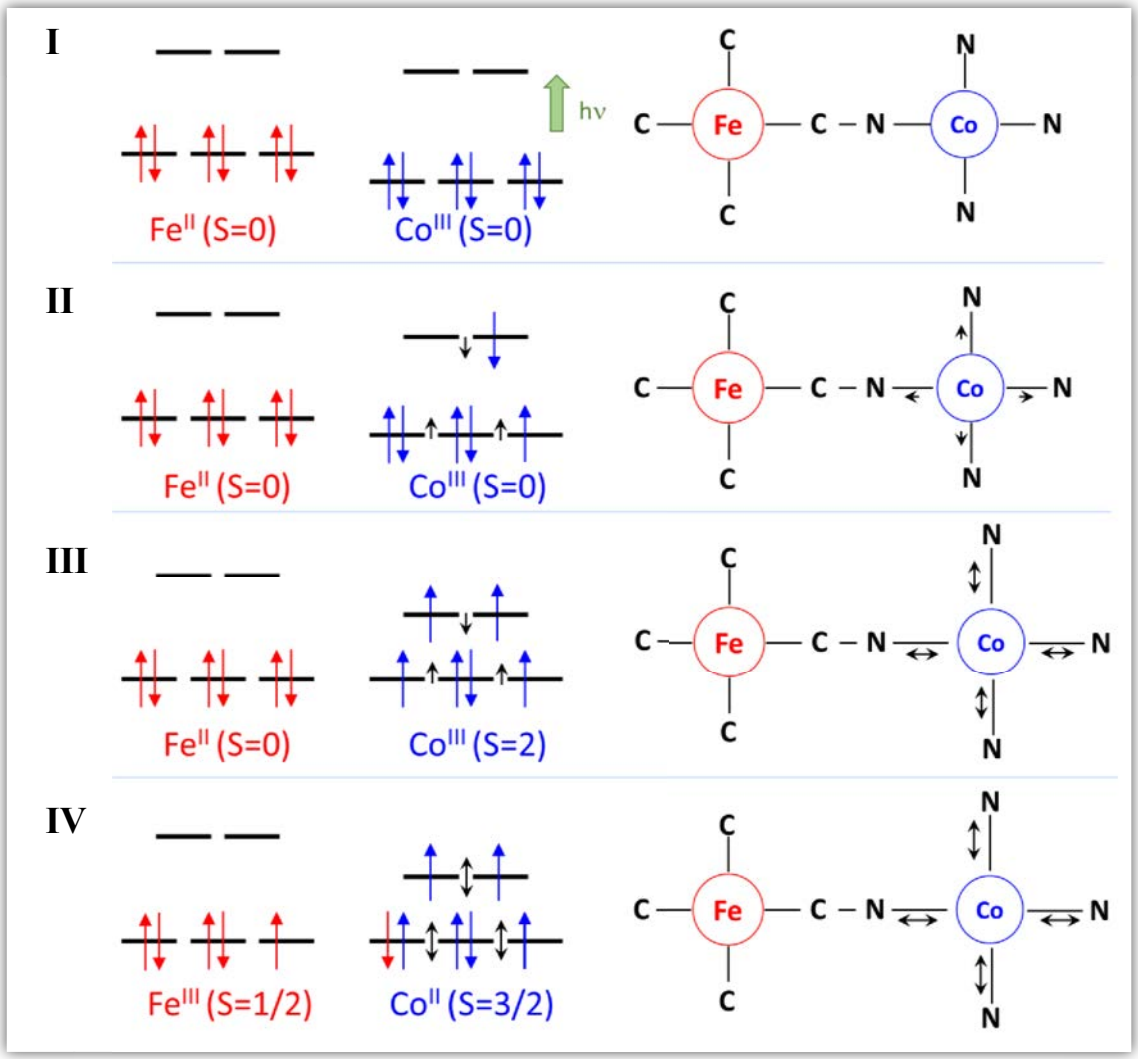

Figure 4.12: Schematic of the possible states involved with electronic and structural changes.

4.6. Discussion

The goal of the study presented in this chapter was to better understand the elementary mechanism of the switching in CoFe PBA compound. More precisely, to determine which process (charge transfer or spin transition) happens first after optical excitation. Our approach to explain these processes is different to the one often discussed in the literature in terms of Charge Transfer Induced Spin Transition CTIST. Here we propose a light-induced excited spin-state trapping (LIESST) process occurring on the Co site and followed by the electron transfer from the Fe to the Co in a second stage (Spin Transition Induced Charge Transfer STICT). This interpretation is based on TD-DFT computations and experimental results obtained by femtosecond optical and XANES pump-probe studies. We clearly observed an intermediate state at 427 nm upon d-d excitation of Co and a coherent oscillation which accompanies the relaxation in the final state. This oscillation is attributed to the coherent structural trapping of the Co HS state which results from the activation and damping of the CoN_6 breathing mode. However, such low frequency Co-N6 breathing mode (650 fs period) was never discussed in the literature so far. In addition, the preliminary results obtained by TR-XANES at LCLS show a change from Fe^{II} to Fe^{III} occurs within less than 170 fs.

A clear answer to the sequence of processes and states involved during the photoinduced CT process requires a deeper investigation of the process to understand better how electronic and structural degrees of freedom change in time and couple to each other.

Optical probes being indirectly structural-sensitive and not element specific. To confirm our approach, it is necessary to perform X-ray absorption studies both at the Co and Fe K edges. We were allocated for beamtime at the XPP station of the LCLS X-FEL to perform such an experiment in summer 2017. The 20 fs RMS time resolution will allow to watch when the electron leaves the Fe and arrives on the Co (opposites shift of the XANES for both edges). The coherent structural trapping, expected to result from Co-N elongation, should translate in oscillation of the time-resolved XANES signal around the Co Edge, as we observed recently during LIESST of a Fe spin-crossover molecule (Lemke *et al.*, 2017).

4.7. Conclusion

The results presented in this chapter 4 open the way for investigating photoinduced charge-transfer process in PBAs. As proof of concept, we studied the prototypical Co-N-C-Fe 3D PBA system. During the last years, several groups developed new synthesis for isolating the Co-N-C-Fe switchable units, at the level of chains, $[Co_4Fe_4]$ cubes, $[Co_2Fe_2]$ squares or [CoFe] pairs (Li *et al.*, 2008; Zhang *et al.*, 2010; Koumousi *et al.*, 2014; Lescouezec *et al.*, 2003; Mercurol *et al.*, 2010; Nihei *et al.*, 2011), able to mimic the bistable structural and electronic properties of CoFe PBA, including photo-induced CT transition conversion. In addition, photo-induced CT conversions have now been reported in various cyanide-bridged bimetallic systems such as MnFe (Tokoro *et al.*, 2014; Ohkoshi & Tokoro, 2012) or CoW (Miyamoto *et al.*, 2016; Chorazy *et al.*, 2016) showing the generalization of the CT switching process. The present study, with the emergence of fs XANES at X-FEL, opens a broad field of investigation for observing and understanding the processes coupling structural and electronic reorganization during the process, by combining femtosecond optical and X-ray spectroscopy, at the level of 3D materials or in isolated [CoFe] pairs in solution.

General Conclusion

The results I have obtained during my PhD on the ultrafast photo-switching dynamics in molecular spin crossover crystals and Prussian blue analogues are presented in this manuscript. For performing such investigations, different experimental tools have been used, namely femtosecond optical spectroscopy at IPR and ultrafast X-ray spectroscopy at the ESRF synchrotron and at the LCLS X-FEL.

The investigation of different types of systems FeII SCO systems shed light on the different excitation processes involved. MLCT and d-d excitation induce different pathways from the initial low spin to the final high spin states, triggering different coherent structural dynamics of the <Fe-N> bond length breathing. The fast activation and damping of this mode is responsible for the structural trapping of the photoinduced high spin state, as evidenced by femtosecond experiments. This work opens the possibility to extend our method to investigate other type of photoactive materials.

Our study on photoinduced charge-transfer process in the 3D PBA Co-N-C-Fe is a proof of concept that fs X-ray and optical spectroscopies can be used to understand how CT and spin-crossover processes couple in time, to switch the physical properties of the material. The emergence of fs XANES at X-FEL, opens a broad field of investigation for observing and understanding the processes coupling structural and electronic reorganization during the process. There is a nice opportunity to extend this work to the emerging CT systems, such as $[Co_4Fe_4]$ cubes, $[Co_2Fe_2]$ squares or [CoFe] pairs or CoW materials able to mimic photo-induced CT transition conversion. Similar questions appear for the study of systems like MnFe PBA, showing stronger structural change with important Jahn Teller distortion and symmetry breaking. Femtosecond structural studies should shed light on how this symmetry breaking takes place and what is the associated structural dynamics. In addition, there is the possibility to induce different dynamics through charge-transfer induced spin transition or through spin-transition induced charge transfer pathways, which will be very interesting to explore in future, as different optical excitation wavelength may induce initial d-d or CT states.

Finally, in addition to the observation of photoswithing dynamics with femtosecond tools, another important goal emerge for controlling and switching the physical properties of this type of materials. Indeed, new techniques allow manipulating materials such as non-linear phononic or THz excitation, which trigger photoinduced phase transition no more through highly excited

initial electronic state, but more gently through the activation of structural degrees of freedom. This will open the possibility to drive ultrafast and coherent photoinduced switching, which the femtosecond probe techniques developed and used in this thesis will easily monitor.

Bibliography

A

Ababei, R., Pichon, C., Roubeau, O., Li, Y.G., Bréfuel, N., Buisson, L., Guionneau, P., Mathonière, C. and Clérac, R., **2013**. Rational design of a photomagnetic chain: Bridging single-molecule magnets with a spin-crossover complex. *Journal of the American Chemical Society*, *135*(39), pp.14840-14853.

Ackermann, W.A., Asova, G., Ayvazyan, V., Azima, A., Baboi, N., Bähr, J., Balandin, V., Beutner, B., Brandt, A., Bolzmann, A… and Zapfe, K., **2007.** Operation of a free-electron laser from the extreme ultraviolet to the water window. *Nature photonics, 1(6)*, pp.336-342.

Alfano, R.R., **2006**. The supercontinuum light source.

Arnett, D.C., Voehringer, P. and Scherer, N.F., **1995**. Excitation dephasing, product formation, and vibrational coherence in an intervalence charge-transfer reaction. *Journal of the American Chemical Society*, *117*(49), pp.12262-12272.

Asahara, A., Nakajima, M., Fukaya, R., Tokoro, H., Ohkoshi, S.I. and Suemoto, T., **2012**. Ultrafast dynamics of reversible photoinduced phase transitions in rubidium manganese hexacyanoferrate investigated by midinfrared CN vibration spectroscopy. *Physical Review B, 86(19)*, p.195138.

Auböck, G. and Chergui, M., **2015**. Sub-50-fs photoinduced spin crossover in [Fe (bpy) 3] 2+. *Nature chemistry*, *7*(8), pp.629-633.

B

Baker Jr, W.A. and Bobonich, H.M., **1964**. Magnetic properties of some high-spin complexes of iron (II). *Inorganic Chemistry, 3(8)*, pp.1184-1188.

Bethe, H.A., **1929**. Splitting of terms in crystals. *Ann. Physik*, *3*(5), p.133.

Bertoni, R., Lorenc, M., Tissot, A., Servol, M., Boillot, M.L. and Collet, E., **2012**. Femtosecond Spin-State Photoswitching of Molecular Nanocrystals Evidenced by Optical Spectroscopy. *Angewandte Chemie International Edition*, *51*(30), pp.7485-7489.

Bertoni, R., Cammarata, M., Lorenc, M., Matar, S.F., Létard, J.F., Lemke, H.T. and Collet, E., **2015**. Ultrafast light-induced spin-state trapping photophysics investigated in Fe (phen) 2 (NCS) 2 spin-crossover crystal. *Accounts of chemical research*, *48*(3), pp.774-781.

Bertoni, R., Lorenc, M., Cailleau, H., Tissot, A., Laisney, J., Boillot, M.L., Stoleriu, L., Stancu, A., Enachescu, C. and Collet, E., **2016**. Elastically driven cooperative response of a molecular material impacted by a laser pulse. *Nature materials*, *15*(6), pp.606-610.

Blaj, G., Caragiulo, P., Carini, G., Carron, S., Dragone, A., Freytag, D., Haller, G., Hart, P., Hasi, J., Herbst, R… and Weaver, M., **2015**. X-ray detectors at the Linac Coherent Light Source. *Journal of synchrotron radiation*, *22*(3), pp.577-583.

Bleuzen, A., Lomenech, C., Escax, V., Villain, F., Varret, F., Cartier dit Moulin, C. and Verdaguer, M., **2000**. Photoinduced Ferrimagnetic Systems in Prussian Blue Analogues CI x Co4 [Fe (CN) 6] y (CI= Alkali Cation). 1. Conditions to Observe the Phenomenon. *Journal of the American Chemical Society*, *122*(28), pp.6648-6652.

Boillot, M.L., Zarembowitch, J. and Sour, A., **2004**. Ligand-driven light-induced spin change (LD-LISC): a promising photomagnetic effect. In *Spin crossover in transition metal compounds II (pp. 261-276)*. Springer Berlin Heidelberg.

Bonifacio, R., Pellegrini, C. and Narducci, L.M., **1984**. Collective instabilities and high-gain regime in a free electron laser. *Optics Communications*, *50*(6), pp.373-378.

Bousseksou, A., Molnár, G., Salmon, L. and Nicolazzi, W., **2011**. Molecular spin crossover phenomenon: recent achievements and prospects. *Chemical Society Reviews*, 40(6), pp.3313-3335.

Bréfuel, N., Collet, E., Watanabe, H., Kojima, M., Matsumoto, N., Toupet, L., Tanaka, K. and Tuchagues, J.P., **2010**. Nanoscale Self-Hosting of Molecular Spin-States in the Intermediate Phase of a Spin-Crossover Material. *Chemistry-A European Journal*, *16*(47), pp.14060-14068.

Bressler, C., Milne, C., Pham, V.T., ElNahhas, A., Van der Veen, R.M., Gawelda, W., Johnson, S., Beaud, P., Grolimund, D., Kaiser, M… and Chergui, M., **2009**. Femtosecond XANES study of the light-induced spin crossover dynamics in an iron (II) complex. *Science*, *323*(5913), pp.489-492.

Buser, H.J., Schwarzenbach, D., Petter, W. and Ludi, A., **1977**. The crystal structure of Prussian blue: Fe4 [Fe (CN) 6] 3. xH2O. *Inorganic Chemistry*, *16*(11), pp.2704-2710.

C

Cailleau, H., Lorenc, M., Guérin, L., Servol, M., Collet, E. and Cointe, B.L., **2010**. Structural dynamics of photoinduced molecular switching in the solid state. *Acta Crystallographica Section A: Foundations of Crystallography*, 66(2), pp.189-197.

Cafun, J.D., Lejeune, J., Baudelet, F., Dumas, P., Itié, J.P. and Bleuzen, A., **2012**. Room-Temperature Photoinduced Electron Transfer in a Prussian Blue Analogue under Hydrostatic Pressure. *Angewandte Chemie International Edition*, *51*(36), pp.9146-9148.

Cambi, L. and Gagnasso, A., **1931**. Iron dithiocarbamates and nitrosodithiocarbamates. *Atti. Accad. Naz. Lincei, 13*, pp.809-813.

Cammarata, M., Eybert, L., Ewald, F., Reichenbach, W., Wulff, M., Anfinrud, P., Schotte, F., Plech, A., Kong, Q., Lorenc, M… and Polachowski, S., **2009**. Chopper system for time resolved experiments with synchrotron radiation. *Review of scientific instruments*, *80*(1), p.015101.

Cammarata, M., Bertoni, R., Lorenc, M., Cailleau, H., Di Matteo, S., Mauriac, C., Matar, S.F., Lemke, H., Chollet, M., Ravy, S… and Collet, E., **2014**. Sequential activation of molecular breathing and bending during spin-crossover photoswitching revealed by femtosecond optical and X-ray absorption spectroscopy. *Physical review letters*, *113*(22), p.227402.

Cartier dit Moulin, C., Villain, F., Bleuzen, A., Arrio, M.A., Sainctavit, P., Lomenech, C., Escax, V., Baudelet, F., Dartyge, E., Gallet, J.J. and Verdaguer, M., **2000**. Photoinduced Ferrimagnetic Systems in Prussian Blue Analogues CI x Co4 [Fe (CN) 6] y (CI= Alkali Cation). 2. X-ray Absorption Spectroscopy of the Metastable State. *Journal of the American Chemical Society*, *122*(28), pp.6653-6658.

Chergui, M., and Collet, E., **2017**. Photoinduced Structural Dynamics of Molecular Systems Mapped by Time-Resolved X-ray Methods. *Chem. Rev., 2017, 117 (16)*, pp 11025–11065

Chollet, M., Guerin, L., Uchida, N., Fukaya, S., Shimoda, H., Ishikawa, T., Matsuda, K., Hasegawa, T., Ota, A., Yamochi, H… and Koshihara, S., **2005**. Gigantic photoresponse in ¼-filled-band organic salt (EDO-TTF) 2 PF 6. *Science*, *307*(5706), pp.86-89.

Chorazy, S., Wang, J. and Ohkoshi, S.I., **2016**. Yellow to greenish-blue colour-tunable photoluminescence and 4f-centered slow magnetic relaxation in a cyanido-bridged Dy III (4-hydroxypyridine)–Co III layered material. *Chemical Communications*, *52*(71), pp.10795-10798.

Collet, E., Lemée-Cailleau, M.H., Buron-Le Cointe, M., Cailleau, H., Wulff, M., Luty, T., Koshihara, S.Y., Meyer, M., Toupet, L., Rabiller, P. and Techert, S., **2003**. Laser-induced ferroelectric structural order in an organic charge-transfer crystal. *Science*, *300*(5619), pp.612-615.

Collet, E., Moisan, N., Baldé, C., Bertoni, R., Trzop, E., Laulhé, C., Lorenc, M., Servol, M., Cailleau, H., Tissot, A. and Boillot, M.L., **2012**. Ultrafast spin-state photoswitching in a crystal and slower consecutive processes investigated by femtosecond optical spectroscopy and picosecond X-ray diffraction. *Physical Chemistry Chemical Physics, 14*(18), pp.6192-6199.

Consani, C., Prémont-Schwarz, M., ElNahhas, A., Bressler, C., van Mourik, F., Cannizzo, A. and Chergui, M., **2009**. Vibrational Coherences and Relaxation in the High-Spin State of Aqueous [FeII (bpy) 3] 2+. *Angewandte Chemie International Edition*, *48*(39), pp.7184-7187.

Costa, J.S., Balde, C., Carbonera, C., Denux, D., Wattiaux, A., Desplanches, C., Ader, J.P., Gütlich, P. and Létard, J.F., **2007**. Photomagnetic properties of an iron (II) low-spin complex with an unusually long-lived metastable LIESST state. *Inorganic chemistry*, *46*(10), pp.4114-4119.

D

de Graaf, C. and Sousa, C., **2010**. Study of the Light-Induced Spin Crossover Process of the [FeII (bpy) 3] 2+ Complex. *Chemistry-A European Journal*, *16*(15), pp.4550-4556.

Decurtins, S., Gütlich, P., Köhler, C.P., Spiering, H. and Hauser, A., **1984**. Light-induced excited spin state trapping in a transition-metal complex: The hexa-1-propyltetrazole-iron (II) tetrafluoroborate spin-crossover system. *Chemical physics letters*, *105*(1), pp.1-4.

Decurtins, S., Gutlich, P., Hasselbach, K.M., Hauser, A. and Spiering, H., **1985**. Light-induced excited-spin-state trapping in iron (II) spin-crossover systems. Optical spectroscopic and magnetic susceptibility study. *Inorganic Chemistry*, *24*(14), pp.2174-2178.

Dia, N., **2013**. Nanoparticules photomagnétiques et agents de contraste à base de réseaux de coordination (Doctoral dissertation, Paris 11).

E, F

Elder, F.R., Langmuir, R.V. and Pollock, H.C., **1948**. Radiation from electrons accelerated in a synchrotron. *Physical Review*, *74*(1), p.52.

Emma, P., Akre, R., Arthur, J., Bionta, R., Bostedt, C., Bozek, J., Brachmann, A., Bucksbaum, P., Coffee, R., Decker, F.J… and Galayda, J., **2010**. First lasing and operation of an ångstrom-wavelength free-electron laser. *Nature photonics*, *4*(9), pp.641-647.

Escax, V., Bleuzen, A., Cartier dit Moulin, C., Villain, F., Goujon, A., Varret, F. and Verdaguer, M., **2001**. Photoinduced Ferrimagnetic Systems in Prussian Blue Analogues CI x Co4 [Fe (CN) 6] y (CI= Alkali Cation). 3. Control of the Photo-and Thermally Induced Electron Transfer by the [Fe (CN) 6] Vacancies in Cesium Derivatives. *Journal of the American Chemical Society*, *123*(50), pp.12536-12543.

Field, R., Liu, L.C., Gawelda, W., Lu, C. and Miller, R.J., **2016**. Spectral signatures of ultrafast spin crossover in single crystal [FeII (bpy) 3](PF6) 2. *Chemistry-A European Journal*, *22*(15), pp.5118-5122.

Fritz, D.M., Reis, D.A., Adams, B., Akre, R.A., Arthur, J., Blome, C., Bucksbaum, P.H., Cavalieri, A.L., Engemann, S., Fahy, S. and Falcone, R.W., **2007**. Ultrafast bond softening in bismuth: Mapping a solid's interatomic potential with X-rays. *Science*, *315*(5812), pp.633-636.

G

Galloway, C.M., Ru, E.L. and Etchegoin, P.G., **2009**. An iterative algorithm for background removal in spectroscopy by wavelet transforms. *Applied spectroscopy*, *63*(12), pp.1370-1376.

Gawelda, W., Cannizzo, A., Pham, V.T., van Mourik, F., Bressler, C. and Chergui, M., **2007**. Ultrafast nonadiabatic dynamics of [FeII (bpy) 3] 2+ in solution. *Journal of the American Chemical Society*, *129*(26), pp.8199-8206.

Gawelda, W., Pham, V.T., Benfatto, M., Zaushitsyn, Y., Kaiser, M., Grolimund, D., Johnson, S.L., Abela, R., Hauser, A., Bressler, C. and Chergui, M., 2007. Structural determination of a short-live excited iron (II) complex by picosecond x-ray absorption spectroscopy. Physical review letters, 98(5), p.057401.

Gao, M., Lu, C., Jean-Ruel, H., Liu, L.C., Marx, A., Onda, K., Koshihara, S.Y., Nakano, Y., Shao, X., Hiramatsu, T… and Miller, R. J. D, **2013**. Mapping molecular motions leading to charge delocalization with ultrabright electrons. *Nature*, *496*(7445), pp.343-346.

Guérin, L., Collet, E., Lemée-Cailleau, M.H., Buron-Le Cointe, M., Cailleau, H., Plech, A., Wulff, M., Koshihara, S.Y. and Luty, T., **2004**. Probing photoinduced phase transition in a charge-transfer molecular crystal by 100 picosecond X-ray diffraction. *Chemical physics*, *299*(2), pp.163-170.

Grunwaldt, J.D. and Baiker, A., **2005**. In situ spectroscopic investigation of heterogeneous catalysts and reaction media at high pressure. *Physical Chemistry Chemical Physics*, *7*(20), pp.3526-3539.

Gudyma, I., Ivashko, V. and Bobák, A., **2017**. Surface and size effects in spin-crossover nanocrystals. *Nanoscale research letters*, *12*(1), p.101.

Gütlich, P., Hauser, A. and Spiering, H., **1994**. Thermal and optical switching of iron (II) complexes. *Angewandte Chemie International Edition*, 33(20), pp.2024-2054.

Gütlich, P., Goodwin H.A, **2004**. "Topics in Current Chemistry, Spin crossover in Transition Metal Compounds, Vol I», Springer Berlin, 234.

Gütlich, P., Goodwin H.A, **2004**. "Topics in Current Chemistry, Spin crossover in Transition Metal Compounds, Vol II», Springer Berlin, 234.

Gütlich, P., Goodwin H.A, **2004**. "Topics in Current Chemistry, Spin crossover in Transition Metal Compounds, Vol III», Springer Berlin, 234.

H

Halcrow, M.A. ed., **2013**. *Spin-crossover materials: properties and applications.* John Wiley & Sons.

Hauser, A., **2004**. Light-induced spin crossover and the high-spin→ low-spin relaxation. In *Spin Crossover in Transition Metal Compounds II* (pp. 155-198). Springer Berlin Heidelberg.

Herrera, J.M., Bachschmidt, A., Villain, F., Bleuzen, A., Marvaud, V., Wernsdorfer, W. and Verdaguer, M., **2008**. Mixed valency and magnetism in cyanometallates and Prussian blue analogues. *Philosophical Transactions of the Royal Society of London A: Mathematical, Physical and Engineering Sciences, 366(1862)*, pp.127-138.

Huse, N., Cho, H., Hong, K., Jamula, L., De Groot, F.M., Kim, T.K., McCusker, J.K. and Schoenlein, R.W., **2011**. Femtosecond soft X-ray spectroscopy of solvated transition-metal complexes:

deciphering the interplay of electronic and structural dynamics. *The journal of physical chemistry letters*, *2*(8), pp.880-884.

I

Iasco, O., Rivière, E., Guillot, R., Buron-Le Cointe, M., Meunier, J.F., Bousseksou, A. and Boillot, M.L., **2015**. FeII (pap-5NO2) 2 and FeII (qsal-5NO2) 2 Schiff-Base Spin-Crossover Complexes: A Rare Example with Photomagnetism and Room-Temperature Bistability. *Inorganic chemistry*, *54*(4), pp.1791-1799.

Ihee, H., Lorenc, M., Kim, T.K., Kong, Q.Y., Cammarata, M., Lee, J.H., Bratos, S. and Wulff, M., **2005**. Ultrafast X-ray diffraction of transient molecular structures in solution. *Science*, *309*(5738), pp.1223-1227.

Ishikawa, T., Aoyagi, H., Asaka, T., Asano, Y., Azumi, N., Bizen, T., Ego, H., Fukami, K., Fukui, T., Furukawa, Y… and Kumagai, N., **2012**. A compact X-ray free-electron laser emitting in the sub-angstrom region. *Nature Photonics*, *6*(8), pp.540-544.

Iwamura, M., Watanabe, H., Ishii, K., Takeuchi, S. and Tahara, T., **2011**. Coherent nuclear dynamics in ultrafast photoinduced structural change of bis (diimine) copper (I) complex. *Journal of the American Chemical Society*, *133*(20), pp.7728-7736.

J

Juban, E.A. and McCusker, J.K., **2005**. Ultrafast dynamics of 2E state formation in Cr (acac) 3. *Journal of the American Chemical Society*, *127*(18), pp.6857-6865.

Johansson, J.O., Kim, J.W., Allwright, E., Rogers, D.M., Robertson, N. and Bigot, J.Y., **2016**. Directly probing spin dynamics in a molecular magnet with femtosecond time-resolution. *Chemical Science*, *7*(12), pp.7061-7067.

Johnson, S.L., Beaud, P., Möhr-Vorobeva, E., Caviezel, A., Ingold, G. and Milne, C.J., **2013**. Direct observation of non-fully-symmetric coherent optical phonons by femtosecond x-ray diffraction. *Physical Review B, 87*(5), p.054301.

K

Kahn, O., 1993. Molecular magnetism. *VCH Publishers, Inc.(USA)*, p.393.

Kieffer, J. and Karkoulis, D., **2013**. PyFAI, a versatile library for azimuthal regrouping. In *Journal of physics: conference series* (Vol. 425, No. 20, p. 202012). IOP Publishing.

Kingsbury, N.G., **1998**, August. The dual-tree complex wavelet transform: a new technique for shift invariance and directional filters. In *Proc. 8th IEEE DSP workshop* (Vol. 8, p. 86). Utah.

Koenig, E. and Madeja, K., **1967**. 5T2-1A1 Equilibriums in some iron (II)-bis (1, 10-phenanthroline) complexes. *Inorganic Chemistry*, *6*(1), pp.48-55.

Kondratenko, A.M. and Saldin, E.L., **1980**. Generating of coherent radiation by a relativistic electron beam in an ondulator. *Part. Accel.*, *10*, pp.207-216.

Kong, Q., Lee, J.H., Lo Russo, M., Kim, T.K., Lorenc, M., Cammarata, M., Bratos, S., Buslaps, T., Honkimaki, V., Ihee, H. and Wulff, M., **2010**. Photolysis of Br2 in CCl4 studied by time-resolved X-ray scattering. *Acta Crystallographica Section A: Foundations of Crystallography*, *66*(2), pp.252-260.

Koshihara, S.Y., Takahashi, Y., Sakai, H., Tokura, Y. and Luty, T., **1999**. Photoinduced cooperative charge transfer in low-dimensional organic crystals. *J. Phys. Chem. B, 1999, 103 (14),* pp 2592–2600.

Koumousi, E.S., Jeon, I.R., Gao, Q., Dechambenoit, P., Woodruff, D.N., Merzeau, P., Buisson, L., Jia, X., Li, D., Volatron, F., Mathonière, C and Clérac, R., **2014**. Metal-to-metal electron transfer in Co/Fe Prussian blue molecular analogues: the ultimate miniaturization. *Journal of the American Chemical Society*, *136*(44), pp.15461-15464.

L

Lemke, H.T., Bressler, C., Chen, L.X., Fritz, D.M., Gaffney, K.J., Galler, A., Gawelda, W., Haldrup, K., Hartsock, R.W., Ihee, H… and Cammarata, M., J., **2013**. Femtosecond X-ray absorption spectroscopy at a hard X-ray free electron laser: application to spin crossover dynamics. *The Journal of Physical Chemistry A*, *117*(4), pp.735-740.

Lemke, H.T., Kjær, K.S., Hartsock, R., van Driel, T.B., Chollet, M., Glownia, J.M., Song, S., Zhu, D., Pace, E., Matar, S.F… and Cammarata, M., **2017**. Coherent structural trapping through wave packet dispersion during photoinduced spin state switching. *Nature communications*, *8*, p.15342.

Lescouëzec, R., Vaissermann, J., Ruiz-Pérez, C., Lloret, F., Carrasco, R., Julve, M., Verdaguer, M., Dromzee, Y., Gatteschi, D. and Wernsdorfer, W., **2003**. Cyanide-bridged iron (III)–cobalt (II) double zigzag ferromagnetic chains: two new molecular magnetic nanowires. *Angewandte Chemie International Edition*, *42*(13), pp.1483-1486.

Létard, J.F., **2006**. Photomagnetism of iron (II) spin crossover complexes—the T (LIESST) approach. *Journal of Materials Chemistry*, *16*(26), pp.2550-2559.

Llopart, X., Campbell, M., San Segundo, D., Pernigotti, E. and Dinapoli, R., **2001**, November. Medipix2, a 64k pixel read out chip with 55/spl mu/m square elements working in single photon counting mode. In *Nuclear Science Symposium Conference Record, 2001 IEEE* (Vol. 3, pp. 1484-1488). IEEE.

Li, D., Clérac, R., Roubeau, O., Harté, E., Mathoniere, C., Le Bris, R. and Holmes, S.M., **2008**. Magnetic and optical bistability driven by thermally and photoinduced intramolecular electron transfer in a molecular cobalt− iron Prussian blue analogue. *Journal of the American Chemical Society*, *130*(1), pp.252-258.

Lorenc, M., Balde, C., Kaszub, W., Tissot, A., Moisan, N., Servol, M., Buron-Le Cointe, M., Cailleau, H., Chasle, P., Czarnecki, P. and Boillot, M.L., **2012**. Cascading photoinduced, elastic, and thermal switching of spin states triggered by a femtosecond laser pulse in an Fe (III) molecular crystal. *Physical Review B*, *85*(5), p.054302.

Lorenc, M., Hébert, J., Moisan, N., Trzop, E., Servol, M., Buron-Le Cointe, M., Cailleau, H., Boillot, M.L., Pontecorvo, E., Wulff, M., Koshihara, S. and Collet, E., **2009**. Successive dynamical steps of photoinduced switching of a molecular Fe (III) spin-crossover material by time-resolved X-ray diffraction. *Physical review letters*, *103*(2), p.028301.

Lorenc, M., Ziolek, M., Naskrecki, R., Karolczak, J., Kubicki, J. and Maciejewski, A., **2002**. Artifacts in femtosecond transient absorption spectroscopy. *Applied Physics B: Lasers and Optics*, *74*(1), pp.19-27.

M

Mariette, C., Trzop, E., Zerdane, S., Fertey, P., Zhang, D., Valverde-Muñoz, F., Real, J.A. and Collet, E., **2017**. Formation of local spin-state concentration waves during the relaxation from photoinduced state in a spin-crossover polymer. *Acta crystallographica Section B: Structural crystallography and crystal chemistry*. *B73,*660-668

Marino, A., Cammarata, M., Matar, S.F., Létard, J.F., Chastanet, G., Chollet, M., Glownia, J.M., Lemke, H.T. and Collet, E., **2016**. Activation of coherent lattice phonon following ultrafast molecular spin-state photo-switching: A molecule-to-lattice energy transfer. *Structural Dynamics*, *3*(2), p.023605.

Marino, A., Chakraborty, P., Servol, M., Lorenc, M., Collet, E. and Hauser, A., **2014**. The Role of Ligand-Field States in the Ultrafast Photophysical Cycle of the Prototypical Iron (II) Spin-Crossover Compound [Fe (ptz) 6](BF4) 2. *Angewandte Chemie International Edition*, *53*(15), pp.3863-3867.

Martin, R.L., **2003**. Natural transition orbitals. *The Journal of chemical physics*, *118*(11), pp.4775-4777.

Marrey, E.J., **1882**. Le fusil photographique, *La Nature*, Vol I, No464, 326.

McCusker, J.K., Walda, K.N., Dunn, R.C., Simon, J.D., Magde, D. and Hendrickson, D.N., **1992**. Sub-picosecond. Delta. S= 2 intersystem crossing in low-spin ferrous complexes. *Journal of the American Chemical Society*, *114*(17), pp.6919-6920.

McMillan, E.M., **1945**. The synchrotron—a proposed high energy particle accelerator. *Physical Review*, *68*(5-6), p.143.

McGravey, J.J. and Lawthers, I., **1982**. Photochemically-induced perturbation of the 1 A⇌ 5 T equilibrium in Fe 11 complexes by pulsed laser irradiation in the metal-to-ligand charge-transfer absorption band. *Journal of the Chemical Society, Chemical Communications*, (16), pp.906-907.

Mercurol, J., Li, Y., Pardo, E., Risset, O., Seuleiman, M., Rousselière, H., Lescouëzec, R. and Julve, M., **2010**. [FeIILSCoIIILS] 2⇔[FeIIILSCoIIHS] 2 photoinduced conversion in a cyanide-bridged heterobimetallic molecular square. *Chemical Communications*, *46*(47), pp.8995-8997.

Miyamoto, Y., Nasu, T., Ozaki, N., Umeta, Y., Tokoro, H., Nakabayashi, K. and Ohkoshi, S., **2016**. Photo-induced magnetization and first-principles calculations of a two-dimensional cyanide-bridged Co–W bimetal assembly. *Dalton Transactions*, *45*(48), pp.19249-19256.

Mokharti, A., Cong, P., Herek, J.L. and Zewail, A.H., **1990**. Direct femtosecond mapping of trajectories in a chemical reaction. *Nature*, 348(6298), p.225.

Moritomo, Y., Nakagawa, T., Fukuyama, Y., Yasuda, N., Oosawa, H., Kim, J.E., Kamioka, H., Kato, K., Tanaka, Y., Kimura, S… and Takata, M., **2009**. Photoinduced dynamics of prussian blue type cyanide. In *Journal of Physics: Conference Series* (Vol. 148, No. 1, p. 012028). IOP Publishing.

Muybridge, E., **1879**. Photographie instantanée des animaux en mouvement, *La Nature*, Vol I, 246.

N

Nasu, K., **1997**. Multistabilities of the Ground States, Proliferations of excitons and photo-induced structural phase transitions. In Relaxations of Excited States and Photo-Induced Structural Phase Transitions (pp. 3-16). Springer, Berlin, Heidelberg.

Nelson, S.M., McIlroy, P.D., Stevenson, C.S., König, E., Ritter, G. and Waigel, J., **1986**. Quadridentate versus quinquedentate co-ordination of some N 5 and N 3 O 2 macrocyclic ligands and an unusual thermally controlled quintet⇌ singlet spin transition in an iron (II) complex. *Journal of the Chemical Society, Dalton Transactions*, (5), pp.991-995.

Nihei, M., Sekine, Y., Suganami, N., Nakazawa, K., Nakao, A., Nakao, H., Murakami, Y. and Oshio, H., 2011. Controlled intramolecular electron transfers in cyanide-bridged molecular squares bychemical modifications and external stimuli. Journal of the American Chemical Society, 133(10), pp.3592-3600.

O

Ohkoshi, S.I., Einaga, Y., Fujishima, A. and Hashimoto, K., **1999**. Magnetic properties and optical control of electrochemically prepared iron–chromium polycyanides. *Journal of Electroanalytical Chemistry*, *473*(1), pp.245-249.

Ohkoshi, S.I. and Hashimoto, K., **2001**. Photo-magnetic and magneto-optical effects of functionalized metal polycyanides. *Journal of Photochemistry and Photobiology C: Photochemistry Reviews*, 2(1), pp.71-88.

Ohkoshi, S.I. and Tokoro, H., **2012**. Photomagnetism in cyano-bridged bimetal assemblies. *Accounts of chemical research*, *45*(10), pp.1749-1758.

P, Q, R

Ponchut, C., Rigal, J.M., Clément, J., Papillon, E., Homs, A. and Petitdemange, S., **2011**. MAXIPIX, a fast readout photon-counting X-ray area detector for synchrotron applications. *Journal of Instrumentation*, *6*(01), p.C01069.

René de Cotret, L.P. and Siwick, B.J., **2017**. A general method for baseline-removal in ultrafast electron powder diffraction data using the dual-tree complex wavelet transform. *Structural Dynamics*, *4*(4), p.044004.

Robin, M.B., **1962**. The color and electronic configurations of Prussian blue. *Inorganic Chemistry*, *1*(2), pp.337-342.

S

Sato, O., Iyoda, T., Fujishima, A. and Hashimoto, K., **1996**. Photoinduced magnetization of a cobalt-iron cyanide. *Science*, *272*(5262), p.704.

Sato, O., Einaga, Y., Fujishima, A. and Hashimoto, K., **1999**. Photoinduced long-range magnetic ordering of a cobalt− iron cyanide. *Inorganic chemistry*, *38*(20), pp.4405-4412.

Sato, O., **2003**. Optically switchable molecular solids: photoinduced spin-crossover, photochromism, and photoinduced magnetization. *Accounts of chemical research*, *36*(9), pp.692-700.

Sato, O., Tao, J. and Zhang, Y.Z., **2007**. Control of magnetic properties through external stimuli. *Angewandte Chemie International Edition*, *46*(13), pp.2152-2187.

Strickland, D. and Mourou, G., **1985**. Compression of amplified chirped optical pulses. *Optics communications*, *55*(6), pp.447-449.

Sokolowski-Tinten, K., Blome, C., Blums, J., Cavalleri, A., Dietrich, C., Tarasevitch, A., Uschmann, I., Förster, E., Kammler, M., Horn-von-Hoegen, M. and von der Linde, D., **2003**. Femtosecond X-ray measurement of coherent lattice vibrations near the Lindemann stability limit. *Nature*, 422(6929), pp.287-289.

Sousa, C., de Graaf, C., Rudavskyi, A., Broer, R., Tatchen, J., Etinski, M. and Marian, C.M., **2013**. Ultrafast Deactivation Mechanism of the Excited Singlet in the Light-Induced Spin Crossover of [Fe (2, 2′-bipyridine) 3] 2+. *Chemistry-A European Journal*, *19*(51), pp.17541-17551.

T, U

Tissot, A., Bertoni, R., Collet, E., Toupet, L. and Boillot, M.L., **2011**. The cooperative spin-state transition of an iron (III) compound [Fe III (3-MeO-SalEen) 2] PF 6: thermal-vs. ultra-fast photo-switching. *Journal of Materials Chemistry*, *21*(45), pp.18347-18353.

Tokoro, H., Matsuda, T., Nuida, T., Moritomo, Y., Ohoyama, K., Dangui, E.D.L., Boukheddaden, K. and Ohkoshi, S.I., **2007**. Visible-light-induced reversible photomagnetism in rubidium manganese hexacyanoferrate. *Chemistry of Materials*, *20*(2), pp.423-428.

Tokoro, H. and Ohkoshi, S.I., **2014**. Multifunctional Material: Bistable Metal–Cyanide Polymer of Rubidium Manganese Hexacyanoferrate. *Bulletin of the Chemical Society of Japan*, *88*(2), pp.227-239.

Ullrich, J., Rudenko, A. and Moshammer, R., **2012**. Free-electron lasers: new avenues in molecular physics and photochemistry. *Annual review of physical chemistry*, *63*, pp.635-660.

V, W, X

Van Kuiken, B.E., Cho, H., Hong, K., Khalil, M., Schoenlein, R.W., Kim, T.K. and Huse, N., **2016**. Time-resolved X-ray spectroscopy in the water window: Elucidating transient valence charge distributions in an aqueous Fe (II) complex. *The journal of physical chemistry letters*, *7*(3), pp.465-470.

Van Veenendaal, M., Chang, J. and Fedro, A.J., **2010**. Model of ultrafast intersystem crossing in photoexcited transition-metal organic compounds. *Physical review letters*, *104*(6), p.067401.

Veksler, V.I., **1944**. DAN (USSR) 44 (1944) 393 und Proc. In *USSR Acad. Sci*(Vol. 43, p. 346).

Verdaguer, M., Bleuzen, A., Marvaud, V., Vaissermann, J., Seuleiman, M., Desplanches, C., Scuiller, A., Train, C., Garde, R., Gelly, G., Lomenech, C. and Villain. F., **1999**. Molecules to build solids: high T C molecule-based magnets by design and recent revival of cyano complexes chemistry. *Coordination Chemistry Reviews*, *190*, pp.1023-1047.

Weidinger, D., Brown, D.J. and Owrutsky, J.C., **2011**. Transient absorption studies of vibrational relaxation and photophysics of Prussian blue and ruthenium purple nanoparticles. *The Journal of chemical physics*, *134*(12), p.124510.

Wolf, M.M., Groß, R., Schumann, C., Wolny, J.A., Schünemann, V., Døssing, A., Paulsen, H., McGarvey, J.J. and Diller, R., **2008**. Sub-picosecond time resolved infrared spectroscopy of high-spin state formation in Fe (II) spin crossover complexes. *Physical Chemistry Chemical Physics*, *10*(29), pp.4264-4273.

Wullf, M., Plech, A., Eybert, L., Randler, R., Schotte, F. and Anfinrud, P., **2003**. The realization of sub-nanosecond pump and probe experiments at the ESRF. European Synchrotron Radiation Facility. *Faraday discussions*, *122*, pp.13-26.

Y, Z

Yokoyama, T., Murakami, Y., Kiguchi, M., Komatsu, T. and Kojima, N., **1998**. Spin-crossover phase transition of a chain Fe (II) complex studied by X-ray-absorption fine-structure spectroscopy. *Physical Review B*, *58*(21), p.14238.

Yoshizawa, K., Mohri, F., Nuspl, G. and Yamabe, T., **1998**. Analysis of photoinduced magnetization in a (Co, Fe) prussian blue model. *The Journal of Physical Chemistry B*, *102*(28), pp.5432-5437.

Zerdane, S., Wilbraham, L., Cammarata, M., Iasco, O., Rivière, E., Boillot, M.L., Ciofini, I. and Collet, E., **2017**. Comparison of structural dynamics and coherence of d–d and MLCT light-induced spin state trapping. *Chem. Sci., 8,* 4978-4986

Zerdane, S., Cammarata, M., Balducci, L., Bertoni, R., Catala, L., Mazerat, S., Mallah, T., Pedersen, M.N., Wulff, M., Nakagawa, K., Tokoro, H., Ohkoshi, S., **2017**. Probing transient photoinduced charge-transfer in Prussian Blue Analogues with time-resolved XANES and optical spectroscopy. *European Journal of Inorganic Chemistry, 00657*

Zhang, Y., Li, D., Clérac, R., Kalisz, M., Mathonière, C. and Holmes, S.M., **2010**. Reversible Thermally and Photoinduced Electron Transfer in a Cyano-Bridged {Fe2Co2} Square Complex. *Angewandte Chemie*, *122*(22), pp.3840-3844.

Zewail, A., **1988**. Laser femtochemistry. *Science*, 242(4886), pp.1645-1653.

Zewail, A.H., **2000**. Femtochemistry: Atomic-scale dynamics of the chemical bond using ultrafast lasers (Nobel Lecture). *Angewandte Chemie International Edition*, 39(15), pp.2586-2631.

Zhang, W., Alonso-Mori, R., Bergmann, U., Bressler, C., Chollet, M., Galler, A., Gawelda, W., Hadt, R.G., Hartsock, R.W., Kroll, T. and Kjær, K.S., **2014**. Tracking excited-state charge and spin dynamics in iron coordination complexes. *Nature*, *509*(7500), pp.345-348.

Annex I

List of Abbreviations

CT	Charge Transfer
CPA	Chirped Pulse Amplification
CTIST	Charge Transfer Induce Spin Transition
CW	Continuous Wave
DFT	Density-Functional Theory
EXAFS	Extended X-Ray Absorption Fine Structure
FWHM	Full Width Half Maximum
IR	Infrared
IRF	Instrumental Response Function
INT	Intermediate state
ISC	Intersystem Crossing
LIESST	Light Induced Exited Spin State Trapping
LMCT	Ligand-Metal Charge Transfer
LS	Low Spin
HS	High Spin
MLCT	Metal-Ligand Charge Transfer
NIR	Near Infrared
STICT	Spin Transition Induced Charge Transfer
SCO	Spin Crossover
TD-DFT	Time-Dependent Density-Functional Theory
VIS	Visible
XAS	X-ray Absorption Spectroscopy
XANES	X-ray Absorption at Near Edge Spectroscopy
X-FEL	X-ray Free Electron Laser

Annex II

List of Publications

Zerdane, S., Wilbraham, L., Cammarata, M., Iasco, O., Rivière, E., Boillot, M.L., Ciofini, I. and Collet, E., Comparison of structural dynamics and coherence of d–d and MLCT light-induced spin state trapping. *Chem. Sci.*, **2017**, 8, 4978-4986

Zerdane, S., Cammarata, M., Balducci, L., Bertoni, R., Catala, L., Mazerat, S., Mallah, T., Pedersen, M.N., Wulff, M., Nakagawa, K. and Tokoro, H., 2017. Probing transient photoinduced charge-transfer in Prussian Blue Analogues with time-resolved XANES and optical spectroscopy. *Eur. J. Inorg. Chem.*. **2017**, doi:10.1002/ejic.201700657

Zerdane, S., Collet, E., Dong, X., Matar, S.F., Wang, H.F., Desplanches, C., Chastanet, G., Chollet, M., Glownia, J.M., Lemke, H.T. and Lorenc, M., 2017. Electronic and structural dynamics during the switching of the photomagnetic complex $[Fe(L_{222}N_5)(CN)_2]$. *Chem. Eur. J.* **2017**, doi:10.1002/chem.201704746

Mariette, C., Trzop, E., **Zerdane, S**., Fertey, P., Zhang, D., Valverde-Muñoz, F., Real, J.A. and Collet, E., **2017**. Formation of local spin-state concentration waves during the relaxation from photoinduced state in a spin-crossover polymer. *Acta Cryst.* **2017**, B73, 660-668

Chemical Science

EDGE ARTICLE

View Article Online
View Journal | View Issue

Cite this: *Chem. Sci.*, 2017, **8**, 4978

Comparison of structural dynamics and coherence of d–d and MLCT light-induced spin state trapping†

S. Zerdane,[a] L. Wilbraham,[b] M. Cammarata,*[a] O. Iasco,[c] E. Rivière,[c] M.-L. Boillot,[c] I. Ciofini[b] and E. Collet*[a]

Received 22nd December 2016
Accepted 19th April 2017

DOI: 10.1039/c6sc05624e

rsc.li/chemical-science

Light-induced excited spin state trapping (LIESST) in Fe^{II} spin-crossover systems is a process that involves the switching of molecules from low (LS, $S = 0$) to high spin (HS, $S = 2$) states. The direct LS-to-HS conversion is forbidden by selection rules, and LIESST involves intermediate states such as ^{1,3}MLCT or ^{1,3}T. The intersystem crossing sequence results in an HS state, structurally trapped by metal–ligand bond elongation through the coherent activation and damping of molecular breathing. The ultrafast dynamics of this process has been investigated in FeN_6 ligand field systems, under MLCT excitation. Herein, we studied LIESST in an $Fe^{II}N_4O_2$ spin-crossover material of lower symmetry, which allowed for quite intense and low-energy shifted d–d bands. By combining *ab initio* DFT and TD-DFT calculations and fs optical absorption measurements, we demonstrated that shorter intermediates enhanced coherent structural dynamics, and d–d excitation induced faster LS-to-HS switching, compared to MLCT.

Introduction

The development of photochemistry and photophysics of coordination compounds requires a good understanding the role of intermediate excited states.[1] Light-induced excited spin state trapping (LIESST) is a process that is able to switch molecules between different spin states, and is the focus of intensive development directed towards photomagnetism in spin-crossover materials.[2–6] Photophysics was deeply investigated in systems based on iron, ruthenium, cobalt, copper, chromium or manganese.[7–11] LIESST has been intensely studied in $Fe^{II}N_6$ spin-crossover materials in which the Fe ion experiences an almost octahedral ligand-field. At low temperature, the ground state is low spin $^1A_1$ (LS, $S = 0$, $t_{2g}^6e_g^0L^0$), where L refers to unoccupied ligand orbitals. At high temperatures the high spin state $^5T_2$ (HS, $S = 2$, $t_{2g}^4e_g^2L^0$) with a higher entropy is favoured. The photoinduced states are long-lived at low temperature, and Hauser observed that LIESST and reverse-LIESST could be induced by weak continuous laser excitation.[12–14] Photochromism in crystals associated with conversion between LS and HS states can be directly observed by optical spectroscopy.[15] LIESST could also induce HS states with structures different from those at thermal equilibrium.[16] LIESST and reverse-LIESST were transiently generated in solids at high temperatures[17,18] and observed by pump-probe techniques, including optical and X-ray spectroscopies and X-ray or electron diffraction.[19–25] The ultrafast molecular expansion during LIESST also drove cooperative, elastic transformations in crystals. It has been shown that more than 7 molecules can undergo switching per photon absorbed.[26,27] Understanding and controlling LIESST is of great interest and the reason why its basic mechanism has been rigorously investigated for several LS molecules in solution.[28–36]

Recent studies of the LIESST mechanism in Fe^{II} systems upon metal–ligand charge transfer (MLCT) excitation were performed with 30–100 femtosecond time resolution. They revealed key features of the intersystem crossing, mainly in terms of the change in electronic states, as summarized in Fig. 1(a).[5,22,23,37–39] The MLCT → HS conversion occurred through MLCT → ^{3}T and ^{3}T → HS conversions of about 120 and 70 fs, respectively. Theoretical electronic-structure calculations used time-dependent approaches to provide intersystem-crossing rates in agreement with these experimental reports.[40] The HS state was structurally trapped in the HS potential through expansion of the FeN_6 core. The electronic population of anti-bonding e_g orbitals moved the equilibrium molecular structure to longer Fe–L bonds within ~170 fs. A theoretical study explained how this electron-phonon coupling activated the breathing of the Fe–L bonds,[41] observed by different techniques sensitive to the change of the ligand field such as XANES[34,38] or optical spectroscopy.[22,38] However, the resulting coherent structural dynamics accompanying LIESST is still poorly described in the literature.

[a]*Univ Rennes 1, CNRS, Institut de Physique de Rennes, UMR 6251, UBL, F-35042 Rennes, France. E-mail: marco.cammarata@univ-rennes1.fr; eric.collet@univ-rennes1.fr*

[b]*Institut de Recherche de Chimie Paris, PSL Research University, CNRS, Chimie ParisTech, 11 Rue Pierre et Marie Curie, F-75005 Paris, France*

[c]*Univ Paris Sud, Université Paris-Saclay, CNRS, Institut de Chimie Moléculaire et des Matériaux d'Orsay, UMR 8182, Orsay, France*

† Electronic supplementary information (ESI) available. See DOI: 10.1039/c6sc05624e

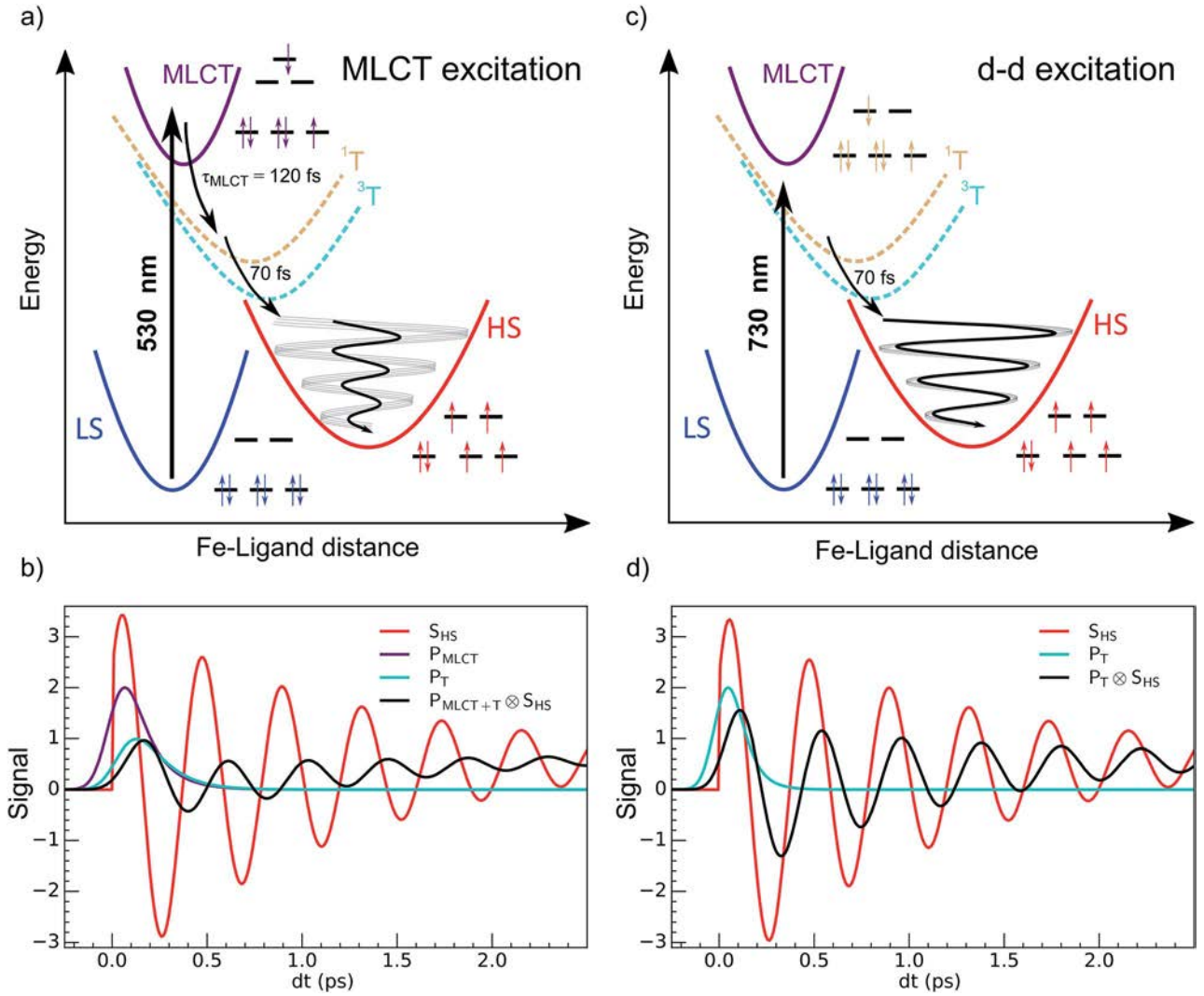

Fig. 1 Schematic process of LIESST. (a) For MLCT excitation, the electronic decays towards less bonding ^{3}T and HS states increased the equilibrium Fe–ligand distance and launched coherent Fe–L breathing. (b) The weak oscillation of an arbitrary schematic signal (black) due to a change in the Fe–L bond length for MLCT excitation was due to decoherence during the relatively long MLCT-to-HS conversion (populations $P_{MLCT}(t)$, purple and $P_T(t)$, cyan), compared to the oscillating signal of a single molecule in the HS potential (S_{HS}, red). (c) d–d excitation process with fast ^{3}T-to-HS conversion. (d) The faster ^{3}T decay (population $P_T(t)$, cyan) towards the HS state maintained a significant average structural coherence in the HS potential (black). The exponential growth of the HS population from the MLCT (population $P_{MLCT}(t)$), or from the ^{3}T intermediate state, led to average coherent oscillating trajectories $S_{HS}(t) \otimes P_{MLCT+T}(t)$ or $S_{HS}(t) \otimes P_T(t)$ with a reduced amplitude and apparent phase shift compared to the single trajectory in the HS state $S_{HS}(t)$.

It corresponds to the activation and damping, in the HS potential[17,18,23] of the average Fe–L distance, which is the main structural reaction coordinate elongating from ~2.0 (LS) to ~2.2 Å (HS). Because of the relatively long MLCT and ^{3}T decays, the HS population occurred on a timescale approaching the half-period of the molecular breathing,[17,18,22,23] inducing important structural dephasing. Consequently, compared to a change in signal related to Fe–L elongation like XANES, the amplitude of the signal oscillations was reduced, as illustrated in Fig. 1(b).[38] The fast damping of the molecular breathing (~300 fs) was due to dissipation of energy towards other modes such as ligand bending also observed by optical spectroscopy, whereas the vibrational cooling of these photoinduced states typically occurred within 2 ps. The direct photoswitching from $S = 0$ to $S = 2$ was impossible, and the process required electronic intermediates such as ^{1,3}MLCT and ^{1,3}T. In addition, because of the almost octahedral symmetry of FeN_6 systems, the d–d photoexcitation (from t_{2g} to e_g) was very weak or was prevented by much more efficient CT excitations. For this reason, LIESST was mainly investigated at femtosecond timescales with MLCT excitations ($t_{2g}^5 e_g^0 L^1$). Hauser used both MLCT and d–d excitation in distinct SCO materials to induce a transient HS state and measure HS → LS relaxation rate dynamics.[42] Juban and McCusker have shown in Cr-(acac)$_3$ that $^4A_2 \rightarrow {}^2$E conversion dynamics differed upon $^4T_2$ or ^{4}MLCT excitation.[8] Herein, we studied LIESST in the Fe^{II} spin-crossover material Fe(pap-5NO$_2$)$_2$, characterized by an FeN_4O_2 core (Fig. 2).[43] This ligand field, of lower symmetry than that of O_h, allowed quite intense

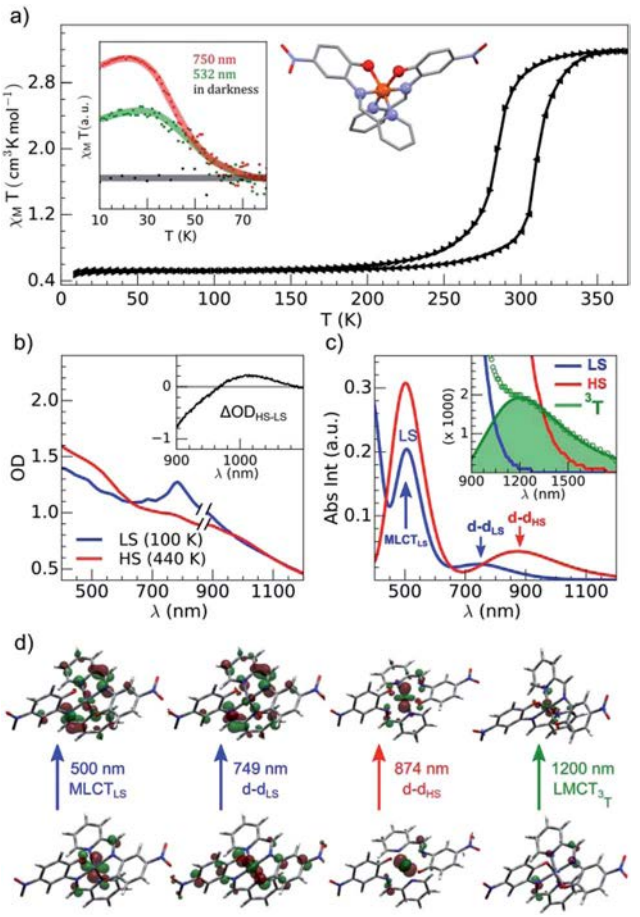

Fig. 2 (a) Temperature dependence of $\chi_M T$ determined with the sample of Fe(pap-$5NO_2$)$_2$: thermal cycle (black) and LIESST under photoexcitation at 532 and 750 nm (inset). (b) OD changed between LS and HS states determined with the compound embedded in a polyvinylpyrrolidone (PVP) film. (c) Calculated absorption spectra with main contributions to absorption bands characterized for a single complex for LS (blue), HS (red) and ^{3}T (green) states. (d) Characteristic orbitals of hole and particle for LS, HS and T states.

d–d bands, which we exploited for low-energy photo-excitation. We showed that d–d excitation, associated with shorter electronic intermediates compared to MLCT excitation, allowed a faster LS-to-HS switching and enhanced the coherence of structural dynamics in the HS potential.

Experimental

Synthetic procedures

In order to limit the presence of strong light-scattering objects (size ≥ 1 μm) for optical pump-probe studies, the Fe^{II}(pap-$5NO_2$)$_2$ samples were prepared by applying the method described in ref. 44 to the compound synthesis.[43] The preparation was achieved at −40 °C under inert atmosphere with the Schlenk technique and in presence of PVP ($(C_6H_9NO)_n$, average MW = 40 000 $gmol^{-1}$). A methanolic solution (14 mL, 1 g PVP) of $Fe^{II}(BF_4)_2$ (124.8 mg, 0.37 mmol) was added to a methanolic solution (26 mL, 1 g PVP) of Hpap-$5NO_2$ (180 mg, 0.74 mmol) previously deprotonated by Et_3N. After 10 min of stirring, the solution was filtered with a glass microfiber membrane (1 μm pore size), then the filtrate was centrifuged, and the powder of particles was dried under vacuum. Elemental analysis (%) calcd (found) for $C_{24}H_{16}O_6N_6Fe$ $(C_6H_9NO)_n(H_2O)_{3n}$ (n = 0.7): C, 51.64 (51.40); H, 4.07 (4.06); N, 14.31 (14.2)%. IR: 1667 and 1290 (PVP), 1584, *1452* (C=N and C=C), 1283, *1252* (phenolato group), 1167, *770*, *685* cm^{-1} (in italics, frequencies specific to LS species). The solid, containing traces of PVP 40000, was used without further treatment to avoid the formation of larger particles. For investigating the ultrafast LIESST dynamics, the sample was processed in the form of transparent films on glass substrates by spin-coating a dispersion of particles in *n*-butanol in the presence of PVP.[21]

Physical measurements

The brown green films of particles appeared to be homogeneous at the sub-millimeter scale. They were characterized by variable-temperature, UV-vis solid-state spectra on a CARY 5000 double-beam spectrophotometer equipped with the Eurolabo variable-temperature cell (21525, KBr windows) and Specac temperature controller (20120). The 100 and 440 K spectra in Fig. 2(b), show all the features previously reported for the high and low-spin phases in the bulk.[43] Magnetic measurements of the powdered sample characterized a spin transition with a thermal hysteresis centered at 297 K (width ΔT = 26 K, Fig. 2(a)) that were comparable to the bulk properties. From the low temperature $\chi_M T$ value, a fraction of paramagnetic residue was assigned to the presence of crystalline defects trapped in the HS state (x_{HS} ~0.15). The photomagnetic behavior derived from LIESST at 10 K was previously reported for the bulk with a 750 nm excitation. It was also observed by illuminating the sample (Fig. 2(a)) with a visible (532 nm, 20 mW cm^{-2}) and 750 nm (15 mW cm^{-2}) excitation (inset Fig. 2(a)). The thermal relaxations towards the LS ground state were completed around 60 K.

DFT and TD-DFT calculation

In order to better understand the structural, electronic and optical properties of Fe^{II}(pap-$5NO_2$)$_2$, calculations were conducted using the density functional theory (DFT) and time-dependent DFT (TD-DFT). A split-valence Pople basis set of double-zeta quality including polarisation and diffuse functions for non-hydrogen atoms (6-31+G(d))[45] was used throughout to describe H, C, N and O atoms, while the Los Alamos LANL2 [46] effective core potential and corresponding triple-zeta basis set was used to respectively describe the core and valence electrons of Fe^{II}. Geometry optimisations of single complexes of Fe(pap-$5NO_2$)$_2$ in vacuum were conducted using the M06-L[47] exchange-correlation functional for the different spin states of singlet (LS, S = 0), quintet (HS, S = 2) and Fe-centred ^{3}T (S = 1) spin triplet. Essentially, ^{3}T should be $^3\Gamma$ due to the C_2 molecular symmetry, but will be referred to as ^{3}T for comparison with FeN_6 systems. Harmonic vibrational frequencies were obtained both in order to calculate IR properties and to verify that the structures obtained were indeed true minima on the potential energy surface.

Electronic excitation energies were calculated using TD-DFT and the PBE0 [48] global hybrid exchange-correlation functional. These states were subsequently used to simulate UV-visible absorption spectra for both the LS, HS and ^{3}T forms of Fe(pap-5NO$_2$)$_2$ at their respective equilibrium geometries.

Using the resulting excitation energies and their calculated oscillator strengths, UV-vis absorption spectra were simulated by convoluting with Gaussian functions centred at the calculated wavelength for each transition. The full width at half-maximum value for the Gaussian functions was set to 0.45 eV.

Fig. 2(c) shows the vertical absorption spectra calculated for the LS, HS and ^{3}T electronic states. Concerning the LS equilibrium geometry, for which singlet-to-singlet excitation energies were determined, two main absorption bands were computed at 500 nm and 749 nm. From inspection of the highest-contributing molecular orbitals involved in these transitions (Fig. 2(d)), it can be seen that, despite contributions from both metal- and ligand-centred orbitals, the transition centred at 500 nm has an MLCT character and is hereafter labelled MLCT$_{LS}$. Similarly, the transition centred at 749 nm has a d–d character and will be referred to as d–d$_{LS}$. Notably, this transition exhibits a small, but non-zero, oscillator strength (0.018 au), emphasizing that the reduced symmetry of the coordination environment from O_h for usual FeN_6 systems to C_2 for this FeN_4O_2 system leads to d–d transitions that are no longer completely forbidden. The character assigned to these transitions was further validated by inspecting plots of the difference in density between the ground and excited states (Fig. 3). In contrast to Fig. 2(d), these plots considered all determinants that form all excited states rather than just those with the largest coefficient.

The d–d transitions for the HS and LS states had a non-negligible intensity with respect to the MLCT transitions due to the reduction of octahedral symmetry. The calculated relative intensities of the HS and LS d–d transitions were consistent since the geometrical distortion from a perfect octahedral symmetry was greater for the HS state than the LS state. More information is provided in ESI.† In addition to singlet-to-singlet (d–d$_{LS}$) excitations, a spin-forbidden, singlet-to-triplet excitation (^{3}d–d$_{LS}$) was computed at 823 nm, slightly lower in energy than d–d$_{LS}$, although no information about its intensity could be obtained due to the spin-forbidden nature of the transition. Considering the HS equilibrium geometry, quintet-to-quintet excitations were determined and, as for the LS state, a d–d$_{HS}$ transition centred at 874 nm was identified. Analogously to d–d$_{LS}$, a small but non-zero oscillator strength was determined for d–d$_{HS}$, again demonstrating the effect of the reduced-symmetry (Fig. 2(b and c)).

The lower energy of d–d$_{HS}$ compared with the d–d$_{LS}$ was attributed to the reduced ligand field resulting from the increased Fe–L distances at the HS equilibrium geometry relative to the LS configuration. An additional band centred at around 500 nm was computed, corresponding to a superposition of LMCT and MLCT transitions for the HS state. Considering the vertical absorption spectrum of the ^{3}T state, another low-energy absorption band corresponding to an excitation at 1200 nm was found, attributed to LMCT character, and will be referred to as LMCT$_{3T}$. Notably, from the inset in Fig. 2(c), it is shown that this band shares no analogue in the absorption spectra computed for either the LS or HS states. From the vibrational frequency calculations at the HS equilibrium geometry, a mode corresponding to the "breathing" of the Fe–L coordination environment was identified at 84 cm^{-1}. This type of breathing mode is characteristic of quasi-octahedral spin crossover compounds. Since this mode corresponds to an oscillation of metal–ligand distances, it can have an observable effect on the d–d$_{HS}$, causing an increase (decrease) in the absorption energy Δ_0, due to the increased (decreased) ligand field imposed by the coordination environment, as observed in other SCO materials.[17,22] In order to assess the modulation of the ligand field through the d–d$_{HS}$ gap with respect to this breathing, 30 structures were generated as a projection along the normal mode, assuming a harmonic mode, and for each of these, the absorption energy d–d$_{HS}$ was vertically re-computed with TD-DFT (Fig. 4). It can be seen that the increased ligand-field strength with shorter Fe–L distances results in a higher Δ_0, while the opposite was observed for longer Fe–L distances. More details are given in ESI† about the optimised geometrical parameters of the singlet, triplet and quintet states. We also show HOMO, LUMO and SOMO orbitals for each spin state investigated (HS, LS, triplet), as well as the orbitals involved in MLCT, d–d and LMCT transitions with their relative contribution, where possible. Both d–d$_{LS}$ and MLCT$_{LS}$ exhibited contributions from ligand orbitals due to the well-known over-delocalisation of orbitals in DFT. We therefore rationalised the difference between d–d and MLCT transitions from the change (or lack thereof) in d-orbital symmetry upon excitation. We use this theoretical characterisation of the optical fingerprints of the LS, HS and intermediate ^{3}T state, in conjunction with femtosecond optical spectroscopy measurements, to ratify different ultrafast LIESST mechanisms observed by pumping particles of LS Fe^{II}(pap-5NO$_2$)$_2$ at two different wavelengths in order to selectively induce LIESST through MLCT or d–d excitation.

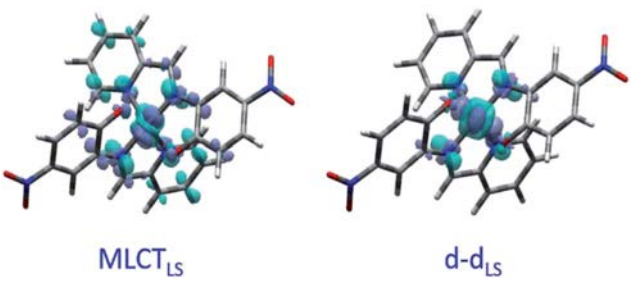

Fig. 3 Density difference plots between ground and excited states for MLCT$_{LS}$ and d–d$_{LS}$ excitations. Dark (light) blue zones indicate areas which increased (decreased) in electronic density upon excitation.

Femtosecond optical pump-probe spectroscopy

For tracking LIESST dynamics in real time we used an optical pump-probe method with 60 fs time resolution (RMS) on LS

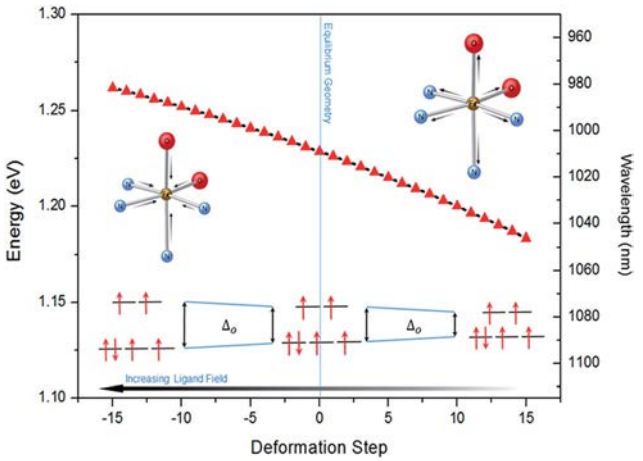

Fig. 4 Modulation of Δ_0 (d–d_{HS} splitting) with respect to a harmonic structural deformation, corresponding to the breathing mode of the in-phase stretching of the Fe–N and Fe–O bonds, calculated at 84 cm^{-1}. The total deformation lies between changes in Fe–N (axial) from 2.074 to 2.172 Å, Fe–N (plane) from 2.144 to 2.307 Å and Fe–O (plane) from 1.967 to 2.074 Å. On the *x*-axis, 0 corresponds to the equilibrium geometry while negative (positive) values indicate shorter (longer) Fe–L distances.

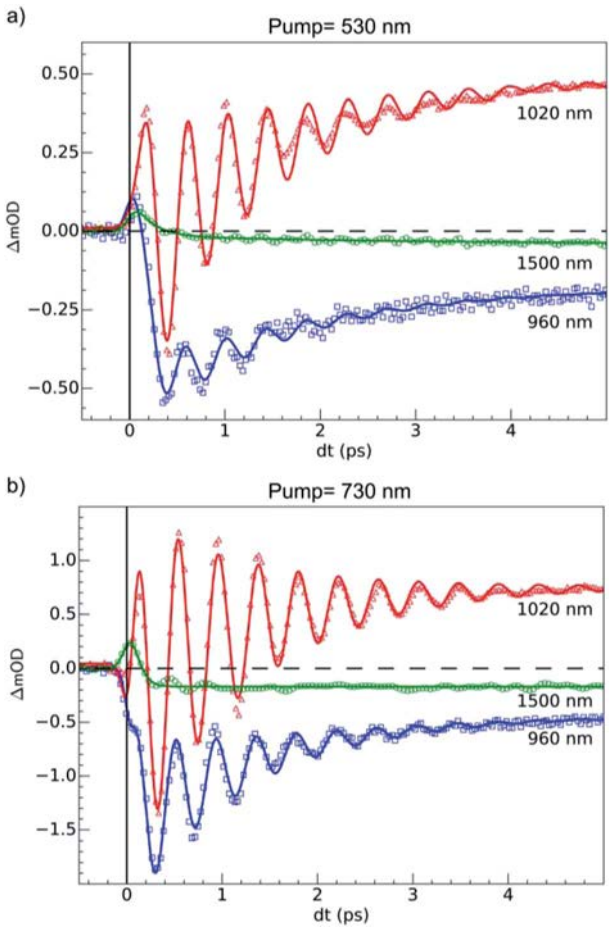

Fig. 5 Time scans at 100 K of relative milli-OD change at selected probing wavelengths revealing 80 (3) cm^{-1} oscillations in the 0–5 ps timescale. (a) Dynamics upon MLCT excitation at 530 nm. (b) Dynamics upon d–d excitation at 730 nm. The fits (solid lines) took into account a transient state, coherent oscillation and the 60 fs IRF. We determined values of $\tau_{MLCT} = 188(10)$ fs, $\tau_{dd} = 70(10)$ fs and an oscillation frequency $\nu_{OSC} = 80(3)$ cm^{-1}.

$Fe^{II}(pap\text{-}5NO_2)_2$ crystals embedded in a thin PVP film spin-coated on a glass substrate. This allowed easy manipulation of samples with homogeneous dispersion at the sub-millimeter scale.

The pump wavelength was set to 530 nm for MLCT excitation and to 730 nm for d–d excitation. We used similar laser excitation fluence in both cases with 4.0(1) μJ mm^{-2} at 530 nm and 4.2(1) μJ mm^{-2} at 730 nm. Time-resolved OD change measurements were performed at selected wavelengths to track the photoswitching dynamics. The femtosecond optical pump-probe experiments were configured in NIR-transmission geometry with a quasi-collinear configuration of pump and probe beams. The sample temperature was controlled with a liquid nitrogen cryostream set for all experiments at 100 K, where the system is LS and the HS-to-LS back relaxation occurs within less than 1 ms. More details are given in the ESI.†

Results and discussion

Photoresponse of LS state to MLCT excitation

OD dynamical time traces probed at 960, 1020, 1500 nm after femtosecond excitation of LS the sample of $Fe(pap\text{-}5NO_2)_2$ at 530 nm (*i.e.*, in the $MLCT_{LS}$ band) are shown in Fig. 5(a). The OD increased at 1020 nm and decreased at 960 nm reproducing the optical fingerprints characteristic of the LS → HS switching obtained with steady state spectra (inset Fig. 2(b)). The time traces also indicated an intermediate signal, better observed at 1500 nm within the first hundreds fs, and damped coherent oscillations at 960 and 1020 nm. These features were very similar to the ones reported for ultrafast optical studies of LIESST in $Fe^{II}N_6$ molecules in solution or in crystals.[17,22,23,39,49] This was due to the local nature of the process in solids that was reported some years ago[21,26] and recently confirmed by a direct comparison of the dynamics of $Fe(bpy)_3^{2+}$ in solution and in crystals.[50] Time-resolved analysis in spectral regions, where HS and LS species almost equally absorbed (such as 1500 nm), allowed an isolated observation of the dynamics of the intermediate state(s) involved during the spin-state photo-switching. For photoexcitation at 530 nm, such intermediate states (INT) could include the initially photoexcited $^{1,3}MLCT$ state ($t_{2g}^5e_g^0L^1$) and $^{1,3}T$ (d–d ligand-field states, $t_{2g}^5e_g^1L^0$) on the pathway towards the HS potential.

Our TD-DFT calculation (Fig. 2) of the triplet spin state indicates a characteristic absorption band around 1200 nm. This band corresponds to an electron transfer from the ligand L to the metal M, and therefore this 1200 nm band of the ^3T state had an LMCT character and was referred to as $LMCT_{3T}$. Since we could not compute the absorption spectra for the ^1T and ^1MLCT states, we used $LMCT_{3T}$ as an approximate global signature of these intermediates using the following qualitative points. Since the orbital energy levels were similar for the ^1T and ^3T states, the $LMCT_{1T}$ band of the ^1T state should also be centred at

around 1200 nm. In addition, the initial ^{1}MLCT state, resulting from excitation of the LS state at 530 nm, should also have a similar low energy LMCT band due to the partial occupation of its t_{2g}-like orbitals. As we see from the $LMCT_{3T}$ state obtained from TD-DFT calculations, these low-energy optical transitions for ^{1,3}T and ^{1,3}MLCT states have no analogue in either the LS or HS species, even though the tail of the d–d_{HS} band extended up to 1500 nm. Experimentally, the optical absorption of LS and HS states was very low, but quite similar, around 1500 nm due to the broadening of the bands. Data around the isosbestic point at 970 nm (Fig. S2†) were strongly affected by coherent oscillation and vibrational cooling. The transient absorption peak measured at 1500 nm globally included the OD signature of intermediates (^{1,3}MLCT and ^{1,3}T states) to probe the HS population under MLCT excitation:

$$\mathrm{MLCT} \xrightarrow{\tau_{MLCT}} \mathrm{HS}.$$

An exponential fit of the data probed at 1500 nm, taking into account our 60 fs RMS instantaneous response function, indicated that the initial MLCT decayed toward the HS state within $\tau_{MLCT} = 188\,(10)$ fs. A slower component $\tau_{VC} = 2.8\,(5)$ ps was also found and attributed to vibrational cooling, as already observed in other SCO materials.[17,18,22,23] The time-resolved OD data at 960 and 1020 nm showed similar features associated with an initial peak and a slower change accompanied by coherent vibrations. We globally analyzed these data with a phenomenological model. It included the exponential decay of the MLCT state excited at $t = 0$ (and other possible intermediates such as ^{1,3}T), populating the final HS state within τ_{MLCT} and was accompanied by a damped oscillation. The signal due to the intermediate species was calculated according to the following equation:

$$P_{MLCT}(t) = \mathrm{IRF}(t) \otimes [\exp(-t/\tau_{MLCT}) \times H(t)]$$

IRF(t) is the Gaussian instrument response function and H(t) is the Heaviside function. The signal due to the oscillation in the HS state is described as follows:

$$s_{HS}(t) = [A_{HS} + A_{OSC}\cos(2\pi\nu_{osc}t)\exp(-t/\tau_{osc}) + A_{VC}\exp(-t/\tau_{VC})] \times H(t)$$

with amplitudes of the signal related to HS population (A_{HS}), oscillation (A_{OSC}) and vibrational cooling (A_{VC}). Herein, τ_{OSC} is the damping of the oscillation with frequency ν_{osc}. However, since the MLCT state was the source of molecules in the HS state, the observed signal $S_{HS}(t)$ corresponded to the convolution of $S_{HS}(t)$ with the MLCT population $P_{MLCT}(t)$:

$$S_{HS}(t) = P_{MLCT}(t) \otimes s_{HS}(t)$$

as schematically shown in Fig. 1(b).

For the fit of the data probed at 960 and 1020 nm (Fig. 5(a)), the physical parameters $\nu_{osc} = 80(3)$ cm^{-1} and $\tau_{MLCT} = 188(12)$ fs were the same for the different probing wavelengths. The 188 fs decay from the MLCT to HS state was in good agreement with the independent fit at 1500 nm. However, the vibrational cooling timescale τ_{VC} and the oscillation damping τ_{osc} were different for each wavelength. It is well known that these timescales depend on the spectral region. The damping constant was $\tau_{osc} = 1.001$ (0.05) ps at 1020 nm and 1.208(0.02) ps at 960 nm, and the vibrational cooling occurred within $\tau_{VC} = 1.56(0.05)$ ps at 1020 nm and 1.68(0.05) ps at 960 nm. Again, these timescales were similar to the values reported for other systems presenting LIESST in solids or in solution.[5,22,23,37–39]

The 80(3) cm^{-1} oscillations were observed, once the HS reached, for OD time traces at 960 and 1020 nm (*i.e.*, close to the d–d_{HS} band (Fig. 2(c)). These were associated with a strong modulation of the ligand field Δ_0 by molecular breathing (Fig. 4). Similar findings were also reported in other SCO crystals, and this oscillation probed around the d–d_{HS} transition was attributed to the breathing of the ligand field.[12,22,23] For FeN_6 systems, this was the main reaction coordinate between the LS and HS structures, which corresponded to the in-phase elongation of the Fe–N bond lengths. Our DFT study on Fe^{II}-(pap-5NO_2)$_2$ revealed a breathing mode in the HS state at 84 cm^{-1}. This completely symmetric vibration mainly involved the FeN_4O_2 core and also corresponded to in phase stretching of Fe–N and Fe–O bonds as shown in Fig. 4. These results indicated that the physical picture for MLCT-induced LIESST in Fe(pap-5NO_2)$_2$, driven by the MLCT decay towards lower states activating and damping molecular breathing, was similar to the one theoretically and experimentally reported for FeN_6 systems (Fig. 1(a)).[17,18,22,23,38,41] The coherent oscillations observed during LIESST were sometimes attributed to an impulsive Raman process activating the LS breathing mode. This possibility can be excluded because the LS breathing frequency was significantly higher (146 cm^{-1}). In addition, an impulsive process would induce sine-like oscillations around zero OD change, whereas the band probed at 1020 nm, where oscillations are stronger, is sensitive to the formation of the HS state.

Photoresponse of LS state to d–d excitation

Additional measurements were also performed at 100 K in the LS state upon d–d excitation at 730 nm generating ligand-field states (^{1,3}T, $t_{2g}^5e_g^1L^0$), with experimental conditions similar to the ones used for MLCT excitation. Time-resolved OD changes for the different probing wavelengths are shown in Fig. 5(b). At 5 ps, the OD increase (decrease) at 1020 nm (960 nm) and a weak change at 1500 nm were characteristic of the formation of the HS state and similar to the changes observed upon MLCT excitation at 530 nm. However, the OD change was larger for d–d excitation when a similar laser fluence was used. For example, at 1020 nm, the OD increased by 0.48 for a 530 nm excitation and by 0.72 for a 730 nm excitation (Fig. 5(b)). In SCO materials, the quantum efficiency has been known to be close to unity, and the OD linearly changed with the number of photons in such low fluence regimes.[26] The ratio of the number of photons contained in the pump laser pulses of 4.2(1) μJ mm^{-2} at 730 nm and 4.0(1) μJ mm^{-2} at 530 nm was $R_{ph} \approx 1.45(5)$. This ratio was close to the ratio of the OD change at 1020 nm between 730 nm and 530 nm excitations: $R_{OD} = 1.5$. These results indicated that

d–d and MLCT excitations generated the final HS state with a very similar quantum yield. The comparison with data at 960 nm yielded a value on the same order, but was more difficult to analyze because 960 nm was closer to the isosbestic point, known to shift by lattice pressure and heating following femtosecond excitation.[21] Additional data are presented in Fig. S2,† where the in-phase oscillations of time traces recorded at different probing wavelengths are characteristic of the global oscillation in wavelength of the d–d_{HS} band with Fe–L oscillation, as discussed in Fig. 4.

Data at 1020 nm, around the maximum of OD change (Fig. 2(b)), were not sensitive to this effect and better suited to observe quantum yield. Around $t = 0$ ps at a 960 nm probing wavelength, the OD decreased for the 730 nm d–d excitation, contrary to the 530 nm MLCT excitation. In addition, the OD changes observed around $t = 0$ ps at 1020 and 1500 nm probe for 730 and 530 nm excitations were similar, but with different relative amplitudes. These observations indicated two different initial states with distinctive spectroscopic signatures, in agreement with TD-DFT calculations of the LS state (Fig. 2(d)).

We identified the initial state as a ^{1,3}MLCT upon 530 nm excitation and as a ^{1,3}T state upon 730 nm excitation. Our calculations showed that photoexcitation of the d–d_{LS} band could induce ^{1}T spin-allowed or ^{3}T spin-forbidden states, but the relative weights of these could not be calculated, and two possible pathways may (co)exist, LS → ^{1}T → ^{3}T → HS and/or LS → ^{3}T → HS. Since Sousa *et al.* calculated ^{1}T → ^{3}T inter-system crossing rates in the 400–2700 fs timescale and ^{3}T → HS in the 60 fs range,[40] it is possible that the d–d_{LS} photoexcitation mainly induced the ^{3}T spin-forbidden states. Femtosecond X-ray fluorescence measurements, as performed by K. Gaffney on $Fe(bpy)_3^{2+}$,[37] may be helpful in the future to discriminate the nature of the initial photo-excited state. In order to fit the time evolution of the optical fingerprints of the different states, we used the kinetic model described for MLCT excitation, now including the exponential decay of the photoinduced T state towards the final HS state as the initial process:

$$T \xrightarrow{\tau_{dd}} HS$$

The fit of the data (Fig. 5(b)) indicated that the HS state was populated after d–d excitation within $\tau_{dd} = 70(10)$ fs. The process was also accompanied by a coherent oscillation, with frequency $\nu_{osc} = 80(3)$ cm^{-1} and damping constant $\tau_{osc} = 1.21(0.02)$ ps at 1020 nm and 1.00(0.02) ps at 960 nm. The vibrational cooling occurred within $\tau_{VC} = 1.33(0.04)$ ps at 1020 nm and 1.49(0.02) ps at 960 nm. The fact that the frequency of the oscillation corresponded to the one observed after MLCT (530 nm) excitation confirmed that the final photoinduced state was the same under d–d (730 nm) excitation, as already indicated by the similar OD changes and photomagnetism. The main difference compared to the MLCT excitation was the faster population of the HS state, since the number of intermediates was reduced in the case of d–d excitation compared to MLCT excitation.

Fig. 6 compares the OD changes for the different probing wavelengths on short timescales. The amplitudes of the changes were scaled for clarity. The OD peak probed at 1500 nm clearly appeared to be longer around $t = 0$ under MLCT than under d–d excitation. Regarding the oscillating components, there were two main differences between the two excitation processes. There was a phase shift, of about 75 fs, between the oscillation observed after MLCT and d–d excitation. Moreover, the relative amplitude of the oscillation, with respect to the OD change between LS and HS states, was larger under d–d excitation than under MLCT excitation.

These features are explained very well by our model, which describes the signal as an initial photoexcited state, (MLCT or T) which exponentially populates the HS potential where molecules undergo damped oscillations. Both effects result from the shorter decay time $\tau_{dd} = 75(10)$ fs under d–d excitation than $\tau_{MLCT} = 188(10)$ fs under MLCT excitation. The T state, with an electronic structure of $t_{2g}^5 e_g^1 L^0$, is a natural intermediate between MLCT ($t_{2g}^5 e_g^0 L^1$) and HS ($t_{2g}^4 e_g^2 L^0$) states, which was observed by X-ray spectroscopy in $Fe(bpy)_3^{2+}$.[37] We therefore performed another fit of the data in Fig. 6 to describe the consecutive decays under MLCT excitation:

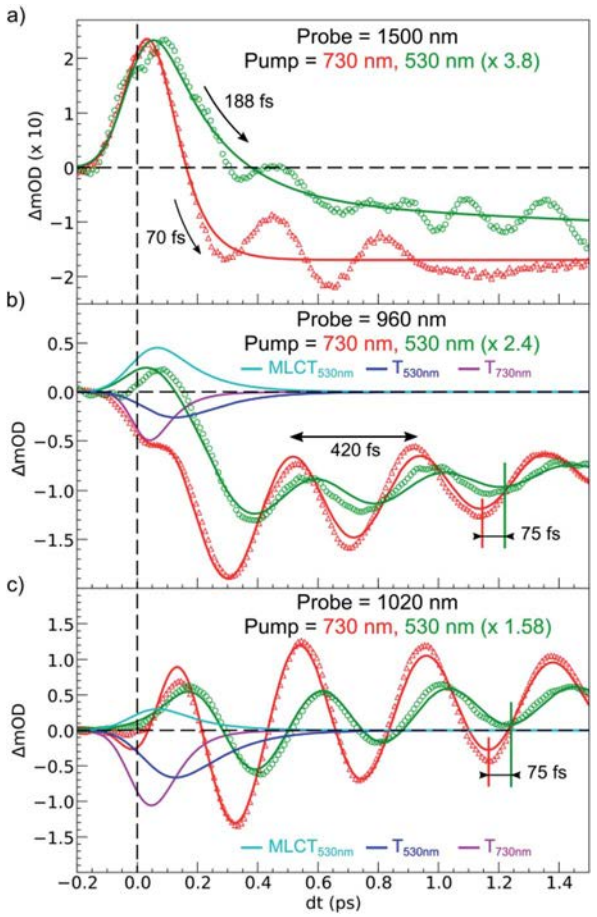

Fig. 6 Comparison of short time scans of relative OD changes at selected probing wavelengths upon $MLCT_{LS}$ excitation at 530 nm and d–d_{LS} excitation at 730 nm. The fit for the 530 nm excitation includes MLCT and T intermediates, whereas the fit for 730 nm includes T only.

$$^{1,3}\mathrm{MLCT} \xrightarrow{\tau_{MT}} {}^{3}\mathrm{T} \xrightarrow{\tau_{TH}} \mathrm{HS}.$$

We independently found τ_{TH} under d–d excitation as $\tau_{TH} = \tau_{dd} = 70(10)$ fs. Therefore, in the fit presented in Fig. 6, we only refined the ^{1,3}MLCT → T decay time constant $\tau_{MT} = 120(10)$ fs. The faster HS population under d–d excitation maintained coherence (amplitude of the oscillation) and more rapidly initiated HS state oscillation, as illustrated by the oscillation phase shift in time. This was due to the fact that the HS population was much faster than the 210 fs half oscillation period, which was the upper limit on the timescale to maintain oscillation coherence in the HS state. Under MLCT excitation, the overall $\tau_{MLCT} = 188(10)$ fs HS population approached the half oscillation period and was responsible for decoherence during the long MLCT-to-HS population, reducing the amplitude of the oscillation. These effects are summarized in Fig. 1(b and d).

Conclusions

This study compared two possible LIESST pathways from LS to HS states under d–d or MLCT photoexcitations. This was made possible by chemical engineering through a ligand design with low symmetry that allowed intense d–d bands while maintaining the spin-crossover and LIESST properties. The sequences MLCT → 3T within 120 fs and 3T → HS within 70 fs were very similar for FeN_6 and the lower symmetry FeN_4O_2 system investigated here. LIESST was associated with the fast activation of the molecular breathing mode since anti-bonding "e_g-like" orbitals were populated, and hence increased the equilibrium Fe–L distance. This structural trapping of the system in the HS potential was similar to other systems.[17,18,22,23] Therefore, the short-lived intermediates were not thermally equilibrated states, since their population had a shorter lifetime than the oscillation period in the potential. They corresponded to an evolution of hot states within the manifold of electronic states involved in the process, where the coherent structural dynamics moved the system between different electronic potentials, on a timescale where wave functions of atomic nuclei and electrons are difficult to separate. The resulting physical picture was consistent with the theoretical model introduced by van Veenendaal.[41] In addition, the speed of the structural trapping through Fe–L elongation was limited by the decay of the MLCT towards the T state, where antibonding orbitals were populated since the initial ^{1}MLCT state had on equally bonding character as the initial LS state. The molecular expansion only began once the T state was reached, which took about 120(10) fs, before decaying towards the final HS state within 70(10) fs. The d–d excitation process instantaneously populated antibonding orbitals, which launched the Fe–L expansion and moved the system towards the HS potential. The HS state was then reached within 70(10) fs. Herein, we could accurately study the coherent structural dynamics during LIESST through the intense d–d_{HS} band in the FeN_4O_2 system, strongly modulated by the Fe–L distance. By reducing the lifetime of intermediates compared to MLCT excitation, d–d excitation allowed a faster LIESST and preserved structural breathing coherence since this molecular reaction coordinate was activated and damped to trap the HS state.

Acknowledgements

This study was supported by the Institut Universitaire de France, Rennes Métropole, ANR (ANR-13-BS04-0002), Centre National de la Recherche Scientifique (CNRS), Fonds Européen de Développement Régional (FEDER) and Région Bretagne (ARED 8925/XFELMAT). This project has received funding from the European Research Council (ERC) under the European Union's Horizon 2020 research and innovation programme (grant agreement No. 648558, STRIGES project).

References

1 C. Daniel, *Coord. Chem. Rev.*, 2015, **282–283**, 19–32.
2 M. A. Halcrow, *Spin-crossover materials : properties and applications*, Wiley, 2013.
3 O. Sato, *Acc. Chem. Res.*, 2003, **36**, 692–700.
4 S.-I. Ohkoshi and H. Tokoro, *Acc. Chem. Res.*, 2012, **45**, 1749–1758.
5 M.-L. Boillot, J. Zarembowitch and A. Sour, in *Top Curr Chem*, Springer Berlin Heidelberg, Berlin, Heidelberg, 2004, pp. 261–276, DOI: 10.1007/b95419.
6 S. Venkataramani, U. Jana, M. Dommaschk, F. D. Sönnichsen, F. Tuczek and R. Herges, *Science*, 2011, **331**, 445–448.
7 J. K. McCusker and A. Vlček, *Acc. Chem. Res.*, 2015, **48**, 1207–1208.
8 E. A. Juban and J. K. McCusker, *J. Am. Chem. Soc.*, 2005, **127**, 6857–6865.
9 M. Iwamura, H. Watanabe, K. Ishii, S. Takeuchi and T. Tahara, *J. Am. Chem. Soc.*, 2011, **133**, 7728–7736.
10 C. Y. Chen, N. Pootrakulchote, T. H. Hung, C. J. Tan, H. H. Tsai, S. M. Zakeeruddin, C. G. Wu and M. Gratzel, *J. Phys. Chem. C*, 2011, **115**, 20043–20050.
11 A. S. Mereshchenko, P. K. Olshin, O. S. Myasnikova, M. S. Panov, V. A. Kochemirovsky, M. Y. Skripkin, P. N. Moroz, M. Zamkov and A. N. Tarnovsky, *J. Phys. Chem. A*, 2016, **120**, 1833–1844.
12 S. Decurtins, P. Gütlich, C. P. Köhler, H. Spiering and A. Hauser, *Chem. Phys. Lett.*, 1984, **105**, 1–4.
13 A. Hauser, *Top. Curr. Chem.*, 2004, **234**, 155–198.
14 A. Hauser, *Chem. Phys. Lett.*, 1986, **124**, 543–548.
15 A. Goujon, F. Varret, K. Boukheddaden, C. Chong, J. Jeftić, Y. Garcia, A. D. Naik, J. C. Ameline and E. Collet, *Inorg. Chim. Acta*, 2008, **361**, 4055–4064.
16 N. Brefuel, E. Collet, H. Watanabe, M. Kojima, N. Matsumoto, L. Toupet, K. Tanaka and J. P. Tuchagues, *Chemistry*, 2010, **16**, 14060–14068.
17 M. Cammarata, R. Bertoni, M. Lorenc, H. Cailleau, S. Di Matteo, C. Mauriac, S. F. Matar, H. Lemke, M. Chollet, S. Ravy, C. Laulhe, J. F. Letard and E. Collet, *Phys. Rev. Lett.*, 2014, **113**, 227402.
18 A. Marino, P. Chakraborty, M. Servol, M. Lorenc, E. Collet and A. Hauser, *Angew. Chem., Int. Ed.*, 2014, **53**, 3863–3867.

19 E. Collet, M. Lorenc, M. Cammarata, L. Guerin, M. Servol, A. Tissot, M. L. Boillot, H. Cailleau and M. Buron-Le Cointe, *Chem.–Eur. J.*, 2012, **18**, 2051–2055.
20 E. Collet, N. Moisan, C. Balde, R. Bertoni, E. Trzop, C. Laulhe, M. Lorenc, M. Servol, H. Cailleau, A. Tissot, M. L. Boillot, T. Graber, R. Henning, P. Coppens and M. Buron-Le Cointe, *Phys. Chem. Chem. Phys.*, 2012, **14**, 6192–6199.
21 R. Bertoni, M. Lorenc, A. Tissot, M. Servol, M. L. Boillot and E. Collet, *Angew. Chem., Int. Ed.*, 2012, **51**, 7485–7489.
22 R. Bertoni, M. Cammarata, M. Lorenc, S. F. Matar, J. F. Letard, H. T. Lemke and E. Collet, *Acc. Chem. Res.*, 2015, **48**, 774–781.
23 A. Marino, M. Cammarata, S. F. Matar, J.-F. Létard, G. Chastanet, M. Chollet, J. M. Glownia, H. T. Lemke and E. Collet, *Struct. Dyn.*, 2016, **3**, 023605.
24 R. M. van der Veen, O. H. Kwon, A. Tissot, A. Hauser and A. H. Zewail, *Nat. Chem.*, 2013, **5**, 395–402.
25 A. Tissot, R. Bertoni, E. Collet, L. Toupet and M.-L. Boillot, *J. Mater. Chem.*, 2011, **21**, 18347.
26 R. Bertoni, M. Lorenc, H. Cailleau, A. Tissot, J. Laisney, M. L. Boillot, L. Stoleriu, A. Stancu, C. Enachescu and E. Collet, *Nat. Mater.*, 2016, **15**, 606–610.
27 R. Bertoni, M. Lorenc, T. Graber, R. Henning, K. Moffat, J. F. Létard and E. Collet, *CrystEngComm*, 2016, **18**, 7269–7275.
28 J. J. Mcgarvey, I. Lawthers, K. Heremans and H. Toftlund, *J. Chem. Soc., Chem. Commun.*, 1984, 1575–1576, DOI: 10.1039/C39840001575.
29 N. Huse, H. Cho, K. Hong, L. Jamula, F. M. F. de Groot, T. K. Kim, J. K. McCusker and R. W. Schoenlein, *J. Phys. Chem. Lett.*, 2011, **2**, 880–884.
30 J. K. McCusker, K. N. Walda, R. C. Dunn, J. D. Simon, D. Magde and D. N. Hendrickson, *J. Am. Chem. Soc.*, 1993, **115**, 298–307.
31 A. L. Smeigh, M. Creelman, R. A. Mathies and J. K. McCusker, *J. Am. Chem. Soc.*, 2008, **130**, 14105–14107.
32 W. Gawelda, V. T. Pham, A. El Nahhas, M. Kaiser, Y. Zaushytsin, S. Johnson, D. Grolimund, R. Abela, A. Hauser, C. Bressler and M. Chergui, *AIP Conf. Proc.*, 2007, **882**, 31.
33 C. Bressler, C. Milne, V. T. Pham, A. ElNahhas, R. M. van der Veen, W. Gawelda, S. Johnson, P. Beaud, D. Grolimund, M. Kaiser, C. N. Borca, G. Ingold, R. Abela and M. Chergui, *Science*, 2009, **323**, 489–492.
34 H. T. Lemke, C. Bressler, L. X. Chen, D. M. Fritz, K. J. Gaffney, A. Galler, W. Gawelda, K. Haldrup, R. W. Hartsock, H. Ihee, J. Kim, K. H. Kim, J. H. Lee, M. M. Nielsen, A. B. Stickrath, W. K. Zhang, D. L. Zhu and M. Cammarata, *J. Phys. Chem. A*, 2013, **117**, 735–740.
35 S. E. Canton, X. Y. Zhang, L. M. L. Daku, A. L. Smeigh, J. X. Zhang, Y. Z. Liu, C. J. Wallentin, K. Attenkofer, G. Jennings, C. A. Kurtz, D. Gosztola, K. Warnmark, A. Hauser and V. Sundstrom, *J. Phys. Chem. C*, 2014, **118**, 4536–4545.
36 S. Nozawa, T. Sato, M. Chollet, K. Ichiyanagi, A. Tomita, H. Fujii, S. Adachi and S. Koshihara, *J. Am. Chem. Soc.*, 2010, **132**, 61–63.
37 W. K. Zhang, R. Alonso-Mori, U. Bergmann, C. Bressler, M. Chollet, A. Galler, W. Gawelda, R. G. Hadt, R. W. Hartsock, T. Kroll, K. S. Kjaer, K. Kubicek, H. T. Lemke, H. Y. W. Liang, D. A. Meyer, M. M. Nielsen, C. Purser, J. S. Robinson, E. I. Solomon, Z. Sun, D. Sokaras, T. B. van Driel, G. Vanko, T. C. Weng, D. L. Zhu and K. J. Gaffney, *Nature*, 2014, **509**, 345–348.
38 H. T. Lemke, K. S. Kjær, R. Hartsock, T. Brandt van Driel, M. Chollet, J. M. Glownia, S. Song, D. Zhu, E. Pace, S. F. Matar, M. N. Nielsen, M. Benfatto, K. J. Gaffney, E. Collet and M. Cammarata, *Nat. Commun.*, 2017, **8**, 15342, DOI: 10.1038/ncomms15342.
39 G. Aubock and M. Chergui, *Nat. Chem.*, 2015, **7**, 629–633.
40 C. Sousa, C. de Graaf, A. Rudavskyi, R. Broer, J. Tatchen, M. Etinski and C. M. Marian, *Chem.–Eur. J.*, 2013, **19**, 17541–17551.
41 M. van Veenendaal, J. Chang and A. J. Fedro, *Phys. Rev. Lett.*, 2010, **104**, 067401.
42 A. Hauser, *Coord. Chem. Rev.*, 1991, **111**, 275–290.
43 O. Iasco, E. Riviere, R. Guillot, M. Buron-Le Cointe, J. F. Meunier, A. Bousseksou and M. L. Boillot, *Inorg. Chem.*, 2015, **54**, 1791–1799.
44 L. Zhang, J.-J. Wang, G.-C. Xu, J. Li, D.-Z. Jia and S. Gao, *Dalton Trans.*, 2013, **42**, 8205–8208.
45 M. J. Frisch, J. A. Pople and J. S. Binkley, *J. Chem. Phys.*, 1984, **80**, 3265–3269.
46 P. J. Hay and W. R. Wadt, *J. Chem. Phys.*, 1985, **82**, 270–283.
47 Y. Zhao and D. G. Truhlar, *Theor. Chem. Acc.*, 2008, **120**, 215–241.
48 C. Adamo and V. Barone, *J. Chem. Phys.*, 1999, **110**, 6158–6170.
49 C. Consani, M. Premont-Schwarz, A. ElNahhas, C. Bressler, F. van Mourik, A. Cannizzo and M. Chergui, *Angew. Chem., Int. Ed.*, 2009, **48**, 7184–7187.
50 R. Field, L. C. Liu, W. Gawelda, C. Lu and R. J. D. Miller, *Chem.–Eur. J.*, 2016, **22**, 5118–5122.

ChemPubSoc Europe

DOI: 10.1002/ejic.201700657

EurJIC European Journal of Inorganic Chemistry
Communication

Photoinduced Charge Transfer | *Very Important Paper* |

Probing Transient Photoinduced Charge Transfer in Prussian Blue Analogues with Time-Resolved XANES and Optical Spectroscopy

Serhane Zerdane,[a] Marco Cammarata*[a] Lodovico Balducci,[a] Roman Bertoni,[a] Laure Catala,[b] Sandra Mazerat,[b] Talal Mallah,[b] Martin N. Pedersen,[c] Michael Wulff,[c] Kosuke Nakagawa,[d] Hiroko Tokoro,[e] Shin-ichi Ohkoshi,[d] and Eric Collet*[a]

Abstract: We studied the transient electron-transfer process in CsCoFe and RbMnFe Prussian Blue analogues by time-resolved X-ray absorption near-edge structure (XANES) and by time-resolved optical spectroscopy. We performed time-resolved studies on CsCoFe nanocrystals dispersed in solution. The XANES results obtained at room temperature clearly evidence Co^{III}(low spin)Fe^{II}→Co^{II}(high spin)Fe^{III} electron transfer between the metal centers through opposite spectral shifts at the Fe and Co edges. We also studied the Mn^{III}(low spin)Fe^{II}→Mn^{II}(high spin)Fe^{III} process in an RbMnFe powder sample at thermal equilibrium and under laser excitation. Optical spectroscopy revealed that the process occurs on the picosecond timescale, as already reported by Raman spectroscopy, and that the lifetime of the photoinduced charge-transfer states is in the 1–10 μs range, depending on the sample and temperature.

Introduction

Control of the physical and chemical properties (e.g., magnetic, optical, conductivity, motion, reactivity, etc.) of materials by light is a challenging field of research from fundamental and technological aspects. Optically switchable materials are extensively studied because of their potential applications in light-based technologies, including optical memory devices and sensors. Several studies involving different kinds of materials have been reported, such as neutral–ionic and insulating-metal charge-transfer systems,[1] metal oxides,[2] photochromic materials,[3] spin-crossover complexes,[4] and cyanide-bridged dimetallic assemblies.[5] For these systems to be useful and to control their light-induced properties, it is compulsory to understand the elementary mechanisms that take place on the short timescale, as this allows structural trapping of new electronic states. Molecule-based materials containing transition-metal ions, such as spin-crossover (SCO) systems and charge-transfer (CT) Prussian Blue analogues (PBAs), possess common behavior involving very strong coupling between the electronic and structural changes after light illumination. The light-induced excited spin state trapping (LIESST) phenomenon has been thoroughly investigated in many spin-crossover materials in the solid state.[6] Transient LIESST and its dynamics have been studied by time-resolved techniques, including optical and X-ray spectroscopy, down to the femtosecond timescale, in solution[7] and in solids.[8] Ultrafast studies were also performed in cyanide-bridged dimetallic assemblies by using time-resolved optical,[9] Raman,[10] X-ray diffraction,[11] and X-ray spectroscopy.[12] Optical and X-ray probe techniques are sensitive to both electronic and structural aspects and are, therefore, particularly interesting for understanding the transformation mechanisms of such materials.[8c] Herein, we use time-resolved X-ray absorption near-edge structure (XANES) to evidence transient charge transfer, induced by a laser pulse (ca. 1 ps = 10^{-12} s), in two types of cyano-bridged photomagnetic networks in the form of nanocrystals for the compound noted CsCoFe and as a powder for the compound noted RbMnFe in the following. The XANES experiments were performed at the ID09 beamline of the ESRF synchrotron, and optical pump–probe studies were performed at the Institut de Physique de Rennes to characterize the lifetime of the transient CT states.

$Cs\{Co[Fe(CN)_6]\}$[5d] and $Rb\{Mn[Fe(CN)_6]\}$[5f] are photomagnetic materials known as Prussian Blue analogues (PBAs), and they consist of a face-centered cubic (fcc) 3D network (Figure 1a). The exact compositions of the studied samples are given in the Experimental Section and the Supporting Informa-

[a] *Univ Rennes 1, CNRS, Institut de Physique de Rennes, UMR 6251, UBL, 35042 Rennes, France*
E-mail: marco.cammarata@univ-rennes1.fr
eric.collet@univ-rennes1.fr
http://marcocamma.free.fr/
http://blogperso.univ-rennes1.fr/eric.collet/
[b] *Univ Paris Sud, Université Paris-Saclay, CNRS, Institut de Chimie Moléculaire et des Matériaux d'Orsay, UMR 8182, 91405 Orsay, France*
[c] *European Synchrotron Radiation Facility, 38000 Grenoble, France*
[d] *Department of Chemistry, School of Science, The University of Tokyo, 7-3-1 Hongo, Bunkyo-ku, Tokyo 113-0033, Japan*
[e] *Division of Materials Science, Faculty of Pure and Applied Sciences, Univ Tsukuba, 1-1-1 Tennodai, Tsukuba, Ibaraki 305-8577, Japan*
Supporting information and ORCID(s) from the author(s) for this article are available on the WWW under https://doi.org/10.1002/ejic.201700657.

tion. The CN^- groups bridge the two metal ions, and Fe is linked to the carbon side of CN^-, and Co and Mn are linked to the nitrogen side. The alkali ions (Cs^I and Rb^I) occupy the tetrahedral sites of the fcc network. The metal ions have octahedral geometry with symmetry very close to O_h. The octahedral crystal field of the ligands splits the 3d orbitals into two sets of t_{2g} and e_g orbitals. The Fe ions are always in the low-spin (LS) state, and the Mn ions are always in the high-spin (HS) state. Although the spin state of Co depends on its oxidation state, Co^{II} is high spin ($S = 3/2$) and Co^{III} is low spin ($S = 0$). For CsCoFe, there are thus two electronic configurations for the Co–Fe pairs, that is, the diamagnetic $Fe^{II}(S = 0)$–$Co^{III}(S = 0)$ and the paramagnetic $Fe^{III}(S = 1/2)$–$Co^{II}(S = 3/2)$. External control parameters such as temperature and light allow switching between the two states, as schematically represented by the potential energy curves in Figure 1b. At low temperature, light illumination allows electron transfer from Fe^{II} to Co^{III} concomitant to a spin change to the higher entropy $Fe^{III}(S = 1/2)$–$Co^{II}(S = 3/2)$ configuration. At thermal equilibrium, the change in spin state on the Co site is associated with structural reorganization (Figure 1c). As the electron populates the antibonding e_g orbitals in the HS state, the Co–N bonds expand by about 0.2 Å, which induces lattice expansion. Different alkali metal atoms such as Cs^I and Rb^I can be included in the tetrahedral sites of the fcc network

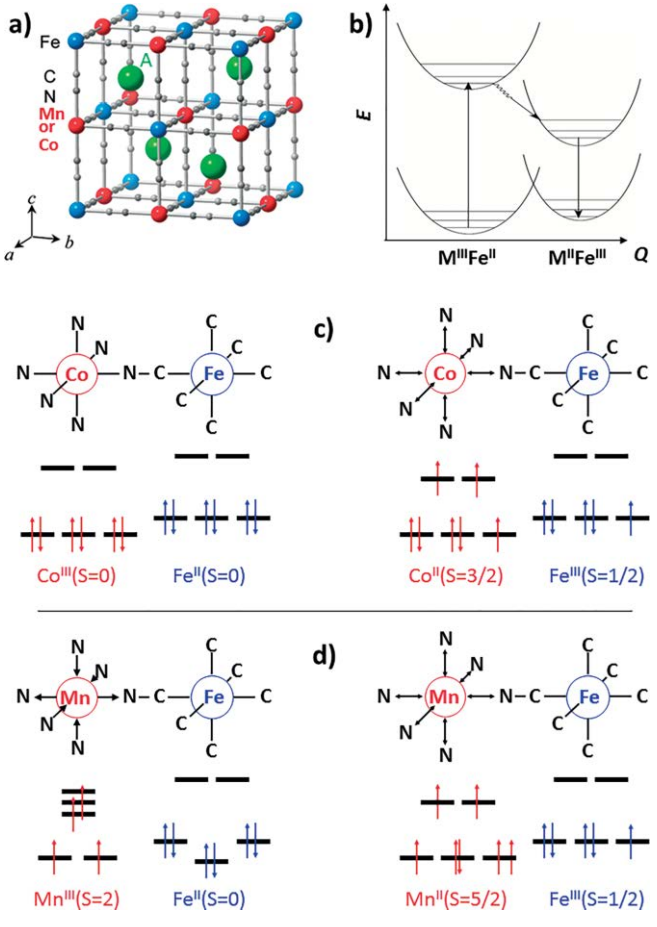

Figure 1. (a) Schematic representation of the 3D structure and (b) potential-energy curves with electronic and structural changes associated with charge-transfer processes in the (c) CsCoFe and (d) RbMnFe systems.

to favor or not to favor the higher volume state. Bleuzen et al. demonstrated by XANES measurements at the Fe and Co edges that it was possible for a given composition of the material to photoinduce the $Co^{III}(LS)Fe^{II}(LS) \rightarrow Co^{II}(HS)Fe^{III}(LS)$ charge transfer at room temperature under pressure.[5d]

For RbMnFe systems, there are also two possible electronic states: the ground state $Mn^{III}(S = 2)Fe^{II}(S = 0)$, and the high-temperature state $Mn^{II}(S = 5/2)Fe^{III}(S = 1/2)$ (Figure 1d). The thermally induced electron transfer was also characterized by XANES studies at the Fe and Mn edges, and here the main structural change occurs around the Mn site.[13] For both systems, the *K*-edge XANES spectra are modified through their sensitivity to charge transfer (resulting in a "rigid shift" in the absorption spectra) and to structural rearrangement (change in the XANES spectrum). As detailed in the Experimental Section, we use these XANES fingerprints to track the electron transfer photoinduced by a femtosecond laser pulse in the CsCoFe and RbMnFe systems by using the experimental setup developed at the ID09 beamline of the ESRF (Figure 2). In addition, we use time-resolved optical spectroscopy to characterize the lifetime of the transient and out-of-equilibrium electron transfer.

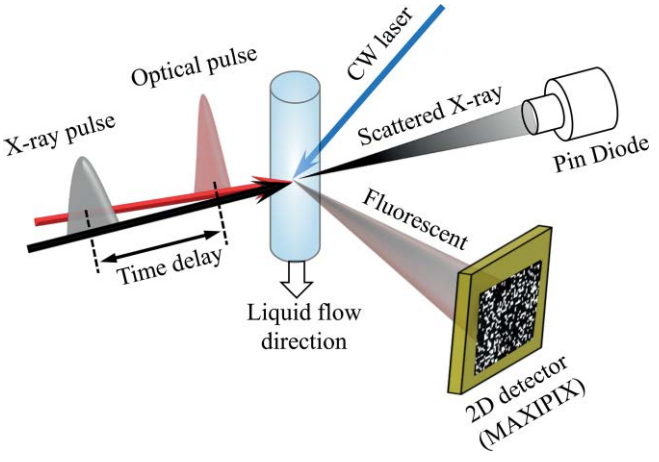

Figure 2. Schematic experimental setup used for time-resolved XANES studies at the ESRF.

Results and Discussion

The CsCoFe nanocrystals dispersed in water studied here are in the diamagnetic $Fe^{II}(S = 0)$–$Co^{III}(S = 0)$ state at room temperature, which allows the phototransformation experiments to be performed at room temperature. We acquired the XANES data from 15 nm sized nanocrystals dispersed in water and excited by 650 nm laser pulses (Figure 2). The XANES changes were monitored by ca. 70 ps X-ray pulses at the ID09 beamline, as shown in Figure 3. Before laser irradiation, the maxima of the X-ray absorption intensities, *I* (au), were around 7728 eV at the Co *K*-edge and around 7130 eV at the Fe *K*-edge. These results are in good agreement with the results obtained by Bleuzen et al.[5d] The spectral changes measured 500 ps after laser excitation (red curve) are very weak. This is often the case in time-resolved studies, because the excitation density used is typically of the order of 1 photon per 100 active sites. Therefore, the

spectral changes due to photoexcited species are better observed by changes in the spectral intensity, $\Delta I = (I_{500\ ps} - I_{off})$, also shown in Figure 3. The difference spectrum at the Co edge shows a spectral shift towards lower energy, characterized by an absorption increase below the Co edge and a decrease just above it. The difference spectrum at the Fe edge shows the opposite spectral shift towards higher energy, with an absorption decrease below the Fe edge and an increase just above it.

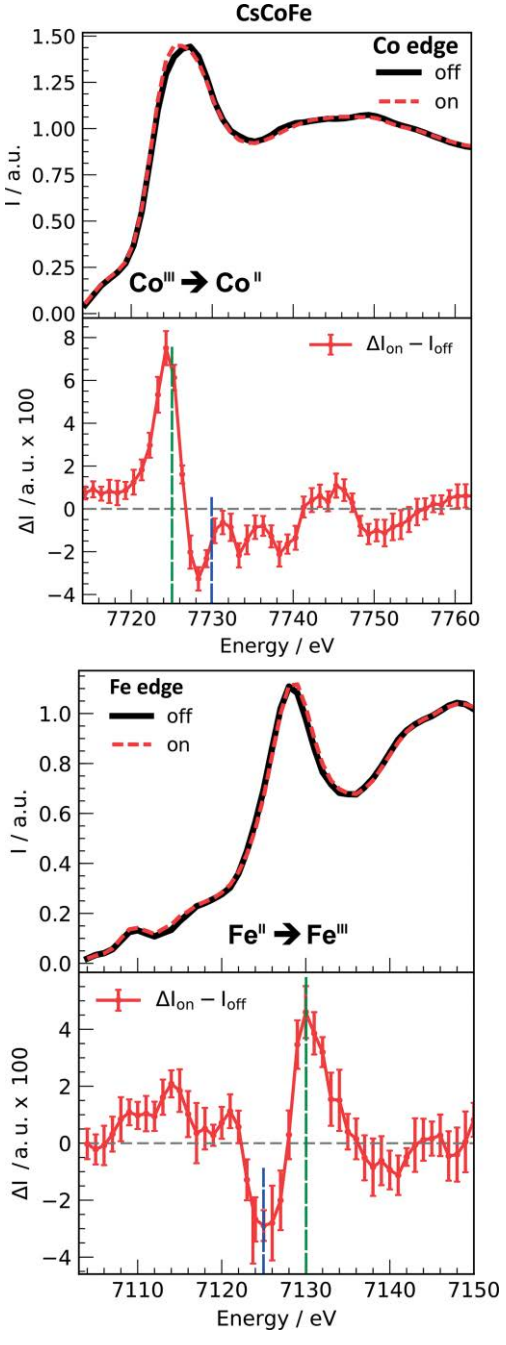

Figure 3. XANES spectra for the CsCoFe nanocrystals at the Fe and Co edges before (black) and 500 ps after laser excitation (red) and the corresponding spectral changes, $\Delta I(t)$.

Such changes in the absorption spectra are characteristic of a change in the formal oxidation state of the metal ions and, therefore, of the $Co^{III}(LS)Fe^{II} \rightarrow Co^{II}(HS)Fe^{III}$ electron transfer.[5d,14] Additional oscillating changes above the Co edge are characteristic of the local structural change around Co owing to spin crossover, as already observed for Fe in the SCO systems.[7h] The transient XANES changes, $\Delta I(t)$, after photoexcitation were measured at photon energies just above and below the Co and Fe absorption edges (Figure 4). These traces indicate that electron transfer occurs within the 100 ps time resolution of the experiment and that the photoinduced $Co^{II}(HS)Fe^{III}$ state has a lifetime longer than 1 ns at room temperature.

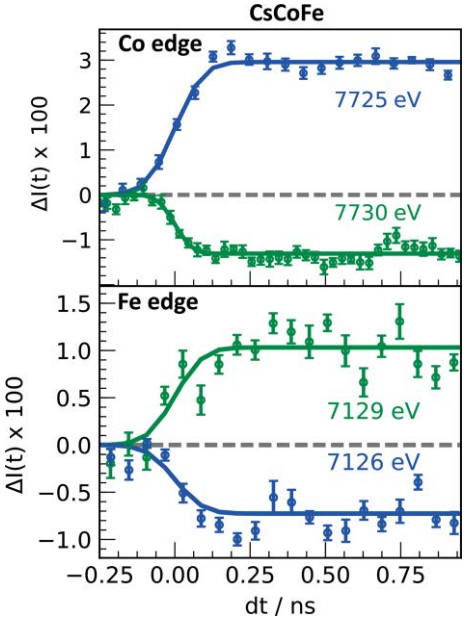

Figure 4. Time scans of the relative absorption changes at selected X-ray energies below and above the Co and Fe edges for the CsCoFe nanocrystals.

Cartier dit Moulin et al. reported that irradiation induced a shift in the pre-edge from 7711 to 7710 eV;[14a] this is difficult to see in Figure 3 because of experimental limitations, but it will be interesting to track in real time in future work.

For tracking the lifetime of the photoinduced $Co^{II}(HS)Fe^{III}(LS)$ state, we performed complementary optical measurements on the experimental setup available at the Institut de Physique de Rennes. We used time-resolved optical spectroscopy to study the relaxation process of the CsCoFe nanocrystals in solution that were photoexcited at room temperature by 650 nm optical pulses.

The probe wavelength was set to 520 nm, which corresponded to the maximum of the $Co^{III}(LS)Fe^{II} \rightarrow Co^{II}(HS)Fe^{III}$ absorption band (Figure S4 in the Supporting Information). The decrease in the time-resolved optical density (OD) after photoexcitation, shown in Figure 5, is due to depopulation of the $Co^{III}(LS)Fe^{II}$ state after photoexcitation and indicates that the $Co^{II}(HS)Fe^{III} \rightarrow Co^{III}(LS)Fe^{II}$ relaxation occurs within a few microseconds at room temperature.

We performed similar studies for the RbMnFe system. In difference to the CsCoFe system, the RbMnFe system is in the $Mn^{II}Fe^{III}$ state at room temperature. Upon cooling, thermal electron transfer leads to the $Mn^{III}Fe^{II}$ state at around 210 K with complete conversion below 190 K. The thermal transition shows

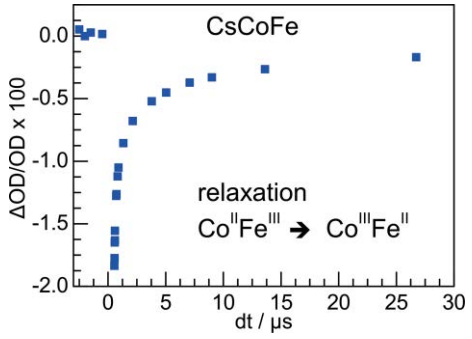

Figure 5. OD change at 520 nm after femtosecond laser irradiation at 650 nm for the CsCoFe nanocrystals.

a thermal hysteresis, and the back conversion towards the Mn^{II}-Fe^{III} state occurs around 300 K.[5f] We measured the X-ray absorption at the Mn edge at room temperature (Figure 6). The maximum around 6551 eV is characteristic of the Mn^{II} state.[13] At lower temperature (210 K), the intensity of this peak decreases, and a new one appears at 6557 eV, which is characteristic of the Mn^{III} state and is indicative of the thermal conversion of Mn^{II} into Mn^{III}, as reported previously.[13] This temperature corresponds to the descending branch of the thermal hysteresis, at which the $Mn^{III}Fe^{II}$ and $Mn^{II}Fe^{III}$ states coexist. We observed additional changes in the difference spectrum under continuous wave laser excitation at 400 nm, which switches the system from the $Mn^{II}Fe^{III}$ state to the $Mn^{III}Fe^{II}$ state.[5f] This is illustrated by a decrease (increase) in the Mn^{II} (Mn^{III}) peak in Figure 6.

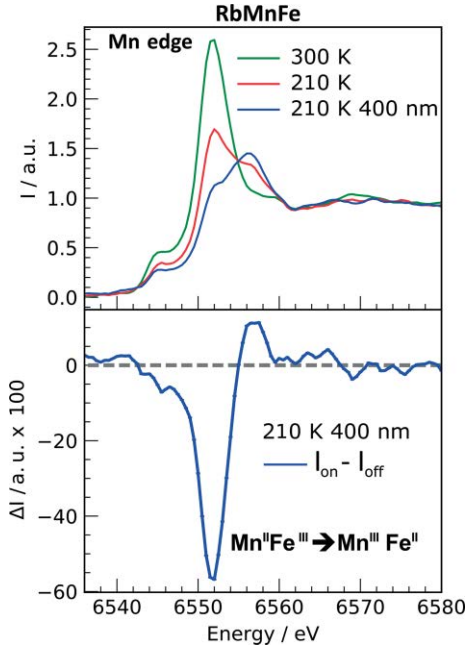

Figure 6. XANES spectra measured at the Mn edge for the RbMnFe compound at room temperature at 210 K and at 210 K under cw laser excitation at 400 nm with the corresponding spectral changes $\Delta I(t)$.

We then performed time-resolved XANES measurements on RbMnFe powder at 200 K. We monitored the transient XANES changes, $\Delta I(t)$, at 6557 eV, and we know that laser pulse photoexcitation at 530 nm is known to induce $Mn^{III}Fe^{II} \rightarrow Mn^{II}Fe^{III}$ electron transfer. The time trace reported in Figure 7 indicates that electron transfer occurs within the ca. 100 ps time resolution of the experiment. Time-resolved optical spectroscopy studies were used to monitor the relaxation process of RbMnFe at 140 K. The relaxation is characterized by transient changes in the optical transmission probed by a femtosecond laser pulse at 650 nm after excitation at 530 nm. The data presented in Figure 8 indicate that $Mn^{II}Fe^{III} \rightarrow Mn^{III}Fe^{II}$ relaxation occurs within ca. 10 μs.

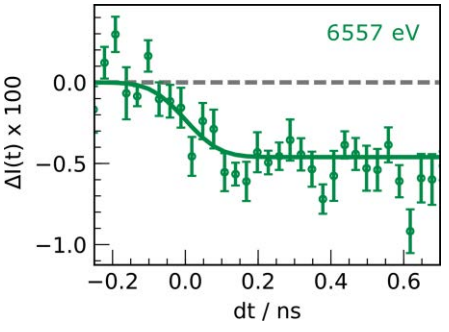

Figure 7. Time scans for relative absorption changes at 6557 eV for RbMnFe after femtosecond laser excitation at 530 nm.

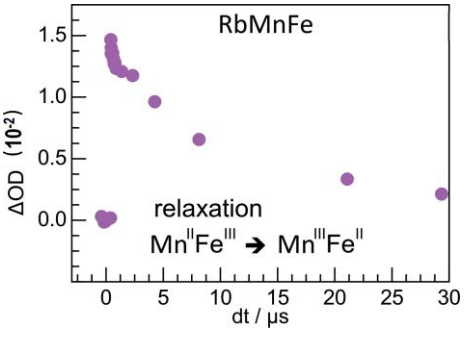

Figure 8. OD changes for the RbMnFe compound at 650 nm after a femtosecond laser pulse at 530 nm.

Conclusions

The present study revealed transient CT states in different PBAs, as characterized by time-resolved optical spectroscopy and time-resolved XANES. The lifetimes of the CT states were in the 1–10 μs range in the 200–300 K temperature range. This study also showed that it was possible to perform time-resolved studies with nanocrystals in solution. It opens new possibilities to extend XANES studies to X-ray free electron lasers to track the intrinsic dynamics at the sub-picosecond timescale, as recently performed for spin-crossover molecules in solution and in crystals.[7h,8c,8e,8h]

Experimental Section

Synthesis and Characterization of $CsCoFe(CN)_6$ Nanocrystals: Nanocrystals noted $CsCoFe(CN)_6$ were prepared by mixing two solutions, one containing $K_3[Fe^{III}(CN)_6]$ and CsCl and one containing

$Co^{II}Cl_2 \cdot 6H_2O$. The nanocrystals present in solution were embedded in polyvinylpyrrolidone (PVP), as already described for other similar nanocrystals.[15] The size of the objects was probed in solution before adding PVP and was found to be close to 15 nm (see Figure S1). The size was confirmed by transmission electron microscopy imaging (see Figure S2). X-ray powder diffraction measurement gave the expected face-centered cubic structure with a cell parameter of 9.96 Å, characteristic of the Fe^{II}–Co^{III} lattice; electron transfer from Co to Fe thus occurred during the synthesis of the nanocrystals.[5d] The infrared spectrum in the 2000–2200 cm^{-1} region has an intense band at 2112 nm corresponding to the asymmetric cyanide vibration of the Fe^{II}–CN–Co^{III} lattice; the weak band at 2070 nm corresponds to the $Fe^{II}(CN)_6^{4-}$ species present at the surface of the 15 nm particles (see Figure S3). Elemental analysis gave the following composition: $Cs_{0.58}\{Co[Fe(CN)_6]_{0.87}\}$. The time-resolved XANES studies were performed on nanocrystals embedded in PVP and dispersed in water. We also studied RbMnFe nanocrystals, which were obtained by adding a solution of manganese chloride to a mixed aqueous solution of rubidium chloride and potassium ferrocyanide. The precipitate was filtered and dried to give a light-brown powdered sample. By controlling the concentration of rubidium chloride in the synthetic solution, samples with different compositions were realized. Elemental analysis of the prepared sample showed that the formula was $RbMn[Fe(CN)_6]_{0.96} \cdot 2.6H_2O$ (394.97): calcd. Rb 21.64, Mn 13.91, Fe 13.86; found Rb 21.98, Mn 13.85, Fe 13.79. A SEM photograph of this sample is provided in Figure S5. Time-resolved optical pump–probe spectroscopy allowed tracking of the lifetime of the charge-transfer states through optical absorption change. We used the optical pump–probe setup described in ref.[16] for which the synchronization between the pump and probe femtosecond amplifiers was electronically tuned for time delays in the 10 ns–1 ms range, whereas a mechanical translation stage set the optical path difference for sub-nanosecond measurements. The experiments were configured in the visible/near-IR transmission geometry with a quasicollinear configuration of the pump and probe beams. We used 60 fs laser pulses at 650 nm (532 nm) to photoexcite CsCoFe (RbMnFe) and at 520 nm (650 nm) to probe the relaxation dynamics. More details about the experimental setup are presented in the paper by Lorenc et al.[16] Time-resolved XANES measurements were performed by using the optical pump/X-ray probe technique at the ID09 beamline. We used the X-ray pulses delivered from the ESRF by using the 16 bunch filling mode. The energy of X-ray emitted by the undulators (U27 and U17) was controlled by opening the gap between the undulators. The X-ray beam passed through a cryocooled (100 K) Si(111) double crystal monochromator and was focused at the sample position with a toroidal mirror. Two choppers were used to decrease the repetition rate of the X-ray train of pulses to 1 kHz.[17] Temporal overlap of the X-ray/optic pulses was measured with a GaAs detector, which is sensitive to both radiations, with a precision of 25 ps, and the time delay between both pulses was electronically controlled. At the overlap position, the optical pump and the X-ray probe had pulse durations of 150 fs and 70 ps, respectively, with focal areas of 120×350 and 60×120 µm, respectively. The sample was excited in a quasicollinear geometry (angle between X-ray and laser beam of ca. 10°). The solution sample was circulated by a closed-loop system through a 0.5 mm capillary tube, and the rate flow was maintained by using a peristaltic pump (Gilson Minipuls 3). A 2D detector (MAXIPIX) was mounted close to the sample (ca. 3 cm) perpendicular to the X-ray propagation direction to minimize the collection of elastic photon scattering. In this geometry, the active window (28.4×28.4 mm^2) covered a solid angle of ca. 0.74 sr (5.89 % of 4π). We used a pin diode to measure simultaneously the transmission and scattered X-ray to normalize the final fluorescence signal (intensity fluctuation, the long decay of the current after each refill).

Acknowledgments

Parts of this research were performed in the frame of the IM-LED LIA (CNRS) and the Japan Society for the Promotion of Science (JSPS) Grant-in-Aid for Specially Promoted Research 15H05697 and JSPS KAKENHI 16H06521 Coordination Asymmetry. This work was supported by the ANR FEMTOMAT (ANR-13-BS04-0002) and the European Union's Horizon 2020 Research and Innovation program under the Marie Skłodowska-Curie Grant Agreement No. 637295.

Keywords: Charge transfer · Magnetic properties · X-ray absorption spectroscopy · Time-resolved spectroscopy

[1] a) M. Gao, C. Lu, H. Jean-Ruel, L. C. Liu, A. Marx, K. Onda, S. Y. Koshihara, Y. Nakano, X. Shao, T. Hiramatsu, G. Saito, H. Yamochi, R. R. Cooney, G. Moriena, G. Sciaini, R. J. Miller, *Nature* **2013**, *496*, 343–346; b) S.-y. Koshihara, Y. Takahashi, H. Sakai, Y. Tokura, T. Luty, *J. Phys. Chem. B* **1999**, *103*, 2592–2600; c) L. Guérin, J. Hébert, M. Buron-Le Cointe, S. Adachi, S. Koshihara, H. Cailleau, E. Collet, *Phys. Rev. Lett.* **2010**, *105*, 246101; d) E. Collet, M. Buron-Le Cointe, M. H. Lemée-Cailleau, H. Cailleau, L. Toupet, M. Meven, S. Mattauch, G. Heger, N. Karl, *Phys. Rev. B* **2001**, *63*, 054105; e) E. Collet, M. H. Lemee-Cailleau, M. Buron-Le Cointe, H. Cailleau, M. Wulff, T. Luty, S. Y. Koshihara, M. Meyer, L. Toupet, P. Rabiller, S. Techert, *Science* **2003**, *300*, 612–615; f) T. Ishikawa, N. Fukazawa, Y. Matsubara, R. Nakajima, K. Onda, Y. Okimoto, S. Koshihara, M. Lorenc, E. Collet, M. Tamura, R. Kato, *Phys. Rev. B* **2009**, 80.

[2] a) M. Fiebig, K. Miyano, Y. Tomioka, Y. Tokura, *J. Appl. Phys.* **1999**, *85*, 5561–5563; b) S. Ohkoshi, Y. Tsunobuchi, T. Matsuda, K. Hashimoto, A. Namai, F. Hakoe, H. Tokoro, *Nat. Chem.* **2010**, *2*, 539–545; c) H. Tokoro, M. Yoshikiyo, K. Imoto, A. Namai, T. Nasu, K. Nakagawa, N. Ozaki, F. Hakoe, K. Tanaka, K. Chiba, R. Makiura, K. Prassides, S. Ohkoshi, *Nat. Commun.* **2015**, *6*, 7037.

[3] a) T. Fukaminato, T. Hirose, T. Doi, M. Hazama, K. Matsuda, M. Irie, *J. Am. Chem. Soc.* **2014**, *136*, 17145–17154; b) M. Irie, T. Fukaminato, K. Matsuda, S. Kobatake, *Chem. Rev.* **2014**, *114*, 12174–12277.

[4] a) S. Decurtins, P. Gütlich, C. P. Köhler, H. Spiering, A. Hauser, *Chem. Phys. Lett.* **1984**, *105*, 1–4; b) A. Hauser, *Top. Curr. Chem.* **2004**, *234*, 155–198; c) A. Goujon, F. Varret, K. Boukheddaden, C. Chong, J. Jeftić, Y. Garcia, A. D. Naik, J. C. Ameline, E. Collet, *Inorg. Chim. Acta* **2008**, *361*, 4055–4064; d) K. D. Murnaghan, C. Carbonera, L. Toupet, M. Griffin, M. M. Dirtu, C. Desplanches, Y. Garcia, E. Collet, J. F. Letard, G. G. Morgan, *Chem. Eur. J.* **2014**, *20*, 5613–5618; e) J.-F. Létard, P. Guionneau, E. Codjovi, O. Lavastre, G. Bravic, D. Chasseau, O. Kahn, *J. Am. Chem. Soc.* **1997**, *119*, 10861–10862; f) K. Ichiyanagi, J. Hebert, L. Toupet, H. Cailleau, P. Guionneau, J. F. Létard, E. Collet, *Phys. Rev. B* **2006**, 73; g) N. Brefuel, H. Watanabe, L. Toupet, J. Come, N. Matsumoto, E. Collet, K. Tanaka, J. P. Tuchagues, *Angew. Chem. Int. Ed.* **2009**, *48*, 9304–9307; *Angew. Chem.* **2009**, *121*, 9468–9471; h) A. Bousseksou, G. Molnar, L. Salmon, W. Nicolazzi, *Chem. Soc. Rev.* **2011**, *40*, 3313–3335; i) E. Trzop, D. Zhang, L. Pineiro-Lopez, F. J. Valverde-Munoz, M. C. Munoz, L. Palatinus, L. Guerin, H. Cailleau, J. A. Real, E. Collet, *Angew. Chem. Int. Ed.* **2016**, *55*, 8675–8679; *Angew. Chem.* **2016**, *128*, 8817–8821; j) J. E. Clements, J. R. Price, S. M. Neville, C. J. Kepert, *Angew. Chem. Int. Ed.* **2016**, *55*, 15105–15109; *Angew. Chem.* **2016**, *128*, 15329–15333; k) E. Collet, M. L. Boillot, J. Hebert, N. Moisan, M. Servol, M. Lorenc, L. Toupet, M. Buron-Le Cointe, A. Tissot, J. Sainton, *Acta Crystallogr., Sect. B* **2009**, *65*, 474–480.

[5] a) M. Verdaguer, A. Bleuzen, V. Marvaud, J. Vaissermann, M. Seuleiman, C. Desplanches, A. Scuiller, C. Train, R. Garde, G. Gelly, C. Lomenech, I. Rosenman, P. Veillet, C. Cartier, F. Villain, *Coord. Chem. Rev.* **1999**, *190–192*, 1023–1047; b) R. Lescouezec, J. Vaissermann, C. Ruiz-Perez, F. Lloret, R. Carrasco, M. Julve, M. Verdaguer, Y. Dromzee, D. Gatteschi, W. Wernsdorfer, *Angew. Chem. Int. Ed.* **2003**, *42*, 1483–1486; *Angew. Chem.* **2003**,

115, 1521–1524; c) A. Dei, *Angew. Chem. Int. Ed.* **2005**, *44*, 1160–1163; *Angew. Chem.* **2005**, *117*, 1184–1187; d) J. D. Cafun, J. Lejeune, F. Baudelet, P. Dumas, J. P. Itie, A. Bleuzen, *Angew. Chem. Int. Ed.* **2012**, *51*, 9146–9148; *Angew. Chem.* **2012**, *124*, 9280–9282; e) H. W. Liu, K. Matsuda, Z. Z. Gu, K. Takahashi, A. L. Cui, R. Nakajima, A. Fujishima, O. Sato, *Phys. Rev. Lett.* **2003**, *90*, 167403; f) H. Tokoro, S. Ohkoshi, *Bull. Chem. Soc. Jpn.* **2015**, *88*, 227–239; g) K. K Orisaku, K. Nakabayashi, S. Ohkoshi, *Chem. Lett.* **2011**, *40*, 586–587; h) K. Zhang, S. Kang, Z. S. Yao, K. Nakamura, T. Yamamoto, Y. Einaga, N. Azuma, Y. Miyazaki, M. Nakano, S. Kanegawa, O. Sato, *Angew. Chem. Int. Ed.* **2016**, *55*, 6047–6050; *Angew. Chem.* **2016**, *128*, 6151–6154; i) O. Sato, T. Iyoda, A. Fujishima, K. Hashimoto, *Science* **1996**, *272*, 704–705; j) F. Volatron, D. Heurtaux, L. Catala, C. Mathoniere, A. Gloter, O. Stephan, D. Repetto, M. Clemente-Leon, E. Coronado, T. Mallah, *Chem. Commun.* **2011**, *47*, 1985–1987; k) M. F. Dumont, E. S. Knowles, A. Guiet, D. M. Pajerowski, A. Gomez, S. W. Kycia, M. W. Meisel, D. R. Talham, *Inorg. Chem.* **2011**, *50*, 4295–4300; l) S. Ohkoshi, S. Takano, K. Imoto, M. Yoshikiyo, A. Namai, H. Tokoro, *Nat. Photonics* **2013**, *8*, 65–71.

[6] M. A. Halcrow, *Spin-Crossover Materials: Properties and Applications*, Wiley, Chichester, **2013**.

[7] a) G. Aubock, M. Chergui, *Nat. Chem.* **2015**, *7*, 629–633; b) W. K. Zhang, R. Alonso-Mori, U. Bergmann, C. Bressler, M. Chollet, A. Galler, W. Gawelda, R. G. Hadt, R. W. Hartsock, T. Kroll, K. S. Kjaer, K. Kubicek, H. T. Lemke, H. Y. W. Liang, D. A. Meyer, M. M. Nielsen, C. Purser, J. S. Robinson, E. I. Solomon, Z. Sun, D. Sokaras, T. B. van Driel, G. Vanko, T. C. Weng, D. L. Zhu, K. J. Gaffney, *Nature* **2014**, *509*, 345–348; c) J. K. McCusker, A. Vlček, *Acc. Chem. Res.* **2015**, *48*, 1207–1208; d) K. Hong, H. Cho, R. W. Schoenlein, T. K. Kim, N. Huse, *Acc. Chem. Res.* **2015**, *48*, 2957–2966; e) J. J. McGarvey, I. Lawthers, K. Heremans, H. Toftlund, *J. Chem. Soc., Chem. Commun.* **1984**, 1575–1576; f) J. K. Mccusker, K. N. Walda, R. C. Dunn, J. D. Simon, D. Magde, D. N. Hendrickson, *J. Am. Chem. Soc.* **1993**, *115*, 298–307; g) C. Bressler, C. Milne, V. T. Pham, A. ElNahhas, R. M. van der Veen, W. Gawelda, S. Johnson, P. Beaud, D. Grolimund, M. Kaiser, C. N. Borca, G. Ingold, R. Abela, M. Chergui, *Science* **2009**, *323*, 489–492; h) H. T. Lemke, K. S. Kjær, R. Hartsock, T. Brandt van Driel, M. Chollet, J. M. Glownia, S. Song, D. Zhu, E. Pace, S. F. Matar, M. N. Nielsen, M. Benfatto, K. J. Gaffney, E. Collet, M. Cammarata, *Nat. Commun.* **2017**, *8*, 15342; i) H. T. Lemke, C. Bressler, L. X. Chen, D. M. Fritz, K. J. Gaffney, A. Galler, W. Gawelda, K. Haldrup, R. W. Hartsock, H. Ihee, J. Kim, K. H. Kim, J. H. Lee, M. M. Nielsen, A. B. Stickrath, W. K. Zhang, D. L. Zhu, M. Cammarata, *J. Phys. Chem. A* **2013**, *117*, 735–740; j) S. E. Canton, X. Y. Zhang, L. M. L. Daku, A. L. Smeigh, J. X. Zhang, Y. Z. Liu, C. J. Wallentin, K. Attenkofer, G. Jennings, C. A. Kurtz, D. Gosztola, K. Warnmark, A. Hauser, V. Sundstrom, *J. Phys. Chem. C* **2014**, *118*, 4536–4545.

[8] a) R. Bertoni, M. Lorenc, H. Cailleau, A. Tissot, J. Laisney, M. L. Boillot, L. Stoleriu, A. Stancu, C. Enachescu, E. Collet, *Nat. Mater.* **2016**, *15*, 606–610; b) R. Bertoni, M. Lorenc, T. Graber, R. Henning, K. Moffat, J. F. Létard, E. Collet, *CrystEngComm* **2016**, *18*, 7269–7275; c) R. Bertoni, M. Cammarata, M. Lorenc, S. F. Matar, J. F. Letard, H. T. Lemke, E. Collet, *Acc. Chem. Res.* **2015**, *48*, 774–781; d) R. Bertoni, M. Lorenc, A. Tissot, M. L. Boillot, E. Collet, *Coord. Chem. Rev.* **2015**, *282–283*, 66–76; e) M. Cammarata, R. Bertoni, M. Lorenc, H. Cailleau, S. Di Matteo, C. Mauriac, S. F. Matar, H. Lemke, M. Chollet, S. Ravy, C. Laulhe, J. F. Letard, E. Collet, *Phys. Rev. Lett.* **2014**, *113*, 227402; f) R. Bertoni, M. Lorenc, A. Tissot, M. Servol, M. L. Boillot, E. Collet, *Angew. Chem. Int. Ed.* **2012**, *51*, 7485–7489; *Angew. Chem.* **2012**, *124*, 7603–7607; g) E. Collet, N. Moisan, C. Balde, R. Bertoni, E. Trzop, C. Laulhe, M. Lorenc, M. Servol, H. Cailleau, A. Tissot, M. L. Boillot, T. Graber, R. Henning, P. Coppens, M. Buron-Le Cointe, *Phys. Chem. Chem. Phys.* **2012**, *14*, 6192–6199; h) A. Marino, M. Cammarata, S. F. Matar, J.-F. Létard, G. Chastanet, M. Chollet, J. M. Glownia, H. T. Lemke, E. Collet, *Struct. Dynamics* **2016**, *3*, 023605; i) A. Marino, M. Buron-Le Cointe, M. Lorenc, L. Toupet, R. Henning, A. D. DiChiara, K. Moffat, N. Brefuel, E. Collet, *Faraday Discuss.* **2015**, *177*, 363–379; j) A. Marino, P. Chakraborty, M. Servol, M. Lorenc, E. Collet, A. Hauser, *Angew. Chem. Int. Ed.* **2014**, *53*, 3863–3867; *Angew. Chem.* **2014**, *126*, 3944–3948; k) S. Zerdane, L. Wilbraham, M. Cammarata, O. Iasco, E. Rivière, M. L. Boillot, I. Ciofini, E. Collet, *Chem. Sci.* **2017**, *8*, 4978–4986.

[9] D. C. Arnett, P. Voehringer, N. F. Scherer, *J. Am. Chem. Soc.* **1995**, *117*, 12262–12272.

[10] A. Asahara, M. Nakajima, R. Fukaya, H. Tokoro, S. Ohkoshi, T. Suemoto, *Phys. Rev. B* **2012**, *86*, 195138.

[11] Y. Moritomo, T. Nakagawa, Y. Fukuyama, N. Yasuda, H. Oosawa, J. E. Kim, H. Kamioka, K. Kato, Y. Tanaka, S. Kimura, F. Nakada, S. Ohkoshi, H. Tanaka, M. Takata, *J. Phys. Conf. Ser.* **2009**, *148*, 012028.

[12] Y. Moritomo, H. Kamioka, T. Shibata, S. Nozawa, T. Sato, S. Adachi, *J. Phys. Soc. Jpn.* **2013**, *82*, 033601.

[13] H. Osawa, T. Iwazumi, H. Tokoro, S. Ohkoshi, K. Hashimoto, H. Shoji, E. Hirai, T. Nakamura, S. Nanao, Y. Isozumi, *Solid State Commun.* **2003**, *125*, 237–241.

[14] a) C. Cartier dit Moulin, F. Villain, A. Bleuzen, M.-A. Arrio, P. Sainctavit, C. Lomenech, V. Escax, F. Baudelet, E. Dartyge, J.-J. Gallet, M. Verdaguer, *J. Am. Chem. Soc.* **2000**, *122*, 6653–6658; b) T. Yokoyama, Y. Murakami, M. Kiguchi, T. Komatsu, N. Kojima, *Phys. Rev. B* **1998**, *58*, 14238–14244.

[15] a) D. Brinzei, L. Catala, N. Louvain, G. Rogez, O. Stephan, A. Gloter, T. Mallah, *J. Mater. Chem.* **2006**, *16*, 2593–2599; b) L. Catala, T. Mallah, *Coord. Chem. Rev.* **2017**, 32–61.

[16] M. Lorenc, Ch. Balde, W. Kaszub, A. Tissot, N. Moisan, M. Servol, M. Buron-Le Cointe, H. Cailleau, P. Chasle, P. Czarnecki, M. L. Boillot, E. Collet, *Phys. Rev. B* **2012**, *85*, 054302.

[17] M. Cammarata, L. Eybert, F. Ewald, W. Reichenbach, M. Wulff, P. Anfinrud, F. Schotte, A. Plech, Q. Kong, M. Lorenc, B. Lindenau, J. Rabiger, S. Polachowski, *Rev. Sci. Instrum.* **2009**, *80*, 015101.

Received: June 4, 2017

Photoinduced Charge Transfer

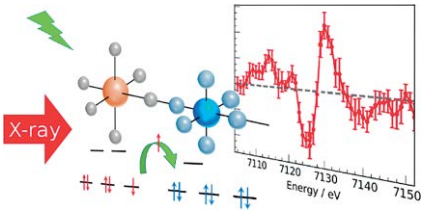

We studied the transient electron-transfer process induced by a femtosecond laser pulse in nanocrystals of CsCoFe and RbMnFe Prussian Blue analogues by time-resolved X-ray absorption near-edge structure and time-resolved optical spectroscopy. The results clearly evidence ultrafast Co^{III}(low spin)$Fe^{II} \rightarrow Co^{II}$(high spin)$Fe^{III}$ and Mn^{III}(low spin)$Fe^{II} \rightarrow Mn^{II}$(high spin)$Fe^{III}$ electron-transfer processes.

DOI: 10.1002/ejic.201700657

10.1002/chem.201704746

WILEY-VCH

COMMUNICATION

Electronic and structural dynamics during the switching of the photomagnetic complex $[Fe(L_{222}N_5)(CN)_2]$

S. Zerdane,[a] E. Collet,*[a] X. Dong,[a] S. F. Matar, [b,c] H. F. Wang,[b] C. Desplanches,[b] G. Chastanet,[b] M. Chollet,[d] J. M. Glownia,[d] H.T. Lemke,[d,e] M. Lorenc,[a] M. Cammarata,*[a]

Abstract: The $[Fe(L_{222}N_5)(CN)_2]$ compound, where $L_{222}N_5$ refers to the macrocyclic Schiff-base ligand, 2,13-dimethyl-3,6,9,-12,18-pentaazabicyclo[12.3.1]octadeca-1(18),2,12,14,16-pentaene, is a photomagnetic Fe^{II} based coordination compound, which undergoes light-induced excited spin-state trapping (LIESST). The low spin state is hexacoordinated and the high spin state heptacoordinated. This system also serves as complex for the design of trinuclear or one-dimensional compounds made of other types of bricks with diverse coordinated metals. Here we study its ultrafast spin-state photoswitching dynamics, by combining femtosecond optical spectroscopy and femtosecond X-ray absorption measurements at the XPP station of the X-ray free-electron laser LCLS. DFT and TD-DFT calculations are used to interpret experimental findings. These studies performed in the solution phase show that LIESST in $[Fe(L_{222}N_5)(CN)_2]$ occurs on the 100 fs timescale under different types of photoexcitation. In addition, we observe coherent oscillations resulting from the structural dynamics accompanying LIESST, which were recently evidenced in more conventional octahedral $Fe^{II}N_6$ systems.

Introduction

The design of materials able to store information on the single molecule level or on assemblies of molecules is a current challenge in information technology. Among all the investigated systems, an interesting class of molecular switches are those undergoing the light-induced excited spin state trapping (LIESST) phenomenon, between low spin (LS) and high spin (HS) states. LIESST was deeply investigated in many spin-crossover materials and especially in $Fe^{II}N_6$ systems.[1] In the solid state, LIESST can be induced at low temperature by conventional techniques since the photoinduced HS state is long-lived.[2] At high temperature, LIESST is transient and can be studied by time-resolved techniques, down to the femtosecond timescale, in solution[3] or in solids[4]. Several studies using optical spectroscopy, X-ray spectroscopy or IR spectroscopy demonstrated that LIESST occurs on the 100 fs timescale from the initial photoexcited state (MLCT, LMCT or d-d) to the HS state. Very recent studies focused on the ultrafast structural dynamics accompanying LIESST. Between the two spin states, an important structural reorganization occurs: the population of antibonding orbitals in the HS state increases the equilibrium Fe-ligand distance. However, as the system reaches the HS potential at a position different from the equilibrium structure, a coherent structural dynamics starts, related to the activation and damping of the breathing mode, i.e. the expansion of the FeN_6 core.[3h, 4c, 4h, 5] In the Fe systems for which LIESST was investigated on femtosecond timescale, the iron is hexacoordinated in both LS and HS states with $Fe^{II}N_6$, $Fe^{II}N_4O_2$ or $Fe^{III}N_4O_2$.

In this paper we study the $[Fe(L_{222}N_5)(CN)_2]$ photomagnetic Fe^{II} coordination compound, involving the $L_{222}N_5$ macrocyclic Schiff-base ligand, 2,13-dimethyl-3,6,9,-12,18-pentaazabicyclo[12.3.1]octadeca-1(18),2,12,14,16-pentaene (Fig. 1). This complex was originally synthesized by Nelson et al. and was found to be in the low-spin state at room temperature.[6] $[Fe(L_{222}N_5)(CN)_2]$ also serves as linker for the design of trinuclear molecular complexes or one-dimensional compounds made of other types of coordinated metal bricks.[7] Its photomagnetic properties allow for example to switch “on” and “off” the magnetic interaction between the photoinduced Fe^{II} HS unit (S = 2) and the Mn^{III} ions in Mn-Fe-Mn trimers. The structure of this complex was revealed in the $[Fe(L_{222}N_5)(CN)_2]\cdot H_2O$ complex by Ababei et al, where the system is LS at 150 K. The Fe^{II} ion is then hexacoordinated (Fig. 1) with 2 cyanido ligands in axial positions (Fe-CN=1.94−1.96 Å) and 4 N atoms from the macrocyclic ligand $L_{222}N_5$ equatorial plane (Fe-N_{eq} =1.84−2.1 Å). The fifth N atom of the $L_{222}N_5$ ligand is uncoordinated since Fe-N = 3.5 Å. Costa et al reported that this system remains LS up to 420 K, but that it undergoes light-induced excited spin-state trapping from LS (S=0) to HS (S=2) states at low temperature, by photoexcitation at 532 nm. This photoinduced HS state remains stable up to a typical temperature T(LIESST) ≈110K, as characterized by magnetic susceptibility measurements after light irradiation.[8] In addition, temperature-dependent diffuse absorption spectra of the hydrated $[Fe(L_{222}N_5)(CN)_2].H_2O$ complex, measured in the 450-850 nm range was also used to characterize the change of electronic state. The switching from LS to HS is associated with an increase of optical absorption above ≈ 640 nm and a decrease below. In the following, we exploit these spectroscopic fingerprints, to study the ultrafast photoswitching dynamics. Ababei et al. also revealed the structure of the complex in its HS state, which appears in the structure of $[(Mn(saltmen)_2Fe(L_{222}N_5)(CN)_2](ClO_4)_2\cdot 0.5CH_3OH$. In this trinuclear complex, the two [Mn(saltmen)] moieties are bridged by one $[Fe^{II}(L_{222}N_5)(CN)_2]$ brick, which is in the HS state. It was found that the HS Fe^{II} metal ion is then heptacoordinated, by 2 axial CN groups (Fe−CN = 2.17−2.18 Å) and the 5 N atoms of the macrocyclic $L_{222}N_5$ ligand (with Fe−N =2.15−2.32 Å, Fig. 1).

[a] S. Zerdane, E. Collet, X. Dong, M. Lorenc, M. Cammarata
Univ Rennes 1, CNRS, Institut de Physique de Rennes, UMR 6251, UBL, F-35042 Rennes, France
E-mail: eric.collet@univ-rennes1.fr, marco.cammarata@univ-rennes1.fr
[b] H. F. Wang, C. Desplanches, G. Chastanet, S. F. Matar,
CNRS, Université de Bordeaux, ICMCB, 87 avenue du Dr A. Schweitzer, Pessac, F'33608, France
[c] Lebanese German University (LGU), Sahel Alam Campus, P.O.BOX 206 Jounieh. Lebanon
[c] M. Chollet, J. M. Glownia, Henrik Lemke
LCLS, SLAC National Laboratory, Menlo Park, 94025, CA, USA.
[d] H.T. Lemke, SwissFEL, Paul Scherrer Institut, Villigen PSI 5232, Switzerland

10.1002/chem.201704746

Here we use femtosecond optical spectroscopy, at the Institut de Physique de Rennes[9] and femtosecond X-ray absorption at the XPP station[10] of the LCLS X-ray Free Electron Laser (X-FEL) to study in real time the photoswitching dynamics of $[Fe(L_{222}N_5)(CN)_2]$ in solution. The sample was photoexcited by ≈50 fs laser pulse at different wavelengths in the [490–680] nm range (see experimental section).

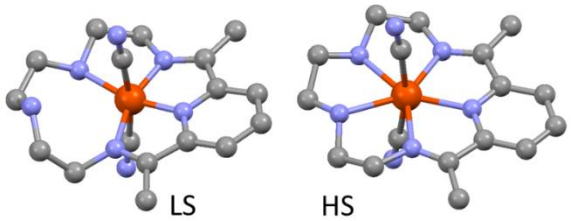

Figure 1. Structures obtained by Ababei et al,[8] in LS $[Fe(L_{222}N_5)(CN)_2]\cdot H_2O$ crystals (left) and in the complex $[(Mn(saltmen))_2Fe(L_{222}N_5)(CN)_2](ClO_4)_2\cdot 0.5CH_3OH$, where HS $[Fe(L_{222}N_5)(CN)_2]$ (right) connects two [Mn(saltmen)] units (not shown).

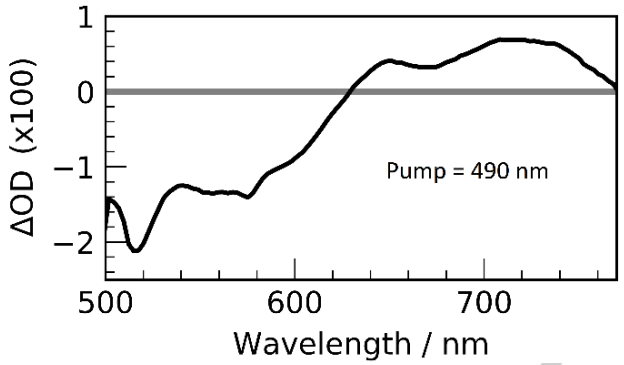

Figure 2. Variation of the optical density (ΔOD) recorded with white-light spectrometer 2 ps after photo-excitation at 490 nm. The OD increase in the IR (above ≈640 nm) and decrease in the visible parts of the spectrum is characteristic of the change from LS to HS states, as observed by LIESST experiments at low temperature.

Results and Discussion

Femtosecond optical spectroscopy was used to study the ultrafast spin-state switching dynamics of $[Fe(L_{222}N_5)(CN)_2]$ dissolved in water at room temperature. We used different pump and probe wavelengths. We measured the spectral optical density change (ΔOD) in the 500-770 nm range with white-light spectroscopy, after photoexcitation at 490 nm (≈10μJ.mm^{-2}). We show in Fig. 2 the OD change measured 2 ps after photo-excitation. The OD decrease below ≈ 640 nm (visible) and OD increase above (IR) are characteristic of the LIESST effect, also characterized by a photomagnetic experiment at low temperature,[8] and the change in figure 2 can be safely attributed photoswitching from LS to HS. Single-wavelength probe (680 nm) measurements gave more details about the switching dynamics induced by 490 nm pump (Fig. 3a). We observe two main steps: a transient peak immediately after laser excitation followed by a fast OD increase and a slower change towards a plateau on the ps timescale. These features are similar to the ones observed during LIESST in $Fe^{II}N_6$ systems with an almost octahedral coordination. The transient peak is the signature of the short-lived MLCT, which rapidly decays towards the HS state with a corresponding OD change within $\tau \approx 100$ fs. The slower OD change within $\tau_{VC} \approx 3$ ps corresponds to vibrational cooling in the HS potential.[3],[4] In addition, a damped oscillation at ≈ 47 cm^{-1} (710 fs period) accompanies the process. The global OD increase in IR and decrease in visible range, observed during conversion from LS to HS state on the ps timescale (Fig. 2), are also observed for photoexcitation at 530, 580 and 680 nm (Fig. 3 b-d). However, the photo-switching dynamics are different, as shown here for the OD change time traces measured at 490 nm probing wavelength for the different excitation wavelengths (Tab. 1).

We measured transient X-ray absorption change (XAS) at the Fe K edge, induced by photoexcitation at 530 nm, at the XPP station of the LCLS X-FEL. The relative change $\Delta I(t)/I_{off}$ at 7125 eV is sensitive to spin-state switching in Fe^{II} materials, including both electronic and structural contributions.[3g-i, 4e] Fig. 4 shows the $\Delta I(t)/I_{off}$ increases after photoexcitation, characteristic of the LS to HS transformation. A Transient change of opposite sign is also observed within the first 100 fs, which highlights the presence of one (or several) short-lived intermediate(s). These XAS results fingerprint the LS to HS spin-state photo-switching, accompanied by coherent oscillation (≈47 cm^{-1}).

To better understand the process, an accurate description of the initial excited states is required, and provided by DFT and time dependent DFT (TD-DFT) calculations.[11] TD-DFT lead to the natural transition orbitals (NTO), through an account for hole–particle pairs involved in the excited states induced by the pump light. TD-DFT as implemented in the Gaussian G09 package[12] was applied for obtaining the NTO of LS $[Fe(L_{222}N_5)(CN)_2]$, starting from geometry optimized molecule with UB3LYP/6-31g(d,p) functional-basis set, found to be similar to the hexacoordinated structure found by X-ray diffraction.[8] Because of the low symmetry of the molecule, the d orbitals of the Fe and the ligand orbitals are mixed. However, from Fig. 5 different types of photo-excitations can be distinguished. In the low energy excitation region, the 680 nm pump excitation corresponds well to the transition calculated at 1.91 eV. The hole has some d non-bonding character and the particle some d anti-bonding character. Both hole and particle NTOs involve the ligand. Given the low symmetry of the system, this excitation is analogous to a d-d transition (d-d excitation is forbidden in octahedral FeN_6 systems and allowed in lower symmetry systems,[13] like FeN_4O_2). We identify another type of d-d excitation at 2.12 eV (close to 580 nm). The hole has some d non-bonding character and the particle some d anti-bonding character, but the particle weight is strong on the CN groups of the ligand. Excitation around 530 nm corresponds to a transition calculated at 2.34 eV, which has a stronger metal-to-ligand charge-transfer character, with high particle weight on the macrocyclic ligand equatorial plane. In the following discussion, 680 nm excitation is referred to as d-d_1, 580 nm as d-d_2 and 530 nm as MLCT for the sake of simplicity.

To understand the nature of the oscillation observed in the photoinduced HS state, we carried G09 molecular vibration calculations in the heptacoordinated HS state. In the low frequency region, we found vibration modes at 30 cm^{-1}, 46 cm^{-1} and 52 cm^{-1}. The modes at 30 and 52 cm^{-1} correspond to ligand torsion modes.

10.1002/chem.201704746
WILEY-VCH

COMMUNICATION

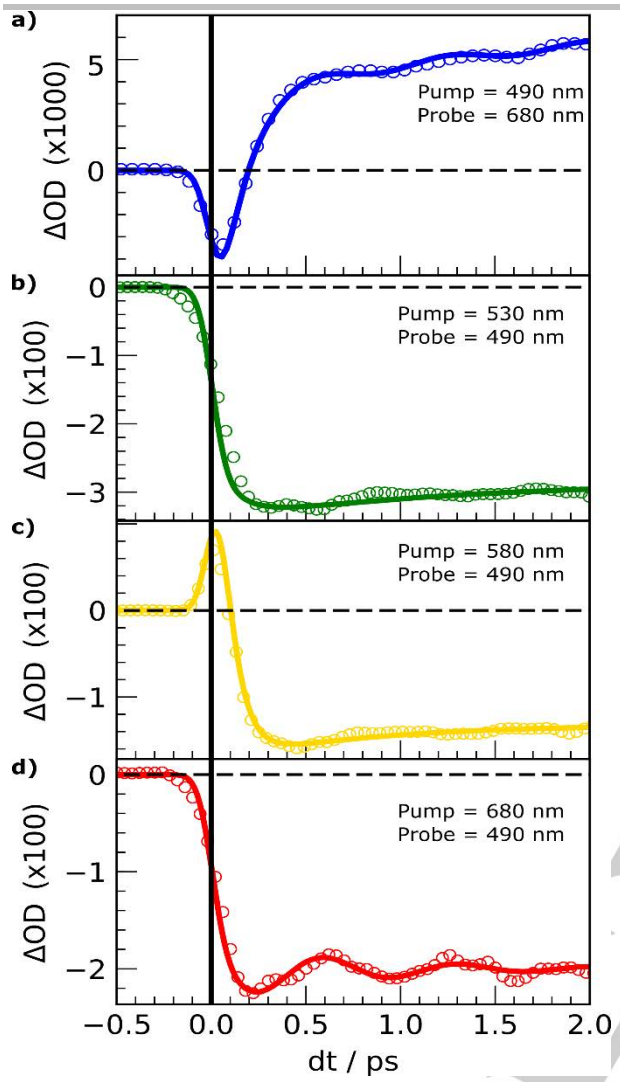

Figure 3. Kinetic traces of ΔOD at selected wavelengths obtained by two-colour pump-probe experiment at room temperature. The solid lines show the fit of the data, with a bi-exponential model describing the intermediate state, the vibrational cooling, and the coherent vibration in a and d.

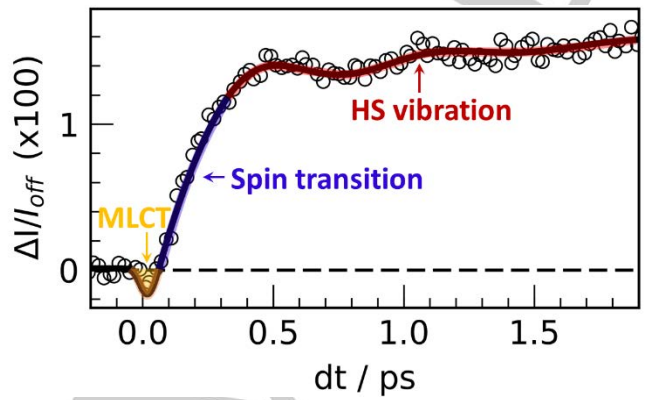

Figure 4. Time resolved change of the relative X-ray absorption $\Delta I(t)/I_{off}$ measured at 7125 eV. The fit (thick line) takes into account the spin transition with the MLCT to HS decay τ =150(10) fs and a damped oscillation with 710 fs period (47 cm^{-1}).

Table 1. Physical parameters used for the fits in Fig. 3-4. τ: LS-to-HS switching, τ_{VC}: vibrational cooling and ν: oscillation frequency.

Pump / probe	Figure	Excitation	τ (fs)	τ_{VC} (fs)	ν (cm^{-1})
490 nm / 680 nm	3a	MLCT	130 (10)	3.1 (2)	47 (1)
530 nm / 490 nm	3b	MLCT	120 (10)	1.2 (1)	-
580 nm / 490nm	3c	d-d	75 (10)	0.7 (1)	-
680 nm / 490 nm	3d	d-d	75 (10)	0.7 (1)	47 (1)
530 nm / 7125 eV	4	MLCT	150 (10)	-	47 (1)

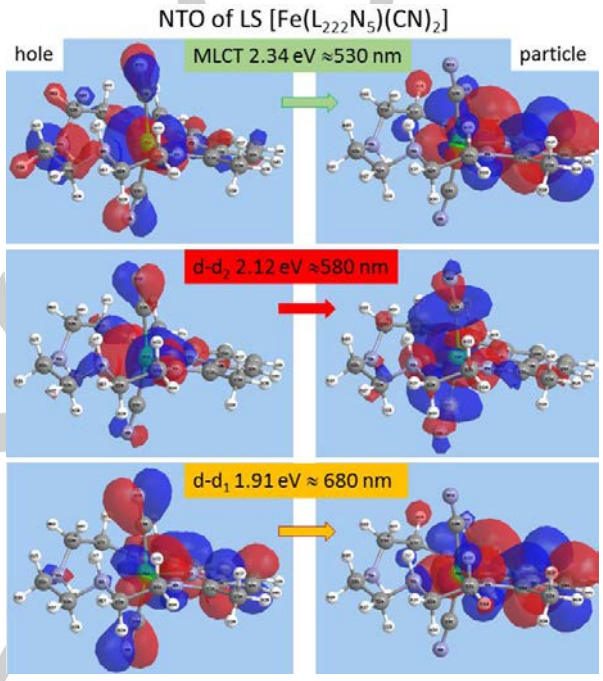

Figure 5. NTO of hole and particle for different excitation wavelengths, showing MLCT-like transition at high energy and d-d-like transitions at low energy.

Fig. 6 shows the main atomic motions for the mode calculated at 46 cm^{-1}, which is of specific interest for interpretation of the observed XANES oscillations. It corresponds to the bending of the NC-Fe-CN axis schematically indicated by the arrows showing opposite motions of Fe and CN groups. This induces small oscillation of some Fe-N bond lengths, as the macrocycle remains almost rigid in this mode. In addition, we found a stretching mode at 183 cm^{-1}, where three Fe-N bonds oscillate in phase and two remain almost constant (Fig. 6). We found another type of stretching mode at 263 cm^{-1}, with in-phase elongation of the two Fe-CN bonds perpendicular to the macrocyclic ligand.

Now a scenario can be built up to explain the experimental results. As both optical and X-ray data evidence (at least) one intermediate state, characterized with a transient peak and a fast change on the fs timescale, we use a phenomenological model to fit the data. It includes an initially photo-induced state (MLCT), which stochastically populates the final HS state where the system undergoes a damped oscillatory motion.

10.1002/chem.201704746

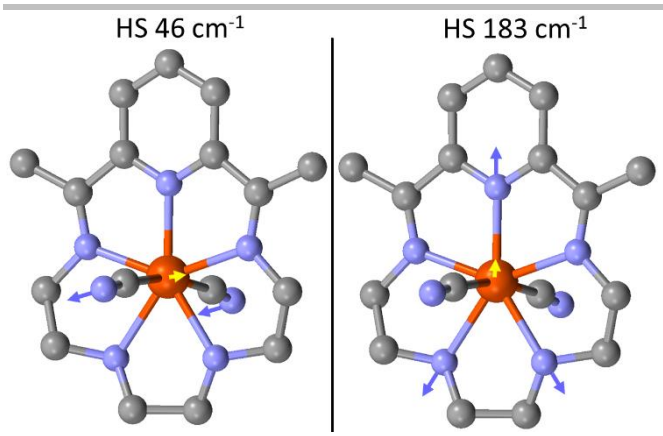

Figure 6. Representation of the vibration modes calculated at 46 cm^{-1} for the the NC-Fe-CN bending and 183 cm^{-1} for some Fe-N stretching in the heptacoordinated HS state.

This simple model, which was used for $Fe(bpy)_3^{2+}$,[3h] is applied to the present XAS data and is able to reproduce all main features of the experimental data (Fig. 4). In particular, photoexcitation at 530 nm (MLCT) creates initially a formal Fe^{3+} state. It was shown in $Fe(bpy)_3^{2+}$ that for the XAS data this change of oxidation state results in a transient negative peak at 7125 eV just after laser excitation, because of the global spectral shift by ≈ 1 eV towards higher energy of the XANES spectra of the MLCT state.[3h] The change towards the HS state (Fe^{II}), accompanied by an increase of the distance between the Fe and the neighbouring atoms is associated with an increase of XAS at 7125 eV, as reported in different systems.

The fit to the XAS time trace in Fig. 4 (& Tab. 1) indicates that the HS state is populated within 150(10) fs and that a 47 cm^{-1} molecular vibration is activated and damped with a 800 fs time constant. Since G09 calculations did not reveal molecular vibrations in the LS state below 55 cm^{-1}, we identify the mode observed as the HS 46 cm^{-1} mode found in molecular calculations (see Fig. 5). This is an indication that the HS state, with heptecoordinated structure, forms rapidly after photo-excitation, although an EXAFS study would be required to state firmly that the complex changes from hexa to heptacoordinated structures. We can also notice that optical pump-probe studies performed up to 80 ps after 490 nm excitation did not reveal slower transformation process (Fig. 7), except the vibrational cooling component (τ_{VC}≈ 1-3 ps). We analyse in a similar way the optical pump-probe data through the OD dynamical time traces shown in Fig. 3, taking also into account a vibrational cooling component. Table 1 lists the physical parameters used for the fits shown in Fig. 3. A time constant $\tau \approx 130(10)$ fs is found for excitation at 490 nm and 530 to describe the decay of the MLCT to the HS state, whereas a 75(10) fs time constant is found for lower energy excitation at 580 and 680 nm to describe the decay of the d-d excitations to the HS state, thus bypassing MLCT. We also observe different optical fingerprints of the intermediates under 530, 580 and 680 nm excitation for the same probing wavelength. Vibrational cooling varies with the probe wavelength, as it is often the case. We also observe the vibration mode at 47 cm^{-1} in Fig. 3a & 3d, but not 3b and 3c, probably because of the signal/noise limitation.

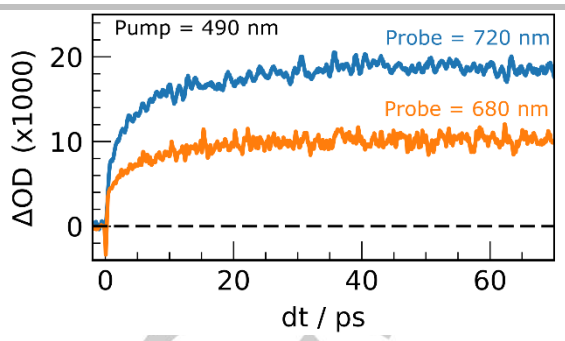

Figure 7. ΔOD time traces at 680 and 720 nm after photoexcitation at 490 nm.

The present study provides experimental results on the LIESST dynamics in the $[Fe(L_{222}N_5)(CN)_2]$ system, with unusual ligand structure. It is then interesting to discuss similarities and differences compared to previous studies of more conventional $Fe^{II}N_6$ systems such as $Fe(bpy)_3^{2+}$, $[Fe(PM\text{-}AZA)_2(NCS)_2]$, $[Fe(phen)_2(NCS)_2]$...[3a, 3h, 4c, 4e, 4h] When these systems are in the LS state, the accessible optical excitation is the MLCT state, as d-d excitation is forbidden, or very weak, because of their almost octahedral symmetry. The main reaction coordinate responsible for their spin state trapping is the elongation of the 6 Fe-N bonds. The FeN_6 breathing mode, with in-phase oscillation of the Fe-N bonds, is then coherently activated during the structural trapping in the HS potential, giving rise to OD or XAS oscillation as the ligand field oscillate. LIESST is also accompanied by the coherent activation of other modes in the HS potential energy surface. For $[Fe(L_{222}N_5)(CN)_2]$, we find a similar time constant $\tau \approx$ 130 fs for the decay towards the HS state after MLCT excitations performed at 530 and 490 nm. However, $[Fe(L_{222}N_5)(CN)_2]$ has a molecular structure different from conventional FeN_6 systems and the structural trapping reaction coordinate is different, with a change from hexacoordinated (LS) to heptacoordinated (HS) and an elongation of the Fe-N and Fe-CN bonds. DFT calculation found HS Fe-ligand modes with Fe-N (183 cm^{-1}, 182 fs period, Fig. 6) or Fe-CN (263 cm^{-1}, 127 fs period) stretching characters, but these are different in nature from the global molecular breathing around 120 cm^{-1} (≈280 fs period) reported in FeN_6 systems. As for $[Fe(L_{222}N_5)(CN)_2]$ the decay from the MLCT to the HS state occurs within ≈ 130 fs, an important structural decoherence occurs during the inter-system crossing for the Fe-N and Fe-CN stretching modes, because their ½ period is shorter than the population time of the HS potential energy surface. These modes are consequently populated incoherently in the HS and cannot give rise to coherent oscillation of XAS or OD signal. For FeN_6 systems, the breathing mode with ≈280 fs period is observed because its half period is longer than the MLCT to HS decay. This condition of half-period longer than the MLCT decay is fulfilled in the case of $[Fe(L_{222}N_5)(CN)_2]$ for the 47 cm^{-1} mode (710 fs period) observed in Fig. 3 and 4, which is coherently populated in the HS potential. This mode modulates XAS and optical data because the associated bending of the NC-Fe-CN groups strongly modifies the local structure around the Fe and also the electronic state. Indeed, because of the sigma character of the Fe-CN bonds, the bending modifies the electronic density around the Fe. For FeN_6 systems, several low-frequency modes are also coherently activated during LIESST, as reported by optical spectroscopy.

Another interesting aspect of $[Fe(L_{222}N_5)(CN)_2]$ compared to FeN_6 systems is that the low symmetry allows optical excitation of the LS state at lower energy than the MLCT, such as d-d excitation at 680 nm. This excitation scheme was also recently discussed in $Fe(pap\text{-}5NO_2)_2$, a FeN_4O_2 ligand-field system, where intense d-d bands were used to induce LIESST.[13] Compared to MLCT excitation, this d-d excitation induces a faster decay towards the HS state and the observed 75 fs timescale is similar to the one found here for $[Fe(L_{222}N_5)(CN)_2]$. This faster decay limits the structural decoherence in the intermediate state(s), which translates in a larger oscillating signal in the final HS state under d-d compared to MLCT excitation, as observed in Fig. 3. Compared to these previous results on more conventional FeN_6 or FeN_4O_2 systems, the present study indicates that the trapping timescales of the HS state, under MLCT (≈ 130 fs) or d-d excitation (≈ 75 fs), are very similar for $[Fe(L_{222}N_5)(CN)_2]$. The different ligand structure involves however different modes in the structural trapping of the process, but only those with ½ period shorter than the population of the HS potential can be observed, and here not those with Fe-N or Fe-CN stretching character. It also should be noticed here that optical pump pulses with duration longer than the MLCT decay preclude the observation of this coherent structural dynamics, as a too long optical pumping will result in dephasing in the population of the HS state. In addition, probe pulses longer than 100 fs will decrease the time resolution, which can make the observation of coherent oscillations difficult or even preclude it. The use of 100 fs (or shorter) optical or X-ray pulses is therefore required to induce and observe coherent structural dynamics. In the present case, the main reason for the structural decoherence is intrinsic to the system and driven by the lifetime of the intermediate(s).

Conclusions

Our femtosecond optical and X-ray absorption studies show that the spin-state switching mechanism in $[Fe(L_{222}N_5)(CN)_2]$ occurs on similar timescales than in more conventional spin-crossover materials of almost octahedral symmetry. The low symmetry of $[Fe(L_{222}N_5)(CN)_2]$ allows both MLCT and d-d like photoexcitations in the LS hexacoordinated state. We found optical fingerprints of these intermediates and a faster decay from d-d to HS than from MLCT to HS, which induces a coherent structural dynamics related to the bending of the N-C-Fe-C-N group. The structural relaxation in the HS state is complex, involving a change of coordination and a large ligand reorganization. We hope that in a near future complementary X-ray-based techniques extending down to the femtosecond range[14] (including spectroscopy, scattering, and diffraction) will make it possible to map in more detail the dynamics of the electronic and structural degrees of freedom, as well as the global structural change from hexacoordinated in the LS state to heptacoordinated in the HS state. This will also help comparing more directly with X-ray the evolution of the structural dynamics as d-d and MLCT excitations induce different pathways on the potential energy surface.

Experimental Section

The complex $[Fe(L_{222}N_5)(CN)_2]$ has been synthesized as already described by Nelson[6]. In details, 1.20 g (6 mmol) of iron chloride tetrahydrate, 1 g (6 mmol) of 2,6-diacetylpyridine, and 0.1 g of sodium dithionite (used as reducing agent to remove traces of trivalent iron ion) were dissolved in 15 mL of methanol and 10 mL of water. The triethylenetetramine (0.876 g, 6 mmol) was added dropwise. The mixture was kept under nitrogen reflux at 75 °C for 16 h approximately (formation of $[Fe(L_{222}N_5)(Cl)_2]$). After filtration to remove traces of impurities, 15 mL of aqueous solution containing an excess of sodium cyanide NaCN (4g; 0.08 mol) and 0.1 g of sodium dithionite was added. This solution was then kept stirring for ca. 6 hours at room temperature. A polycrystalline powder is formed. The solid formed is then filtered and washed with 10 mL of degassed water and dried under vacuum. Finally 0.9 g (yield ~ 40%) of dark purple powder was collected. This powder was then disolved in water for ultrafast experiments.

The time resolved studies of aqueous solution of $[Fe(L_{222}N_5)(CN)_2]$ were performed at room temperature, using two complementary pump/probe techniques. For femtosecond optical pump-probe spectroscopy with ≈60 fs time resolution (RMS), different wavelengths were used for photoexcitation (490, 530, 580 and 680 nm) with similar excitation fluences (≈ 10 $\mu J.mm^{-2}$). Time-resolved OD change measurements were performed at selected wavelengths to track the photoswitching dynamics. The femtosecond optical pump-probe experiments were configured in visible-NIR transmission geometry with a quasi-collinear configuration of pump and probe beams. More details about the experimental set-up are presented in the paper by Lorenc et al.[9] The time resolved X-ray absorption signal of aqueous solution of $[Fe(L_{222}N_5)(CN)_2]$ was also measured at room temperature, using the optical pump / X-ray probe technique through total fluorescence at the X-ray Pump Probe station, LCLS.[10] Lemke et al presented the XAS experimental set-up in more details.[3i] We used a C(111) double crystal monochromator to probe X-ray absorption at 7125 eV, which is known to be very sensitive to the spin state switching in FeII systems. The relative X-ray to optical pulses arrival time was recorded using the timing tool diagnostic.[15] The overall time resolution was found to be ~50 fs RMS.

Acknowledgements

Use of the Linac Coherent Light Source (LCLS), SLAC National Accelerator Laboratory, is supported by the U.S. Department of Energy, Office of Science, Office of Basic Energy Sciences under Contract No. DE-AC02-76SF00515. M.Ca. and E.C. thank ANR (ANR-13-BS04-0002 FEMTOMAT and ANR-15-CE32-0004 BioXFEL) and Centre National de la Recherche Scientifique (CNRS) (PEPS SASLELX) for financial support. Part of this work was performed in the frame of the COST action ECOSTBio. S.Z. thanks Région Bretagne for financial support (ARED 8925/XFELMAT).

Keywords: spin crossover • x-ray absorption spectroscopy • time-resolved spectroscopy • intersystem crossing • LIESST

[1] a) S. Decurtins, P. Gütlich, C. P. Köhler, H. Spiering, A. Hauser, *Chemical Physics Letters* **1984**, *105*, 1-4; b) M. A. Halcrow, *Spin-crossover materials : properties and applications*, Wiley, **2013**.
[2] A. Hauser, *Top Curr Chem* **2004**, *234*, 155-198.
[3] a) G. Aubock, M. Chergui, *Nature Chemistry* **2015**, *7*, 629-633; b) W. K. Zhang, R. Alonso-Mori, U. Bergmann, C. Bressler, M. Chollet, A. Galler, W. Gawelda, R. G. Hadt, R. W. Hartsock, T. Kroll, K. S.

Kjaer, K. Kubicek, H. T. Lemke, H. Y. W. Liang, D. A. Meyer, M. M. Nielsen, C. Purser, J. S. Robinson, E. I. Solomon, Z. Sun, D. Sokaras, T. B. van Driel, G. Vanko, T. C. Weng, D. L. Zhu, K. J. Gaffney, *Nature* **2014**, *509*, 345-348; c) J. K. McCusker, A. Vlček, *Accounts of Chemical Research* **2015**, *48*, 1207-1208; d) K. Hong, H. Cho, R. W. Schoenlein, T. K. Kim, N. Huse, *Accounts of Chemical Research* **2015**, *48*, 2957-2966; e) J. J. McGarvey, I. Lawthers, K. Heremans, H. Toftlund, *Journal of the Chemical Society, Chemical Communications* **1984**, 1575-1576; f) J. K. Mccusker, K. N. Walda, R. C. Dunn, J. D. Simon, D. Magde, D. N. Hendrickson, *Journal of the American Chemical Society* **1993**, *115*, 298-307; g) C. Bressler, C. Milne, V. T. Pham, A. ElNahhas, R. M. van der Veen, W. Gawelda, S. Johnson, P. Beaud, D. Grolimund, M. Kaiser, C. N. Borca, G. Ingold, R. Abela, M. Chergui, *Science* **2009**, *323*, 489-492; h) H. T. Lemke, K. S. Kjær, R. Hartsock, T. Brandt van Driel, M. Chollet, J. M. Glownia, S. Song, D. Zhu, E. Pace, S. F. Matar, M. N. Nielsen, M. Benfatto, K. J. Gaffney, E. Collet, M. Cammarata, *Nat. Commun.* **2017**, *8*, 15342; i) H. T. Lemke, C. Bressler, L. X. Chen, D. M. Fritz, K. J. Gaffney, A. Galler, W. Gawelda, K. Haldrup, R. W. Hartsock, H. Ihee, J. Kim, K. H. Kim, J. H. Lee, M. M. Nielsen, A. B. Stickrath, W. K. Zhang, D. L. Zhu, M. Cammarata, *Journal of Physical Chemistry A* **2013**, *117*, 735-740; j) S. E. Canton, X. Y. Zhang, L. M. L. Daku, A. L. Smeigh, J. X. Zhang, Y. Z. Liu, C. J. Wallentin, K. Attenkofer, G. Jennings, C. A. Kurtz, D. Gosztola, K. Warnmark, A. Hauser, V. Sundstrom, *Journal of Physical Chemistry C* **2014**, *118*, 4536-4545.

[4] a) R. Bertoni, M. Lorenc, H. Cailleau, A. Tissot, J. Laisney, M. L. Boillot, L. Stoleriu, A. Stancu, C. Enachescu, E. Collet, *Nat Mater* **2016**, *15*, 606-610; b) R. Bertoni, M. Lorenc, T. Graber, R. Henning, K. Moffat, J. F. Létard, E. Collet, *Crystengcomm* **2016**, *18*, 7269-7275; c) R. Bertoni, M. Cammarata, M. Lorenc, S. F. Matar, J. F. Letard, H. T. Lemke, E. Collet, *Acc Chem Res* **2015**, *48*, 774-781; d) R. Bertoni, M. Lorenc, A. Tissot, M. L. Boillot, E. Collet, *Coordination Chemistry Reviews* **2015**, *282-283*, 66-76; e) M. Cammarata, R. Bertoni, M. Lorenc, H. Cailleau, S. Di Matteo, C. Mauriac, S. F. Matar, H. Lemke, M. Chollet, S. Ravy, C. Laulhe, J. F. Letard, E. Collet, *Physical Review Letters* **2014**, *113*, 227402; f) R. Bertoni, M. Lorenc, A. Tissot, M. Servol, M. L. Boillot, E. Collet, *Angew Chem Int Ed Engl* **2012**, *51*, 7485-7489; g) E. Collet, N. Moisan, C. Balde, R. Bertoni, E. Trzop, C. Laulhe, M. Lorenc, M. Servol, H. Cailleau, A. Tissot, M. L. Boillot, T. Graber, R. Henning, P. Coppens, M. Buron-Le Cointe, *Phys Chem Chem Phys* **2012**, *14*, 6192-6199; h) A. Marino, M. Cammarata, S. F. Matar, J.-F. Létard, G. Chastanet, M. Chollet, J. M. Glownia, H. T. Lemke, E. Collet, *Structural Dynamics* **2016**, *3*, 023605; i) A. Marino, M. Buron-Le Cointe, M. Lorenc, L. Toupet, R. Henning, A. D. DiChiara, K. Moffat, N. Brefuel, E. Collet, *Faraday Discuss* **2015**, *177*, 363-379; j) A. Marino, P. Chakraborty, M. Servol, M. Lorenc, E. Collet, A. Hauser, *Angewandte Chemie-International Edition* **2014**, *53*, 3863-3867.

[5] M. Cammarata, K. Y. Lin, J. Pruet, H. W. Liu, J. Brodbelt, *Anal Chem* **2014**, *86*, 2534-2542.

[6] S. M. Nelson, P. D. A. McIlroy, C. S. Stevenson, E. Konig, G. Ritter, J. Waigel, *Journal of the Chemical Society, Dalton Transactions* **1986**, 991-995.

[7] R. Ababei, C. Pichon, O. Roubeau, Y. G. Li, N. Brefuel, L. Buisson, P. Guionneau, C. Mathoniere, R. Clerac, *J Am Chem Soc* **2013**, *135*, 14840-14853.

[8] J. S. Costa, C. Balde, C. Carbonera, D. Denux, A. Wattiaux, C. Desplanches, J.-P. Ader, P. Gütlich, J.-F. Létard, *Inorganic Chemistry* **2007**, *46*, 4114-4119.

[9] M. Lorenc, C. Balde, W. Kaszub, A. Tissot, N. Moisan, M. Servol, M. Buron-Le Cointe, H. Cailleau, P. Chasle, P. Czarnecki, M. L. Boillot, E. Collet, *Physical Review B* **2012**, *85*.

[10] M. Chollet, R. Alonso-Mori, M. Cammarata, D. Damiani, J. Defever, J. T. Delor, Y. Feng, J. M. Glownia, J. B. Langton, S. Nelson, K. Ramsey, A. Robert, M. Sikorski, S. Song, D. Stefanescu, V. Srinivasan, D. Zhu, H. T. Lemke, D. M. Fritz, *Journal of Synchrotron Radiation* **2015**, *22*, 503-507.

[11] R. L. Martin, *The Journal of Chemical Physics* **2003**, *118*, 4775-4777.

[12] M. J. e. a. Frisch, *Gaussian, Inc., Wallingford CT* **2016**.

[13] S. Zerdane, L. Wilbraham, M. Cammarata, O. Iasco, E. Rivière, M. L. Boillot, I. Ciofini, E. Collet, *Chem. Sci.* **2017**, *8*, 4978-4986.

[14] M. Chergui, E. Collet, *Chemical Reviews* **2017**, *117*, 11025-11065.

[15] M. Harmand, R. Coffee, M. R. Bionta, M. Chollet, D. French, D. Zhu, D. M. Fritz, H. T. Lemke, N. Medvedev, B. Ziaja, S. Toleikis, M. Cammarata, *Nature Photonics* **2013**, *7*, 215-218.

Entry for the Table of Contents (Please choose one layout)

Layout 1:

COMMUNICATION

We study ultrafast light-induced excited spin-state trapping in the photomagnetic complex $[Fe(L_{222}N_5)(CN)_2]$ by femtosecond optical and X-ray absorption studies. The study, supported by theoretical calculations, reveals different switching pathways involving coherent structural dynamics

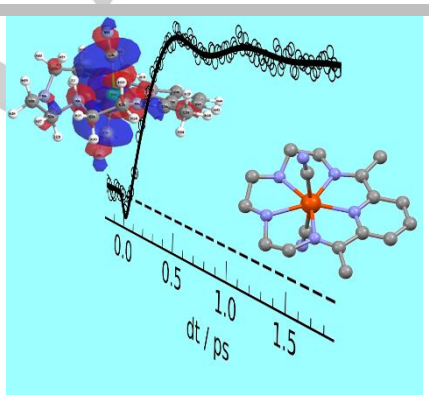

Ultrafast LIESST

S. Zerdane, E. Collet, X. Dong, S. F. Matar, H. F. Wang, C. Desplanches, G. Chastanet, M. Chollet, J. M. Glownia, H.T. Lemke, M. Lorenc, M. Cammarata,**

Page No.* – *Page No.

Electronic and structural dynamics during the switching of the photomagnetic complex $[Fe(L_{222}N_5)(CN)_2]$

Acta Cryst B STRUCTURAL SCIENCE CRYSTAL ENGINEERING MATERIALS
ISSN 2052-5206

Formation of local spin-state concentration waves during the relaxation from a photoinduced state in a spin-crossover polymer

Céline Mariette,[a] Elzbieta Trzop,[a] Serhane Zerdane,[a] Pierre Fertey,[b] Daopeng Zhang,[c,d] Francisco J. Valverde-Muñoz,[c] José-Antonio Real[c] and Eric Collet[a]*

[a]Institut de Physique de Rennes, UMR 6251, Univ. Rennes 1, CNRS, Campus de Beaulieu, 35042 Rennes, France, [b]Synchrotron SOLEIL, BP 48, L'Orme des Merisiers, Saint Aubin, 91192 Gif-sur-Yvette Cedex, France, [c]Instituto de Ciencia Molecular (ICMol), Universidad de Valencia, C/ Catedrático José Beltrán Martínez 2, 46980 Paterna, Spain, and [d]College of Chemical Engineering, Shandong University of Technology, Zibo 255049, China. *Correspondence e-mail: eric.collet@univ-rennes1.fr

Received 3 March 2017
Accepted 24 May 2017

Edited by C. Lecomte, Université de Lorraine, France

Keywords: photo-crystallography; phase transitions; aperiodicity; symmetry breaking.

The complex relaxation from the photoinduced high-spin phase (PIHS) to the low-spin phase of the bimetallic two-dimensional coordination spin-crossover polymer $[Fe[(Hg(SCN)_3)_2](4,4'\text{-bipy})_2]_n$ is reported. During the thermal relaxation, commensurate and incommensurate spin-state concentration waves (SSCWs) form. However, contrary to the steps forming at thermal equilibrium, associated with long-range SSCW order, the SSCWs forming during the relaxation from the PIHS phase correspond to short-range order, revealed by diffuse X-ray scattering. This is interpreted as resulting from the competition between the two types of SSCW order and another structural symmetry breaking, due to ligand ordering, occurring at low temperature and precluding long-range SSCW order.

1. Introduction

Advanced crystallography methods have played an important role in material science for connecting their macroscopic properties to microscopic physics or chemistry. It is fair to say that in this regard Philip Coppens pioneered different types of developments and applications of the field, such as X-ray charge-density analysis (Koritsanszky & Coppens, 2001). In relation to the present research paper, we can also mention the importance of photo-crystallography and its extension to the time domain (Kim *et al.*, 2002; Chen *et al.*, 2003; Coppens *et al.*, 2010; Coppens, 2015) or the investigation of aperiodic structural modulation, at the origin of unusual electrical conductivity in β-(BEDT-TTF)$_2$I$_3$ (Leung *et al.*, 1985) for example.

Among a wealth of materials, showing various types of functions related to structural reorganizations, and which can be driven by external stimuli, spin-crossover (SCO) molecular crystals (Halcrow, 2013; Real *et al.*, 2005; Bousseksou *et al.*, 2011) are very interesting in terms of structural science related to the emergence of functions. These molecular systems are made up of transition-metal atoms in a ligand field, showing bistability between low-spin (LS) and high-spin (HS) states. A thermal conversion from LS to HS states can occur as high temperature favors the HS state of higher entropy (Gütlich & Hauser, 1990). Owing to the electronic redistribution, the HS state is less bonding and corresponds to a higher molecular volume because of an important metal–ligand bond elongation (Huby *et al.*, 2004; Pillet *et al.*, 2004; Guionneau, 2014; Kusz *et al.*, 2001; Collet *et al.*, 2006, 2009). This structural deformation, involving macroscopic volume change, plays an

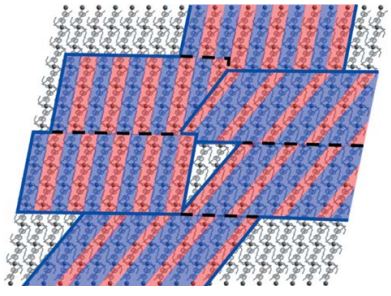

important role in the light-induced electronic spin state trapping (LIESST) as well as reverse-LIESST (Decurtins *et al.*, 1985; Goujon *et al.*, 2008; Marchivie *et al.*, 2002; Trzop *et al.*, 2007; Clements *et al.*, 2016; Hauser, 1986). Time-resolved structural studies, including femtosecond XANES and picosecond X-ray diffraction, have shown that SCO crystals excited by a femtosecond laser pulse undergo complex out-of-equilibrium dynamics. The molecular structural trapping occurs at the molecular level on the 100 fs timescale (Cammarata *et al.*, 2014; Bertoni *et al.*, 2012; Bertoni, Cammarata *et al.*, 2015; Lemke *et al.*, 2015; Zhang *et al.*, 2014; Tissot *et al.*, 2011). It is followed on the ns timescale by lattice expansion, driven by molecular expansion (Bertoni, Lorenc, Cailleau *et al.*, 2016; Bertoni, Lorenc *et al.*, 2015) and on the µs timescale by lattice heating (Collet, Lorenc *et al.*, 2012; Bertoni, Lorenc, Graber *et al.*, 2016). Philip Coppens helped us to explore deeper in the time-domain analysis of the structural changes involved, which is difficult to analyze when the molecular conversion rate is low (Collet, Moisan *et al.*, 2012).

Materials' response to external stimuli is not always as simple as the sum of independent responses of molecules constituting the crystal. In the case of SCO materials, the molecular packing in crystals is associated with elastic coupling between molecules, mediated over a long range through the lattice, which can drive cooperative SCO (Buron-Le Cointe *et al.*, 2012; Tissot *et al.*, 2011; Spiering & Willenbacher, 1989; Slimani *et al.*, 2015; Enachescu *et al.*, 2015; Nicolazzi *et al.*, 2008). In the short range, the molecular packing and the elastic energy costs, related to important structural changes, can also be at the origin of elastic frustration (Watanabe *et al.*, 2016; Paez-Espejo *et al.*, 2016). It can generate stepwise conversions of the fraction of HS molecules γ_{HS} with temperature, as recently discussed in recent reviews (Shatruk *et al.*, 2015; Ortega-Villar *et al.*, 2016). Structural studies of several Fe^{II} systems have reported periodic and aperiodic long-range order of LS and HS states (Boinnard *et al.*, 1994; Chernyshov *et al.*, 2003; Huby *et al.*, 2004; Reger *et al.*, 2001; Money *et al.*, 2007; Luan *et al.*, 2015; Yamada *et al.*, 2006; Sato *et al.*, 2009; Bréfuel *et al.*, 2009, 2010; Collet, Watanabe *et al.*, 2012; Bonnet *et al.*, 2008; Clements *et al.*, 2016; Pillet *et al.*, 2012). In addition, similar HS–LS ordering phenomena were reported for a reduced number of Fe^{III} (Griffin *et al.*, 2011; Li *et al.*, 2013; Vieira *et al.*, 2013; Murnaghan *et al.*, 2014; Harding *et al.*, 2015), Co^{II} (Bhar *et al.*, 2012) and Mn^{III} (Fitzpatrick *et al.*, 2015) complexes. This long-range ordering of molecules in HS and LS states corresponds to the formation of spin-state concentration waves, *i.e.* a periodic spatial modulation of the probability for a crystalline site to populate the HS state (Collet, Watanabe *et al.*, 2012; Marino *et al.*, 2015; Watanabe *et al.*, 2016; Trzop *et al.*, 2016).

We have recently reported a multi-step thermal equilibrium conversion process from complete HS to complete LS phases, in the bimetallic two-dimensional coordination polymer $[Fe[(Hg(SCN)_3)_2](4,4'\text{-bipy})_2]_n$ associated with different intermediate phases with different HS–LS long-range orders on the steps. This multi-step conversion therefore shows similar features to the Devil's staircase-type phase transition in the γ_{HS} *versus* T conversion (Trzop *et al.*, 2016). In addition, more conventional structural phase transitions, related to symmetry breaking related to molecular distortion and/or ligand ordering, can also occur in SCO materials and be coupled or not to the change of spin state (Watanabe *et al.*, 2013; Bréfuel *et al.*, 2009, 2010). Here we present a structural analysis of the photoinduced SCO phenomena in the bimetallic two-dimensional coordination polymer $[Fe[(Hg(SCN)_3)_2](4,4'\text{-bipy})_2]_n$ (1). We briefly summarize thermal equilibrium phase transitions and the structural nature of their changes to focus on the multi-step relaxation process from the photoinduced HS state.

2. Phase transitions at thermal equilibrium for (1)

The multistep spin-state conversion of the two-dimensional bimetallic coordination polymer (1) is illustrated by the thermal dependence of $\chi_M T$ product (χ_M = magnetic susceptibility, T temperature) shown in Fig. 1. It is governed by the thermal population of the diamagnetic LS and paramagnetic HS states and is consequently scaled to the evolution of the fraction of molecules in the HS state γ_{HS}. Magnetic measurements and crystallographic studies revealed different phases and their crystalline structures, already presented in detail elsewhere (Trzop *et al.*, 2016; Zhang *et al.*, 2017), are schematically represented in Fig. 1.

In the interval 300–190 K, $\chi_M T \simeq 3.67$ cm^3 K mol^{-1} corresponds to a phase where the Fe^{II} centers are in the HS ($S = 2$, $\gamma_{HS} = 1$) state. This is the high-spin (HS) high symmetry (hs) phase (HS^{hs}, $P\bar{1}$). In the crystalline structure, there is a single Fe^{II} site lying on an inversion center. In the HS^{hs} phase, the asymmetric unit consists of one axially coordinated N atom belonging to a 4,4′-bipy ligand and two equatorial N atoms belonging to two crystallographically distinct NCS groups (Fig. 2). The average Fe1—N bond length of the $[Fe^{II}N_6]$

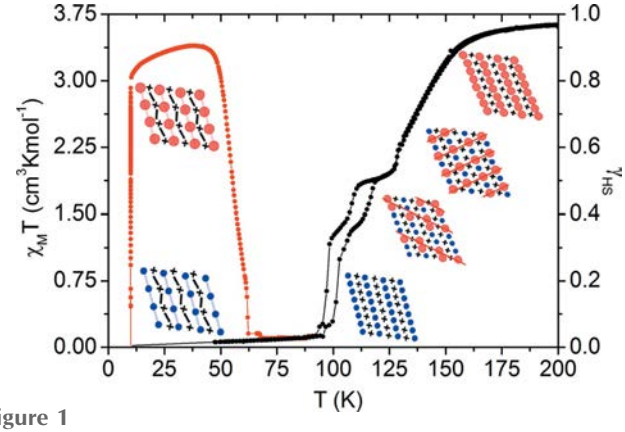

Figure 1
Temperature dependence of $\chi_M T$ (left axis), scaled to HS fraction γ_{HS} (right axis) in the 10–300 K range at thermal equilibrium for (1) (black curves) and in the warming mode after photoexcitation at 10 K by a laser at 660 nm (red curve). The different structures of the bimetallic coordination polymer made of Fe^{II} (HS = red, LS = blue spheres) and Hg^{II} (crosses) connected by (4,4′-bipy) ligands (lines) are schematically represented, with stripes (red lines) forming on the steps.

octahedron, ⟨Fe1—N⟩ = 2.158 (3) Å, is typical for Fe^{II} cations in the HS state. Below 170 K, $\chi_M T$ drops rapidly towards a plateau in the 108–125 K range, indicating that 50% of the Fe sites are in the HS and in the LS states. We have shown that a symmetry breaking occurs on the plateau (Trzop *et al.*, 2016). This cell doubling is characterized by the appearance of superstructure Bragg peaks at $\mathbf{q}_c = \frac{1}{2}\mathbf{a}^* + \frac{1}{2}\mathbf{b}^* + \frac{1}{2}\mathbf{c}^*$, where $\mathbf{a}^*$, $\mathbf{b}^*$ and $\mathbf{c}^*$ refer to the reciprocal lattice of the high-symmetry phase. The structural refinement reveals two different Fe sites: site 1 is mainly LS as characterized by ⟨Fe1—N⟩ ≃ 1.962 (3) Å, whereas site 2 is mainly HS with ⟨Fe2—N⟩ ≃ 2.146 (3) Å. The structure then consists of stripes of molecules in mainly HS or LS states and alternating along $\mathbf{q}_c$ in an ...HS–LS–HS–LS... sequence (Fig. 3*a*). This spin-state concentration wave, commensurate with the high-symmetry lattice, corresponds to a spatial modulation of the HS fraction,

$$\text{SSCW}^{\text{com}}: \quad \gamma^{c}_{HS}(r) = \gamma^{c}_{HS} + (\eta^{c}/2) \times \cos(\mathbf{q}_c \cdot \mathbf{r}), \qquad (1)$$

where X-ray studies give $\gamma^{c}_{HS} \simeq 0.5$ and $\eta^{c} \simeq 0.9$ (Trzop *et al.*, 2016) at 117 K.

On cooling further, a second plateau appears in the interval 96–108 K, where an incommensurate modulation appears, characterized by satellite reflections at $\mathbf{q}_i = 0.48\mathbf{a}^* + 0.35\mathbf{b}^* + 0.42\mathbf{c}^*$. Superspace crystallography showed that it corresponds to a phase where the spatial modulation of the HS fraction is incommensurate with the lattice (Fig. 3*b*). This spin-state concentration wave, incommensurate with the molecular packing, is described as follows

$$\text{SSCW}^{\text{incom}}: \quad \gamma^{i}_{HS}(r) = \gamma^{i}_{HS} + (\eta^{i}/2) \times \cos(\mathbf{q}_i \cdot \mathbf{r}), \qquad (2)$$

with $\gamma^{i}_{HS} = 0.34$ and $\eta^{i} = 0.85$ at 102 K. Since there is no group–subgroup relationship between the SSCW^{com} and the $\text{SSCW}^{\text{incom}}$, the transition between the two phases is reconstructive and first order. These features, related to the formation of different long-range ordered HS–LS sequences on the thermal steps, present some analogies with Devil's staircase-type transformations (Bak & von Boehm, 1980; Fisher & Selke, 1980; Aubry, 1983; Bak & Bruinsma, 1982).

Below ∼95 K the system reaches the low-spin phase of high symmetry (LS^{hs}), which is isostructural to the HS^{hs} phase. The unique Fe site is now LS with ⟨Fe1—N⟩ = 1.961 (3) Å at 90 K. Apart from these intramolecular metric changes, driving volume change, the LS^{hs} structure does not present other relevant differences with respect to the HS^{hs} structure at 220 K (Fig. 2).

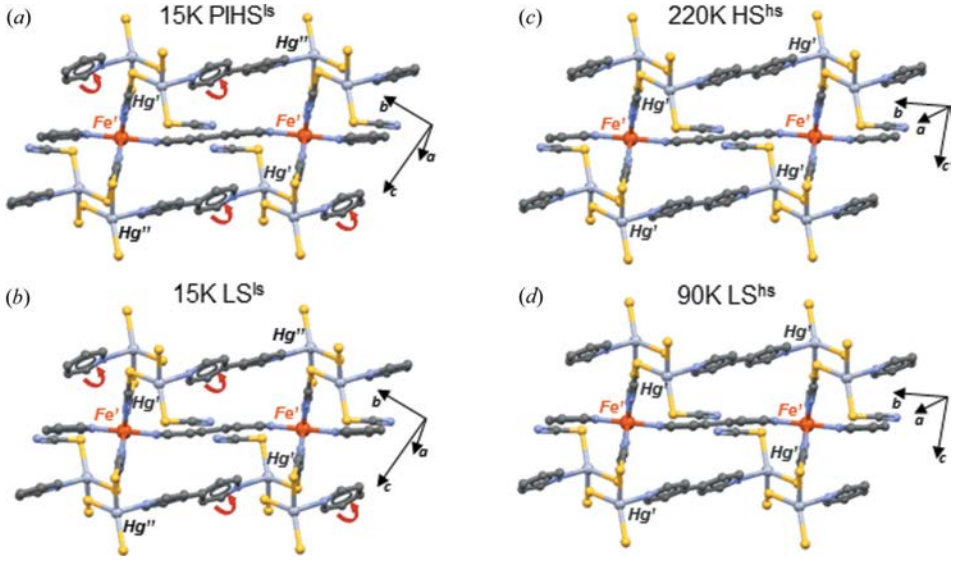

Figure 2
Structures of the isostructural high-symmetry HS^{hs} [220 K, (*c*)] and LS^{hs} [90 K, (*d*)] phases and of the isostructural $PIHS^{ls}$ [15 K, (*a*)] and LS^{ls} [15 K, (*b*)] phases. The symmetry breaking is associated with ligand ordering (tilting of bipy). The unit cell axes are given in the high- and low-symmetry cells. $PIHS^{ls}$ and LS^{ls} are the photoinduced HS low-symmetry (ls) and LS low-symmetry (ls) phases.

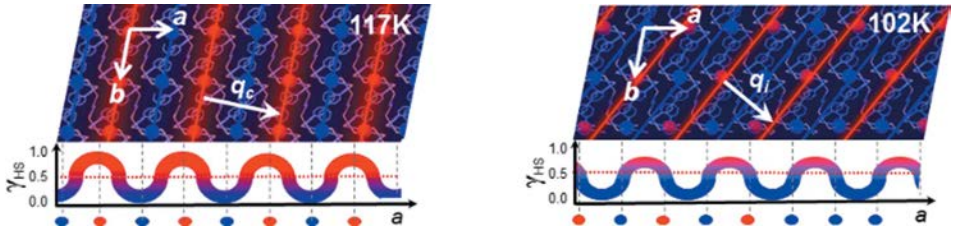

Figure 3
The commensurate spin-state concentration wave SSCW^{com} forming along $\mathbf{q}_c$ (117 K, left) and incommensurate $\text{SSCW}^{\text{incom}}$ (102 K, right) forming along $\mathbf{q}_i$ (projected), showing HS (red) and LS (blue) stripes. The schemes below show the spatial evolution of γ_{HS} over crystalline sites.

3. Ligand ordering in low-symmetry low-spin and photoinduced high-spin phases

Below 85 K, a structural symmetry breaking occurs towards a low-symmetry LS phase (LS^{ls}; Zhang *et al.*, 2017). It corresponds to another unit-cell doubling with respect to the high-symmetry HS^{hs} and LS^{hs} unit cells, with the appearance of Bragg peaks at $\mathbf{q}_L = \frac{1}{2}\mathbf{b}^* + \frac{1}{2}\mathbf{c}^*$. In this doubled unit cell, the $[Fe(\mu\text{-}4,4'\text{-bipy})]^{2+}_n$ chains are made of non-centrosymmetric Fe^{II} sites linked by planar centrosymmetric 4,4′-bipy bridges, while the $[[Hg(SCN)_3]_2(\mu\text{-}4,4'\text{-bipy})]$ units are constituted of two crystallographically distinct Hg(1,2) centers bridged by a non-centrosymmetric 4,4′-bipy bridge. Consequently, several structural rearrangements occur as shown in Fig. 2. The main feature related to this symmetry breaking is the relative twisting of the pyridine rings bridging the two Hg sites while pyridine rings of Fe sites remain planar in the LS^{ls} phase. This is due to the fact that with the cell doubling the inversion symmetry between the pyridine rings

connecting the Fe atoms remains, whereas the one between the pyridine rings connecting the Hg atoms are lost.

We have also reported that the system undergoes LIESST: the magnetic susceptibility of an LS sample at 10 K increases from $\chi_M T \simeq 0.09\ cm^3\ K\ mol^{-1}$ and saturates around $3.0\ cm^3\ K\ mol^{-1}$ after irradiation with red light (λ = 633 nm; Zhang *et al.*, 2017). Once the light irradiation is stopped and the temperature is increased, at a rate of $0.3\ K\ min^{-1}$, $\chi_M T$ reaches a maximum around $3.40\ cm^3\ K\ mol^{-1}$ at 38 K. It is characteristic of the thermal population of the different microstates arising from the zero-field splitting of the photoinduced HS phase (PIHS, $S = 2$). Interestingly, the structure of the photoinduced HS state is not the same as that of the fully HS state existing at thermal equilibrium above 220 K. Previous photocrystallographic studies have shown that with respect to the HS^{hs} structure, the photoinduced state has a low symmetry. The structure of this $PIHS^{ls}$ state is isostructural to the LS^{ls} phase, also characterized by the presence of Bragg peaks at $\mathbf{q}_L = \frac{1}{2}\mathbf{b}^* + \frac{1}{2}\mathbf{c}^*$ with respect to the HS^{hs}. The unit cell also contains a single non-centrosymmetric Fe^{II} site with an average Fe—N bond length $\langle Fe1—N\rangle$ = 2.141 (3) Å, characteristic of the formation of the HS state. This symmetry breaking is also associated with the twisting of the pyridine rings connecting the Hg atoms, as for the LS^{ls} phase (Fig. 2). More details about the LS^{ls} and $PIHS^{ls}$ crystalline structures can be found in Zhang *et al.* (2017).

During the thermal relaxation above 39 K, the magnetic susceptibility drops rapidly and returns to the initial value characteristic of the LS state around 62 K, indicating a complete relaxation from PIHS to LS states. However, this thermal relaxation does not occur in a single step. The derivative curve (Fig. 4) indicates that the relaxation rate is not monotonic, as it is slowing down in the 50–60 K range, where $\gamma_{HS} \simeq 0.5$ and $\gamma_{HS} \simeq 0.33$ are characteristic of steps observed during the thermal crossover, and becomes faster around 60 K. It therefore appears of interest to explore deeper in the analysis of the relaxation process from the $PIHS^{ls}$ phase to track the formation of SSCWs during the relaxation process, and to compare the structural orders with those observed at thermal equilibrium.

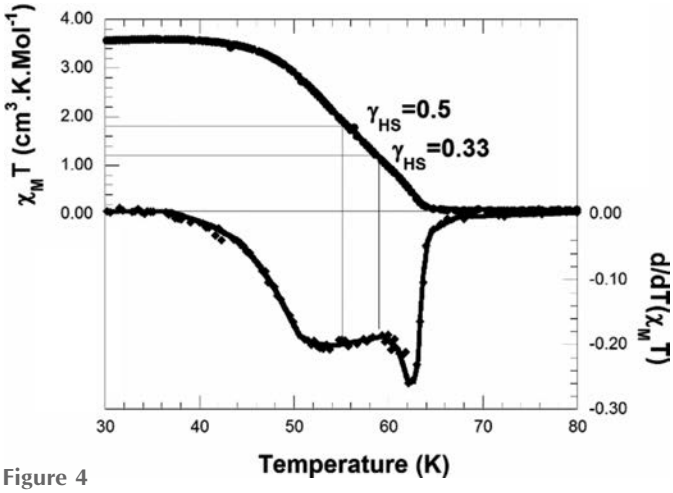

Figure 4
Temperature dependence of $\chi_M T$ in the 30–80 K range in the warming mode after photoexcitation at 10 K by a laser at 633 nm (top half). The derivative with temperature (bottom half) shows a slower relaxation in the 50–60 K range and a faster relaxation above 60 K towards the LS state.

4. Multi-step thermal conversion *versus* thermal relaxation from photoinduced high-spin state

In order to study in detail the structural changes involved in the processes, we performed X-ray diffraction experiments on the CRISTAL beamline at the SOLEIL synchrotron. Single-crystal measurements were performed at different temperatures, before and after light irradiation. We investigated both the thermal phase transitions and the relaxation process from the $PIHS^{ls}$ phase through the evolution of the Bragg peaks and diffuse scattering. We used a He-flow cryojet (Cryocool G2b LT from Cryo Industries of America) to cool the sample down to 20 K, where the $PIHS^{ls}$ phase has a lifetime much longer than 1 h. It is then easy to generate the $PIHS^{hs}$ state with laser excitation, at 633 or 658 nm (Zhang *et al.*, 2017) or at 532 nm in the present work, and then to collect X-ray diffraction data on the diffractometer (Newport-Rigaku Oxford Diffraction, equipped with the Atlas detector). For data analysis, we used the *CrysAlis* software. The wavelength was tuned at 0.513450 Å, using an Si 111 double-crystal monochromator and sagittal focusing. The unit-cell parameters and orientation matrix were refined using *CrysAlisPro* software (Rigaku, 2015). In order to extract the intensity profile along very precise directions, we adopted a two-step method. After unit-cell refinements, parallel (**a***, **b***) reciprocal planes were reconstructed with a resolution of $0.002\ Å^{-1}$ along the **b*** direction. The intensity was then averaged over 20 unit cells to reconstruct a three-dimensional reciprocal unit. Profiles were extracted after a subsequent refinement of the basis vector in the averaged unit cell. In order to increase the contrast, diffuse-scattering profiles were analyzed after filtering from major parasite reflections and Bragg peaks.

The $SSCW^{com}$ forming on the plateau at $\gamma_{HS} \simeq 0.5$ at thermal equilibrium is characterized by the appearance of superstructure Bragg peaks at $\mathbf{q}_c = \frac{1}{2}\mathbf{a}^* + \frac{1}{2}\mathbf{b}^* + \frac{1}{2}\mathbf{c}^*$. Fig. 5 shows that these superstructure peaks are as sharp as general Bragg peaks and characteristic of a long-range ordered $SSCW^{com}$. In a similar way, the satellite reflections at $\mathbf{q}_i = 0.48\mathbf{a}^* + 0.35\mathbf{b}^* + 0.42\mathbf{c}^*$ (102 K, Fig. 5), which appear on the low-temperature plateau, are also sharp and related to the aperiodic but long-range $SSCW^{incom}$. The fit used Gaussian functions with similar FWHM ($0.008 \pm 0.002\ Å^{-1}$) for the different peaks. This width is mainly limited by the experimental resolution.

It is important to recall that the symmetry at T = 95 K is the same as the high-symmetry one, which is reflected in the diffraction image by the fact that the scattered intensity at $\mathbf{q}_c$ and $\mathbf{q}_i$ completely vanishes.

Below 85 K, new superstructure Bragg peaks appear at $\mathbf{q}_L = \frac{1}{2}\mathbf{b}^* + \frac{1}{2}\mathbf{c}^*$,which are characteristic of the symmetry breaking in the LS^{ls} phase, associated with twisting of the pyridine rings. These peaks measured here at 30 K (Fig. 6) are also as sharp as general Bragg peaks, leading us to conclude again that there is

a long-range ligand order at low temperature. The fit in Fig. 6 used Gaussian functions for Bragg peaks and superstructure reflections, with similar FWHM (0.007 ± 0.002 Å^{-1}). The latter value defines our experimental resolution, which is comparable with the one measured on our laboratory set-up.

The photoswitching, showed by magnetic measurements, from LS^{ls} to PIHS^{ls} is characterized by a structural distortion without symmetry breaking. X-ray diffraction measurements allowed a unit-cell volume increase to be seen around 25 Å^3 (Fig. 7), related to the increase of the Fe—N bonds between LS and HS states. This unit-cell volume change is comparable with the ∼35 Å^3 volume increase from LS (90 K) to HS (300 K), which also includes thermal contraction in addition to lattice contraction due to bond shrinking during the spin-state conversion. It is responsible for the shift of the Bragg peaks after photo-excitation, as seen in Fig. 6. The volume contraction observed on warming is characteristic of the relaxation towards the low-spin state and the superstructure peaks at $\mathbf{q}_L$ indicate the relaxation towards the LS^{ls} phase.

It starts at around 45 K and goes on in a non-monotonic way up $\simeq$ 60 K, where the initial volume of the LS state is reached anew. The volume change during the relaxation from the photoinduced HS state occurs at temperatures in good agreement with magnetic data (Fig. 4), and a kind of plateau or slowing down during the relaxation around 50–55 K. These temperatures correlate well with the magnetic data where the relaxation slows down in this temperature range.

Analysis of the diffraction signal in reciprocal space provides key information on the structural processes involved during the relaxation from the PIHS^{ls} phase towards the LS^{ls} phase. On one hand, it should be underlined that the superstructure Bragg peaks, observed at $\mathbf{q}_L = \frac{1}{2}\mathbf{b}^* + \frac{1}{2}\mathbf{c}^*$, are always present during the relaxation (Fig. 6). We could not detect a significant change in the width of these superstructure peaks related to the ligand ordering. We therefore conclude that the

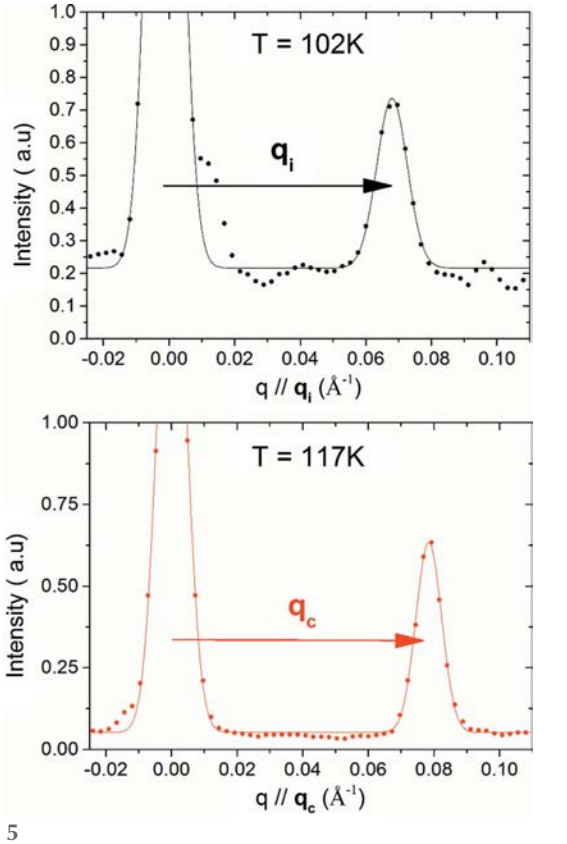

Figure 5
Diffracted X-ray intensity in reciprocal space, reconstructed from diffraction images, showing sharp superstructure Bragg peaks at $\mathbf{q}_c = \frac{1}{2}\mathbf{a}^* + \frac{1}{2}\mathbf{b}^* + \frac{1}{2}\mathbf{c}^*$ at 117 K (bottom). These are related to the formation of the SSCW^{com} on the plateau where $\gamma_{HS} \simeq 0.5$. The sharp satellite reflections observed at $\mathbf{q}_i = 0.48\mathbf{a}^* + 0.35\mathbf{b}^* + 0.42\mathbf{c}^*$ at 102 K are related to the formation of the SSCW^{incom} on the plateau where $\gamma_{HS} \simeq 0.34$ (top).

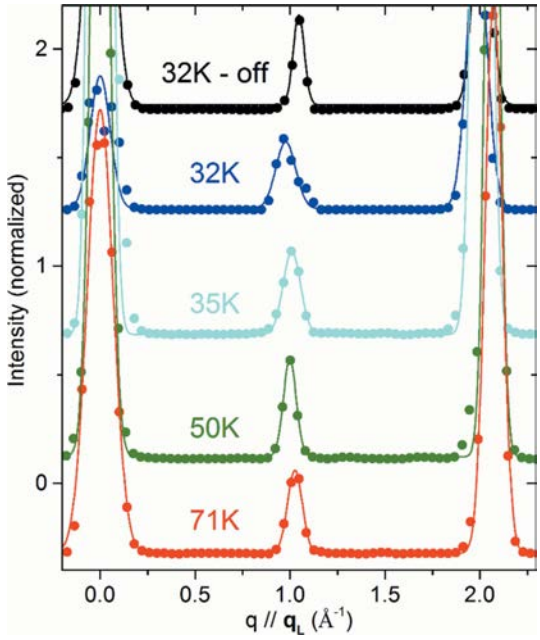

Figure 6
Diffracted X-ray intensity along $\mathbf{q}_L$ between Bragg peaks, showing similar sharp superstructure peaks at $\mathbf{q}_L = \frac{1}{2}\mathbf{b}^* + \frac{1}{2}\mathbf{c}^*$ at 32 K in the LS^{ls} and PIHS^{ls} and at higher temperature during the thermal relaxation from PIHS^{ls} state. The shift of the Bragg peaks along $\mathbf{q}_L$ from the reference Bragg peak at $\mathbf{q} = 0$ is due to lattice expansion at 32 K before and after laser excitation and contraction during relaxation from PIHS.

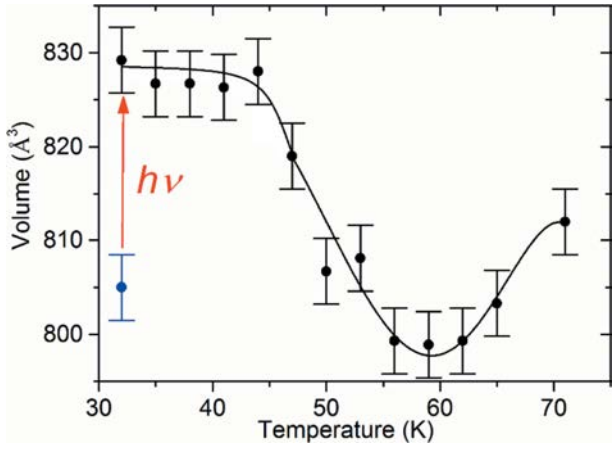

Figure 7
Evolution of the unit-cell volume at 32 K from LS^{ls} to PIHS^{ls} with laser irradiation at 532 nm, and during the thermal relaxation towards the LS^{ls} at higher temperature.

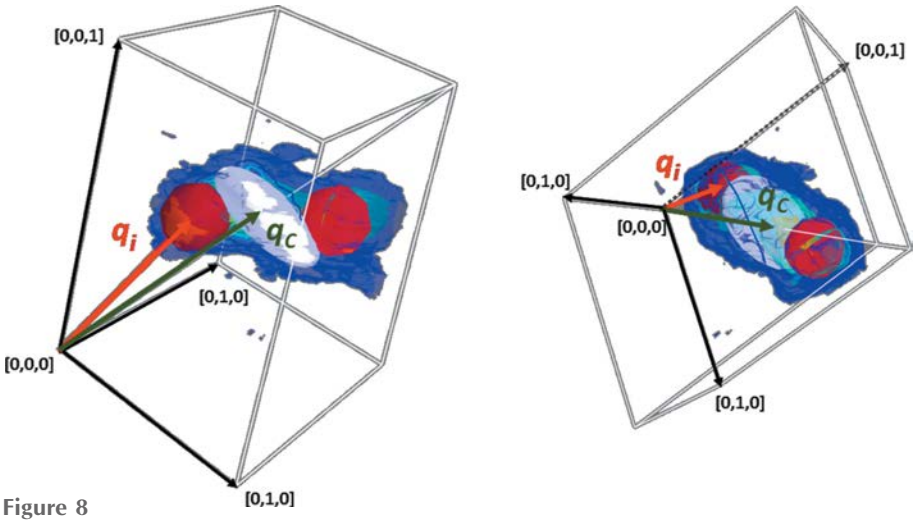

Figure 8
Three-dimensional reconstruction of the diffuse scattering at T = 53 K. Red spheres and white ellipsoids are constructed to fit the diffuse-scattering shape observed around $\mathbf{q}_i$ and $\mathbf{q}_c$, respectively. The white box represents the edges of the reciprocal unit cell and is given by the position of the general Bragg peaks, which are not shown for clarity. This figure enhances the anisotropic shape of the diffuse X-ray scattering around $\mathbf{q}_c = \frac{1}{2}\mathbf{a}^* + \frac{1}{2}\mathbf{b}^* + \frac{1}{2}\mathbf{c}^*$ and isotropic shape around $\mathbf{q}_i = 0.48\mathbf{a}^* + 0.35\mathbf{b}^* + 0.42\mathbf{c}^*$.

photo-switching process, which involves mainly Fe—N elongation, does not induce ligand disorder. Ligands are probably frozen at such a low temperature. On the other hand, we observe an important scattering signal around $\mathbf{q}_c$ and $\mathbf{q}_i$ during the relaxation process (Figs. 8 and 9). X-ray scattering at these specific positions in reciprocal space is characteristic of the formation of SSCW^{com} and SSCW^{incom}. However, we do not observe sharp satellite or superstructure Bragg peaks, contrary to what is observed at thermal equilibrium (Fig. 5). Instead, diffuse scattering is observed around $\mathbf{q}_c$ and $\mathbf{q}_i$ in the 47–56 K range. Above 59 K this diffuse-scattering signal around $\mathbf{q}_c$ and $\mathbf{q}_i$ disappears.

The diffuse-scattering signals around $\mathbf{q}_c$ and $\mathbf{q}_i$ are reminiscent of the spatial fluctuation of the symmetry breaking order parameters and reveal the local formation of the SSCW^{com} and SSCW^{incom}. The coexistence of diffuse signal around $\mathbf{q}_i$ and $\mathbf{q}_c$ at all temperatures results in a complicated peanut-like shape of the diffuse scattering (Fig. 8). Three-dimensional fitting of this shape with three ellipsoids was not possible because of overparametrization. Nevertheless, the resulting iso-intensity surfaces are well reproduced by considering an isotropic pattern around $\mathbf{q}_i$ and a disc shape around $\mathbf{q}_c$. Profiles were extracted around $\mathbf{q}_i$ and $\mathbf{q}_c$ directions (Fig. 9). Owing to the interpenetration of the ellipsoids, 2 maxima are systematically observed at $\mathbf{q}_i$ and 3 maxima at $\mathbf{q}_c$.

We used Lorentzian functions to fit the diffuse signal along $\mathbf{q}$,

$$I(\mathbf{q}) = I_0 + \frac{I_M}{1 + \mathbf{q}^2\xi^2}, \qquad (3)$$

from which we extract the inverse correlation lengths ξ along different $\mathbf{q}$ directions. The broader diffuse scattering at 45 K corresponds to correlation extending over ∼2 unit cells, whereas the sharper diffuse scattering around 51 K corresponds to correlation extending over ∼11 unit cells.

This result can be discussed with regard to a previous study of the stepwise relaxation of another SCO material, where clear X-ray diffraction Bragg peaks signalling the long-range formation of the HS–LS sequence was revealed on the relaxation step (Pillet *et al.*, 2012). Our case constitutes a next step in complexity. The first reason is the multi-step ordering happening during the thermal conversion. However, the key point is certainly the symmetry breaking associated with the twist of the ligand, arising at low temperature. This was not the case in the study reported by Pillet *et al.* (2012), where LS and PIHS states had exactly the same symmetry. The symmetry breaking we observe below 85 K is associated with the ligand ordering along $\mathbf{q}_L$ and characterized by a first symmetry-breaking order parameter. It should be underlined that this symmetry-breaking order parameter has different symmetry from the one related to the formation of the SSCW^{com} ($\mathbf{q}_c$) or of the SSCW^{incom} ($\mathbf{q}_i$). Therefore, reaching the SSCW^{com} or SSCW^{incom} phase from the PIHS^{ls} phase implies a reconstructive phase transition, as there is no group–subgroup relationship between these phases.

Such a first-order transition requires significant thermal energy. On the other hand, a recent theoretical study underlined that the step may hardly appear during the relaxation process because the long-range HS–LS order is difficult to form (Watanabe *et al.*, 2016). This energy barrier, in addition to the two competing ordering phenomena between the formation of local SSCW^{com} (around $\mathbf{q}_c$) and local SSCW^{incom} (around $\mathbf{q}_i$) explains the local character of the SSCW observed during the relaxation. The fit of the diffuse-scattering signal indicates that the spatial orders related to the formation of local SSCW^{com} and local SSCW^{incom} extends over characteristic correlation lengths between 2 and 10 unit cells depending of the temperature and the $\mathbf{q}$ vector. The formation of small domains might be explained by mismatch domain walls between SSCW^{com} and SSCW^{incom} and/or antiphase boundaries associated with a spatial phase shift of the SSCW, as represented schematically in Fig. 10. These 'stacking faults' preclude long-range order.

5. Conclusion

Phase transitions related to spin-crossover phenomena, at thermal equilibrium or during the relaxation from a photo-induced HS state to an LS state, are in most cases single-step and isostructural processes. Sometimes more complicated phase transitions may occur, involving symmetry breaking

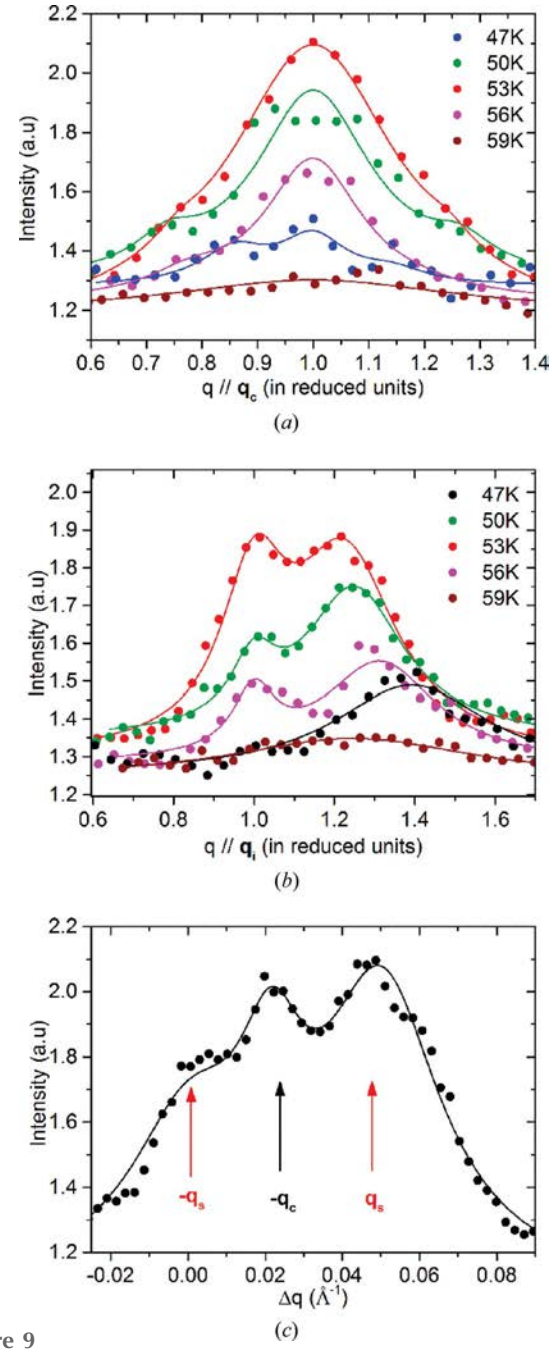

Figure 9
Intensity profiles of the diffuse scattering around $\mathbf{q}_c = \frac{1}{2}\mathbf{a}^* + \frac{1}{2}\mathbf{b}^* + \frac{1}{2}\mathbf{c}^*$ (*a*) and $\mathbf{q}_i = 0.48\mathbf{a}^* + 0.35\mathbf{b}^* + 0.42\mathbf{c}^*$ (*b*) extracted from intensity volume as shown in Fig. 8. Continuous lines are the result of a fit with two or three Lorentzian functions respectively. Part (*c*) shows a profile along the direction $(+\mathbf{q}_i, -\mathbf{q}_i)$ at $T = 53$ K confirming the presence of three maxima.

and/or the formation of SSCWs. Diffraction techniques powerfully reveal the nature of the symmetry breaking and the structural changes involved (intra- and/or intermolecular). The present study reveals an unusual relaxation process from the photoinduced HS state, where HS–LS sequences spatially form, but on short-range order only, as directly shown by the appearance of a diffuse-scattering signal. This type of measurement opens new possibilities to investigate, beyond the average crystalline structure, out-of-equilibrium transformations of materials (Guerin *et al.*, 2010), especially when induced by light excitation.

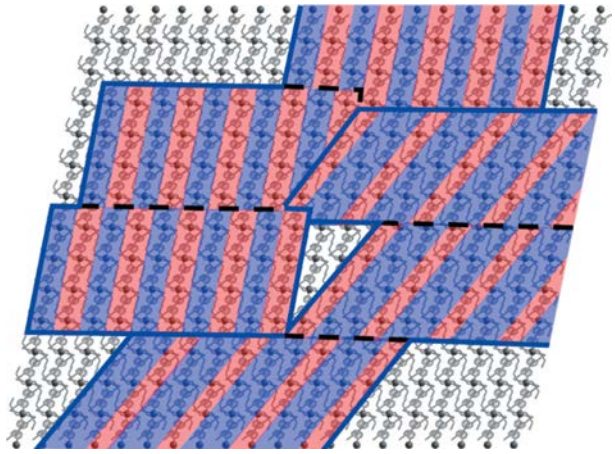

Figure 10
Schematic representation of the formation of locally ordered $SSCW^{com}$ where HS (red) and LS (blue) states alternate on the crystalline sites and $SSCW^{incom}$ domains. Local order may result from the formation of antiphase boundaries (discontinuous lines) between the same 'phases' and domain walls (continuous lines) between $SCCW^{com}$ and $SSCW^{incom}$ domains.

Acknowledgements

This work was supported by the Spanish Ministerio de Economia y Competitividad (MINECO), FEDER, Unidad de Excelencia and the Generalitat Valenciana through PROMETEO/2016/147. FJVM thanks MINECO for a pre-doctoral (FPI) grant. DZ thanks the support from the Natural Science Foundation of China. ET thanks CNRS for post-doctoral funding. EC thanks the National Research Agency and Rennes Metropole for equipment funding.

Funding information

The following funding is acknowledged: Ministerio de Ciencia e Innovación (grant No. CTQ2013-46275-P; grant No. CTQ2016-78341-P); Unidad de Excelencia (grant No. MDM-2015-0538); Generalitat Valenciana (grant No. PROMETEO/2016/147); Natural Science Foundation of China (grant No. 21671121); National Research Agency (grant No. ANR-13-BS04-0002).

References

Aubry, S. (1983). *J. Phys. Fr.* **44**, 147–162.
Bak, P. & Bruinsma, R. (1982). *Phys. Rev. Lett.* **49**, 249–251.
Bak, P. & von Boehm, J. (1980). *Phys. Rev. B*, **21**, 5297–5308.
Bertoni, R., Cammarata, M., Lorenc, M., Matar, S. F., Létard, J. F., Lemke, H. T. & Collet, E. (2015). *Acc. Chem. Res.* **48**, 774–781.
Bertoni, R., Lorenc, M., Cailleau, H., Tissot, A., Laisney, J., Boillot, M. L., Stoleriu, L., Stancu, A., Enachescu, C. & Collet, E. (2016). *Nat. Mater.* **15**, 606–610.
Bertoni, R., Lorenc, M., Graber, T., Henning, R., Moffat, K., Létard, J. F. & Collet, E. (2016). *CrystEngComm*, **18**, 7269–7275.

Bertoni, R., Lorenc, M., Tissot, A., Boillot, M. L. & Collet, E. (2015). *Coord. Chem. Rev.* **282–283**, 66–76.
Bertoni, R., Lorenc, M., Tissot, A., Servol, M., Boillot, M. L. & Collet, E. (2012). *Angew. Chem. Int. Ed.* **51**, 7485–7489.
Bhar, K., Khan, S., Costa, J. S., Ribas, J., Roubeau, O., Mitra, P. & Ghosh, B. K. (2012). *Angew. Chem. Int. Ed.* **51**, 2142–2145.
Boinnard, D., Bousseksou, A., Dworkin, A., Savariault, J. M., Varret, F. & Tuchagues, J. P. (1994). *Inorg. Chem.* **33**, 271–281.
Bonnet, S., Siegler, M. A., Costa, J. S., Molnar, G., Bousseksou, A., Spek, A. L., Gamez, P. & Reedijk, J. (2008). *Chem. Commun.* pp. 5619–5621.
Bousseksou, A., Molnar, G., Salmon, L. & Nicolazzi, W. (2011). *Chem. Soc. Rev.* **40**, 3313–3335.
Bréfuel, N., Collet, E., Watanabe, H., Kojima, M., Matsumoto, N., Toupet, L., Tanaka, K. & Tuchagues, J. P. (2010). *Chem. Eur. J.* **16**, 14060–14068.
Bréfuel, N., Watanabe, H., Toupet, L., Come, J., Matsumoto, N., Collet, E., Tanaka, K. & Tuchagues, J. P. (2009). *Angew. Chem. Int. Ed.* **48**, 9304–9307.
Buron-Le Cointe, M., Hébert, J., Baldé, C., Moisan, N., Toupet, L., Guionneau, P., Létard, J. F., Freysz, E., Cailleau, H. & Collet, E. (2012). *Phys. Rev. B*, **85**, 064114.
Cammarata, M., Bertoni, R., Lorenc, M., Cailleau, H., Di Matteo, S., Mauriac, C., Matar, S. F., Lemke, H., Chollet, M., Ravy, S., Laulhe, C., Letard, J. F. & Collet, E. (2014). *Phys. Rev. Lett.* **113**, 227402.
Chen, L. X., Shaw, G. B., Novozhilova, I., Liu, T., Jennings, G., Attenkofer, K., Meyer, G. J. & Coppens, P. (2003). *J. Am. Chem. Soc.* **125**, 7022–7034.
Chernyshov, D., Hostettler, M., Tornroos, K. W. & Burgi, H. B. (2003). *Angew. Chem. Int. Ed.* **42**, 3825–3830.
Clements, J. E., Price, J. R., Neville, S. M. & Kepert, C. J. (2016). *Angew. Chem. Int. Ed.* **55**, 15105–15109.
Collet, E., Boillot, M.-L., Hebert, J., Moisan, N., Servol, M., Lorenc, M., Toupet, L., Buron-Le Cointe, M., Tissot, A. & Sainton, J. (2009). *Acta Cryst.* B**65**, 474–480.
Collet, E., Buron-Le Cointe, M. & Cailleau, H. (2006). *J. Phys. Soc. Jpn*, **75**, 011002.
Collet, E., Lorenc, M., Cammarata, M., Guérin, L., Servol, M., Tissot, A., Boillot, M. L., Cailleau, H. & Buron-Le Cointe, M. (2012). *Chem. Eur. J.* **18**, 2051–2055.
Collet, E., Moisan, N., Baldé, C., Bertoni, R., Trzop, E., Laulhé, C., Lorenc, M., Servol, M., Cailleau, H., Tissot, A., Boillot, M. L., Graber, T., Henning, R., Coppens, P. & Cointe, M. B. (2012). *Phys. Chem. Chem. Phys.* **14**, 6192–6199.
Collet, E., Watanabe, H., Bréfuel, N., Palatinus, L., Roudaut, L., Toupet, L., Tanaka, K., Tuchagues, J. P., Fertey, P., Ravy, S., Toudic, B. & Cailleau, H. (2012). *Phys. Rev. Lett.* **109**, 257206.
Coppens, P. (2015). *Struct. Dyn.* **2**, 020901.
Coppens, P., Benedict, J., Messerschmidt, M., Novozhilova, I., Graber, T., Chen, Y.-S., Vorontsov, I., Scheins, S. & Zheng, S.-L. (2010). *Acta Cryst.* A**66**, 179–188.
Decurtins, S., Gutlich, P., Hasselbach, K. M., Hauser, A. & Spiering, H. (1985). *Inorg. Chem.* **24**, 2174–2178.
Enachescu, C., Nishino, M., Miyashita, S., Boukheddaden, K., Varret, F. & Rikvold, P. A. (2015). *Phys. Rev. B*, **91**, 104102.
Fisher, M. E. & Selke, W. (1980). *Phys. Rev. Lett.* **44**, 1502–1505.
Fitzpatrick, A. J., Trzop, E., Muller-Bunz, H., Dirtu, M. M., Garcia, Y., Collet, E. & Morgan, G. G. (2015). *Chem. Commun.* **51**, 17540–17543.
Goujon, A., Varret, F., Boukheddaden, K., Chong, C., Jeftić, J., Garcia, Y., Naik, A. D., Ameline, J. C. & Collet, E. (2008). *Inorg. Chim. Acta*, **361**, 4055–4064.
Griffin, M., Shakespeare, S., Shepherd, H. J., Harding, C. J., Létard, J. F., Desplanches, C., Goeta, A. E., Howard, J. A. K., Powell, A. K., Mereacre, V., Garcia, Y., Naik, A. D., Müller-Bunz, H. & Morgan, G. G. (2011). *Angew. Chem. Int. Ed.* **50**, 896–900.
Guerin, L., Hebert, J., Buron-Le Cointe, M., Adachi, S., Koshihara, S. Y., Cailleau, H. & Collet, E. (2010). *Phys. Rev. Lett.* **105**, 246101.
Guionneau, P. (2014). *Dalton Trans.* **43**, 382–393.
Gütlich, P. & Hauser, A. (1990). *Coord. Chem. Rev.* **97**, 1–22.
Halcrow, M. A. (2013). *Spin-Crossover Materials: Properties and Applications.* New York: Wiley.
Harding, D. J., Phonsri, W., Harding, P., Murray, K. S., Moubaraki, B. & Jameson, G. N. L. (2015). *Dalton Trans.* **44**, 15079–15082.
Hauser, A. (1986). *Chem. Phys. Lett.* **124**, 543–548.
Huby, N., Guérin, L., Collet, E., Toupet, L., Ameline, J.-C., Cailleau, H., Roisnel, T., Tayagaki, T. & Tanaka, K. (2004). *Phys. Rev. B*, **69**, 020101.
Kim, C. D., Pillet, S., Wu, G., Fullagar, W. K. & Coppens, P. (2002). *Acta Cryst.* A**58**, 133–137.
Koritsanszky, T. S. & Coppens, P. (2001). *Chem. Rev.* **101**, 1583–1628.
Kusz, J., Spiering, H. & Gütlich, P. (2001). *J. Appl. Cryst.* **34**, 229–238.
Lemke, H. T., Kjaer, K. S., Hartsock, R., Brandt van Driel, T., Chollet, M., Glownia, J. M., Song, S., Zhu, D., Pace, E., Nielsen, M. N., Benfatto, M., Gaffney, K. J., Collet, E. & Cammarata, M. (2015). *arXiv*: 1601.01244.
Leung, P. C. W., Emge, T. J., Beno, M. A., Wang, H. H., Williams, J. M., Petricek, V. & Coppens, P. (1985). *J. Am. Chem. Soc.* **107**, 6184–6191.
Li, Z.-Y., Dai, J.-W., Shiota, Y., Yoshizawa, K., Kanegawa, S. & Sato, O. (2013). *Chem. Eur. J.* **19**, 12948–12952.
Luan, J., Zhou, J., Liu, Z., Zhu, B., Wang, H., Bao, X., Liu, W., Tong, M.-L., Peng, G., Peng, H., Salmon, L. & Bousseksou, A. (2015). *Inorg. Chem.* **54**, 5145–5147.
Marchivie, M., Guionneau, P., Howard, J. A. K., Chastanet, G., Letard, J. F., Goeta, A. E. & Chasseau, D. (2002). *J. Am. Chem. Soc.* **124**, 194–195.
Marino, A., Buron-Le Cointe, M., Lorenc, M., Toupet, L., Henning, R., DiChiara, A. D., Moffat, K., Brefuel, N. & Collet, E. (2015). *Faraday Discuss.* **177**, 363–379.
Money, V. A., Carbonera, C., Elhaïk, J., Halcrow, M. A., Howard, J. A. K. & Létard, J. (2007). *Chem. Eur. J.* **13**, 5503–5514.
Murnaghan, K. D., Carbonera, C., Toupet, L., Griffin, M., Dirtu, M. M., Desplanches, C., Garcia, Y., Collet, E., Letard, J. F. & Morgan, G. G. (2014). *Chem. Eur. J.* **20**, 5613–5618.
Nicolazzi, W., Pillet, S. & Lecomte, C. (2008). *Phys. Rev. B*, **78**, 174401.
Ortega-Villar, N., Muñoz, C. M. & Real, A. J. (2016). *Magnetochemistry*, **2**, 16.
Paez-Espejo, M., Sy, M. & Boukheddaden, K. (2016). *J. Am. Chem. Soc.* **138**, 3202–3210.
Pillet, S., Bendeif, E.-E., Bonnet, S., Shepherd, H. J. & Guionneau, P. (2012). *Phys. Rev. B*, **86**, 064106.
Pillet, S., Hubsch, J. & Lecomte, C. (2004). *Eur. Phys. J. B*, **38**, 541–552.
Real, J. A., Gaspar, A. B. & Munoz, M. C. (2005). *Dalton Trans.* pp. 2062–2079.
Reger, D. L., Little, C. A., Young, V. G. & Pink, M. (2001). *Inorg. Chem.* **40**, 2870–2874.
Rigaku (2015). *CrysAlisPro.* 1.171.38.41 or 1.171.37.35h. Rigaku Oxford Diffraction, Oxford, England.
Sato, T., Nishi, K., Iijima, S., Kojima, M. & Matsumoto, N. (2009). *Inorg. Chem.* **48**, 7211–7229.
Shatruk, M., Phan, H., Chrisostomo, B. A. & Suleimenova, A. (2015). *Coord. Chem. Rev.* **289–290**, 62–73.
Slimani, A., Boukheddaden, K. & Yamashita, K. (2015). *Phys. Rev. B*, **92**, 014111.
Spiering, H. & Willenbacher, N. (1989). *J. Phys. Condens. Matter*, **1**, 10089–10105.
Tissot, A., Bertoni, R., Collet, E., Toupet, L. & Boillot, M.-L. (2011). *J. Mater. Chem.* **21**, 18347.
Trzop, E., Buron-Le Cointe, M., Cailleau, H., Toupet, L., Molnar, G., Bousseksou, A., Gaspar, A. B., Real, J. A. & Collet, E. (2007). *J. Appl. Cryst.* **40**, 158–164.

Trzop, E., Zhang, D., Piñeiro-Lopez, L., Valverde-Muñoz, F. J., Carmen Muñoz, M., Palatinus, L., Guerin, L., Cailleau, H., Real, J. A. & Collet, E. (2016). *Angew. Chem. Int. Ed.* **55**, 8675–8679.

Vieira, B. J. C., Coutinho, J. T., Santos, I. C., Pereira, L. C. J., Waerenborgh, J. C. & da Gama, V. (2013). *Inorg. Chem.* **52**, 3845–3850.

Watanabe, H., Brefuel, N., Collet, E., Toupet, L., Tanaka, K. & Tuchagues, J. P. (2013). *Eur. J. Inorg. Chem.* **2013**, 710–715.

Watanabe, H., Tanaka, K., Bréfuel, N., Cailleau, H., Létard, J.-F., Ravy, S., Fertey, P., Nishino, M., Miyashita, S. & Collet, E. (2016). *Phys. Rev. B*, **93**, 014419.

Yamada, M., Hagiwara, H., Torigoe, H., Matsumoto, N., Kojima, M., Dahan, F., Tuchagues, J.-P., Re, N. & Iijima, S. (2006). *Chem. Eur. J.* **12**, 4536–4549.

Zhang, D., Trzop, E., Valverde-Munoz, F. J., Piñeiro-López, L., Muñoz, M. C., Collet, E. & Real, J. A. (2017). *Cryst. Growth Des.* **17**, 2736–2745.

Zhang, W. K. *et al.* (2014). *Nature*, **509**, 345–348.